Design of electrical adaptive stimulators for different pathological contexts : a global approach

Florian Kölbl

▶ **To cite this version:**

Florian Kölbl. Design of electrical adaptive stimulators for different pathological contexts : a global approach. Electronics. Université de Bordeaux, 2014. English. NNT : 2014BORD0253 . tel-01191392

HAL Id: tel-01191392
https://theses.hal.science/tel-01191392

Submitted on 1 Sep 2015

HAL is a multi-disciplinary open access archive for the deposit and dissemination of scientific research documents, whether they are published or not. The documents may come from teaching and research institutions in France or abroad, or from public or private research centers.

L'archive ouverte pluridisciplinaire **HAL**, est destinée au dépôt et à la diffusion de documents scientifiques de niveau recherche, publiés ou non, émanant des établissements d'enseignement et de recherche français ou étrangers, des laboratoires publics ou privés.

université de BORDEAUX

Thèse de Doctorat

de l'Université de Bordeaux

École doctorale des Sciences Physiques et de l'Ingénieur

Spécialité Electronique

Préparée au Laboratoire IMS

Par Florian Kölbl

Design of electrical adaptive stimulators for different pathological contexts, a global approach

---

Soutenue le 1 Décembre 2014

Après avis de :

M. Andreas Demosthenous	Professeur des Universités - University College London
M. David Guiraud	Directeur de Recherches - LIRMM, INSERM

Devant la commission d'examen formée de:

M. Andreas Demosthenous	Professeur des Universités - University College London	Rapporteur
M. David Guiraud	Directeur de Recherche - LIRMM, INSERM	Rapporteur
M. Abdelhamid Benazzouz	Directeur de Recherche - IMN, INSERM	Examinateur
M. Guy Cathébras	Professeur des Universités - Université de Montpellier 2	Examinateur
M. Eric McAdams	Professeur des Universités - INSA Lyon	Examinateur
M^{me} Noëlle Lewis	Professeur des Universités - Université de Bordeaux	Directrice de thèse
M^{me} Sylvie Renaud	Professeur des Universités - INP Bordeaux	Co-directrice de thèse

1441 • 1896 • 2014
Université de Bordeaux

Thèse réalisée
dans le laboratoire **IMS**
au sein de l'équipe **Elibio**.

Université de Bordeaux
Laboratoire IMS
CNRS UMR-5218
351, cours de la Libération
33405 TALENCE Cedex

REMERCIEMENT

BIEN que ce document soit rédigé en anglais, je me permets d'écrire ces quelques mots en français. Je voudrais en tout premier lieu remercier Claude Pellet pour m'avoir accueilli dans le laboratoire IMS pendant la réalisation de ces travaux de thèse.

Mes sincères remerciements vont à Sylvie Renaud et Noëlle Lewis qui ont dirigé cette thèse et m'ont encadré durant trois années. Merci pour votre soutien sans faille et en toutes circonstances, l'aide précieuse et les longues discussions. Il est agréable de travailler à vos côtés et vous m'avez fait "grandir".

Je tiens à remercier chaleureusement David Guiraud et Andreas Demosthenous, rapporteurs de cette thèse, pour leurs lecture et commentaires sur ce manuscrit. Je remercie également les membres du jury, Eric McAdams ainsi que Guy Cathébras, son aide m'a d'ailleurs été précieuse concenrnant les technologies HV, et je ne pourrais en oublier le président, Abdelhamid Benazzouz ; merci d'avoir accepté d'être dans ce jury et merci pour ces quelques années de collaboration intense qui m'ont fait découvrir des horizons scientifiques que je n'aurai pas pensés abordables avant ma thèse.

Je signe seul ce manuscrit, cependant je peux m'empêcher d'avoir une pensée pour beaucoup de personnes qui y ont contribué :

- Gilles pour ces trois années de travail commun. Comment ne pas te consacrer ce paragraphe ? Ces moments sont inoubliables pour moi, nous avons réussi à allier la bonne humeur et l'acharnement même dans les moments difficiles. Je suis fier d'avoir travaillé avec toi,

- Jocelyn Sabatier pour le temps passé sur la modélisation de l'électrode, ces longues discussions sur la modélisation,

- Aswhin Mangalore, nous n'avons travaillé ensemble que sur la fin de ces travaux et pourtant je suis toujours surpris du chemin parcouru,

- les petites mains qui ont contribué aux réalisations, figures, circuits ; j'ai eu de nombreux stagiaires : Florent Berthier, Mathieux Rosé, Raphael Guillaume, Kaitlyn Waldie, Mohamed Kaber Sidi El Messioub et Jonathan Castelli,

- les biologistes sans qui ce travail n'aurait pas de sens : Fredéric Naudet, Emilie Faggiani, Bastien Ribot, Blaise Yvert, Sébastien Joucla et Ajay Pal.

Je voudrais également remercier tous ceux qui m'ont supporté et aidé au quotidien : Yannick, Jean, François, Gwendal, Matthieu, Fillipo, Jean-Baptiste, Adam, Antoine, Arnaud, Adeline, Farida, Simone... et de manière générale les membres d'Elibio, AS2N et BioEM. Merci aussi à mes amis proches : Sandra, Christelle, Rémy, Laure, Charlotte...

Merci également à ma famille, Martine et Joseph, Simone, Gisèle et Fernand, ainsi Blandine, Pierre et Eléonore qui a apporté du sourire à ma dernière année de thèse ! Vous m'avez toujours soutenu, je voulais vous dédier ce travail.

RÉSUMÉ

La stimulation électrique des tissus neuronaux est une technique largement utilisée dans la recherche en neuroscience et à des fins thérapeutiques. Ce travail est une contribution à la conception des circuits et systèmes électroniques de stimulation. De tels circuits sont requis dans quatre projets multi-disciplinaires en cours dans l'équipe Elibio de l'IMS, présentés dans ce document :

- *STN-Oscillations* (ANR 08-MNPS-036) concernant l'étude de la *Stimulation Cérébrale Profonde* (SCP),
- *HYRENE* (ANR 2010-Blan-031601), ayant pour but le développement d'un système hybride de restauration de l'activité motrice dans le cas d'une lésion de la moelle épinière,
- *BRAINBOW* (European project FP7-ICT-2011-C), ayant pour objectif l'élaboration de neuro-prothèses innovantes capables de restaurer la communication autour de lésions cérébrales,
- *CENAVEX* (ANR et NSH AN13-NEUIC-0001-01), visant au développement d'un système de stimulation en boucle fermée pour le contrôle de la respiration.

Cette thèse propose une approche de conception globale qui aboutira au développement d'un système multi-applications, prenant en compte les spécificités de chaque contexte.

Dans un premier temprs, afin d'évaluer les contraintes liées à l'expérimentation *in vivo* et *in vitro*, deux stimulateurs spécifiques ont été réalisés. Le premier permet la SCP chronique du rat, résout la contrainte énergétique à l'aide d'une gestion dynamique de l'alimentation. Ce dispositif a été fabriqué et implanté *in vivo* avec succès. Une expérimentation à long terme a été effectuée afin de valider ses propriétés sur l'animal. Dans un second temps, un autre stimulateur a été conçu en utilisant un FPAA (*Field Programmable Analog Array*). La conception de ce circuit se concentre sur l'équilibrage des charges nécessaire à l'innocuité des sytèmes. L'architecture obtenue permet une stimulation biphasique adaptative résultant en un faible courant équivalent de fuite (moins d'un nano Ampère).

Afin d'aboutir à un stimulateur multi-application, un travail préliminaire de modélisation de l'impédance de l'électrode, l'élément de charge du circuit de stimulation, a été mené. Une méthode de mesure et d'identification d'un modèle non-linéaire est détaillée, basée sur une approche par multi-modèles et fractionnaire.

L'approche multi-application est ensuite mise en oeuvre, basée sur un effet d'échelle pour le dimensionnement des stimulateurs. Cet effet d'échelle lie la géométrie de l'électrode, le nombre de canaux requis par application et les niveaux de courant mis en jeu : cet effet permet de proposer une architecture de circuit multi-application. Un circuit intégré démontrant la faisabilité d'un tel système a été conçu, fabriqué et testé avec succès. Un système de stimulation multi-application basé sur ce circuit a été conçu, permettant de nouvelles recherches sur les quatre contextes physiopathologiques présentés.

Enfin, un critère de mérite dédié à la stimulation est proposé. Ce critère prend en compte l'efficacité énergétique et l'équilibrage des charges afin d'évaluer le degré d'optimisation d'un circuit ou d'un système. Un tel critère de mérite est un concept novateur qui devrait permettre une optimisation rationnelle des architectures de stimulation.

Mots Clés :

Stimulation Electrique, Système Nerveux, Impédance des Electrodes, Conception de Circuits Intégrés Analogiques.

ABSTRACT

ELECTRICAL stimulation of neural tissues is a widely used technique for both neuroscience explorations and innovative medical devices. This work is a contribution to the design of electrical stimulation circuits and systems. Stimulators are part of the experimental setup in several multi-disciplinary projects conducted at IMS (group *Elibio*), presented in this document:

- *STN-Oscillations* (French ANR 08-MNPS-036), studying *Deep Brain Stimulation* mechanisms (DBS),
- *HYRENE* (French ANR 2010-Blan-031601), aimed at developing a hybrid system coupling artificial and biological neural networks to restore locomotion after spinal cord lesion,
- *BRAINBOW* (European Project FP7-ICT-2011-C), working on designing a neuro-prosthesis capable of restoring lost communication between neuronal circuits,
- *CENAVEX* (French ANR and American NSH AN13-NEUIC-0001-01), proposing a novel design for a closed-loop system for respiration control.

This thesis integrates the specificities of each context and considers global therapeutic application issues, with the aim of proposing an original, global approach to designing the architecture of a multi-application stimulator.

First, in order to evaluate the constraints related to our *in vivo* and *in vitro* contexts, an embedded stimulator for chronic DBS experiments in rodents was developed and successfully implanted *in vivo*. This design was optimized for power management during long-term experiments. The stimulator characteristics were assessed with behavioural tests on a rat population. Then a second, specific stimulator was designed using *Field Programmable Analog Arrays* for accurate charge balancing, as well as to fulfil strong constraints to ensure tissue integrity. The proposed charge-sensing architecture produced adaptive biphasic stimulation with sub-nano ampere DC-equivalent current.

With a view to a global approach to stimulator design, an accurate model of the electrode impedance was built, to represent the concrete load of a stimulator. A measurement protocol based on biphasic current-controlled solicitations and a modelling procedure relying on an original fractional multi-model are described.

The first step in this multi-application design approach was to investigate an electrical sizing scale effect. This involves electrode geometry, the number of channels per application, and the implied current levels. A proof-of-concept ASIC was designed and successfully tested. A board for adaptive stimulation was then able to be deployed in the ongoing research projects.

Finally, a dedicated Figure of Merit is proposed for stimulation. This criterion takes energy efficiency and charge balancing into account to quantify the degree of optimization of a circuit or system. This Figure of Merit is a novel concept that facilitates rational optimization of stimulation architectures.

Keywords:
Electrical Stimulation, Nervous System, Electrodes Impedance, Analog IC Design.

CONTENTS

INTRODUCTION

ACTIVE implantable medical devices are used to treat numerous pathologies. Based on combined advances in neuroscience and electronics, a growing number of neuroprostheses, from Deep Brain Stimulation for Parkinson's Disease to promising retinal implants, have been designed and implanted, significantly improving patients' quality of life. Stimulation implants are complex heterogeneous systems, systematically designed for a specific application, with a corresponding set of specifications and constraints. The design workflow is thus a challenging step in developing novel therapeutic devices. This research was conducted in the *Elibio* group, which focuses on electronics interacting with biology, with a special interest in adaptive circuits involved in hybrid, closed-loop systems. In the group's ongoing multidisciplinary projects, stimulation circuits are used to induce a physiological response after pathological signature recognition. Considering the variety of application targets, a global approach was adopted to designing stimulation circuits and systems, resulting in the design and fabrication of a multi-application system.

To reach this final objective, preliminary research was conducted into specific systems addressing one *in vivo* and one *in vitro* applications. These investigations highlighted the general design rules of stimulation circuits, as well as illustrating the differences between state of the art stimulation systems. The terminal load of stimulators - electrodes - was also studied. The electrode-tissue interface is naturally dependent on the application and thus highlights its specificities. As electrode-tissue impedance is a required quantity in sizing electrical stimulation front-ends, it is a natural starting point for a global design approach.

This document is divided into three parts. The first part explores the scientific context. Chapter 1 provides an overview of the basic principles of electrical stimulation of the nervous system, illustrated with the physiopathological context of the research projects. Chapter 2 describes materials, circuits, and systems for electrical stimulation, based on the state of the art.

The second part presents two specific designs that have been implemented. Chapter 3 explains the design, fabrication, testing, and biological assessment of an embedded stimulator for chronic Deep Brain Stimulation in rodents, with a special focus on optimizing power consumption. Chapter 4 presents the design of a solution addressing tissue safety and stimulation efficiency, tested using *Field Programmable Analog Arrays*, in collaboration with the CaDSP research group at *Georgia Institute of Technology* (Atlanta, USA). This system is an example of charge balancing optimization.

The third part formalizes the global stimulator design approach. Chapter 5 is dedicated to electrode-tissue impedance, giving details of a measurement bench and an *in vivo* compatible protocol, leading jointly to the identification of a fractional, non-linear model. Chapter 6 outlines the principle of the multi-application architecture. A scale effect, combining loading impedance and current level, is presented as the starting point for the design flow. The design of a proof-of-concept IC and its integration in a system are then explained. Chapter 7 proposes a stimulation-dedicated Figure Of Merit (FOM), quantifying the degree of optimization, based on the previous work - the two specific designs and the multi-application approach - and a collaboration with the Sensors Systems and Circuits research group at *University College London* (UK). The FOM was based on energy efficiency and the charge-balancing metric explored in part II, thus facilitating further optimization of a multi-application stimulation system.

PART I

SCIENTIFIC CONTEXT

"Men whose research is based on shared paradigms are committed to the same rules and standards for scientific practice. That commitment and the apparent consensus it produces are prerequisites for normal science, i.e., for the genesis and continuation of a particular research tradition."

T. S. KUHN, *Structures of Scientific Revolutions*, P. 11, 1962

CHAPTER 1

ELECTROPHYSIOLOGY AND NERVOUS SYSTEM

ELECTRICAL stimulation is a widely-used technique for induce reactions in excitable cells and tissues. Electronic implants have extended the range of possible therapeutic application. However, electrical stimulation is still a subject of research: in electrophysiology, an accurate understanding of the phenomena underlying tissue excitability leads to improvements in actual implants, thus increasing patients' quality of life. In the electrical engineering field, electrical stimulation applications are challenging in terms of integration and adaptation to their context.

Dealing with these aspects requires a general understanding of electrical stimulation. While the history of electrophysiology and electrical engineering share common references, state-of-the-art electrical stimulation is closely linked to biology. This chapter explains external stimulation and its applications. A historical approach is followed by a detailed description of the biology of the neural system and neural excitable cells. An explanation of the principle behind electrical cells is followed by four examples of electrophysiological stimulation likely to be covered by a multi-application stimulation system.

1.1 A brief history of electrical stimulation

The link between biology and electricity has been made for more than two millennia, however it was not studied really as long as understanding of both biological and electrical phenomena was weak. A general time-line of the evolution of stimulation is constructed in figure 1.1(a). The first modern foundation of experimental electrophysiology was performed around 1660 by the Dutch biologist Jan Swammerdam. One of these experiments is illustrated in the figure 1.1(b). This setup is based on a nerve-muscle preparation, on which an 'irritation' of the nerve can be performed, inducing a mechanical reaction of the muscle. The irritation was performed with a silver wire that could cause electrical stimulation (Cobb, 2002).

First enhancements of the stimulation were made at the end of the 19th century. The first demonstration of a stimulation basic circuit was performed after the invention of Leyden jar, the first electrical storage device. The best example is the experiment performed by Galvani and Aldini (1792) as illustrated by figure 1.1(c), on 'animal electricity'. This experiment illustrated the electrical nature of the neural impulse and allowed a first investigation correlating stimulation strength and mechanical response. It is also the first demonstration of functional electrical stimulation on a limb.

Further and similar experiments were performed by Volta (1800). In a letter dated of 1800, A. Volta signs a major contribution on both electrophysiology and electrical engineering, with the description of the first electrochemical battery. The test of such devices was highly qualitative as no clear electrical unit system was defined. Consequently, Volta describes effects of this electricity on body, and writes the first description of 'crackling and boiling' sensations.

Half a century later, advances have been performed, giving a better understanding of neural mechanisms. The electrical current is associated to the neural electrical activity by Matteucci (1842), using first electrical measurements by galvanometers. This discovery allows a direct quantification of the neural cell response to the stimulation. Next advance comes from Helmholtz (1850), who measured the celerity of the electrical signal propagation on the nerve and performed the first quantitative study of an electrical stimulation on excitable cells. It can be noticed that these two major advances were performed in a historical context of major advances in physics and more specifically at the time of the first formulation of modern electro-magnetic theory by Maxwell (1863).

The 20st century is the time of the fundamental advances for stimulation. The evolution

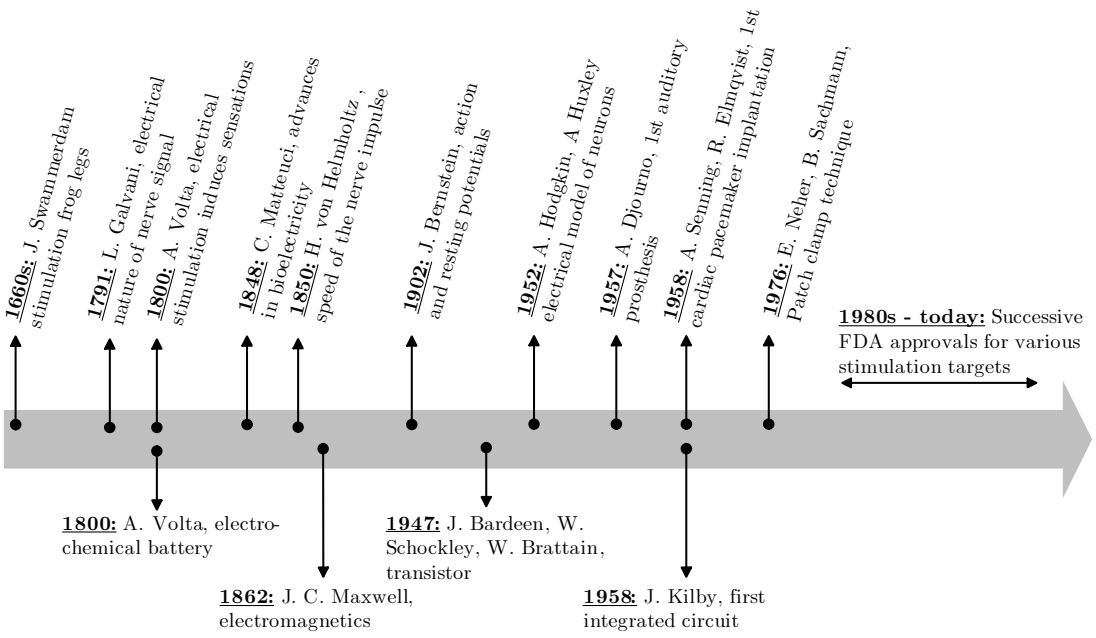

(a)

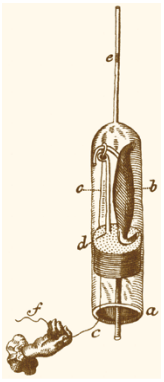

(b)

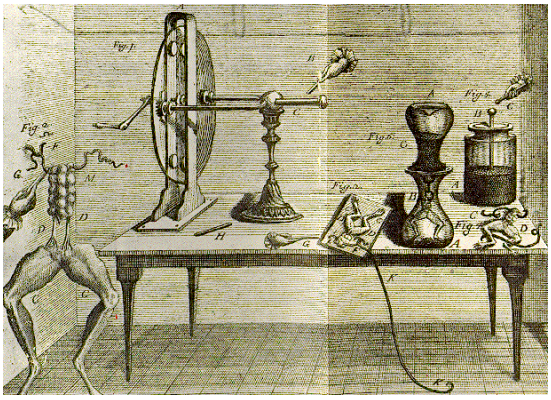

(c)

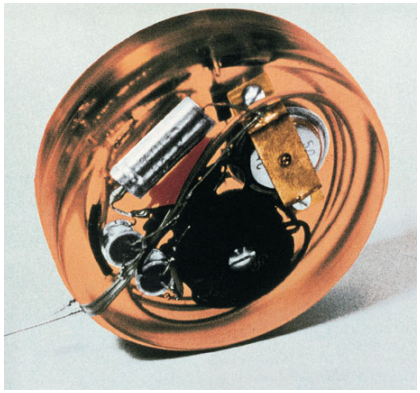

(d)

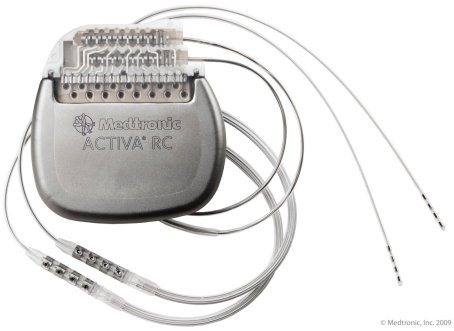

(e)

Figure 1.1 – *(a) Key dates for the history of electrophysiology for neural stimulation and electrical engineering. (b) Nerve-muscle preparation from Swammerdam (1758) (c) Illustration of the laboratory of L. Galvani with limbs and electrical generators from Galvani and Aldini (1792) (d) Image of the first implanted cardiac pacemaker in 1958 (photography from Siemens) (e) Image of recent implant for Deep Brain Stimulation (image from Medtronic)*

of both physics and biology allows scientists to conduct quantitative experiments and propose explanation of observed phenomena. One illustration of these explanations is the first application of the electro-chemistry laws to electrophysiology. In the beginning of the 1900s, the Nernst law is applied to the neural cell by Bernstein (1902). In the middle of this century and with the growing of the Big Science (as defined by Weinberg (1961)), a succession of discoveries led to a better understanding of the stimulation and the possibility of integration for stimulation circuits. Bio-realistic neural models are developed by Curtis and Cole (1940) and then by (Hodgkin and Huxley, 1952) that are rewarded by a Nobel prize in 1963. Simultaneously, in the electrical engineering field, once can note the discovery of the transistor by J. Bardeen, W. Schokley and W. Brattain and invention of planar fabrication processes by J. Kilby.

All these contributions made possible the use of electrical stimulation for therapeutic purposes. The first implanted electrical prosthesis were developed in the late 1950s, with discrete semiconductors. The first attempt of auditory recovery by stimulation of the auditory nerve was performed by Djourno and Eyries (1957). Shortly after, the first cardiac pacemaker was developed and successfully implanted by Elmgvist et al. (1963). These events were the beginning of extended research on applications of stimulation for different pathologies. The recent advances in neuroscience led to the understanding of different physiopathological mechanisms and successful clinical trials are since the 1980s leading to the approval of new implants.

1.2 Addressing excitable cells and tissues

At least two kinds of excitable cells, producing an electric activity when stimulated with electrical or non-electrical stimulus, can be found:

- **muscles fibers:** these cells can be excited to produce an electrical activity inducing contraction,
- **neuronal cells:** these cells initiate and propagate electrical activity along the nervous system.

This section focuses on this last kind of excitable cells. Hereafter, elements for a better understanding of the electrical activity of the nervous system are given, to be linked with the external electrical stimulation protocols related to this work.

1.2.1 The nervous system: an input for therapeutic stimulation

The nervous system is the part of the living organism in charge of the coordination and transmission of voluntary and involuntary actions and signals between the different parts of the organism. At a microscopic level, the nervous system is mostly composed of neurons and glial cells. Neurons can be of various types, however they have in common the transmutation of a physical stimulus to an electrical signal and its transmission. Glial cells mostly maintain the homoeostasis of the nervous system. The repartition of these two groups of cells can vary with the spatial distribution on the nervous system. For electrical stimulation, one can focus on the neural cell as its physiology explains the transduction from electrical stimulus to the biological reaction.

As illustrated in figure 1.2(a) the nervous system of vertebrates can be separated into the central nervous system (CNS) and the peripheral nervous system (PNS). The CNS consists in the brain, exerting centralized control over the body organs, and the spinal cord that is a

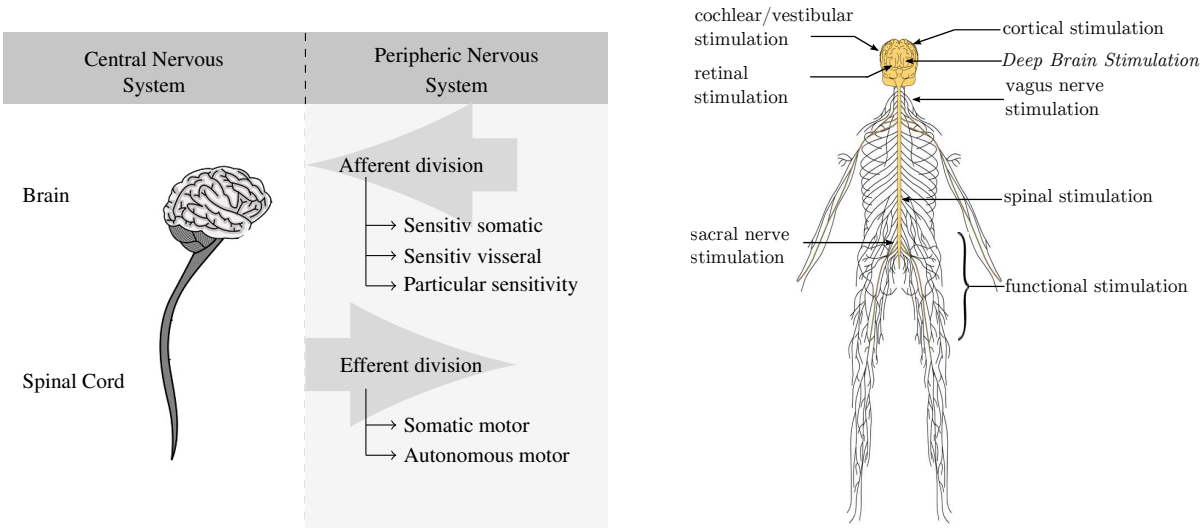

Figure 1.2 – *(a) Overview and structural representation of the nervous system; (b) Illustration of the main approved therapeutic targets for electrical external stimulation along the nervous system.*

tubular bundle containing neural cells extending from the brain. This last structure is not only a transmission pathway, but contains neural circuits controlling numerous reflexes and central pattern generators.

The PNS mainly consists in nerves that ensure the connexion of the CNS to the limbs and organs. It can be subdivided into two main sections as summed up by figure 1.2(a), considering the direction of the neural signal propagation:

- **the afferent division** transmits the neural signal from the sensitive neurons to the CNS; different kinds of information can be transmitted, from the somatic or visceral system to other information involved in the maintain of homoeostasis; this pathway is a source of information for the CNS to provide feedback;

- **the efferent division** transmits neural signal from the CNS to the motor neurons controlling muscles and to the glands. This section controls the biologic actuators.

Both CNS and PNS can be electrically stimulated. Historically, first attempts of electrical stimulation were conducted on the PNS as the physiological reactions are the most obvious. The main targets for electrical stimulation are summed up in figure 1.2(b). Basically, therapeutic applications involving stimulation can be separated in different categories:

- **the sensory feedback applications:** by stimulating the afferent division of the PNS. A famous example of such treatment is the cochlear implant providing hearing in case of deafness. First tries of auditory stimulation have been made by Djourno and Eyries (1957) more than half century ago, and system integration has been remarkable since then as explained by Zeng et al. (2008). Cochlear implant is probably the most commonly implanted PNS stimulation hardware, however technology improvement are still in progress, as expressed by Wilson and Dorman (2008). An other example is artificial vision, that has been demonstrated only a decade after Djourno attempts that the stimulation of the visual cortex can induce vision sensation (Brindley and Lewin (1968)); however recent evolutions in technologies resulted in implants for retinal stimulation as shown in Margalit et al. (2002), that successfully increased patients visual perception as explained in

Chow et al. (2004). More recently, successful integration of acceleration micro-sensors and multi-channel stimulators made possible the development of vestibular prostheses as detailed in Wall Iii et al. (2003) or Gong et al. (2008). The sensation feedback has also been a research interest for prosthetic limbs as in Dhillon and Horch (2005). The main challenge of sensory feedback applications is the understanding of the perception encoding in the neural signal; consequently the different applications lead in highly specific research objectives.

- **the motor control applications:** by stimulating specific efferent nerves, voluntary motion or motor rhythms can be controlled of restored. Functional electrical stimulation (FES) is one particular kind of stimulation aiming at movement rehabilitation after lesions such as spinal cord injuries. Tests have been conducted and movement restoration can be performed in some cases as summed up by Hamzaid and Davis (2009). However other applications aim at restoring non-motor function. For example sacral stimulation can be used to in case of faecal (see Jarrett et al. (2004)) or urinary (see Egon et al. (1998)) incontinence after spinal cord injuries. Also the respiratory rhythm can be controlled using efferent PNS stimulation, more precisely the phrenic nerve, as explained in Bellemare and Bigland-Ritchie (1984) or Mantilla and Sieck (2011), leading to techniques of pacing as shown by DiMarco et al. (2002). Stimulation techniques of the efferent PNS have a wide spectrum of applications.

- **the CNS stimulation:** this category can be subdivided in two sub-categories, separating the stimulation of the brain structures and of the spinal cord. The stimulation of the spinal cord is already successfully used for treatment of chronic pain as explained in Linderoth and Foreman (1999). Recent advances also suggest spinal cord stimulation as an interesting approach for movement rehabilitation, as explained by Jackson and Zimmermann (2012), and successful rehabilitation of injured spinal structures was also achieved by Courtine et al. (2009) with a combination of drugs and electrical stimulation. Spinal cord stimulation leads to numerous motor applications as it is a natural target for combination of the afferent and efferent neural signal, providing a simple access to motor control neural circuits. Then, the stimulation of the brain structures also leads to different applications. *Deep Brain Stimulation* (DBS) is now a well used technique for different neurology pathologies such as Parkinson disease (see Limousin et al. (1995a)), chorea (see Collins et al. (2010)) or depression (see Mayberg et al. (2005)). As for DBS, the stimulation targets are deep nuclei structures of the brain and underlying phenomena are not clearly identified. However other structures can be targeted, as for example the auditory cortex for suppression of tinnitus as explained by De Ridder et al. (2004). A last example of indirect CNS stimulation can be observed considering the sacral nerve stimulation for epileptic seizures suppression as explained in Binnie (2000). If the stimulation is located on a the PNS, it induces de-synchronization of brain electrical activity and permits to prevent, abort or terminate seizures. All these applications address highly connected structures of the brain and if the therapeutic approach shows improvement in patients' quality of life, the patho-physiological mechanisms are not clearly identified, leading to possible future improvement and new applications.

All these applications have in common the kind of target cell: the neuron. Consequently, similarities can be oberved on used stimuli, electrodes and stimulation hardware. For a better understanding of these similarities, let us consider the mechanisms of activation of neural cells.

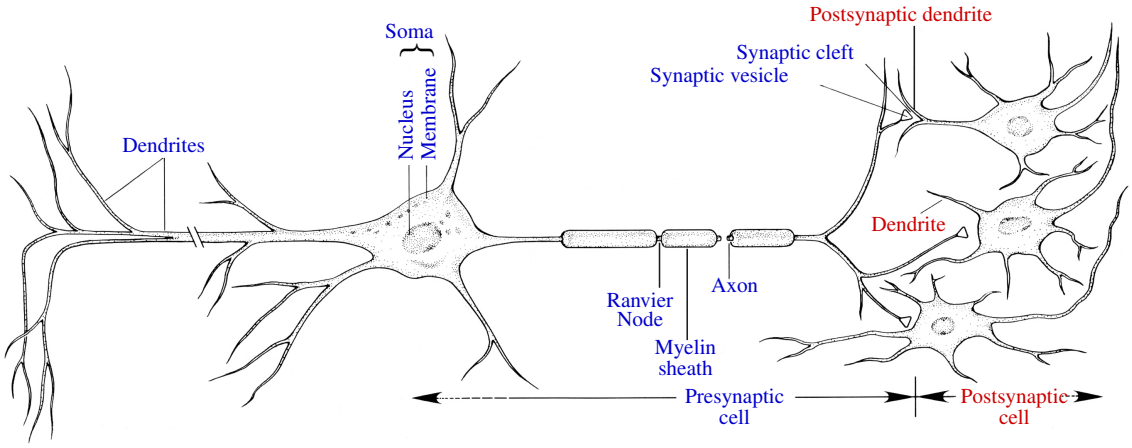

Figure 1.3 – *Anatomical structure of the neuron (adapted from Kandel et al. (2000))*

1.2.2 The neural cell

Neuron anatomy

Although different kinds of neural cells coexist in the nervous system, the global structure of the neuron remains identical; this cell, represented in figure 1.3, can be subdivided in four morphologically defined regions: the cell body, the dendrites, the axon and the pre-synaptic terminals (see Kandel et al. (2000)).

The cell body, or soma, is the central part of the neuron. It contains the nucleus that holds most of the genetic information. It is therefore the place where most of proteins occur. The membrane of the cell section is responsible for non-linear processing. If the total input stimulus exceed a certain threshold, an electrical activity event is generated.

The dendrites are the branched projections of a neuron that play the role of input devices. The overall shape is metaphorically called the dendritic tree. This part conducts the electro-chemical stimulation received from the other neural cells to the soma.

The axon, on the opposite side, plays the role of the output device of the neural cell. It consists in an elongated fiber that extends from the soma to the terminal endings and transmits the neural signal to downstream neurons through synapses to post-synaptic dendrites. The geometry of this part of the cell is highly variable. Most axons of the nervous system are thin (between 0.2 and $20\ \mu m$ in diameter (Kandel et al., 2000)), compared to the cell body ($50\ \mu m$ or more). If the CNS contains entire cells, the PNS nerves mainly consist in cable-like bundle of axons that propagate signals initiated at axon hillock in the CNS. Axons are insulated by a sheath of myelin, a dielectric material, that prevents the electrical current from leaving the axon. This sheath is periodically interrupted by the nodes of Ranvier, consisting in constriction of the myelin over the axon. At the nodes of Ranvier, the axon is uninsulated and therefore capable of generating electrical activity over a certain threshold. This succession of insulated and uninsulated sections forms the basis of the neural signal propagation saltatory conduction.

At the interface between two neurons, the synapse is in charge of the signal transmission. The mechanisms of synaptic transmission can be based on excitation either inhibition of the post-synaptic cell in case of sufficient electrical activity of the pre-synaptic cell. Synapses are involved in learning phenomena and also define the connections in a neural zone and between parts of the nervous system.

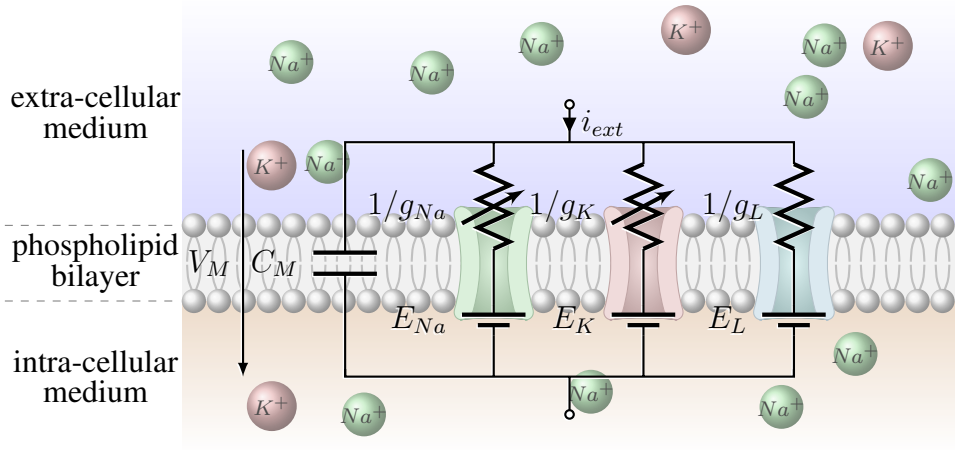

Figure 1.4 – *Physical description and equivalent circuit of membrane ionic exchanges ; for convenience only Na^+ and K^+ ions are represented, however both intracellular and extracellular media are electrically neutral.*

Neuron physiology

The electrical signal of the neuron is the evolution versus time of an electrical potential difference between the intra and extra-cellular media. This voltage is resulting from the separation formed by the cell membrane that surrounds every neuron. Ionic concentrations and exchanges through this membrane are responsible for these electrical phenomena. Let us consider the membrane voltage as represented in Figure 1.4:

$$V_{mem} = V_{intra\ cellular} - V_{extra\ cellular} \tag{1.1}$$

At the equilibrium, when no perturbation or stimulation occurs, ionic concentrations in the intra and extra-cellular media are not equal resulting in a resting potential; major concentration differences can be observed on K^+ and Na^+ species. The resting potential can be calculated from the Nernst equation (Feiner and McEvoy, 1994), usual values are between -60 and $-70mV$.

The cell-membrane consists in a phospholipid bilayer as graphically represented in figure 1.4. It acts as a powerful electrical insulator. As a consequence it can be modelled by a capacitor. However ion transport through the membrane can occur due to the presence of transmembrane proteins that act as ion channels or ion pumps, exchanging one or more ion kinds. A first accurate quantitative description of resulting electrical phenomena was developed by Hodgkin and Huxley (1952). This model results in a differential equation of the form:

$$C_{mem}\frac{dV_{mem}}{dt} = -\sum_k I_k + i_{ext} \tag{1.2}$$

where the I_k represent the contributions of the different ions in the intra extra-cellular media. More accurately these contributions are represented by channel conductances imposed by the protidic structures and a reversal potential that can be obtained by applying the Nernst law over the specy they conduce. Figure 1.4 illustrates a simple model with consideration of the K^+, Na^+ and a leakage channels. Imposed stimuli are represented by i_{ext}. Physically, this i_{ext} can be imposed to the cell using patch-clamp techniques as in Hamill et al. (1981). Such techniques use intra-cellular stimulation and are obviously invasive; the external stimulation that is in concern for therapeutic purpose can nevertheless be understood from observation of this invasive method.

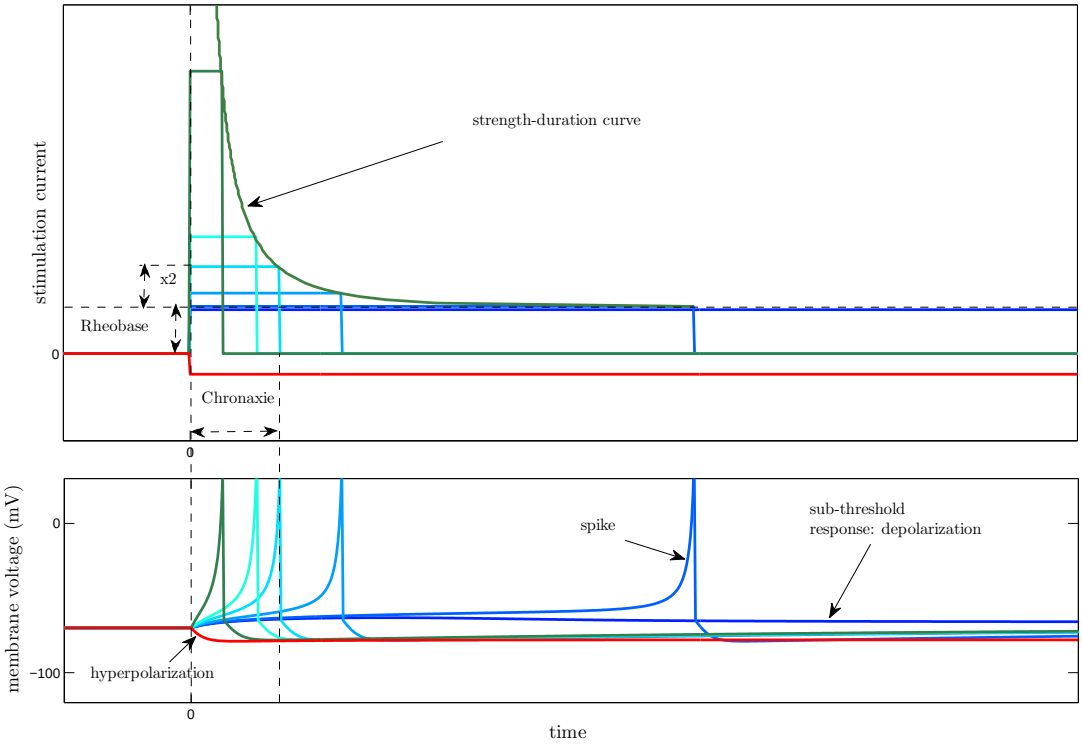

Figure 1.5 – *Strength-duration curve illustrated with the results of the voltage membrane evolution for different stimuli*

Electrical signalling involves brief changes from the resting potential due to alterations in the flow of electrical current across the membrane; alterations result from the opening and closing of ion channels made by trans-membrane proteins, and thus change the value of the electrical conductances. The evolution of the membrane voltage versus the external current can be viewed on figure 1.5. For a positive current the membrane voltage increases. If a certain threshold potential (generally around $-55mV$) is reached, the neuron generates a peak activity called the action potential. In case of a sub-threshold stimulation, the neuron only depolarizes, and is more sensitive to additional stimulation. The virtual current firing the neuron with an infinite stimulation is called the rheobase (Plonsey and Barr, 2007). For twice the rheobase, the time required to fire the neuron is defined as the chronaxie as illustrated on the upper curve in Figure 1.5. Basically, the time to induce a spike is decreasing when the current increases, forming a hyperbolic strength-duration curve for the stimulus shape.

On the contrary, if a reverse current is applied, the membrane voltage decreases and the cell is hyper-polarized. In this case, before the cell returns to the resting potential, the current required to induce an action potential is higher than the rheobase. From Figure 1.5 it can also be observed that just after the peak of the action potential, the membrane is hyper-polarized as well and returns slowly to the resting potential. This phenomenon is called the refractory period during which the response to a stimulus is decreased.

Neural signal propagation

Neural signal propagation can be examined both on a single cell and between two different cells. The propagation in a cell is of major concern to understand basic mechanisms of electrical stimulation; it also governs the propagation of signal on nerves that are mainly composed of

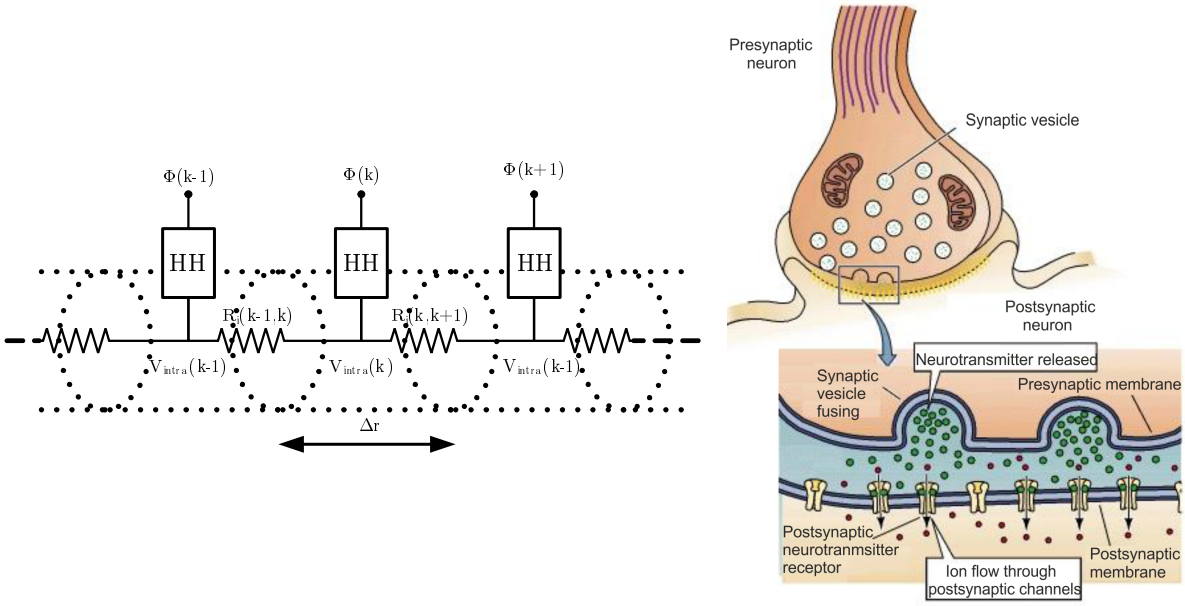

(a) (b)

Figure 1.6 – *(a) Discrete schematic representation of the axon fibre as a distributed resistive part and Hodgkin Huxley elements, (b) Illustration of a chemical synapse from KIN450 (2009)*

axons. Synaptic propagation is the key for a global understanding of tissues interactions inside the CNS. Both phenomena are illustrated in Figure 1.6.

Once an action potential is generated on the neuron surface, it propagates by saltatory conduction. As described in Figure 1.3, the axon can be seen as a succession of myeline isolated sections and Ranvier nodes where ions exchange can take place and provoke a new action potential. The distance between two Ranvier nodes or simply the distance between the ionic active sections induces an intracellular resistance resulting from local ionic gradient concentration. These considerations allow for the representation of Figure 1.6(a), and lead to a cable partial differential equation for both unmyelinated (see Rattay (1986)) and myelinated fibers (see McNeal (1976)). The action potential is thus transmitted over the cell with ionic transport as an electrical signal would be on a cable. The velocity of the action potential is defined by the proportion of myeline that covers the fiber; this phenomenon is not modulated by other conditions.

Between two neurons, the action potential has to cross a synaptic gap. Synapses can be electrical either chemical; nevertheless this last type represents the majority of synapses in vertebrates. An illustration of chemical synapses is presented in Figure 1.6(b). The depolarization of the pre-synaptic cell activates the release of neurotransmitter molecules into the synaptic cleft, which then binds to receptors on the post-synaptic cell. This binding opens ion channels, thus initiating a change in membrane potential in the post-synaptic cell. If the transmission is sufficient, it results in an action potential in the post-synaptic cell. Whether the synaptic potential has an excitatory or inhibitory effect will depend on the type of receptor in the post-synaptic cell for a particular neurotransmitter. Chemical synapses are capable of variable signalling and thus can produce complex behaviours. They can mediate either excitatory or inhibitory actions and produce electrical changes in the post-synaptic cell that last from milliseconds to many minutes. Chemical synapses also amplify neuronal signals, so that even a small pre-synaptic nerve terminal can alter the response of a large post-synaptic cell. Such phenomena highly

modulate the global neural activity and explain the complexity of neural circuits.

1.3 Mechanism of extra-cellular stimulation

1.3.1 The external electrical field

When designing a stimulation circuit or material, the choice of the controlled quantity that is delivered to the tissue via the electrode is of major concern. If first therapeutic implants were mostly designed to provide voltage controlled signal, modern stimulators generally give the choice between voltage or current stimulation. In recent systems, a current controlled stimulus is preferred, as further illustrated in the document.

Inducing a neural response is performed by controlling the cell external electric field ($\overrightarrow{E}$), governed by Maxwell equations. The electric field induces the electrical potential in space, corresponding to the extra-cellular potential expressed in equation 1.1. For classical electrophysiology studies, the electric field in the biological medium can be considered under the quasi-static approximation, as this hypothesis leads to satisfying first approximation results (Joucla and Yvert, 2012).

A first analysis of the extra-cellular electric field consists in reasoning with point monopole sources, ie. local points in the space emitting a current I. The electric field can be expressed by the negative gradient of a scalar potential V:

$$\overrightarrow{E} = -\nabla V \tag{1.3}$$

Considering the extracellular medium as homogeneous with an electrical conductivity of σ, Ohm's law implies:

$$\nabla V = -\frac{\overrightarrow{J}}{\sigma} \tag{1.4}$$

where $\overrightarrow{J}$ is the current density. Bipolar electrodes or more complex electrodes can be mathematically expressed as the combination of electrical monopoles (Plonsey and Barr, 2007), so as an elementary point source. Considering previous equations, if the monopole delivers a current I, the current density magnitude can be determined at a distance r from the point source as:

$$\| \overrightarrow{J} \| = \frac{I}{4\pi r^2} \tag{1.5}$$

Consequently, by substitution and after integration:

$$V(r) = \frac{I}{4\pi\sigma r} \tag{1.6}$$

This last equation leads to a simple representation of the electrical potential in the medium. An illustration of two quasi-point monopole field is shown in figure 1.7(a). The left monopole is supplied with a constant negative current and the right monopole has a constant potential of $0V$, as an electrical ground. This basic representation corresponds to twisted electrode that are commonly used in electro-physiology context. Equation 1.6 gives a basic understanding; the contours near the dipoles describe circles, and in between two monopoles lines merge as the superposition of potential is imposed by the linearity of the medium.

An illustration of the electrical potential for a needle electrode is given in figure 1.7(b). Under the quasi-static approximation, Poisson equation based problems can be solved using

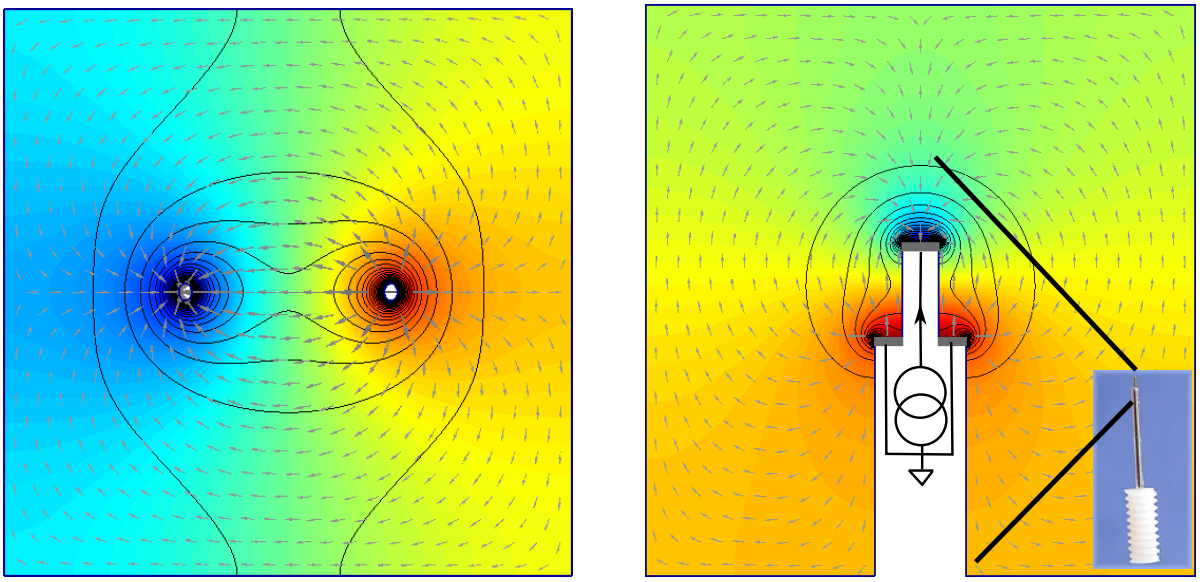

(a) (b)

Figure 1.7 – *Finite element simulation of the Poisson equation for two problems, one pole is driven with a negative current and the other is an electrical ground; the electrical field contours are shown with black lines, the colors correspond to the potential (deep blue for lowest potential, red for the highest), and vector arrows represent the current density over space: (a) for a combination of two quasi-point monopoles (b) for a classical needle electrode geometry.*

finite element methods. From the drawn figures, it can be observed that the active electrode lowers the extra-cellular potential of near cells. The current density is on the example of the needle electrode mainly concentrated between the ground plane and the active pole; potential is rapidly changing near the needle and the potential is more stable as the distance with the electrode decreases. Locally, at the surface of the neural cell, the electrical potential can be assimilated to the extra-cellular potential $V_{extra\ cellular}$ of equation 1.1.

1.3.2 Triggering excitable cells

The low potential shown in the previous paragraph is not sufficient to explain the triggering of near neural cells. It can be demonstrated (Rattay, 1989), considering the cable equation of the signal propagation, that sub-threshold phenomena can be approximated by a first order system, and that the triggering phenomena are linked to the second order derivative of the external potential versus the neural axon axis. One can define an equivalent source for neuron triggering called the activation function f_a:

$$f_a\left(r',t\right) = \lambda \frac{\partial^2 V_{extra\ cellular}}{\partial r'^2} = \lambda \frac{\partial^2\ V\left(r\right)|_{r'}}{\partial r'^2} \tag{1.7}$$

where r' is a restriction of the space coordinate r to the axon fibre axis, and λ is a proportionality factor.

As written by Rattay (1989), if the membrane voltage is decomposed into its average value and $\tilde{V}_{mem}$ the variations around the resting potential, we write:

$$\tau \frac{\partial \tilde{V}_{mem}\left(r'\right)}{\partial t} = f_a\left(r'\right) \tag{1.8}$$

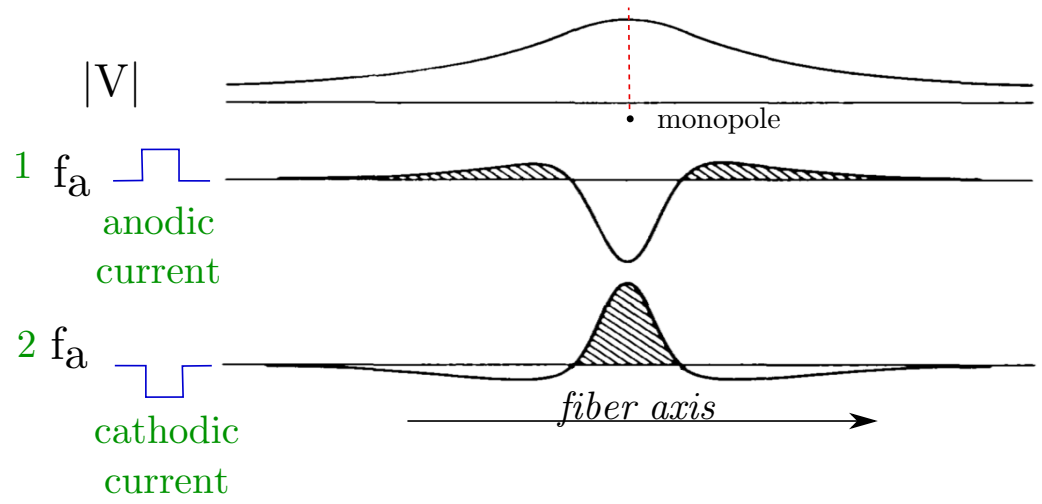

Figure 1.8 – *Illustration of the spatial stimulation of an unmyelinated fiber by a monopole and prevision of depolarized and hyper-polarized zones (adapted from (Rattay, 1989))*

where τ is the time constant of the equivalent first order approximation of the cell operating under the threshold. This last equation implies that the cell is depolarized if the activation function is positive and hyper-polarized if the function is negative.

This principle is illustrated by Figure 1.8. The external field geometry is illustrated in the upper curve. Lower curves show the second order derivative of this shape, in case of a positive (*Anodic*) current (1) and negative (*Cathodic*) current (2). Both cases generate positive activation areas, however the cathodic stimulation produces a high amplitude central positive zone. The anodic stimulation produces lateral areas with lower amplitude. As the activation function is proportional to the membrane voltage variation through the factor λ, it can be observed that for the same amplitude, the cathodic stimulation is more efficient to trigger the cells. Moreover, in the case of the cathodic stimulation, the triggered cells are concentrated near the stimulation monopole; referring to the needle shape presented in Figure 1.7(b), this area is located directly near the active pole.

1.3.3 Wave-shape for external stimulation

The electrical stimulus is therefore designed over a negative current. This cathodic phase shape is imposed by the same reasoning than explained for the intra-cellular stimulation strength-duration, as the rheobase and chronaxy can be extended for extracellular stimulation (Holsheimer et al., 2000). However the stimulation with a time-defined constant cathodic current I_{cathod} pulse is not sufficient to provide safe external stimulation.

As mentioned in Merrill et al. (2005b), the signal has to be charge-balanced to provide a stimulation that will not result in electro-chemical reactions on the electrode surface or in the tissue, due to the accumulation of residual electrical charges. Consequently, charge-balancing gives a numerical condition on the current stimulus that can be expressed as:

$$\langle Q_{stim} \rangle = \int_0^{T_{stim}} i_{stim}(t) \cdot dt = 0 \tag{1.9}$$

where T_{stim} is the stimulation period. There is no clear limit on the maximal timing under which charge-balancing has to be performed, however a short term (over the range of the minute)

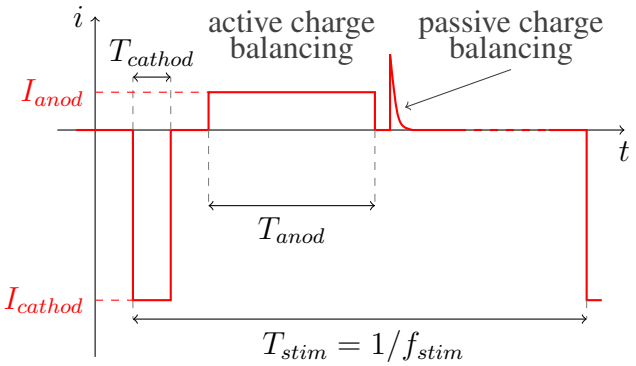

Figure 1.9 – *Typical current stimulation waveform with active and/or passive charge balancing*

unbalanced external stimulation leads to strong lesions of the tissue surrounding the electrode as observed by Meissner et al. (2004).

Charge-balancing has then an impact on the global stimulation shape. A second phase of reverse current has to be provided. This principle is illustrated in Figure 1.9. The charge balancing can be provided through two different strategies:

- Active charge compensation: a positive or anodic current pulse is delivered to the electrode. In order not to hyper-polarize neurons targeted by stimulation (Merrill et al., 2005b) or depolarize untargeted cells in lateral zones, the anodic current I_{anod} is generally lower than the cathodic current. Anodic time duration T_{anod} is then chosen to have a global charge equal to over a stimulation period. Under the assumption that current are constants, the anodic duration for charge balancing is calculated from:

$$T_{anod} = T_{cathod} \cdot \frac{I_{cathod}}{I_{anod}} \tag{1.10}$$

- Passive charge compensation: electrode is discharged through a resistor. This technique is the most efficient to ensure tissue safety, however, the resulting current peak value is not controlled and a high current value can hyper-polarize target neurons (Merrill et al., 2005b) or depolarize untargeted cells. Lowering this peak current supposes to increase the discharge resistor and thus increase the charge balancing time.

A time period of null current is generally added between the cathodic and anodic pulses. As mentioned by Merrill et al. (2005b), it prevents from hyper-polarizing the cells that were triggered by the anodic phase and guaranties the effectiveness of the stimulation. This timing is in most situations equal to or lower than the cathodic pulse duration.

More complex waveforms can be found in the literature. These complex shapes are mostly composed of individual biphasic wave-shapes as described in figure 1.9, generally with an amplitude modulation (Wu et al., 2002). Other attempts of non-rectangular wave-shapes have been performed in different contexts as described by Sahin and Tie (2007). Such signals can lower the activation threshold, increase the charge injection capacity of electrode or lower the energy over a period. However, the use non-rectangular waveforms remains marginal and will not be considered in this document.

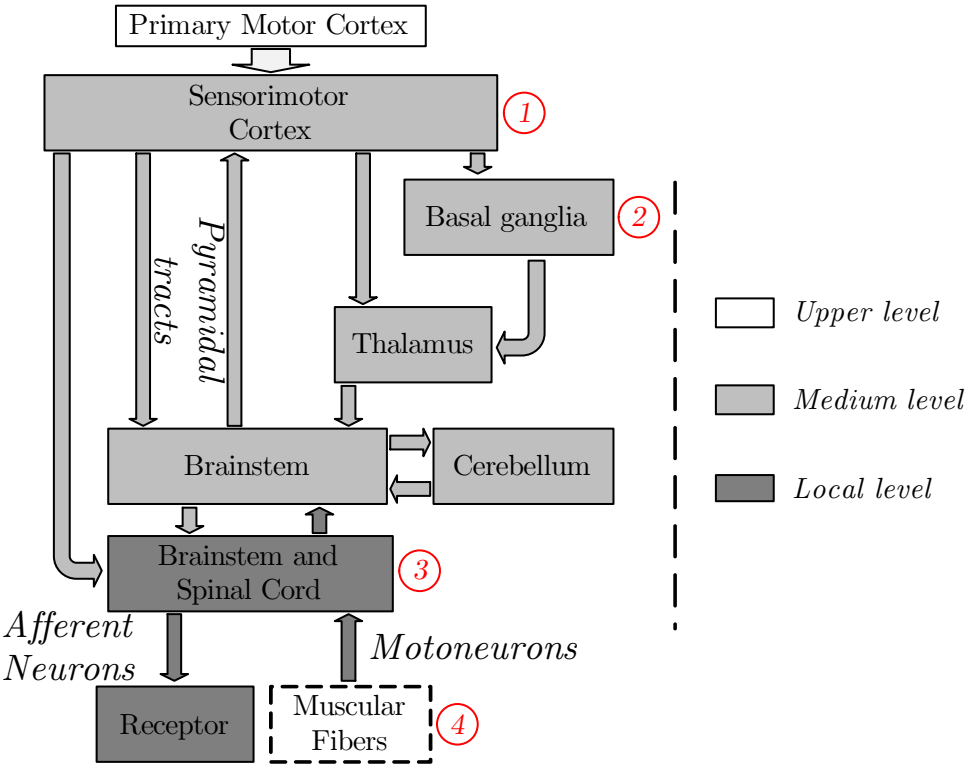

Figure 1.10 – *Functional description of the motor pathway anatomy; the pathway can be subdivided into three levels: the upper level constructing movement orders, the medium level initiating, coordinating and correcting with feedback signals, and the local level connected directly to the afferent and efferent fibres. Numbers in the figure correspond to the order of presentation of pathological context in the next sections.*

1.4 Electrical stimulation in different contexts over the motor pathway

Along this document, four particular contexts of stimulation will be of concern, corresponding to four research projects conducted in our research group an related to stimulation. These contexts share similarities as they involve the nervous system; however, their objectives are mainly separated due to the related physiopathology. This section aims at explaining these contexts, in an order following the motor pathway .

1.4.1 Overview of the motor pathway

Neurons involved in the motor pathway are various and of different kinds. The entire structure of the nervous system is involved, from the preparation of the movement order, to the actuation of muscles, the afferent induced sensation and error correction for an effective and accurate motion. All involved cells respect an anatomic and physiological hierarchy. A block diagram of this functional hierarchy is shown in figure 1.10. This structure is mainly divided in three parts: the upper level includes the zones where the movement is decided, the medium level includes the circuits responsible for the regulation of the movement and the local level contains the cells generating and conducting the electrical signal to the muscle, as well as the sensory signals.

A movement is initiated from the cortical zones, that can include the sensory-motor cortex, the association areas, the memory or emotions areas. However, the incoming information always

converges to the sensory-motor cortex that commands, decomposes and generates a sequence to initiate the movement. These types of cortical tissues are studied in the '*Brainbow*'[1] project.

Under the cortical zones the signal is partially relayed to sensory and motor signals to the Brainstem via the Pyramidal tracts and the Thalamus. However, the signal converging through the Thalamus is also partially processed by the Basal Ganglia. These structures are in charge of eliminating undesired movement and initiating the signal of the movement via moto-neurons. Dysfunctions of these structures induce motor pathologies such as Huntington chorea or Parkinson's disease that are addressed with the Deep Brain Stimulation that will also be studied in this manuscript[2].

The descending signal reaches then the Brainstem where it is regulated by the Cerebellum. This structure plays the role of a regulator or a corrector. It takes into account the incoming afferent signal to regulate the descending motor control signal to lessen the error between the desired movement and the effective motion. Once the correct motor signal is elaborated, it is conducted to the spinal cord. This structure contains afferent and efferent connections that are directly connecting the muscles and the receptors. However, the spinal cord also includes rhythms generators called Central Pattern Generators that produce the direct signals to drive the actuator, considering the afferent information. The stimulation of such structures is an item in the '*Hyrene*'[3] project. A last example of stimulation is also of concern considering the terminal moto-neurons in contact with the muscles; this kind of stimulation is made in the '*Cenavex*'[4] project where the motion of the diaphragm is controlled.

1.4.2 The BRAINBOW Project: a new approach on cortical prosthesis

As the motor pathway upper level is composed of cortical zones, it seems to be a natural place for rehabilitation. However, only very recently scientific interest has been devoted to *in vivo* cognitive neural prostheses for rehabilitation. The first ever hippocampal prosthesis improving memory function in behaving rats has been presented in recent papers, as illustrated in (Song et al., 2009).

The realisation of such prostheses implies that we know how to interact with neuronal cell assemblies, taking into account the intrinsic spontaneous activation of neural networks and understanding how to drive them into a desired state in order to produce a specific behaviour. The long-term goal of replacing damaged brain areas with artificial devices requires the development of neural network models to be fed with the recorded electro-physiological patterns, and yield the correct brain stimulation aimed at recovering the desired functions.

Investigations are then based on a closed loop hardware, which back-end consists in a multi-channel stimulation system. As the target tissues for stimulation are not clearly identified, the system used should adapt to a large variety of electrodes, and have a large variation of stimulation parameters.

1.4.3 *Deep Brain Stimulation* for Parkinson's Disease

The Parkinson's Disease is a neuro-degenerative disease, first observed by James Parkinson in 1817, that can be defined as the syndromes associated to specific neuropathologic lesions. The major syndromes of the disease are motor perturbations such as bradykinesia, akinesia, resting

[1] European project FP7-ICT-2011-C
[2] STN-Oscillation, French ANR 08-MNPS-036
[3] French ANR 2010-Blan-031601
[4] French ANR and American NSH AN13-NEIC-0001-01

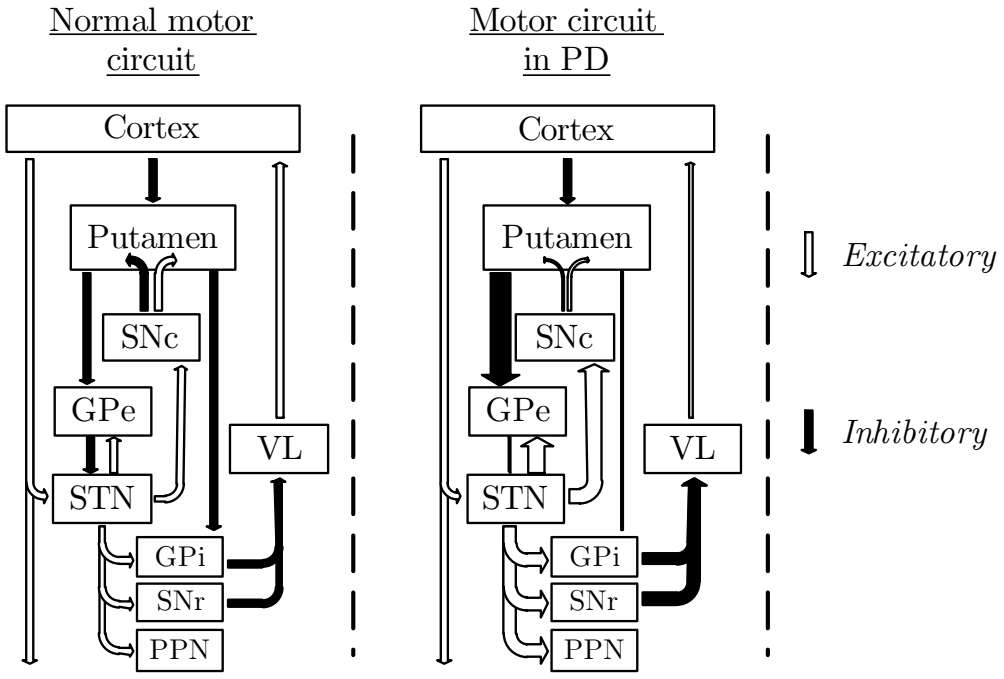

Figure 1.11 – *Schematic representation of the physio-pathology of Parkinson's Disease over the Basal ganglia. The normal motor control circuit is based on excitatory or inhibitory connections of different ganglia. PD results from a loss of dopaminergic neurons in the Substanca Nigra pars compacta (SNc), moving the equilibrium over a complex loop made by the Putamen, the Globus Pallidus external (GPe), the Subthalamic Nucleus (STN), the GLobus Pallidus internal (GPi), the Substanca Nigra pars reticula (GPr), the PedunculoPontine Nucleus (PPN) and the Ventral Lateral (VL) thalamus.*

tremor, rigidity and postural disorders. These symptoms result from the progressive degeneration of dopaminergic neurons of the *Substanca Nigra pars compacta* (SNc), a part of basal ganglia (Ehringer and Hornykiewicz, 1998). This degeneration implies a disorganization in the electrical activity of the motor loop control formed by the basal ganglia as illustrated by Figure 1.11.

A therapeutic medication is often the first solution to reduce symptoms. Treatments are based on the compensation of the dopaminergic neuron depletion by an intake of Levo-Dopa (L-Dopa), a precursor of the dopamine that crosses the protective blood-brain barrier whereas the dopamine in itself cannot. This approach is a solution against the three major symptoms of the disease (akinesia, tremors and rigidity), however, its efficiency is decreasing with time; it results in apparition of disabling complications such as induced diskynesia as described by Hauser (2009).

A second approach can be chosen when chemical medication becomes inefficient. This treatment consists in a high frequency (around $130\,Hz$) stimulation of basal ganglia structure with an implanted stimulator and electrode. For the PD, the first attempt of *Deep Brain Stimulation* (DBS) treatment was applied in the Ventral Intermediate Nucleus (VL) (Benabid et al., 1991), which stopped tremors; afterwards and considering the physio-pathological loop illustrated by Figure 1.11, studies on stimulation of other structures were performed, like in the Globus Palidus pars interna (GPi), or Sub Thamalamic Nucleus (STN) (Limousin et al., 1995b). Presently, the electrodes of DBS implanted devices for PD are mostly placed in the STN as this therapy eliminates tremors, akinesia and rigidity (Limousin et al., 1995a). Effects of DBS are similar to those observed with surgical lesioning of structures involved in the physiopathology of PD Bergman et al. (1990), a therapy that was abandoned due to unacceptable risks. The STN DBS is

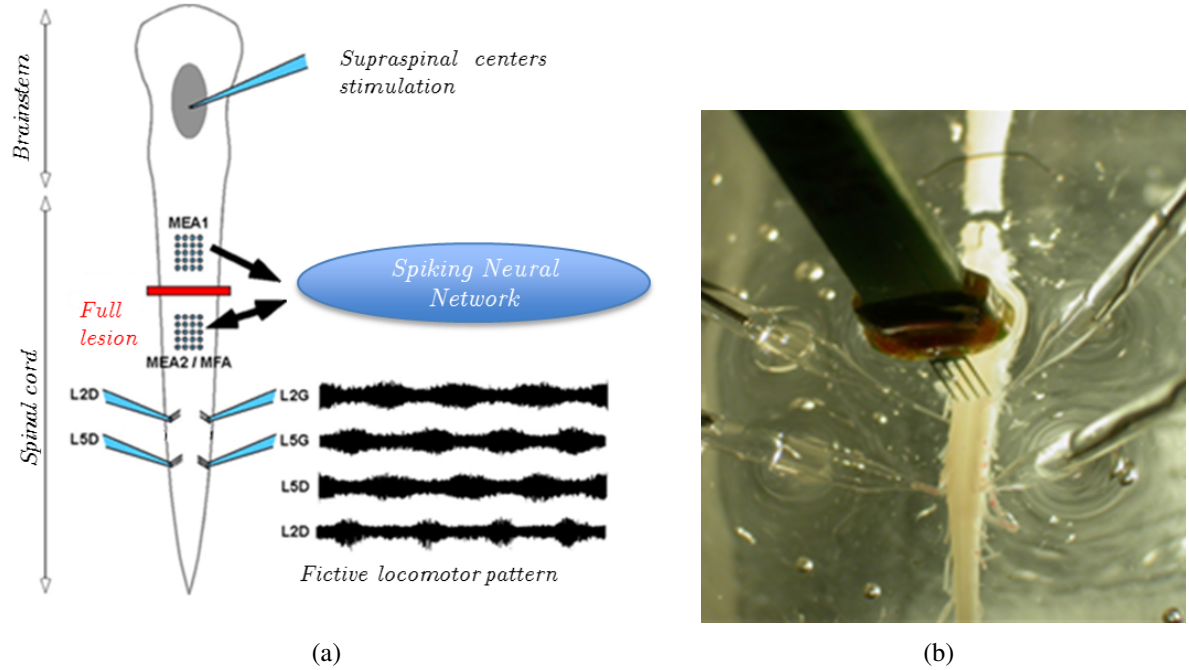

(a) (b)

Figure 1.12 – *Illustration of the HYRENE project (a) the injured spinal cord is prepared for generation of commands ordered by stimulation in the brainstem; motor-like activity is observed on lumbar ventral roots; the setup consists in micro-electrodes array for recording and stimulating spinal neurons; the bridge between the two arrays is performed by neuromorphic circuits. (b) Photography of one MEA fork placed in the ex vivo spinal cord; four glass micro-pipette electrodes are placed for lumbar activity recording.*

mainly considered to induce an inhibition of this structure and lessen the excitatory output to all others structures as it can be observed in the Figure 1.11, limiting the electrical disorganization of overall basal ganglia activity.

However, even if the effect of DBS on PD symptoms is well established, the exact underlying mechanism remains unclear as expressed by Hammond et al. (2008). Moreover, this surgery can lead to side effects. The majority of them is linked with the surgery (Benabid, 2003), nevertheless adverse events such as psychiatric disorders, cognitive changes, dyskinesia, dysarthria as described in Kleiner-Fisman et al. (2006), and weight gain as described by Rieu et al. (2011), can be observed. Further researches aim at DBS therapy by devices improvements and limiting side effects. This kind of research requires to mimic the human therapy on animal model for a long period, so that motor and behavioural tests can be performed.

1.4.4 The HYRENE project: spinal stimulation for functional rehabilitation

Following spinal cord injury, electrical stimulation of the spinal cord below the the lesion is a promising way to restore locomotion, as already shown by Giszter (2008), Borton et al. (2013) and Nishimura et al. (2013). One of the physiological role of the spinal cord is to generated locomotor rhythms via Central Pattern Generators; an example of rhythmic activity as observed in the efferent nerve of an *ex vivo* spinal cord of a mouse is illustrated in Figure 1.12(a). This kind of oscillatory signal can also be generated when the spinal cord is isolated from the upper level descending commands, as first assessed *ex vivo* by Kjaerulff and Kiehn (1996), and also confirmed *in vivo* on animals and humans (see Dimitrijevic et al. (1998), Ichiyama et al. (2005)

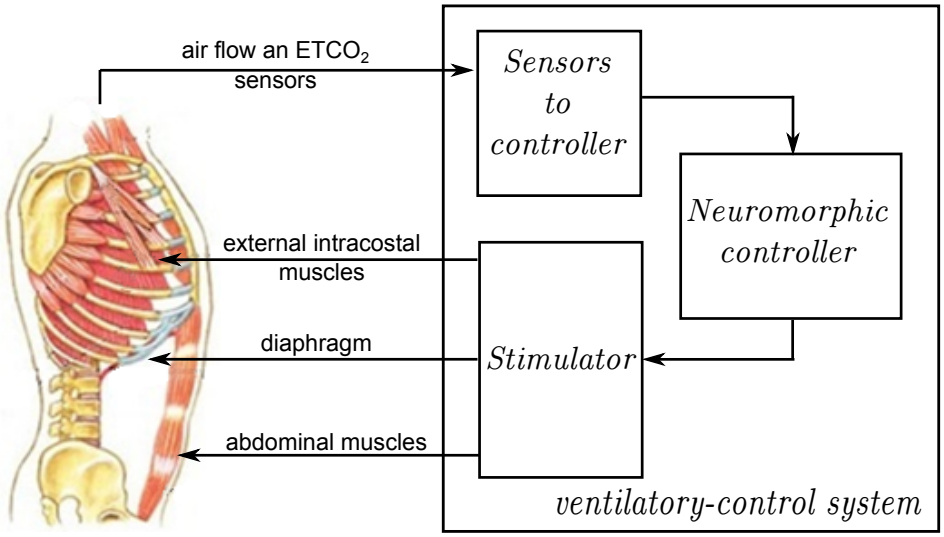

Figure 1.13 – *Illustration of the closed-loop strategy for ventilatory control prosthesis: the physiological demand is sensed by monitoring the air flow and CO_2 concentration, a neuromorphic controller integrates these informations to control the stimulation of muscles involved in the respiration.*

and Minassian et al. (2007)).

The use of small intra-spinal electrodes for electrical stimulation is a way to activate accurately spinal circuitry that controls motor signals. Based on this approach, new experiments aiming in the development of innovative neuroprosthesis have been defined. One example is shown in Figure 1.12. The goal of this experiment is to observe locomotor neural activity on lumbar efferent axons, on L2/5 ventral roots recorded with glass micro-pipettes electrodes.

As shown in Figure 1.12(a), the upper efferent commands are induced in *ex vivo* conditions using electrical stimulation of the brainstem. In case of a partial or total lesion of the spinal cord over the lumbar section, the efferent signals are stopped. The *'Hyrene'* project aims at generating descending commands over a lesion using a bridge with two micro-electrode arrays (MEA); these MEA are placed over the lesion to record electrical activity of the spinal cord and under the lesion to provide electrical micro-stimulation. An artificial CPG is also implemented and connected between the recording and stimulation sites in charge of controlling the stimulation pattern. One of the challenges of this project is to propose an adapted hardware setup to realize this hybrid connection.

1.4.5 The CENAVEX project: stimulation for a closed-loop ventilatory control system

If motor disabilities are the most considered consequences of spinal cord injuries, respiration control is also a critical issue. In case of cervical cord injury, and because the diaphragm is innervated by moto-neurons of the phrenic nerve that have efferent roots on cervical vertebrae from C3 to C5, ventilatory control can be partially or totally lost.

Respiratory control has already been addressed by electrical stimulation, as for example by phrenic nerve stimulation (Bellemare and Bigland-Ritchie, 1984; Mantilla and Sieck, 2011). More recently, intra muscular stimulation of the diaphragm has been considered for patients without intact phrenic nerves or unilateral phrenic function, as shown in DiMarco (2005) and Onders et al. (2009). Stimulation of extra-diaphragmatic respiratory muscles (intra-costal muscles and abdominal muscles) can also also stabilize the rib cage and enhance ventilation to

make it more efficient Walter et al. (2011).

The open-loop stimulation strategy currently utilized for pacing has major limitations including the need for manually tuned stimulation parameters and inability to alter stimulation parameters on muscle fatigue or on changing metabolic demand. The *'CENAVEX'* project proposes the design, development and prototype realization of a novel closed-loop control system as illustrated in Figure 1.13. It will specifically address the challenge of simultaneously adapting the rhythm and pattern of oscillatory drive to achieve effective and efficient control of the respiratory function using neuromorphic hardware. A neuromorphic controller will receive inputs from measurements on ventilatory systems and will drive a stimulator which targets three muscular groups: the external intra-costal muscles, the diaphragm and the abdominal muscles.

1.5 Partial conclusion

The excitability of neural cells and the possibility of external electrical stimulation form the basis of a large number of therapeutic protocols. This chapter described the different types of applications. The requirements for a stimulation waveform were explained, considering the electro-physiology of neurons; due to triggering and tissue safety conditions, this waveform is common to the numerous applications.

This link between different contexts is balanced by the differences in local physiological parameters specific to the target tissues, suggesting the possibility of a global approach based on a scale-effect between different contexts. However, this scale-effect would only be effective if similar points of convergence were observed in materials and circuits for electrical stimulation, as described in the next chapter.

CHAPTER 2

MATERIALS AND INTEGRATED CIRCUITS FOR EXTRA-CELLULAR STIMULATION

PATHOLOGIES and disabilities of the nervous system are the subject of constant research that has produced a variety of therapeutic solutions. Thanks to the excitability of the tissues involved, electrical stimulation is a promising tool, depending on both electrodes and circuits for successful technological advances.

The following sections give an overview of the electrodes, front-end circuits, and stimulation systems reported in recent literature. The overall characteristics and parameters of existing systems are extracted and analysed.

2.1 Electrodes for extra-cellular stimulation

The physical interface between a biological tissue and an electronic circuit is formed by the electrode. At this precise location, the electronic conduction of electrical circuits is transduced in ionic conduction, as described in the previous chapter. Being the final load, this part is crucial in the development of stimulation circuit. The electrode determines the maximal voltage at the required maximal current and pulse-width through its impedance. However, the electrode is sized or mainly chosen by physiologists, reducing the degrees of freedom on the optimization of the global stimulation system.

The electrode is chosen for a particular target during the design process taking into account geometrical and materials considerations. As the volume of triggered cells is determined by the spatial second derivative of the potential, the geometry of the electrode is the main parameter of choice. A first categorization can be made between large electrodes ($> 2000\mu m^2$), called macro-electrodes, and smaller geometries called micro-electrodes:

- Macro-electrodes are used to stimulate large structures containing an important number of cells. An illustration of such electrodes is given in Figure 2.1(a). Such electrodes are commonly used for Deep Brain Stimulation where structures of few mm^3, like the Sub Thalamic Nucleus or the Globus Pallidus, have to be triggered. Macro-electrodes often require a high current (in the range of mA) to activate the tissue and the number of stimulation channels is small. As an example, both electrodes of Figure 2.1(a) are used for DBS, the left one for small rodents delivering up to $1mA$ with only one possible channel; the right electrode is commonly implanted for DBS on human patients with 4 pads; with existing commercial stimulators, two pads can be selected, driving one channel requiring a stimulation current up to $25.5mA$; some recent circuits allow field steering using more than 2 pads by spatial repartition of the current as explained in Chaturvedi et al. (2012) and illustrated in Appendix A.

- Micro-electrodes are used to trigger a few cells and ideally a localized group of cells. Two different geometries are shown in Figures 2.1(b) and 2.1(c). Such electrodes are designed to improve their focality and stimulate controlled volumes as performed in Joucla et al. (2012). Different geometries have been developed, from planar forks as in Figure 2.1(c) to arrays of needles. These geometries can also been modified to develop 3D electrodes as in John et al. (2013) or used on soft substrates for particular tissue stimulation, as for the retina in Wang et al. (2010) for instance. Such electrodes are often specific to a particular application and various designs can be found in the literature. The number of channels is generally high (more than 8), forming Micro-Electrodes-Arrays (MEA).

Examples of geometries of macro- and micro-electrodesand their associated electrical potential repartition are presented in Appendix A.

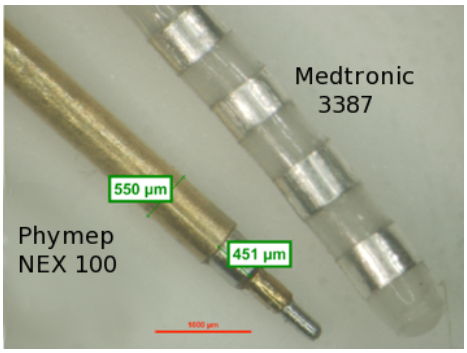

(a)

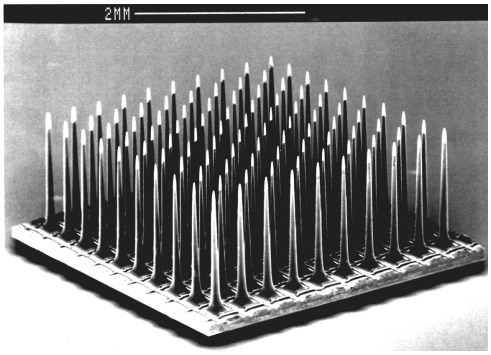

(b)

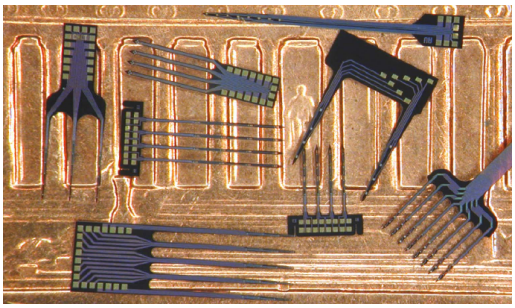

(c)

Figure 2.1 – *(a) Macro-electrodes used in DBS for PD, left electrode (NEX100, Phymep France) is used for rodents, right electrode (Medtronic 3387) is used for humans (b) Example of needles MEA (image from Normann (2003), Utah Array) used for cortical applications, electrodes are placed on a silicon plane allowing for direct bonding on interface chip (c) Samples of fork-like MEA (image from Wise et al. (2008), Michigan Probes) placed on the center of an American penny.*

The geometry of an electrode has a direct impact on its impedance. This characteristic will be further detailed in chapter 5 using quantitative approaches. However, a first qualitative modelling can be provided as the interface between the metal contact and the biological electrolyte is mainly capacitive. The capacitance is directly proportional to the electrode area. Between the two metal-to-electrolyte interfaces, the extra-cellular medium can be modelled in first approximation by its resistivity.

The first approximation of electrode response to a current stimulation waveform is drawn in Figure 2.2(a). Macro-electrodes have larger capacitance and lower resistance (C in the range of nF and R in the range of $k\Omega$) than micro-electrodes (C in the range of pF and R from $10k\Omega$ to several $M\Omega$). The exact impedance can vary over time after implantation due to glial deposition on the surface in contact with the tissue

The electrode is also sized considering the charge required to be injected to trigger cells. Over a certain charge for a given surface, the stimulation can induce electro-chemical reactions and damage the surrounding tissue. The maximal cathodic charge is thus dependent on the electrode area as first observed by McCreery et al. (1990) and quantified by Shannon (1992) as:

$$log\left(\frac{I_{cath}T_{cath}}{A}\right) = k - log\left(I_{cath}T_{cath}\right) \tag{2.1}$$

where k is an empirical value measured originally around 1.8; this equation is illustrated by Figure 2.2(b). This law is, from the designer point-of-view, also limiting the maximal current and

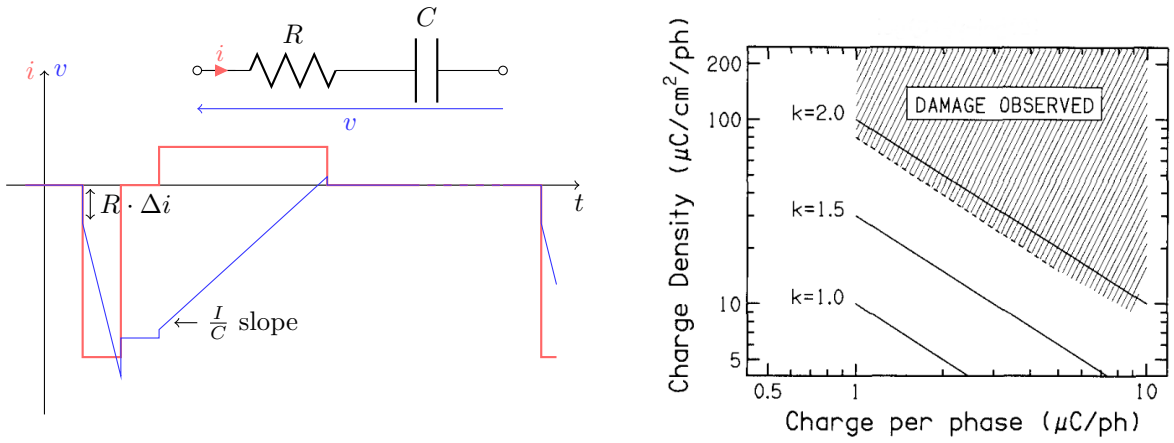

(a) (b)

Figure 2.2 – *(a) Representation of the first approximation electrode impedance model and voltage response to a typical biphasic current stimulation waveform, (b) Illustration of the maximal charge per phase density versus charge per phase; a limit between observed tissue damage and safe stimulation is represented by line of* $k \approx 1.8$ *(original Figure from Shannon (1992))*

in order to prevent from damaging tissues, the electrical current range of a particular stimulator must be chosen under this limit. This maximal injected charge limit can be re-considered by changing electrode material and recent developments aim at increasing the possible injected charge as explained in Cogan (2008).

Consequently, the electrode of a particular context is part of the stimulation system, resulting in constraints in terms of integration, electrical quantities extrema and tissue safety. This entity is the key-point of the electrical to biological transduction and the multitude of neuro-stimulation contexts is resulting in a multitude of dedicated electrodes. The systems developed to drive these electrodes are described in the next section, taking into account their similarities.

2.2 Electronics for extra-cellular stimulation

2.2.1 Architectures of current-mode front-end circuits

The generic front-end for current-mode electrical stimulation consists in a current source connected to an electrode using a combination of switches. As a unique current source can only provide a mono-polar current, different architectures combining switches and sources have been developed to allow the injection of positive or negative current and thus ensure charge balancing. Three structures, presented in Figure 2.3(a), are basically used in stimulation circuits.

One source, passive balancing

Structure $i)$ in Figure 2.3(a) is based on one current source and two switches. This topology can only provide biphasic stimulus with passive charge balancing. Such circuits are suitable for embedded systems because of their asymmetric power supply and the simplicity of driving requirements. This topology is based on only few components and is thus easily integrated on IC.

Nevertheless, this topology only allows for passive charge balancing and a compromise based

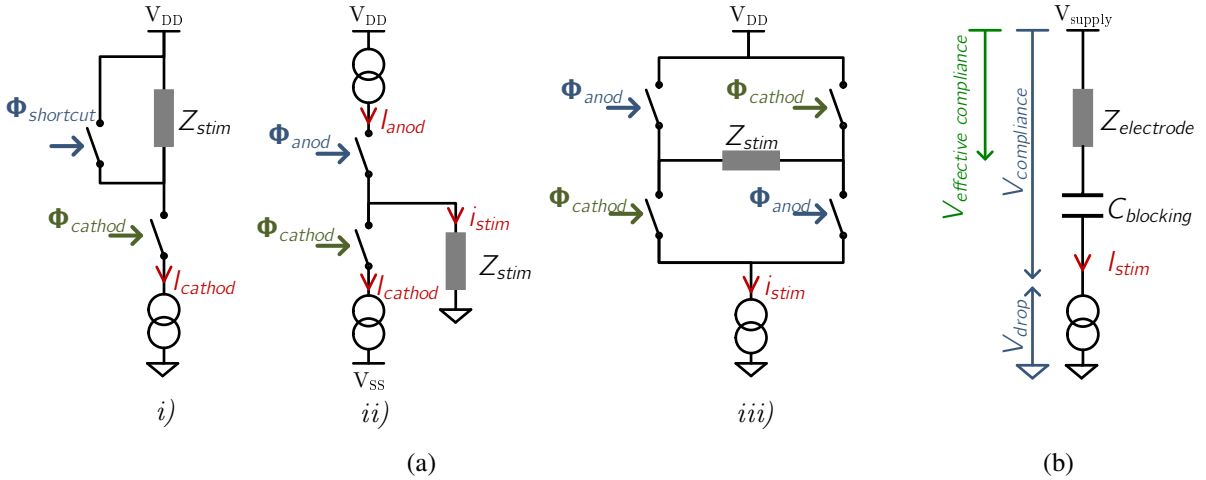

Figure 2.3 – *(a) Circuits used for biphasic stimulation front-end. For structures i) and iii), the ground signal is the lowest potential of the supply source, for structure ii) the ground signal is the middle point of the symmetrical supply. (b) Schematic of a single source loaded by the blocking capacitor and the electrode, highlighting the involved compliance and effective compliance voltages.*

on the electrode impedance has to be found between a discharge with a low peak current and a long duration, or with a high peak current and a short duration. A high peak current is limiting the stimulation effectiveness as it can hyper-polarize target cells and a long discharge is limiting the stimulation frequency in safe conditions (i.e. a full discharge for total charge balancing). A solution with a gradually decreased resistor has been developed by Techer et al. (2004), however, it implies the use of various integrated resistors and additional circuits, resulting in a complex structure far from the simplicity of the original structure.

Two sources, active balancing

Active charge balancing requires a second current source as illustrated in Fig. 2.3(a) $ii)$. Anodic and cathodic currents are generated by separate sources and two switches control the timing of stimulation pulses. The electrode is referenced to the ground potential, consequently, the power supply must be symmetric. This architecture requires a more complex powering circuitry. As the resulting biasing power is approximately twice as high as for the previous topology, this architecture is less suitable for low power embedded systems. Moreover, if the supply is symmetric, the voltage compliance over the load is only V_{supply}, as the electrode is referenced to the ground potential.

This topology is also not really efficient in terms of charge balancing. The presence of two sources at the highest and lowest potentials makes mandatory the use of respectively P and N transistors. Therefore, the current sources are not perfectly paired and charges resulting from balancing errors can accumulate at the bio-electronic interface. If matching calibration techniques can be applied, a third switch is often added in that topology to provide passive discharge. More complex circuits can be designed to perform accurate charge balancing without passive discharge as it will be detailed in chapter 4.

One source, active balancing

A third architecture is often used in stimulation systems, providing active charge balancing with one current source and four switches as shown in Fig. 2.3(a) iii). The current polarity through the electrode is changed, using switches organized in H-bridge structure. The supply voltage is then asymmetric. The use of only one current source allows a reduction of the global power consumption and simplifies the charge balancing. Passive charge balancing can also be performed by breaking the symmetry of switch command or by adding a fifth switch in parallel with the stimulation load.

Nevertheless, this structure cannot be used with multi-channel electrodes that have a common current return path; in such a configuration, asynchronous stimulation of different channels can cause short-circuits between electrodes and possibly able damages by involuntary charge injection in the tissue. In this case the structure of Figure 2.3(a) ii) is the only solution to provide biphasic current stimulation.

A mix between the two last structures waw also studied in the literature, as for example in Harnack et al. (2008) and Nadeau and Sawan (2006). The use of two parallel structures with two sources and active balancing, working as source and sink, is a possible solution to double the voltage compliance ($2 \times V_{dd}$ under a symmetric $\pm V_{dd}$ supply) over the electrode. It removes any connection to a fixed potential, which is not technically possible on all electrodes, particularly on MEAs.

2.2.2 The DC-blocking capacitor

Whatever the adopted topology, there is a risk of involuntary charge accumulation in the tissue, due to the superposition of small leakage currents and charge unbalance. Moreover, there is for every circuit a risk of failure that can result in direct current flow to the electrode. To prevent from such a situation, a DC blocking capacitor must be placed in series with the electrode. In Fig. 2.3(a), Z_{stim} is the combination of the electrode impedance and the DC blocking capacitor. With European standard for implantable electronic prostheses (EN45502-1, 1998), the use of this blocking capacitor is mandatory for therapeutic applications. This component plays different roles as described by Liu et al. (2008). Considerations on sizing rules related this capacitor are summed up in this next paragraph.

The main objective of the blocking capacitor is to provide "block DC, pass AC". Any DC value is blocked without discrimination of the cause, even if an active component of the circuit fails. As illustrated on Figure 2.3(b), it can be noted that the DC value is blocked after a certain time $T_{blocking}$:

$$T_{blocking} = C_{blocking} \frac{V_{compliance}}{I_{DC}} \tag{2.2}$$

where $C_{blocking}$ is the capacity used for the blocking capacitor, I_{DC} the leakage current and $V_{compliance}$ the maximal voltage over the electrode for the used topology defined by:

$$V_{compliance} = V_{supply} - V_{drop}|_{min} \tag{2.3}$$

where $V_{drop}|_{min}$ is the minimal drop voltage depending on the current source topology.

Equation 2.2 can also be considered as a "block DC" after a fixed injected charge $Q_{blocking} = C_{blocking} V_{compliance}$. Thus, on a time window that is largely bigger than the stimulation period, reducing the value of the blocking capacitor reduces the maximal error charge injection and ensures tissue safety. However, this remark on the capacitance is directly balanced by considering voltage changes over a time window equal to the pulse duration. In this case, as the blocking

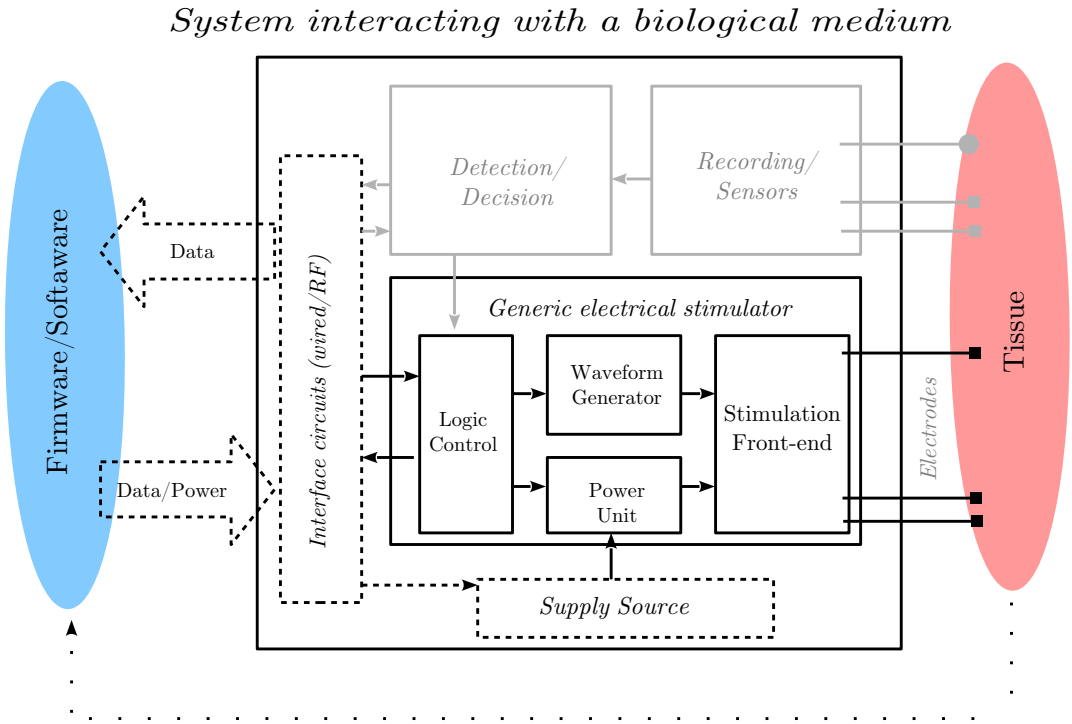

Figure 2.4 – *Overview of a stimulation system and its use in the heterogeneous context of systems interacting with biological medium. The full system overview goes from the tissue, determining the electrode geometry and stimulation front-end specifications, to the interconnection to other circuits, to the user interface.*

capacitor and the electrode are in series, the effective compliance over the electrode can be expressed as:

$$V_{effective\ compliance} = V_{compliance} - \frac{1}{C_{blocking}} \cdot |I_{cath\ max}| T_{cath\ max} \tag{2.4}$$

Consequently, the designer choice is to increase the blocking capacitor value to limit the voltage over this component and limit the constraints on the stimulation front end. The global impedance Z_{stim} must be taken into account when determining the maximum output voltage at the highest current values, to choose the appropriate voltage supply.

Some contributions in the literature explicitly aim at avoiding this component as in Sit and Sarpeshkar (2007). These authors are motivated by the difficulty of large capacitance integration in small systems and particularly in systems with a high number of stimulation channels; however, size reducing techniques have been addressed as in Liu et al. (2006) or Liu et al. (2011). Ensuring fail safe conditions without DC blocking capacitor has not been addressed in the literature and seems not possible as active components can be subject to various defects along time. Consequently the blocking capacitor will always be considered as part of stimulator output in the next sections.

2.2.3 Stimulation systems and constraints

If first generations of stimulation systems (first pacemakers as described in Haddad et al. (2006), first DBS implants...) were based on a minimal architecture providing only stimulation tuning possibilities, the need for more complex experiments and smart therapeutic devices led to

the design of more complex architectures. Recent stimulators are not only based on stimulation front-end and are often part of complex systems. The main blocks and peripheral components of a stimulation system are summed up in Figure 2.4.

The stimulation front-end is the only instance of the stimulator in contact with the electrode and the basic front-end topologies were described in a previous section. However, this block requires generally a particular supply (in the range of $10V$) due to the electrode impedance and stimulation currents. DC/DC converters and technologies compatible with the required supply voltages are then mandatory for the stimulation front-end. Additionally, waveform generators, often composed of DACs and logic finite-state-machines are necessary to drive front-ends. In case of systems with a high number of channels, a dedicated logic block is generally necessary.

The stimulation system in itself is also connected to other circuits: circuits to exchange stimulation parameters or orders, recording or sensing circuits allowing closed-loop configuration, and hardware links to software or firmware interfaces. This communication can lead to the development of RF interface blocks. As the embedded power source is a challenging issue, recent stimulation systems include circuits for data and power transmission, or power management circuits.

All these additional blocks vary over application contexts and hare designed considering the particular requirements associated with a therapeutic context.

2.3 State of the art of stimulation circuits and systems

A study of the literature has been performed on the existing stimulation systems. Results are summed up in Table 2.1 and a statistical analysis is illustrated by figure 2.5. The number of designed systems is important and the main issues of electrical stimulation circuit (power consumption, charge balancing, system integration...) are addressed, each contribution focusing on a specific issue depending on the application.

A first note that can be drawn from Table 2.1 is that the therapeutic applications cover the spectrum of nervous system possible targets. A minority of systems are not explicitly attached to a particular application without attempting a multi-application approach. Only Dupont et al. (2012) initiates a global approach but without confronting the developed setup to a variety of electrodes defining the application contexts.

The second consideration is the relative consensus over the current stimulation. The distribution of stimulators with respect to the output controlled quantity is shown in Figure 2.5(a). Only few circuits are voltage controlled and marginal attempts to design charge based stimulation have been made by Vidal and Ghovanloo (2010). As it can also been observed on Table 2.1, the majority of voltage-mode stimulators are discrete systems. This is explained by the simplicity of voltage stimulator circuit and its ease of integration on freely moving small animal (see Qian et al. (2011) or Russold and Jarvis (2007)), or for the development of a specific experimental setups.

source	I/V	# of channel(s)	technology	# of switch per channel	# of source per channel	biphasic	V_{supply} (V)	V_{comp} (V)	$(I/V)_{min}$	$(I/V)_{max}$	discharge	application	Die Size (mm^2)
Abdelhalim and Genov (2011)	I	N.I.	0.13 CMOS	2	2	yes	3		$5\mu A$	$1.2mA$	A	N.I.	N.I.
Arabi and Sawan (1999)	I	4	1.2 CMOS	4	1	yes	N.I.		0	$6.3mA$	A	Neuromuscular	16
Arfin et al. (2009)	I	4	0.5 CMOS	4	$1(\times 4)$	yes	5		$0.1mA$	$1mA$	A	N.I.	N.I.
Arfin and Sarpeshkar (2012)	I	1	0.35 CMOS	N.I.	N.I.	yes	N.I.				N.I.	N.I.	N.I.
Azin et al. (2011)	I	4	0.35 CMOS	2	2	yes	5	4, 68	0	$94.5\mu A$	A/P	N.I.	N.I.
Bihr et al. (2013)	I	N.I.	0.18 HV CMOS	2	2	yes	15	13	0	$15mA$	A	N.I.	N.I.
Blum et al. (2007)	V	16	0.35 CMOS	N.I.	N.I.	yes	3.8				N.I.	N.I.	N.I.
Bontorin et al. (2009)	V	N.I.	discrete	N.I.	N.I.	yes	15		$0V$	$15V$	A	N.I.	N.A.
Boyer et al. (2000)	I	1	discrete	4	1	yes	N.I.				A	sacral nerve	N.A.
Chang et al. (2004)	I	1	0.35 CMOS	N.I.	N.I.	yes	3.3		0	$2.8mA$	A	nerve	N.I.
Chang et al. (2006)	I	1	0.35 HV CMOS	4	1	yes	13.5		0	$11.3mA$	A	spinal cord	N.I.
Chen et al. (2010)	I	254	0.18 HV CMOS	5	$1(\times 2)$	yes	± 12		0	$5\mu A$	A/P	retinal	27
Chun et al. (2013)	I	N.I.	65n CMOS	6	2	yes	3		0	$8\mu A$	A/P	N.I.	N.I.
Chun et al. (2010)	I	N.I.	0.35 HV CMOS	4	1	yes	20		0	$1mA$	A	N.I.	0.04
Constandinou et al. (2008)	I	3	0.35 CMOS (10V process)	8	1	yes	10		0	$735\mu A$	A/P	vestibular	1.71
Coulombe et al. (2007)	I	16	0.18 CMOS	N.I.	N.I.	yes	3.3				A	visual cortex	8.96
DeMarco et al. (2003)	I	9	1.2 CMOS	2	2	yes	± 7		0	$400\mu A$	A	retinal	4.84
Dommel et al. (2009)	I	2	0.35 HV CMOS	N.I.	2	yes	20		$20\mu A$	$1,24mA$	A/P	retinal	N.I.
von Dongen and Serdijn (2013)	V	2	0.18 HV CMOS	6/2	N.I.	yes	3.5	10	0	$10V$	A	N.I.	N.I.
Dupont et al. (2012)	V/I	1	discrete	0	N.I.	yes	N.I.				N.I.	N.I.	N.A.
Eftekhar et al. (2007)	I	8	0.35 CMOS	4	1	yes	3.3		$100\mu A$	$5mA$	A	FES	3
Ewing et al. (2013)	I	2	discrete	2	1	yes	3.6	< 20	$13\mu A$	$1mA$	P	DBS	N.A.
Fang et al. (2007)	V	1	0.18 CMOS	0	N.I.	yes	3.3				A	N.I.	N.I.
Farahmand et al. (2012)	I	8	discrete	4	1	yes	3.3	< 23	0	$400\mu A$	A	DBS	N.A.
Ferrandez et al. (2007)	I	10	discrete	N.I.	N.I.	yes	N.I.		$25\mu A$	$200\mu A$	A	cortical	N.A.
Forni et al. (2012)	I	1	discrete	1	1	no	6		$50\mu A$	$120\mu A$	N.A.	DBS	N.A.
Georgiou and Toumazou (2005)	I	16	0.8 CMOS	N.I.	1	yes	4.2	3.7	0	$700\mu A$	A	cochlear	21
Gong et al. (2006)	I	16	0.18 CMOS	4	1	yes	1.8			$80\mu A$	A	retinal	N.I.
Gudnason et al. (1999)	I	4	2 CMOS	4	$1(\times 2)$	yes	N.I.	10	0	$2mA$	A	FES	12
Harnack et al. (2008)	I	1	discrete	4	2	yes	3	< 18	$50\mu A$	$600\mu A$	A	DBS	N.A.
Hitzelberger et al. (2001)	I	12	0.7 CMOS	4	1	yes	3.3		$1\mu A$	$2mA$	A	FES	42
Hu and Gordon (2008)	I	1	0.5 CMOS	2	2	yes	± 1.5		$100pA$	$35\mu A$	A	N.I.	0.2
Dai Jiang et al. (2011)	I	1	0.6 HV CMOS	4	1	yes	18		0	$1.02mA$	A	vestibular	8.19
Jiang et al. (2012)	I	1	0.6 HV CMOS	4	1	yes	12		0	$1mA$	A/P	vestibular	21.42
Kelly and Wyatt (2011)	V	1	1.5 CMOS	0	N.I.	yes	± 1.75				A	N.I.	N.I.
Langlois et al. (2010)	I	5	0.6 SOI CMOS	2	1	yes	30		$1mA$	$16mA$	P	nerve	N.I.

Lee et al. (2013)	I	4	0.5 CMOS	2	1(×2)	yes	4.6		$80\mu A$	$2.48mA$	A	DBS	2.25
Lee et al. (2008)	I	8	0.18 CMOS	N.I.	N.I.	yes	N.I.		$3\mu A$	$135\mu A$	N.I.	DBS	2.25
Liu et al. (2000)	I	20	1.2 CMOS	N.I.	N.I.	yes	9		0	$600\mu A$	A	retinal	N.I.
Liu et al. (2006)	I	1	0.35 CMOS	4	2(×2)	yes	5			$1mA$	A	N.I.	N.I.
Liu et al. (2011)	I	2	0.6 SOI CMOS	4	1	yes	12				P	FES	4
Liu et al. (2012)	I	4	0.6 SOI CMOS	6	1(×2)	yes	18		$1mA$	$8mA$	P	FES	27.3
Nadeau and Sawan (2006)	I	1	0.8 HV CMOS	8	1(×2)	yes	±10	18.25	0	$2mA$	A	Neuromuscular	10.96
Noorsal et al. (2012)	I	4	0.35 HV CMOS	3	2	yes	20		$4\mu A$	$1mA$	A/P	epiretinal	0.2
Nowak et al. (2011)	I	1	discrete	N.I.	N.I.	yes	N.I.				N.I.	DBS	N.A.
Ortmanns et al. (2007)	I	116	0.35 HV CMOS	2	1(×2)	yes	35		0	$500\mu A$	A	epiretinal	22
Qian et al. (2011)	V	1	discrete	0	N.I.	yes	N.I.		0	$2.5V$	P	DBS	N.A.
Russold and Jarvis (2007)	V	1	discrete	0	1	no	N.I.				N.I.	DBS	N.A.
Shahrokhi et al. (2010)	V	128	0.35 CMOS	4	1	yes	3.3				N.I.	cortical	8.5
Shen and Chu (2010)	I	1	0.35 CMOS	4	1	yes	3.3		0	$165\mu A$	A	DBS	N.I.
Shulyzki et al. (2010)	I	1	0.35 CMOS	4	1	yes	3.3		$20\mu A$	$250\mu A$	A	cortical	0.02
Sit and Sarpeshkar (2007)	I	1	0.7 HV CMOS	3	1(×2)	yes	$15(-9,+6)$		0	$1mA$	A	N.I.	1.44
Sivarprakasam et al. (2005)	I	8	1.5 CMOS	N.I.	1(×2)	yes	±6.5		$10\mu A$	$600\mu A$	A/P	retinal	4.84
Soulier et al. (2008)	I	1	0.35 HV CMOS	3	1(×2)	yes	N.I.				A/P	FES	N.I.
Suaning and Lovell (2001)	I	50	2 CMOS	4	1(×2)	yes	N.I.		$65\mu A$	$2mA$	A	retinal	31.28
Tan et al. (2011)	I	1	0.35 CMOS	2	2	yes	3		$10\mu A$	$10mA$	A	FES	N.I.
Techer et al. (2004)	I	2	0.8 HV CMOS	N.I.	1	yes	N.I.		$20\mu A$	$5mA$	P	FES	15.3
Tokuda et al. (2009)	I	1	0.35 CMOS	2	2	yes	5		$50\mu A$	$1.05mA$	A	retinal	0.04
Töreyin and Bhatti (2012)	V	1	discrete	4	0	yes	2.4				A	N.I.	N.A.
Troyk et al. (2012)	I	16	0.8 BiCMOS	N.I.	N.I.	yes	5		$0.5\mu A$	$63.5\mu A$	A	N.I.	N.I.
Valente et al. (2010)	I	1	0.35 HV CMOS	N.I.	N.I.	yes	12				N.I.	DBS	N.I.
Valente et al. (2012)	I	3	0.35 HV CMOS	2	1	yes	12				A	DBS	0.71
Vidal and Ghovanloo (2010)	charge	1	discrete	N.I.	N.I.	yes	N.I.				A	N.I.	N.A.
Williams and Constandinou (2013)	I	8	0.18 HV CMOS	4	1	yes	11.5		0	$504\mu A$	A	FES	5.4
Zhang et al. (2011)	I	1	discrete	0	1	no	N.I.	6	$25\mu A$	$245\mu A$	N.A.	DBS	N.A.
Zheng et al. (2012)	I	1	discrete	2	2	yes	N.I.				A	N.I.	N.A.

Table 2.1 – *Review of recently published stimulation circuits and systems in the literature (abbreviations note 1: 'N.I' sets for not indicated, 'N.A.' for not applicable), (abbreviation note 2: 'DBS' sets for Deep Brain Stimulation, 'FES' for Functional Electrical Stimulation), (abbreviation note 3: 'A' sets for active charge balancing as primary charge balancing technique, 'P' sets for passive charge balancing as the only charge balancing technique)*

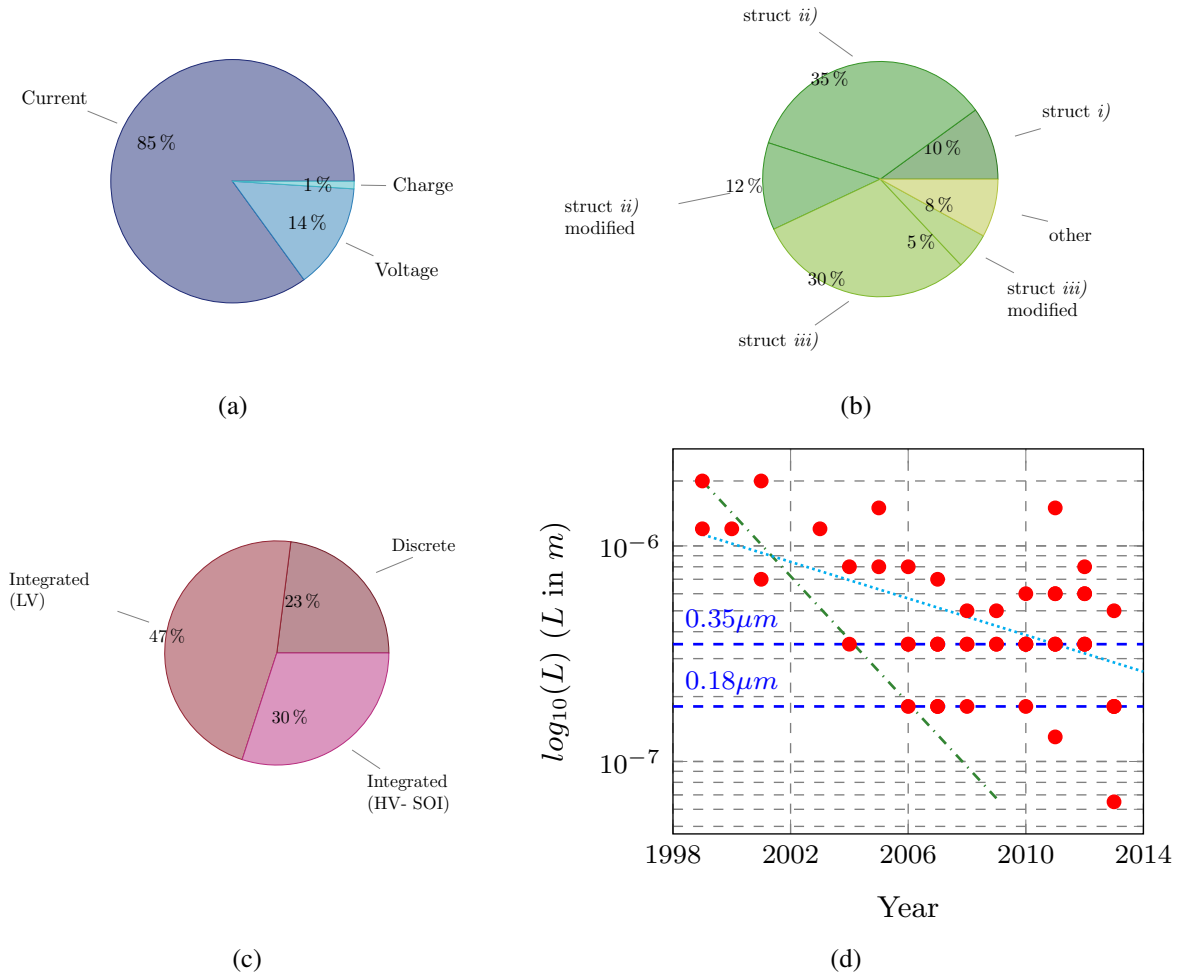

Figure 2.5 – *Graphical representation of design choices observed from the literature about stimulation circuits: (a) output controlled quantity; (b) used topology for current controlled stimulators, with respect to the Figure 2.3(a); (c) technological choice between discrete or integrated and integration process; (d) evolution of process gate length (red dots correspond to the process minimal gate length; in green - parallel to the Moore's law starting from the highest stimulator gate length in 1999; in cyan - linear interpolation of the gate length with time).*

Among current controlled stimulators, topology distribution is presented in Figure 2.5(b). A majority of systems is based on structures *ii)* or *iii)* of Figure 2.3(a), providing active charge balancing. Only few systems perform passive charge balancing with structure *i)* and only marginal and relatively recent designs do not perform any balancing then limiting the stimulator to few components. It can also be noted that both structures *ii)* or *iii)* can be modified. Such modifications are motivated by different objectives:

- allow for more flexibility by mixing the structures as in Nadeau and Sawan (2006),
- optimize a given characteristic, as in Liu et al. (2006) with the H-bridge with reduced blocking capacitor value, or in Chun et al. (2013) to improve the front-end voltage compliance,
- drive specific electrodes, especially multi-polar electrodes with unusual geometries as in Dommel et al. (2009).

Other structures remain marginal. However, as systems are highly specific, the developed stimulators present a variable number of sources and switches per channel, due to different connectivities to electrodes, various passive discharge techniques or uncommon requirements. This number of sources and switches is a sizing factor for such systems, as increasing this number has a direct impact on waveform generation and control.

Table 2.1 also includes information about technologies and reported die size. The correlation between the die size and the number of channels is unclear, mostly due to specific requirements resulting in additional circuits. As an example retinal implants impose severe constraints as mentioned by Chen et al. (2010) where a 256-channel system is fabricated in a $27mm^2$ area; on the opposite, other targets such as vestibular implants have fewer constraints on space as illustrated by the area of circuits from Constandinou et al. (2008) or Jiang et al. (2012). The die size also appears to be decorrelated from the used technology.

Technological choices are detailed in Figures 2.5(c) and 2.5(d). From Figure 2.5(c), it can be noted that almost a quarter of stimulation systems are made of discrete components. This choice is independent of the publication year and is still made especially for research study as performed in Harnack et al. (2008), Forni et al. (2012) or Qian et al. (2011). Other circuits are based on CMOS technology. It is noticable that a third of the systems are based on HV (or marginally SOI) processes. This choice is motivated by the need for high voltages due to the electrode impedance. Technology evolution for stimulators is plotted in Figure 2.5(d); gate lengths are at relative high values compared to today's available technologies and the evolution is slow compared to Moore's evolution. Since 2006, all circuits use sub-micron technologies; a majoritary used technological length are $0.35\mu m$ and $0.18\mu m$, and only few circuits have a smaller gate lengths. This slow evolution can be explained by two factors:

- the need for reliable circuit based on reliable technologies is crucial for medical applications,
- the diminution of the gate length is associated with a decrease of supply level; however, the geometry of the electrode and associated current levels remain stable, so that following gate length reduction would imply less compliance on the output stage.

The evolution of stimulation circuits is not closely linked with silicon area reduction; current challenges are the integration of more peripheral functions, and complex heterogeneous system design.

2.4 Partial Conclusion

This chapter reviewed the numerous stimulation materials and circuits described in the literature, leading to the conclusion that:

- electrodes are specific to each application,
- as these electrodes are mainly current controlled, tissue safety is ensured with a blocking capacitor,
- a small number of front-end topologies are used to drive the electrodes and designing a stimulator often implies a specific improvement to these topologies.

These simple assertions suffice to design cell-triggering systems for therapeutic purposes, as explained in chapter 1. These similarities in both physiological and technological aspects

encouraged a reflection on a global approach, aimed at producing electrical systems that adapt to biological requirements. The next part of this document describes two sample designs, devised as case studies to optimize a specific point suited to the particular application. The third part of this section outlines the design of a global stimulation approach, based on both electrode impedance considerations and electronic topologies, converging in a multi-application system.

PART II

DESIGNING SPECIFIC STIMULATORS

"Science is not sacrosanct. The mere fact that it exists, is admired, has results is not sufficient for making it a measure of excellence. Modern science arose from global objections against earlier views and rationalism itself, the idea that there are general rules and standards for conducting our affairs, affairs of knowledge included, arose from global objections to common sense. "

P. K. FEYERABEND, *Against Method*, P. 223, 1975

CHAPTER 3

DESIGNING A STIMULATOR FOR LONG-TERM IN VIVO EXPERIMENTS ON RODENTS

For over 30 years, Deep Brain Stimulation has been used as a therapeutic approach for increasing patients' quality of life in degenerative neural disorders, such as Parkinson Disease. The effects of DBS on motor activity are well established, but the underlying phenomena and side effects are not clearly understood, leading to various experiments on animal models.

Neurological disorders can be modelled in animals, in order to recreate physiological states and behavioural outcomes. PD is traditionally induced using a chemical neurotoxin that exerts high selectivity on neural populations of basal ganglia involved in the pathology. Clinical features of PD are induced in primates by intravenous injections of 1-methyl-4-phenyl-1,2,3,6-tetrahydropyridine (MPTP), as demonstrated by Bankiewicz et al. (1986). While primate models are suitable for surgery with the same implants developed for humans, population studies remain expensive and difficult. Other models have been developed using rodents. PD-like disorders can also be induced by intravenous injection of MPTP, as reported by Heikkila et al. (1984). PD-like or hemi-PD-like disorder models may be obtained in rats and mice using bi- or unilateral intra-cerebral injection of 6-hydroxydopamine (6-OHDA), as described by Ungerstedt (1968). As 6-OHDA selectivity produces similar abnormalities to those seen in human PD patients, these models are widely used for research into the DBS action mechanism, as noted in Nowak et al. (2011). Moreover, this technique is suitable for studying therapeutic effects of DBS on major PD symptoms, such as tremors, akinesia, and rigidity.

Contrary to primates, commercial human DBS implants cannot be used in rodents. Thus accurate modelling of the DBS mechanism in small rodents required the development of specific embedded stimulators to mimic the therapeutic effect on human patients. This chapter describes the design and validation of a stimulator for long term DBS in PD-induced rodent populations. This highly-specific system is based on constraint evaluation and full chain design, from electronics to mechanical support and surgery. Its electrical properties are examined and results of *in vivo* experiments are reported.

3.1 Issues on Deep Brain Stimulation devices for experiments on animal models and existing systems

Before reviewing and comparing the existing solutions, important properties related to DBS devices will be considered, according to the objectives previously announced: apply to the rodent the therapeutic conditions used for humans and be able to perform chronic stimulation on a freely moving animal.

3.1.1 Specific stimulator properties and corresponding design constraints

Bilateral stimulation

Chemically induced parkinsonism Bankiewicz et al. (1986); Heikkila et al. (1984); Ungerstedt (1968); Nowak et al. (2011) can be either unilateral or bilateral. However, for DBS mechanism studies, behavioural evaluation has to be performed on groups of animals. In order not to induce dis-symmetry in movement, bilateral Parkinsonism is used in majority of studies. This implies to implant two electrodes, one for each right and left subthalamic nucleus, and provide an adapted stimulation.

On rodents, the distance between the right and left subthalamic nuclei is relatively small ($5mm$ according to the rat brain atlas of *Paxinos and Watson, 1986*), and electrodes have to

be implanted over a short operative time to limit the impact of anaesthesia on the animal. A simple solution to face this problem is to design mechanically coupled electrodes. Hence, the stimulation can be made separately, with a two-channel system, or combined, with a one-channel system delivering twice the current needed on a single electrode.

The bilateral stimulation results then in design constraints on the electrodes and on the level of the delivered current. In this chapter the required stimulation current is considered as the sum of the currents for both hemispheres.

Programmability

The DBS waveform is periodic and its frequency f_{stim} is an important parameter. Frequencies less than $10Hz$ are known to increase motor symptoms of PD, whereas frequencies over $50Hz$ tend to decrease them; furthermore, the current threshold decreases as the frequency increases as explained by Volkmann et al. (2006). A generally accepted compromise to lower current levels is to set up stimulation frequency to $130Hz$, however, this parameter can be changed if unsatisfactory physiological responses are observed. All stimulation parameters (frequency, amplitude and pulse duration, as shown in Fig. 1.9) should be tuned to obtain motor symptom reduction, as observed in a freely moving animals.

Moreover, these parameters can change after the electrodes implantation and have then to be re-adjusted easily; some protocols even impose to stop stimulation, as for example MRI imaging. As long-term stimulation will be addressed, the design of the system must allow the easy tuning of the waveform parameters and the storage of a given experimental configuration.

Freely moving animal

This point is crucial in order to correctly evaluate therapeutic effect of DBS on rodent, especially complex motor activity and depression-like behaviour as made in Delaville et al. (2012).

Motor activity evaluation can be done using various tests. The most commonly used is the evaluation of locomotor activity in the open-field (Matsumura et al., 1995; Spieles-Engemann et al., 2010; Dulawa et al., 1999). This test supposes an ease of access in the space; other motor tests have been developed to evaluate rigidity and catalepsy, which are two symptoms of PD, like for example the bar-test Wu et al. (2007). Parkinsonian non-motor disorders can also be quantified by the elevated plus maze (Carobrez and Bertoglio, 2005), where the rodent has access to closed or open arms of the maze (anxiety-like behaviour), or sucrose preference (Sclafani and Ackroff, 2003), for which the animal is placed in the presence of two bottles to drink (depression-like behaviour). All these behavioural tests require the use of special equipments and the free motion of the animal in various areas without discomfort of being linked to an electrical device.

The resulting constraint for the stimulator is to be embedded on the rodents. Consequently, the volume and weight have to be managed. The volume is linked to the system placement in or on the body. The weight has to be bearable for the animal. We adopted an upper weight limit considering the physiology of the animal model: this limit corresponds to 5% of the average weight (around $400g$) of a male *Sprague Dawley* rat, the commonly used specie for physiological experiments. The entire system (electronics, battery and cases) has to be less than $20g$ to limit impact on animal.

Stimulation lifetime

The embedded supply source has to provide enough energy for long term experiments, to be replaced or recharged. Consequently, the overall power consumption has to be as small as possible without interfering with needs inherent to tissue safety. This condition has to be taken into account at all steps of the stimulator design, from the front-end circuit topology to the global system powering strategy, including the choice of embedded battery.

Re-usability and cost

DBS studies on action mechanisms or side effects evaluation are based on chronic population experiments. The cost of the stimulation system has a big impact on the feasibility of experiments. The ideal stimulator for rodent experimental setup can be re-used for several experiments. In this case the battery has to be changed easily without excessive additional cost.

The need for cost effectiveness also has a repercussion on the adopted technology. Most of available stimulators are designed on chips, although custom Application Specific Integrated Design solutions can be costly solutions. All integrated solutions also have the drawback of being less flexible than the ones using off-the-shelf components, making them less adapted for therapy enhancement studies. However, the use of discrete electronics impact is not in favour of the system miniaturization.

3.1.2 Existing embedded stimulators for rodents

First used methods for electrical stimulation on freely moving rodents were based on rotating wire placed over animal's cage (Matsumura et al., 1995). For the time of stimulation the animal had a wire plugged over their skull. However, this solution limits the number of behavioural testing to an area defined by cable length; exploration of outlying area can induce tensions on animal skull where the electrode is fixed to the skull.

Several embedded DBS systems have already been designed for rodents, trying to satisfy previously reported constraints. We propose to review these solutions, focusing on one important criterion: the location of circuit in rodent body.

Two studies (Russold and Jarvis, 2007; Harnack et al., 2008) have reported systems with an electronic part implanted in the abdominal area of rodents, connected to an electrode implanted in the brain. The major advantage is that the animal can move easily after surgery. Nevertheless this choice presents major risks consecutive to the surgery, like infections, especially in the abdomen region. It is then mandatory to use biocompatible materials.

In both studies, stimulation parameters are programmed using RF links; in Harnack et al. (2008), communication is done using Reed-switches and the RF emitter is a tubular device containing the animal during the programming of stimulation. Of course, the animal movements are highly restricted and DBS action cannot be evaluated during programming. The battery is inside the animal body, implanted with the circuit, which requires additional surgery to change it, with additional risk of infection. Moreover the use of RF link has a cost on global power consumption. In Russold and Jarvis (2007) no detail is given on tissue safety and Harnack et al. (2008) use charge balanced current waveforms. This first kind of DBS device is not adapted for experiments on rodents since it provides a high risk of side effects for a short time of action.

A second kind of embedded stimulator has been described in Nowak et al. (2011) and Lee et al. (2010). Both devices are wearable stimulators placed in vests. This solution solves two drawbacks of implanted devices: first, side effects of surgery are limited to electrode insertion and it is not necessary for electronics to be biocompatible as it is not in contact with tissues.

Second, the battery is accessible on the back of the rodent and can be changed for long term experiments.

Nevertheless, such experiments are limited: animals also have to be placed in separated cages; even though, they can tear off their vest, and they risk severe brain damage if the electrodes are pulled out. The use of these wearable devices is in the end too risky for long term experiments, even if both systems of Nowak et al. (2011) and Lee et al. (2010) respect electrical conditions of tissue safety.

A third type of stimulators are detailed in Qian et al. (2011) and Forni et al. (2012). These stimulators fixed to the skull whit dental cement while electrodes are implanted in the brain. The risk of infection is limited compared to the first category of stimulators. Moreover, the risk of breaking the device is small if its volume and weight are limited. In Qian et al. (2011) the battery cannot be changed due to the chosen packaging. In Forni et al. (2012), the entire stimulator device can be separated from the head allowing a simple battery change and the use of MRI apparatus during the experiment. Nevertheless authors of Forni et al. (2012) did not consider the standards Merrill et al. (2005b) for safe electrical stimulation.

To conclude, the latter stimulator category seems to be the most suitable for long term experiments. All presented stimulators (Nowak et al., 2011; Harnack et al., 2008; Russold and Jarvis, 2007; Lee et al., 2010; Qian et al., 2011; Forni et al., 2012) were designed for unilateral stimulation, a setup only suitable for 6-OHDA-induced hemi-parkinsonism. As neurodegenerative diseases are bilateral, this chapter describes a system which allows bilateral implantation of electrodes in the STN of both cerebral hemispheres. For bilateral stimulation only one stimulation channel is needed but the maximum current has to be doubled.

This system is the first DBS device developed for chronic long-term experiments on populations of rodents, respecting all safety procedures as summarized previously. Hereafter the circuit design, architecture and sizing are described, as well as considerations on power optimization, battery selection, and the specificities of the package attached to the implanted electrodes.

The front-end stimulation is the only part of the DBS device directly connected to the electrodes. This circuit is in charge of delivering the adequate current to the tissue. It may work under a high output voltage considering the impedance loading while respecting charge balancing.

3.2 Front-End Stimulation circuit

To realize the embedded DBS system, the H-bridge topology presented in the previous chapter was chosen; this topology is the most adapted for low power application since the power supply is asymmetric. The system, described in Fig. 3.1, uses two levels of supply voltage. A low voltage supply V_{dd}, from the batteries, is connected to the current source and control circuits. The H-bridge is supplied with the high level voltage V_{HV} generated by a DC/DC converter.

V_{dd} is fixed by the choice of battery technology, and can vary due to the state of charge. In order to deliver a constant waveform over time, the stimulus generator uses a supply-voltage-independent current source. The schematic of this source is explained in section 3.2.1. Additional circuits for timing control and voltage-level conversion are described in section 3.2.2.

3.2.1 Supply-voltage-independent programmable current source

A current source (see Fig. 3.1) that can be controlled using a variable resistance and switched ON and OFF was designed to limit the impact of biasing on the power consumption. Transistors

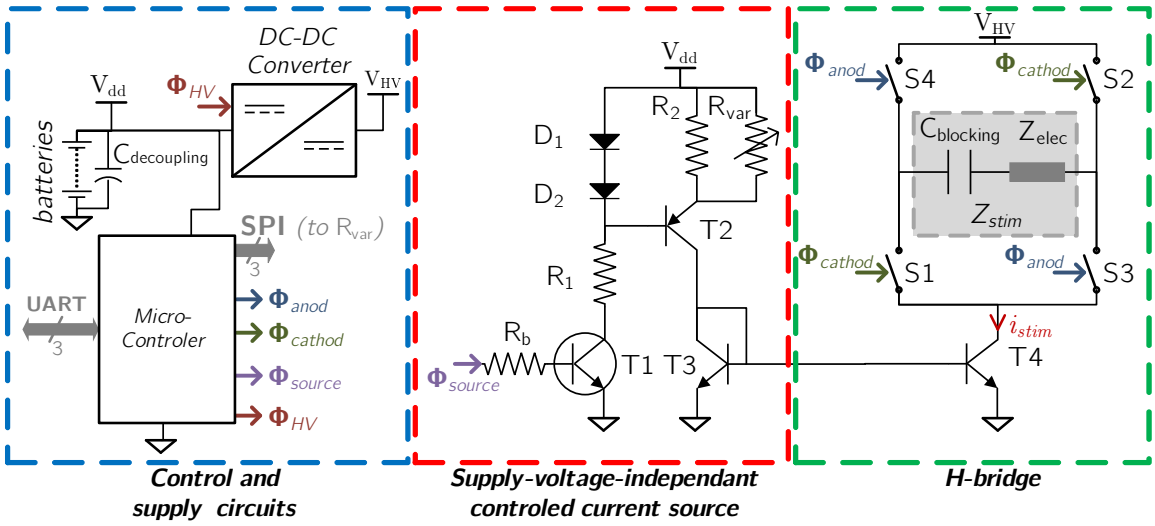

Figure 3.1 – *Overall schematic of the developed DBS system. The circuit is divided in three parts.* (c) *The stimulation current* (i_{stim}) *is delivered to the load* (Z_{stim}) *composed of the electrode* (Z_{elec}) *and the blocking capacitor* ($C_{blocking}$)*, by a H-bridge topology (green rectangle).* (b) *The current value is fixed by a supply voltage independent current source (red rectangle).* (a) *Supply circuits and a micro-controller (blue rectangle) drive blocks* (c) *and* (b).

$T3$ and $T4$ are forming a current mirror to link the source output to the front-end stimulation. In order to reach accurate copying, $T3$ and $T4$ are matched transistors included in the *BCV61C* part. The current source is formed by the combination of $D1$, $D2$, $T2$, $R2$ and R_{var}. To reach accurate values and reproducibility, $D1$, $D2$, $T2$ and $R2$ can be found in package using a *PSSI2021SAY*. Assuming that emitter and collector currents of $T2$ are equal, the biasing current is:

$$i_{c\,T2} = \frac{2V_{D\,on} - V_{be\,on}}{R2 // R_{var}} \tag{3.1}$$

where $V_{D\,on}$, $V_{be\,on}$ are voltages across the diodes and the BJT base-emitter junction. Both $V_{D\,on}$ and $V_{be\,on}$ can be considered as constant values if a sufficient biasing current is provided. If necessary, this condition can be reached by lowering the value of $R1$. Transistor $T1$ is used as an ON/OFF switch, so that minimum voltage across $R1$ is determined by:

$$V_{R1\,min} < V_{dd} - 2V_{D\,on} - V_{ce\,sat\,T1} \tag{3.2}$$

Contributions of $R2$ and R_{var} can be separated. $R2$ ensures a fixed minimum current (in our case $i_{R2} = 15\mu A$) and R_{var}, when decreasing, increases stimulation current.R_{var} is a digitally programmable resistance (*MAXIM MAX5484*). The resistance variation is then linear, coded on a 10 bits value; the expression of the global stimulation current is then:

$$i_{stim} = i_{R2} + \frac{(2V_{D\,on} - V_{be\,on})}{R_{min} + D \cdot R_q} \tag{3.3}$$

where D is the 10 bits value coding the resistance ($D \in [\![0, 1023]\!]$), R_q is the quantum of resistance ($Rq = 50\Omega$) and $Rmin$ ($Rmin = 110\Omega$) is the minimum resistance of R_{var}. From this equation, one can observe that the variation law of current is a hyperbolic function of R_{var} code as illustrated in the figure 3.2(a). Such variations have already been used for neural electrical stimulation Lee et al. (2010) and seem adapted to *DBS*, where higher values of current are not often used unless there is electrode misplacement during surgery Volkmann et al. (2006).

Power on the H-bridge depends directly on electrode impedance Z_{stim} and i_{stim}; the power consumption of the programmable current source is approximated by:

$$P_{source} \approx V_{dd} \left(\frac{V_{dd} - 2V_{D\,on} - V_{ce\,sat\,T1}}{R1} + i_{stim} \right) \tag{3.4}$$

The first term is due to the current source biasing and can be reduced by increasing $R1$ with respect to equation 3.2. The second term is directly linked to the required stimulation current. The supply voltage V_{dd} could be decreased, depending on the battery technology choice which will be detailed in section 3.3.

3.2.2 Control and supply circuits

The control circuit generates the switch commands for cathodic and anodic pulses Φ_{cathod} and Φ_{anod} by driving analog switches realized with a *MAX4623*, and sends the values of the required current levels through the command of the variable resistance using a Serial Peripheral Interface (*SPI*) link. This circuit also controls the current source bias voltage Φ_{source} and the command of the high-voltage power supply Φ_{HV}. A typical stimulation pattern is described in Fig. 3.2(c).

Parameters necessary to define a standard current stimulus as in Fig. 3.2(c) are: current sign and value, as well as timing of the cathodic and anodic phases.

Current sign management is done by generating cathodic and anodic signals in the right orders. The programming of a current value is performed with a *SPI* link, driving the variable resistance described in previous section (a 10 bits variable digital resistance with 1 code volatile memory register). As currents are coded on 10-bits values, two bytes are sent by the *MCU* to generate each current value. However, for a given *SPI* baud-rate, this procedure is limited by the interval between two current pulses. In typical case, the inter-pulse timing, see Fig. 1.9, for *DBS* is $60\mu s$.

The most challenging section is the switching between cathodic and anodic values. Limiting the SPI baud-rate allows to minimize the MCU frequency, and thus the power as explained in the next section. The anodic code is stored in the resistance's non-volatile register when initializing a new waveform, and is no longer transmitted; immediately after, the cathodic code is transmitted to the tap register to generated the first cathodic pulse. During the inter-pulse delay of each stimulation period, the non-volatile-register is copied in the resistance's tap register using a one byte communication (between markers t_1 and t_2 on Fig. 3.2(c)) to generate the anodic current. After the anodic phase, i.e. at the end of the stimulation waveform, the cathodic code is re-sent using two bytes to the tap register (between markers t_3 and t_4), configuring the current source for the next stimulation period. A timing difference ($t_2 - t_1 < t_4 - t_3$) can be observed on the logic output of the SPI Slave Select. With this strategy and a limited baud-rate of $147.5\ kbit \cdot s^{-1}$, the minimal inter-pulse delay is:

$$T_{inter-pulse} = \frac{N_{bits}}{BR} \geq \frac{8}{147.5\ 10^3} = 54.24\mu s \tag{3.5}$$

With this current source and time resolution ($500ns$), charge balancing has a limited accuracy and a maximal equivalent DC current error was measured at $520nA$ with a *pico-ammeter/voltage source Keithley 6487*. In order to decrease this unbalance, once every 256 periods (approximatively $2s$) a passive discharge was implemented, so that the maximal error was reduced to $72nA$; the additional DC blocking capacitor prevents from any residual charge on the tissue.

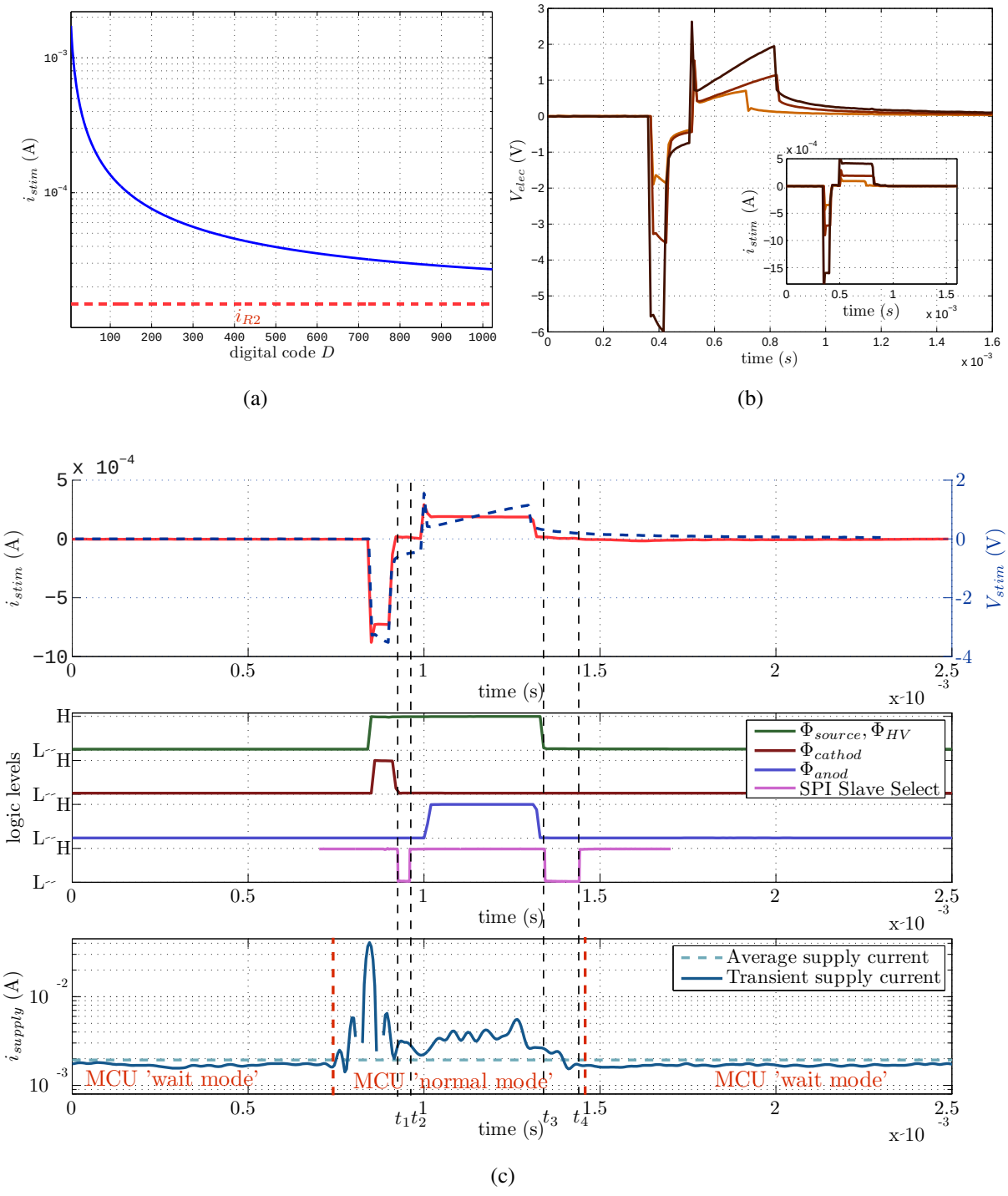

Figure 3.2 – *(a) Graphical representation of the stimulation current i_{stim} as a function of the digital code of the variable resistance. (b) Electrode response for biphasic stimulation of $I_{cathod} = 400$, 800 or $1600\mu A$ and $60\mu s$ pulse. (c) Recorded chronogram of a typical stimulus ($60\mu s$ of $750\mu A$ cathodic current, charge balanced with a $250\mu A$ current pulse and $60\mu s$ of inter-pulse delay with a frequency of $130Hz$), corresponding logic commands and supply current.*

As illustrated in Fig. 3.1, the high voltage level necessary to provide current stimulation is generated from the embedded battery through a DC/DC switched mode power supply. The used topology is a Boost-Converter (*Linear Technology LT3494*) that levels up the voltage. The voltage across electrodes was measured for different levels of current (Kolbl et al., 2013). As voltage depends on both current value and pulse width, a measurement was conducted on saline solution with maximum values (i.e. $2mA$ and $500\mu s$) and the maximum measured voltage was near $8V$, a set of electrode response voltages are presented in figure 3.2(b). The boost converter has to provide sufficient voltage for the electrode and for the voltage drop of DC blocking capacitor, switches and the current source. Moreover, the electrode impedance is known to increase after surgical implantation Lempka et al. (2009a). To ensure stimulation in any situation, a high voltage supply of $17.6V$ was used in the front-end. This level can be adapted by changing external components of the used Boost-Converter.

3.3 Considerations on system supplying

As often for embedded medical applications, the most challenging constraints for this chronic stimulator are the required power and energy. The power is imposed by the load, the system requirements and the circuit topology. In 3.3.1 our strategy to minimize the power consumption is presented. The energy challenge is related to the need for chronic stimulation, with minimal disturbance for the animal carrying the power source. In 3.3.2 the available battery technologies will be discussed, and a suitable choice in this context is proposed.

3.3.1 Power management

In order to be integrated on animal's skull, the volume and weight of the overall system have to be minimized. As the most prominent part of miniaturized systems are dedicated to power sources, the overall power of the system has to be optimized without influencing developed functionality. The power consumed by the system presented in Fig. 3.1 is given by:

$$P_{stimulator} = P_{\mu C} + P_{source} + P_{H-bridge} + P_{boost} \tag{3.6}$$

where $P_{\mu C}$ is the power of the MCU (Fig. 3.1 (a)), P_{source} is the power consumed by the controlled current source (Fig. 3.1 (a)), $P_{H-bridge}$ is the power consumed in the H-bridge (Fig. 3.1 (c)) and P_{boost} is the power consumed by the step-up DC/DC converter (Fig. 3.1 (a)).

in a previous section, it was set that the current source power consumption can be reduced by limiting the diode current of $D1$, $D2$ (see Fig. 3.1). Moreover this current source can be turned off when not used by blocking transistor $T1$ (see Fig. 3.1). $P_{H-bridge}$ is approximated to the load power consumption as the switches equivalent resistor is negligible compared to the electrode's.

To evaluate and optimize the remaining terms, $P_{\mu C}$ and P_{boost}, both the mode of operation and the MCU frequency have to be taken into account. Typical *DBS* stimulus waveform, consists of short current pulses regarding the stimulation period. For example, consider a frequency of $130Hz$, a cathodic pulse of $60\mu s$, an inter-pulse of $60\mu s$ and an anodic pulse of $600\mu s$ (i.e.. a cathodic current 10 times higher than the anodic current), the percentage of the period $1/f_{stim}$ during which no stimulation is applied to electrode is:

$$1 - f_{stim} \cdot (T_{anodic} + T_{cathodic} + T_{inter-pulse}) \approx 0.906 \tag{3.7}$$

This simple consideration implies that the stimulation hardware can be turned off most of the time (typically, more than 90% of time) and can be turned off.

Technology	**Typical applications**	**Energy density** (mWh/g)
Lithium Iodine (Li/I_2)	CP	$210 - 270$
Litium-Manganes Dioxyde (Li/MnO_2)	CP - Nstim - DDS	$230 - 270$
Lithium-Carbon Monofluoride (Li/CFx)	Nstim - CD	≈ 440
Lithium-Silver Vanadium Oxyde (Li/SVO)	CP - Nstim - CD	≈ 270
Lithium-Thionyl Chloride ($Li/SOCl_2$)	CD - DDS	≈ 500
Li-ion	Cochlear Implant (Secondary batteries)	

CP	: Cardiac Pacemaker	$(30 - 1000\mu W)$
Nstim	: Neurostimulators	$(30\mu W - 10mW)$
DDS	: Drug Delivery Systems	$(100\mu W - 2mW)$
CD	: Cardiac Defibrillator	$(30 - 100\mu W)$

Table 3.1 – *Typical battery technologies used for different types of IMD corresponding to different power requirements*

P_{boost} is inversely proportional to the efficiency of the Boost converter, and related to the output current. This current cannot be controlled since it is directly the stimulation current, but can be smoothed by adding decoupling capacitors of high values at the step-up output. Nevertheless, the boost circuit input power is also determined by its quiescent current. A boost IC (*LT3494*) that can be turned in a shut-down mode, changing the quiescent current from $65\mu A$ to $1\mu A$ was chosen. Φ_{HV} (see Fig. 3.1) controls the boost circuit commutation between the *active* and *power saving* mode, as illustrated in Fig. 3.2(c).

The most power consuming part of the system is the MCU. $P_{\mu C}$ can be separated in a static part and a frequency-dependent term:

$$P_{\mu C} = P_{stat} + P_{CPU} = P_{stat} + k \cdot f_{clk} V_{dd}^2 \tag{3.8}$$

where k is a constant in Farad, that depends on the processor technology and sizing. The static power of the MCU (*Freescale MC9S08SH8*) is determined by its operating mode. In *'normal'* mode, the static power is maximal and all peripherals are turned on. In *'Wait'* mode, the static power is decreased and the *CPU* goes to a standby mode from which recovery is fast. One *'Stop'* mode can be used to limit even more power consumption but its recovery time is incompatible with the need for fast events described on Fig. 3.2(c). The clock frequency used for the *CPU* unit of the MCU has a proportional impact on power consumption. This power saving strategy has been applied on the developed system as shown in chronogram of Fig. 3.2(c).

The current source and step-up are turned on before cathodic command is applied to the H-bridge (see Fig. 3.2(c)). This activation corresponds to the first action of the MCU, changing

from *'Wait'* to *'Normal'* mode. After the anodic pulse, the MCU is set under *'Wait'* mode again, just after shutting down the current source and the DC/DC converter.

With this strategy, the supply current value is limited when no stimulation current is applied. Nevertheless f_{clk} has to be taken into account when the MCU is in *'Normal'* mode, i.e. when a stimulus is applied or when the stimulation system is receiving stimulation parameters. All these events are processed using hardware interrupts. The associated sub-routines have to be executed in time periods that are negligible compared to stimulation patterns, even configured for the shorter pulse duration ($60\mu s$). A clock frequency of $f_{clk} = 2MHz$ was set; this value is much higher than traditionally adopted clock frequencies (Russold and Jarvis, 2007; Harnack et al., 2008) (under the MHz), but gives better results on power consumption. The resulting transient supply current was measured as presented in Fig. 3.2(c). The average supply current is $1.9mA$, and the peak current around $40mA$ on a short period (less than $10\mu s$). The transient supply remains stable during the stimulation period except when the MCU is experiencing recovery time in the *'Wait'* mode.

3.3.2 Choice of supply sources

The supply source able to deliver a current profile as in Fig. 3.2(c), and have the maximal energy with a system weight limit of $20g$ as specified in section 3.1.1 as to be included in the system. As the current source is independent of the supply voltage, the low voltage supply V_{dd} can be chosen between $2.9V$ and $5.5V$.

Human oriented Implanted Medical Devices (*IMD*) batteries have been of interest since the first implantation of pacemakers about 50 years ago as summed up by Latham (2004). Supply sources occupy $25 - 60\%$ of their volume (Schmidt and Skarstad, 2001), and technology improvements have enhanced patients' quality of life, by limiting surgery. Different technologies are used for human oriented *IMD*, depending on the therapeutic target and associated power requirement (Latham, 2004; Schmidt and Skarstad, 2001; Bock et al., 2012; Wei and Liu, 2008), as summarized in Table 3.1; lithium technology is largely dominant for these applications.These technologies are potentially interesting for our stimulator; however, the weight of batteries used for human IMD largely exceeds $20g$. And regarding overall performances, weight and size reduction affects the total embedded energy as well as reduces available power, as the surface of electrode plates is smaller.

A dedicated study to find the optimal power source was conducted, respecting the cost-effectiveness needs for chronic population implantation. In order to evaluate most adapted technologies for this system, commercially accessible batteries of less than $20g$ were compared. Based on available datasheets, maximal constant current was extracted and related to cell voltage to compute the available power; the energy was computed using the capacity and the cell voltage; both parameters can then be normalized with the weight of the element. Results are shown in terms of energy versus power and energy density versus power density (see Fig. 3.3). This study only takes into account the average nominal power as a first criterium. To support the peak power observed in Fig. 3.2(c), a secondary source acting like a decoupling capacitor will be chosen, as explained later in the section.

From Fig. 3.3 it can be observed that not only lithium batteries are potential candidates for our application. Zinc technologies, except for Zn/Ag_2O, tend to have available energy higher than lithium technologies. The $NiMH$, Zn/MnO_2 and $LiPo$ batteries tend to deliver more power than other technologies. The analysis of the energy density versus power density in Fig. 3.3(b) results in three groups of candidates:

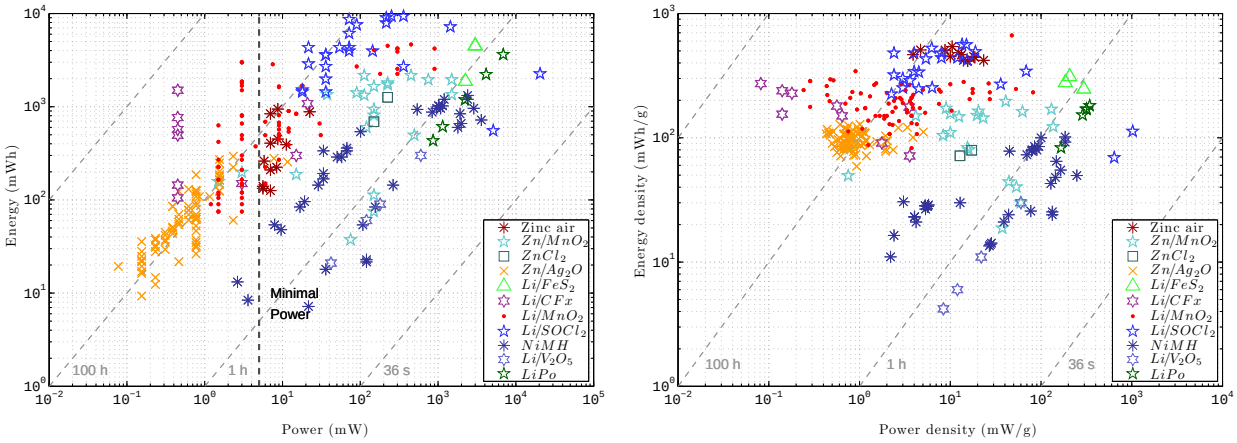

(a) (b)

Figure 3.3 *– Evaluation of small (commercially available less than $20g$) batteries technologies: Zinc/Air, Zinc/Manganese dioxide (Zn/MnO_2), Zinc chloride ($ZnCl_2$), Zinc/Silver oxide (Zn/Ag_2O), Lithium/Iron disulfide (Li/FeS_2), Lithium/Polycorbon Mono-fluoride (Li/CFx), Lithium/Manganese dioxide (Li/MnO_2), Lithium/thyonil chloride ($Li/SOCl_2$), Nickel Metal Hydrure ($NiMH$), Lithium/Vanadium pentoxide (Li/V_2O_5), Lithium polymer (LiPo); (a) energy versus power (b) energy versus power density*

- The first one is composed of $NiMH$, Li/V_2O_5, $LiPo$ and Zn/Ag_2O. It is characterized by a reduced energy density compared to others technologies ($\leq 102mWh/g$). Such batteries cannot supply the stimulator more than approximately 16 hours per gram, whereas their power density could be adapted (except for Zn/Ag_2O).

- The second group is composed of Li/CFx and the majority of Li/MnO_2 batteries; these batteries show higher energy density but have a reduced power density that makes them not suitable for the application.

- The last group is composed of Zinc/Air, Li/FeS_2 and $Li/SOCl_2$ technologies. These technologies allow for long term stimulation, their minimal energy density is higher than $3.102mWh/g$ (corresponding in our case to approximately 48 hours of stimulation per gram), and have satisfying specific power. Only few models of small Li/FeS_2 are available, which are not adapted for our specific spacial design needed for skull implantation.

Tests were performed with both $Zinc/Air$ and $Li/SOCl_2$ batteries. Nominal voltages are $3.6V$ for $Li/SOCl_2$ and $1.35V$ for Zinc/Air cells ($1.6V$ in open circuit), so that three *Zinc/Air* cells in series are mandatory. *Zinc/Air* cells packaging (button package) makes them more suitable for the final version of the stimulator. A *PowerOne zinc/air p675 Implant plus* batteries was used for both tests and animal implantation.

It will now be focused on the requirement for peak power supplying. To prevent from unexpected reset of digital parts, a decoupling capacitor was used as a secondary source to supply the current peak observed in Fig. 3.2(c). Ceramic capacitors are simple and good candidates for such a task as their power density is much larger than conventional batteries, even if their energy density is reduced. Using a triangle approximation of the observed peak current, the minimal decoupling capacitance providing less than $100mV$ voltage drop for the supply profile can be

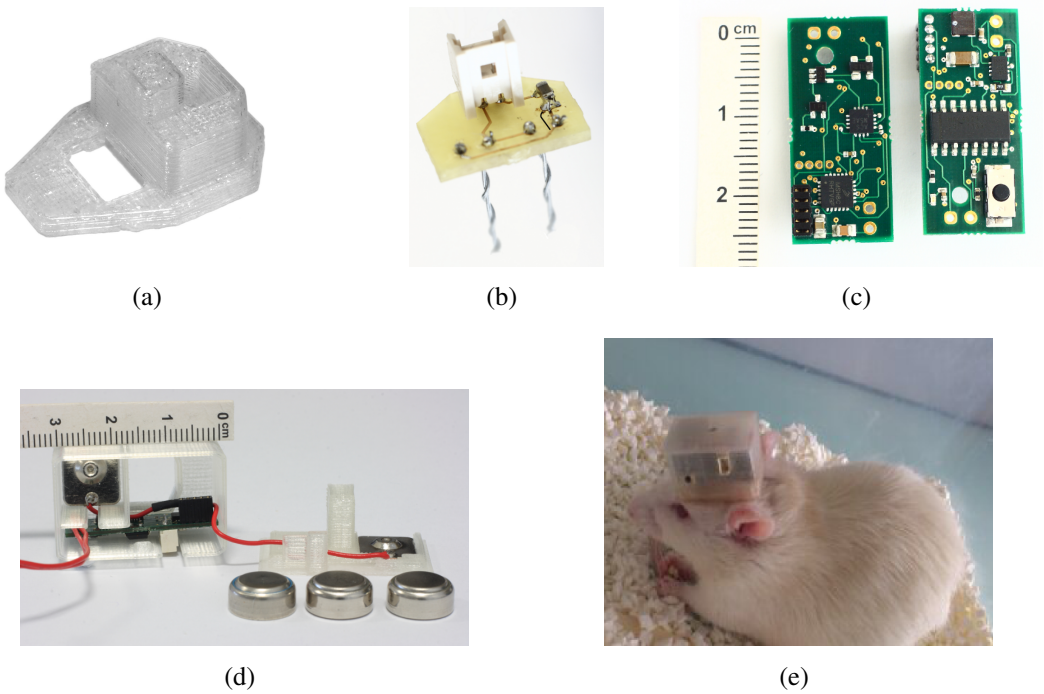

(a) (b) (c)

(d) (e)

Figure 3.4 – *Stimulator, circuit packaging and implantation on rodents' skull. (a) Electrode container; this part is fixed with cement on the cranium of the rodent. (b) Custom electrodes for bilateral STN stimulation; both electrodes are in parallel and the support board includes the blocking capacitor. (c) Electrical stimulator board. (d) Assembled stimulator in container, shown with used Zinc/Air batteries, the top is then screwed on the electrode container after the surgery. (e) Stimulator chronically implanted on a rat; a three wire cable is connected to the device only for waveform programming, stimulation remains active during all experiment phases.*

determined by:

$$C_{decoupling} \geq \frac{Q}{\Delta V_{min}} \approx \frac{(I_{max} - I_{average})\,\Delta t}{2\Delta V_{min}} = 16\mu F \tag{3.9}$$

Ceramic capacitors with these values can be found in package as small as 0603 (1608 $Metric$), so that impact on the final design size is negligible.

3.4 Implantation on rodent skull and and first assessement

3.4.1 Mechanical implantation

All components from schematics presented in Fig. 3.1, except electrodes and associated blocking capacitor, have been integrated on a 6 layers printed circuit board (length: $30mm$, height: $14mm$) as presented in Fig. 3.4(c). As for external control, a reset switch for fast stimulation stopping and a three-wire RS-232 access for stimulation programming were used. MCU flashing can be performed via a dedicated on-board connector, allowing for stimulation program and user interface release without hardware replacement.

The circuit, batteries and electrodes were fixed on the skull using custom plastic packaging, designed using a 3D printer. The package is divided in two main parts:

- *The electrode container:* (Fig. 3.4(a)) this part, attached on the rodent's skull by surgery and fixed with dental cement, supports the electrodes for both left and right cerebral

hemispheres, the blocking capacitor and an external connector (Fig. 3.4(b)). The plastic shape was designed as small as possible in order to limit the impact on animal behaviour after surgery and acts as mechanical support for the second part's mounting.

- *The stimulator container:* this part(Fig. 3.4(d)) is designed to fix the stimulation board and batteries on the skull. The top of the box includes a drilled column for the system to be screwed to the electrode container and to turn on the global system by contacting both poles of electrical supply.

The plastics shape was fabricated with a *Makerbot Replicator 2* with *natural PLA (polylactic acid polymer)* material. The height of the global system when mounted on the animal was $24mm$. The use of a two parts system allows for device retrieval and facilitates MRI or other analysis. It also allows stimulator re-use when the rodent is sacrificed.

A custom electrode system has been developed. This system permits a two sided implantation in one surgery of two electrodes. The distance between the two electrodes is set according to the rat brain atlas of *Paxinos and Watson (1986)* and corresponds to the distance between the two targeted STN. The electrodes support board is shown in Fig. 3.4(b). A high value high voltage capacitor ($10\mu F$ under $25V$ *MURATA* $0603[1608Metric]$) is embedded as close as possible to the electrodes to provide DC current blocking in any case and lessen the impact of passive components surface on stimulator main board. The developed electrodes are needle-like two wire electrodes of twisted tungsten (built from *tungsten Wire .008" Bare, .0110" Coated, Phymep, France*). Electrode diameter has been chosen to be similar with a widely used electrode for mono-lateral electrical stimulation of *STN* on rodents. A first pole is made by a wire section. For the second pole, the current return half-cell electrode was constructed by a $2mm$ long wrap of the second conductor. The distance between the two poles is $1mm$. Electrodes are associated in parallel (both cathodes are connected together, both current-return paths are connected together), and connected in series with the blocking capacitor.

The overall stimulator has a weight of $13.8g$, under the limit of $20g$ for the targeted rodent.

3.4.2 Summary of device characteristics and comparison with existing systems

The objective was to develop a stimulator that allows safe chronic bilateral DBS of freely moving small rodents and reproduces the human therapeutic conditions. In section 3.1.1, we exposed constraints that such devices have to respect for experiments on animal populations: bilateral stimulation, programmability, adaptation to freely moving animal, stimulation life time and re-usability in a context of low cost devices. The design choices we made respect these specifications and our system was both electrically and *in vivo* characterized.

The performances of the designed stimulator are discussed in comparison with state-of-the-art systems for rodents, referenced in section 3.1.1. In Russold and Jarvis (2007), the stimulator was only tested in saline solution and Nowak et al. (2011) and Lee et al. (2010) give no detailed information about *in vivo* experiments, so only Harnack et al. (2008), Qian et al. (2011) and Forni et al. (2012) were examined; results are shown in Table 3.2. The first part sums up characteristics related to *in vivo* experiments, whereas the second part synthesizes important electrical features. It can be noted that none of these *in vivo* used devices are based on ASIC solutions.

Stimulators are presented in a chronological order. Most recent devices are fixed on the skull, which certainly provides greater ease of handling and reduces the risk of infection. Nevertheless

	Harnack et al. (2008)	Qian et al. (2011)	Forni et al. (2012)	This work
Biphasic	yes	yes	no	yes ($I_{DC} \leq 72nA$)
Bilateral	no	no	no	yes
Programmable	yes	yes	no	yes
Removable	no	no	yes	yes
Fixation	implanted	skull	skull	skull
$I_{min}(\mu A)$	50	V.M.	50	26 ≈13p.h.
$I_{max}(\mu A)$	600	V.M.	120	2036 ≈1018p.h.
resolution	12 steps	50 steps		10 bits non linear
$V_{max}(V)$	18	2.5	5	17
$f_{stim}(Hz)$	131	$2 - 250$	130	$10 - 300$
time resolution		$30\mu s$		$500ns$
Lifetime (days)	21	90	7 *(R.B.)*	6 *(R.B.)*

V.M. : Voltage Mode
p.h. : per hemisphere
R.B. : removable batteries

Table 3.2 – *Stimulators for rodent comparison*

the implantable device presented by Harnack et al. (2008) has electrical features compatible with required properties for DBS, in terms of current range and maximal voltage. In Qian et al. (2011), stimulation is in voltage mode, and limited to small values that could be problematic when considering focal electrode with higher impedance. This is not compatible with our specification for current mode, ensuring a better control of injected charge. In Forni et al. (2012), stimulation is in current mode but long-term tissue safety is compromised by the absence of biphasic charge balancing.

The limited performance of the developed system in term of lifetime stimulation can be explained by the hardware capacity to generate a more complex waveform than in Forni et al. (2012). The digital part in our system is faster than Harnack et al. (2008) and Qian et al. (2011), thus can reach better timing precision and accurate charge balancing. Moreover, the development of a two-piece mechanical packaging as in Forni et al. (2012) allows for changing batteries without any additional surgery, so that the life time of the stimulation on one animal can be easily increased. Electrical stimulators in the literature are often realized with ASICs, nevertheless all of chronic *in vivo* demonstrated devices use discrete components. This consideration can be explained by the need of cost-effectiveness, related to long-term experiments on animal populations.

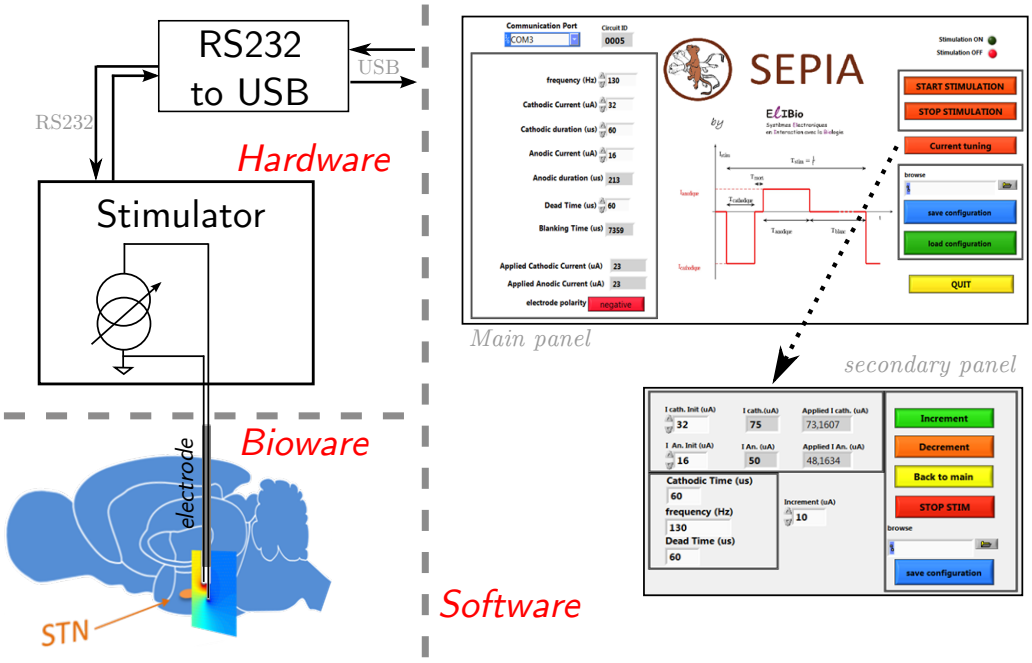

Figure 3.5 – *Schematic representation of the global chain of stimulation, from implantation in the bioware, to a synthetic view of the stimulator as a parametric current source tuned by a dedicated software interface*

3.4.3 Software level for stimulation tuning

The programming of the stimulus is performed with the animal awake and free of movement. Only a cable is connected to the stimulator case during observation for stimulus tuning. As the pressure on the connector is light, it remains possible for the communication to be interrupted however it avoids the risk to hurt the animal in case of sudden movement. The stimulus programming cable is connected from the RS232 interface of the embedded micro-controller to a PC through a *FTDI* RS232 to USB converter. A schematic view of the programming chain is drawn on Figure 3.5.

A dedicated software interface have been developed for the stimulator. This interface permits half duplex communication with the embedded stimulator. The hardware systematically sends an identification number (each ID is unique for an experiment on a population) and a flag if a stimulation is currently ON. The interface allows to turn ON or OFF the stimulus and to send a full set of parameters. Cathodic and anodic current amplitudes, cathodic and interpulse durations and the frequency are user-defined, the charge balancing is processed by the software through the anodic duration computation. A secondary panel can be opened allowing the cathodic current to be increased from a user-defined step with automatic charge balancing. This last option permits fast and easy stimulus tuning on the freely moving animal, as the field triggering the cells is easily tunable by the physiologists without focusing on stimulus parameters.

3.4.4 Surgery and experimental validation of the device implantation

The stimulator was implanted and tested on an adult male Sprague−Dawley rat weighing $324g$. Surgical and experimental procedures were performed in accordance with European Communities Council Directive 2010/63/UE and National Institute of Health Guide for Care and Use of Laboratory Animals.

A first anaesthesia was induced using a mixture of *Xylazine* $(10mg/kg)$ and *Ketamine*

($7.5mg/kg$). Custom concentric bipolar electrodes for both cerebral hemispheres were then implanted simultaneously in the STN under stereotaxic conditions according to the atlas of Paxinos and Watson (1986).

After this first implantation, the stimulation hardware was not directly screwed on the skull to limit post-surgical risks. Smoothed angles in the electrode support enhance the healing and thus limit animal awareness of additional material on the top of the head. We observed no skin reaction, infection or rejection phenomena against the *PLA* electrode container. The stimulator container was fixed on the animal eight days after the implantation of the stimulating electrodes, during a short and light anaesthesia induced using *isoflurane* (5% during 1 to 2 min) to prevent rat sudden movements during the placement.

Electrical parameters of chronic stimulation were chosen according to those used in the stimulated Parkinsonian patient showing reversal of motor deficits. The frequency was fixed to $130Hz$ and pulse width to $60\mu s$. The stimulation intensity was gradually increased (by steps of $50\mu A$) in order to determine the required level. Based on these tests, we used an intensity of $400\mu A$ per side, which was just below the threshold ($450\mu A$) inducing the manifestation of abnormal involuntary movements. The rat was then chronically stimulated for 3 weeks during which the animal presented normal behaviour without any visible discomfort.

3.5 Experimental validation of the stimulation effectiveness on long term implanted population of rodents

The electrical validation of the stimulation waveform is not sufficient to assess effective stimulation rodents for therapy modelling. In order to validate the stimulator on the animal, an experiment on a population was conducted. As the electric parameters of the electrical characteristics are already tested, the experiment has for major objective to evaluate the behaviour of animals with the stimulation and with a parkinsonian lesion.

3.5.1 Materials and methods

The validation was conducted on Sprague Dawley rats weighing around $350g$. Rats were housed 4 per cage before the implantation of the stimulator, one per cage after, and maintained in a 12-h light/12-h dark cycle at a constant temperature ($24°C$) with free access to food and water. All experiments were performed in accordance with the European Communities Council Directive of November 24, 1986 (86/609/EEC). The experimental protocol and its timeline are summed up in figure 3.6. The population of rats was subdivided into two groups: a sham (non-parkinsonian) group ($n = 4$) and a group of parkinsonian animals ($n = 5$).

A first surgery was performed on all animals at day 1 to induce the neurologic lesions. The intra-cerebral injection was performed under anaesthesia induced by intra-peritoneal injection of ketanime hydrochloride ($75mg/kg$) and xylazine hydrochloride ($10mg/kg$). Before the anaesthesia the parkinsonian group received a treatment of desipramine ($0.4\%, 5ml/kg$) to prevent from the toxicity of 6-OHDA on noradrenergic neurons by inhibition of the re-uptake of norepinephrine. An intra-cerebral injection was then performed in the Medial forebrain Bundle (MFB) under stereotaxic conditions according to the atlas of Paxinos and Watson (1986). The sham rats received an injection of $NaCl$ 0.9%; the parkinsonian group received an injection of 6-OHDA ($6.7mg$, *sigma*) in $4\mu L$ of NaCl 0.9% solution. Both groups received antibiotics ($100\mu L$ Borgal 7.5% in intramuscular injection) and analgesic ($100\mu L$ Ketofen in subcutaneous injection) after the surgery .

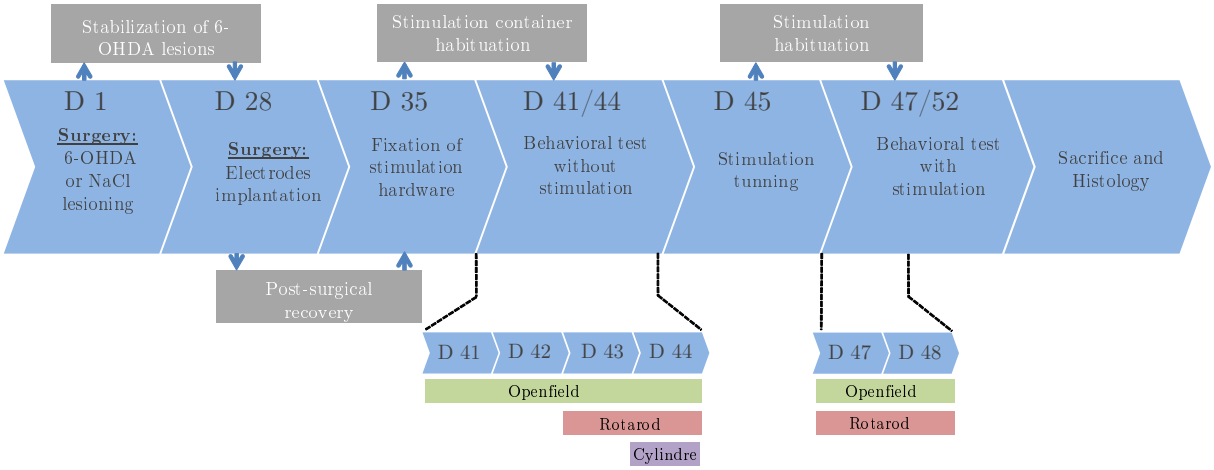

Figure 3.6 – *Time line of the protocol for stimulator for small rodent validation on a population composed of both sham and parkinsonian groups.*

Both group were implanted with electrodes after a delay of 27 days for post-surgical recovery. As previously performed, electrodes were placed under anaesthesia (*Xylazine* ($10mg/kg$) and *Ketamine* ($7.5mg/kg$)), and under stereotaxic conditions. One week of post-surgical recovery passed before placing the stimulator on the electrodes and fixing it on the animal's head. An extra delay of 6 days was imposed to allow for stimulation container habituation. The stimulation waveform was tuned on day 45 for each animal individually as for human. The frequency was fixed to $130Hz$ and pulse width to $60\mu s$. The stimulation intensity was gradually increased (by steps of $50\mu A$) in order to determine the required level. The rats from the sham group were placed under the threshold inducing the manifestation of abnormal involuntary movements. The 6-OHDA group was stimulated over the disappearance of akinesia. A last delay of 2 days was imposed to allow for stimulation habituation.

Between days 41 and 44, and days 47 and 48 behavioural test were performed to evaluate animals motor activity and coordination. Three different tests have been performed. The cylinder test was used according to Schallert et al. (2000). This test determines eventual asymmetries in the motor activity of the rat. Then the locomotor activity was evaluated using actimetry in Open Field (*IMetronic, France*) as assessed in Belujon et al. (2007) for PD symptoms. This test consists in quantification of horizontal and upswing movements per 10 minutes. Each animal performed 20 minutes of test each day of behavioural test phase for habituation on the test and results are based on the fifth day of this phase. The last test is based on the use of the Rotarod (*FOUR ROTA-ROD, Med associates inc*). This method evaluates the motor coordination by measuring the bearing on an accelerating wheel (from 2 to 20 rpm in 5 minutes, the time spent is taken from the fifth falling). The used protocol consists in one day of habituation and one day of test.

All surgeries were assessed after the experiment and sacrifice of animals. After an anaesthesia with sodic pentabarbital, animals were perfused from the aorta with $250\ mL$ of Phosphate Buffered Saline solution ($0.01M$). Tissues were then fixed with $300\ mL$ of paraformaldehyde (4%). The brain was then placed in sucrose (20%) solution for 2 days before being frozen with isopenthane between $-40/-50°C$ and preserved at $-80°C$ before slicing. Histological section have been performed, slices of $50\mu m$ have been made and coloured with cresyl violet to evaluate effectiveness of surgical lesion and electrode placement.

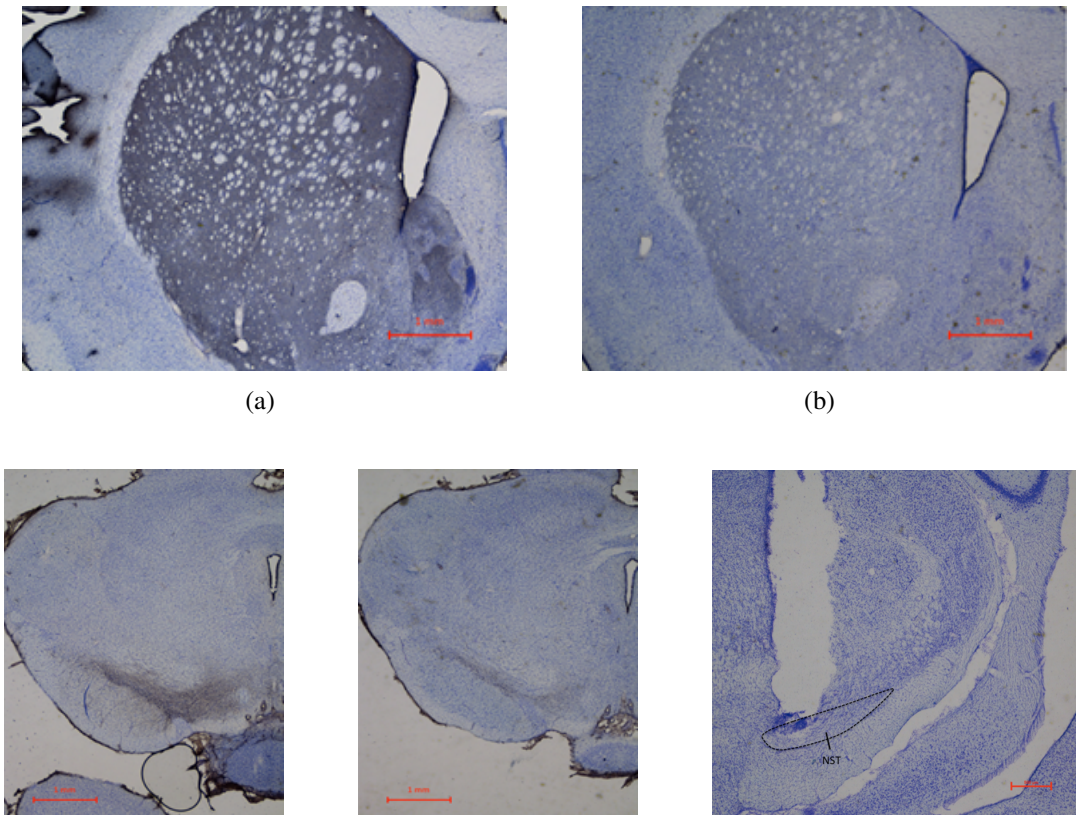

Figure 3.7 – *(a) Slice of the striatum of a sham animal. (b) Slice of the striatum of a 6-OHDA animal. (c) Slice of the SNc of a sham animal. (d) Slice of the SNc of a 6-OHDA animal. (e) Slice of the STN of a sham animal.*

3.5.2 Results

The results can be subdivided in two sections. The first histologic results assess from the surgery and confirm the used protocol. Then the behavioural evaluations allow to consider the effectiveness of the stimulator on a population of rodents regarding PD symptoms.

Histologic results

Photographs of histologic characterizations are presented in Figure 3.7. The effectiveness of the 6-OHDA lesion on the treated group can be assessed in comparison with the sham group. Both Figures 3.7(b) and 3.7(d) compared to Figures 3.7(a) and 3.7(c) show less dark colour. This confirms the deterioration of soma and axons of dopaminergic neurons of the 6-OHDA group.

The slice shown on Figure 3.7(e) allows to confirm two elements. First the hole induced by electrodes implantation ends near the STN confirming that stimulation was performed on target tissues. Moreover no deterioration of cells or tissue damage induced by the delivery of the electric current can be observed.

Behavioural results

The cylinder test results made possible the evaluation of the lesions resulting from the injection of 6-OHDA. An eventual asymmetry of the behaviour would mean an asymmetry in

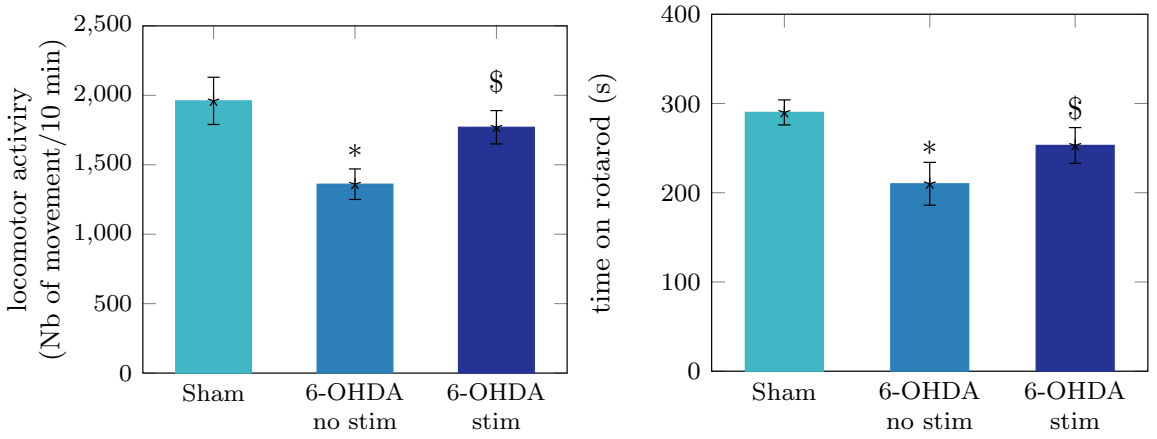

(a) (b)

Figure 3.8 – *Results of behavioural tests over the population of rat for the embedded stimulator: (a) effect of the DBS on actimetry of rats, the y-axis represents the number of movements in 10 minutes ($* = (p < 0.05)$ versus Sham group, $\$ = (p < 0.05)$ versus 6-OHDA without stimulation group), (b) effect of the DBS on motor coordination evaluated with the Rotarod, the y-axis represents the time spent on the Rotarod ($* = (p < 0.05)$ versus Sham group, $\$ = (p < 0.05)$ versus 6-OHDA without stimulation group).*

the lesions between the right and left hemispheres. After comparison of left and right behaviours, one rat of the 6-OHDA was eliminated from the population.

Quantitative results of the Open Field and Rotarod tests are drawn in Figure 3.8. The results of the actimetry on Figure 3.8(a) give two elements. First a significant decrease of movement can be observed on 6-OHDA animals without electrical stimulation ($p = 0.017$ [1]), confirming the presence of parkinsonian symptoms. Moreover the increase of movement between the 6-OHDA without and with stimulation is significant ($p = 0.021$ [1]) meaning that the stimulation with the developed embedded stimulator permits to the 6-OHDA group to recover the basal locomotor activity ($p = 0.165$ [1]).

This effectiveness of the stimulation is then assessed on motor coordination from Figure 3.8(b). The degradation of coordination between the sham group and the 6-OHDA group without stimulation is significant ($p = 0.032$ [1]), and the restoration of this coordination is significantly increased on the 6-OHDA group with the stimulation compared to results without stimulation ($p = 0.041$ [1]). The coordination tend to be at the basal level of coordination observed on sham animals ($p = 0.249$ [1]).

3.6 Partial conclusion

These results confirm the effectiveness of stimulation using the system developed in this project. PD symptoms were characterized by a significant locomotor deficit, induced by pathologic modelling with 6-OHDA. The motor deficit was then significantly attenuated using the current waveform provided by the stimulator. These experiments validated the three implant specifications:

- the stimulator was accepted by the animal for long periods (more than three weeks),

[1] calculated using a non-parametric non-paired Mann Withney t-test

- current stimulation was efficiently delivered to the tissue and significantly attenuated PD symptoms,
- stimulation was electrically safe for the target tissue, as no lesions were induced in tissue surrounding the electrode.

The stimulator was designed to meet physiological constraints, electronically tested, and assessed via *in vivo* experiments. The only report on this entire process in the literature was in Forni et al. (2012), where the hardware developed only addressed hemi-parkinsonism. This type of rigorous process is a key step in validating *in-vivo* instrumentation.

Finally, the system was developed to meet requirements specific to its experimental context and was antagonistic to a global approach. It also highlighted the need for power optimization in implanted hardware. However, the level of optimization required was not quantifiable as no unified criteria were available in the literature.

CHAPTER 4

DESIGNING STIMULATORS FOR ACCURATE CHARGE BALANCING ON FIELD PROGRAMMABLE ANALOG ARRAY

In the context of electrical stimulation, the development of adaptive, closed-loop architectures for future neuro-prostheses is a challenge. These systems are based on circuits capable of detecting biological events and stimulating target tissues. Stimulating the spinal cord is a way of inducing motor activity and is, therefore, a favoured target for functional rehabilitation. At this level, the stimulation circuit is triggered by decision circuits and has to deliver a stimulation pattern that maintains tissue safety and ensures long-term effectiveness. This section reviews the main issues affecting effectiveness, related to considerations on the DC blocking capacitor. It then summarizes existing charge-balancing approaches and, finally, describes a new charge-metering structure, developed for our experimental context.

4.1 Charge balancing issues

4.1.1 DC blocking capacitor and related weakness

The charge balancing strategy is one key point in designing safe stimulation circuits. However, as the DC blocking capacitor is mandatory for electronic implant as mentioned in chapter 2, residual unbalances are often not taken into account. The capacitor stops the DC signal component and forces the global balance. As expressed in chapter 2, the blocking capacitor is the only solution to ensure charge balancing even in case of failure of a stimulation channel. Moreover, it has been recently shown in Nonclercq et al. (2012) that, in case of circuit failure in some multi-channels configurations, a DC current flow cannot be avoided in specific situations even when using blocking capacitors. This shows that the DC blocking capacitor only is not sufficient to ensure safety.

Moreover, even with a one-channel, the impact of this component on the stimulation effectiveness is usually not discussed. As explained in chapter 1, the cathodic pulse responsible for triggering target cells is usually set by increasing the current on a fixed duration. Once the required threshold current is reached, a charge Q_c is injected during the cathodic phase. This charge is supposed to be balanced with the anodic charge Q_a. In the case of a charge unbalance:

$$Q_c \neq -Q_a \tag{4.1}$$

This inequality can be expressed as an equivalent DC current considering the following equation:

$$I_{DC\,error} = \frac{(Q_c + Q_a)}{T_{stim}} = f_{stim}\,(Q_c + Q_a) \tag{4.2}$$

where T_{stim} and f_{stim} are the stimulation period and corresponding frequency. Two cases can be considered:

- $|Q_c| < Q_a \Rightarrow I_{DC\,error} > 0$ which means an over compensation,
- $|Q_c| > Q_a \Rightarrow I_{DC\,error} < 0$ which means an under compensation.

This last case can lead to a loss of stimulation effectiveness. The over compensation does not affect stimulation effectiveness and will not be further discussed

The current stimulation with under compensation and the associated DC blocking capacitor voltage are presented on Figure 4.1. As the capacitor integrates the charge over time, the equivalent negative DC current $I_{DC\,error}$ induces a progressive decrease of the capacitor voltage V_C corresponding to:

$$\Delta V_C = \frac{I_{DC\,error}}{C_{DC}} \Delta T \tag{4.3}$$

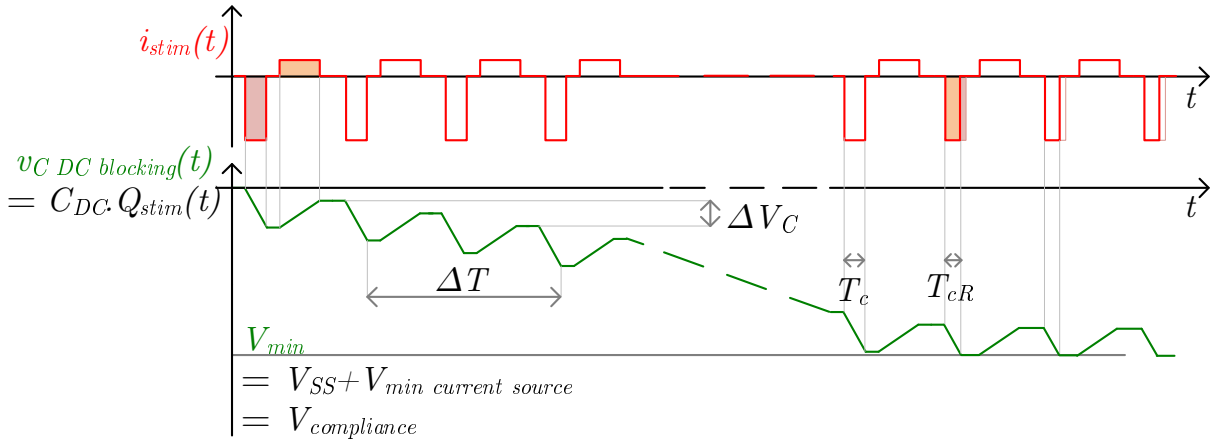

Figure 4.1 – *Stimulation current and blocking capacitor voltage ($v_{C\ DC\ blocking}(t)$) in case of an under balanced stimulus. The cathodic charge (surface in red) is before the steady state larger than the anodic charge (surface in orange); in steady state, the influence of the DC blocking capacitor forces the cathodic charge to be reduced and equal to the opposite of the anodic charge.*

with C_{DC} the capacitance of the DC blocking capacitor and ΔT the time window. This voltage reaches the minimal voltage set by the compliance of the circuit in a certain time. Before this time, the equivalent DC current is applied to the tissue. After this time, as illustrated on right side of Figure 4.1, the waveform is balanced by the blocking capacitor, so that only the minimal charge Q_{cR} is injected; it can be quantified by:

$$Q_{cR} = -Q_a < Q_c \tag{4.4}$$

As the cathodic current remains the same, the cathodic duration decreases of the time ΔT_c that can be quantified as:

$$\Delta T_c = T_c - T_{cR} = \frac{Q_c - Q_{cR}}{|I_c|} = \frac{Q_c + Q_a}{|I_c|} = \frac{-I_{DC\,error}}{f_{stim}|I_c|} \tag{4.5}$$

ΔT_c is directly proportional to the charge unbalance. This time variation can have a high impact as explained in chapter 1 (strength-duration curve for stimulation can be approximated with hyperbolic function). This implies that a small change of cathodic time duration would require a huge current increase.

Consequently, if the use of the blocking capacitor prevents from tissue damages with one stimulation channel, the value of charge balancing is still critical for the effective electrical stimulation of cells.

4.1.2 Techniques for accurate charge balancing

In addition to the topologies described in chapter 2, some circuits emphasing the need for accurate charge balancing have been recently developed. Three main strategies emerge as explained in the following section, illustrated with chosen examples from the literature.

Source matching

The dual source stimulation topology presented in chapter 2 is the most sensitive architecture to mismatch. As the two sources are formed in CMOS technology by P and N devices, matching

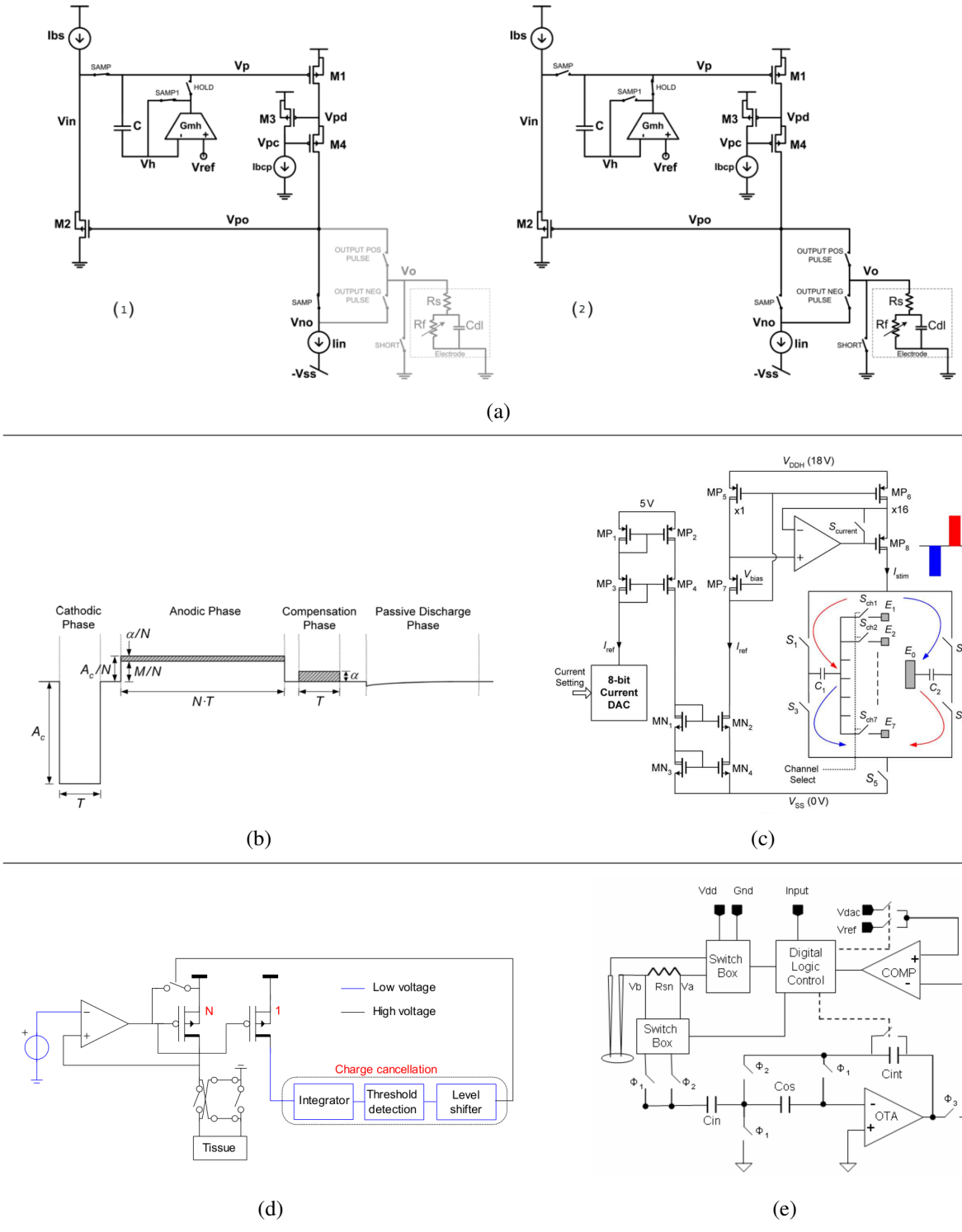

Figure 4.2 – *Review of most competitive topologies for accurate charge balancing: (a) from Sit and Sarpeshkar (2007) illustrating the source matching technique, here with a dynamic matching based on a memory cell; (b) and (c) from Dai Jiang et al. (2011) performing modifications of the waveform with additional balancing sequences; (d) from van Dongen and Serdijn (2010) illustrating the charge estimation and (e) from Fang et al. (2007) as an example of charge metering technique.*

of the anodic and cathodic sources must be accurately tuned. Even with careful mismatch reduction techniques, as in Chun et al. (2010), additional techniques have to be employed to ensure the balance of anodic and cathodic charges. A first solution consists in calibration of the DACs generating the wave-shape as performed by Greenwald et al. (2013). In this case, the weighted current sources used for the DAC are electrically calibrated after the fabrication - at the startup - to lessen the conversion errors.

Dynamic matching of the two sources can also be performed as in Sit and Sarpeshkar (2007). The used topology is shown in Figure 4.2(a). In this case the only the cathodic source is a standard source, while the anodic source is implemented using a current memory cell. Before each stimulation period, a sampling phase is added as illustrated by the schematic on the left. The cathodic source I_{in} is shorted to the anodic mirror made by $M1$, $M3$ and $M4$ and the gate control voltage over $M1$ is memorized through the capacitor C. Then, as shown in the schematic on the right of Figure 4.2(a), $M1$ acts as a source with exactly I_{in}, and both cathodic and anodic pulses are applied on the electrode through the negative and positive pulses switches.

These techniques give interesting results in terms of charge balance ($I_{DC\,error} \approx 6nA$ in Sit and Sarpeshkar (2007)); however, the anodic current is with such techniques always the opposite of the cathodic value, adding a risk of cells hyperpolarization as the waveform cannot be optimized.

Additional compensation phases

An other solution is to take into account the charge unbalance due to the parasitic phenomena such as the discretization of the stimulus parameters resulting in a quantum of charge. Additional phases can be added to the stimulation shape, generally after the anodic phase.

An example of such a technique can be found in Dai Jiang et al. (2011), showing both an additional active anodic phase and a passive compensation. The second anodic phase - as illustrated by Figure 4.2(b) - is in charge of compensating the first anodic period due to parameters rounding; this error is estimated by calculus. As this phase is still an active compensation, a small charge error can still be injected due to imperfections of the DAC. This error is then balanced using a passive discharge of the electrode. The circuit of Dai Jiang et al. (2011) (see Figure 4.2(c)) is based on a standard H-bridge structure with one additional switch.

This technique generally implies the use of one or more additional switches, and additional circuits evaluating the duration of active compensation; moreover the duration of the passive discharge is a function of the accuracy of the previous phases and the peak current of the passive phase is not clearly controlled. However, this technique gives the best results in terms of charge balancing ($I_{DC\,error} \approx 1nA$ in Dai Jiang et al. (2011)).

Charge estimation and metering

A third group of charge balancing circuit is based on adaptive injected charge evaluation. As the main objective of stimulation safety is to cancel the injected charge, this technique seems the most direct way to generate perfectly balanced wave-shape. Two different techniques can be observed.

The first technique is based on charge estimation. It uses an additional circuit that integrates the generated current, thus computes a charge value to be balanced in the waveform. A illustration of this technique is shown in Figure 4.2(d) from van Dongen and Serdijn (2010). The stimulation front-end is based on a H-bridge structure, and the source is minored using a second output transistor connected to an integrator, which output is an image of the injected charge. The main

drawback of such a topology is that if saturation or other parasitic phenomena take place on the load, they are not taken into account: the second copy of the current, feeding the integrator, has its own biasing that is independent from the stimulation load. This can potentially lead to charge imbalance.

In order to prevent from such errors, a direct charge metering can be performed as illustrated in Figure 4.2(e) from Fang et al. (2007). In this example, a current measurement is performed next to the electrode by a resistive component. This resistor voltage is sensed and integrated, using a switched-capacitor circuit to give a charge measurement. This value is used to control the stimulation front-end switches. This technique is supposed to give good results as the target quantity is directly measured and controlled. However, only relative results on the charge unbalance are presented in Fang et al. (2007) (0.2% of the injected charge), which does not permit comparison with other techniques.

4.2 Experimental Context

4.2.1 Floating Gate based FPAA

If digital prototyping is commonly performed on *Field Programmable Gate Arrays*, analog design less often uses *Field Programmable Analog Arrays*. These components have been developed in the 80's as summed up by Gulak (1995). First prototypes were based on transconductors, bipolar interconnecting circuits or switched-capacitors. A new approach on FPAA has been developed by the CADSP laboratory from the *Georgia Institute of Technology*, bases on *Floating Gate* (FG) devices.

An illustration of a *Floating Gate MOS* transistor (FGMOS) is provided in Figure 4.3. As explained by Hasler (2005), FG devices can be implemented using standard CMOS process. As observed in Figure 4.3(a), the FGMOS is essentially a standard MOS or PFET transistor whose gate is isolated using two capacitors. As a result the biasing of the transistor is determined by its gate remaining charge. A first poly-to-poly-silicon capacitor can be considered as illustrated by Figure 4.3(b), isolating the gate input from the floating gate. A second capacitor is a n-well to poly-silicon junction, driven by a potential V_{tune}. This capacitor is used for the tuning of the charge trapped on the floating gate; the tuning is more accurate than in FGMOS devices used in a digital context (memory cells for example).

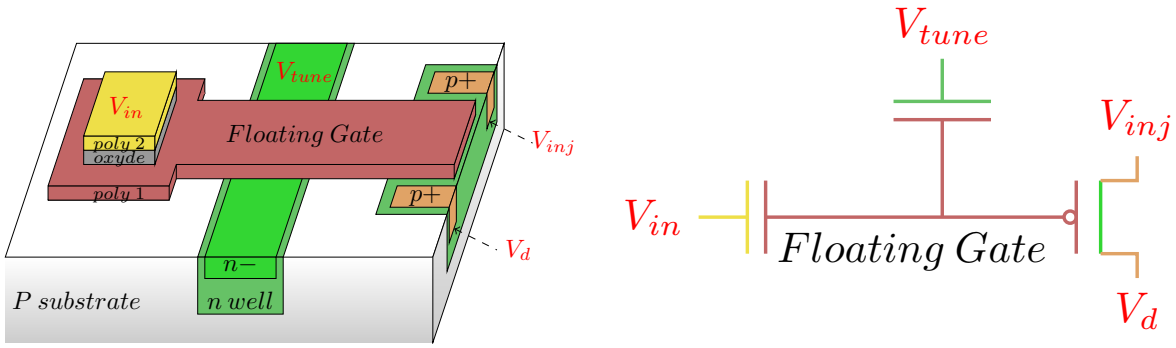

(a) (b)

Figure 4.3 – *(a) FGMOS transistor using a standard MOS process, (b) FGMOS equivalent schematic. (Figures adapted from Hasler (2005))*

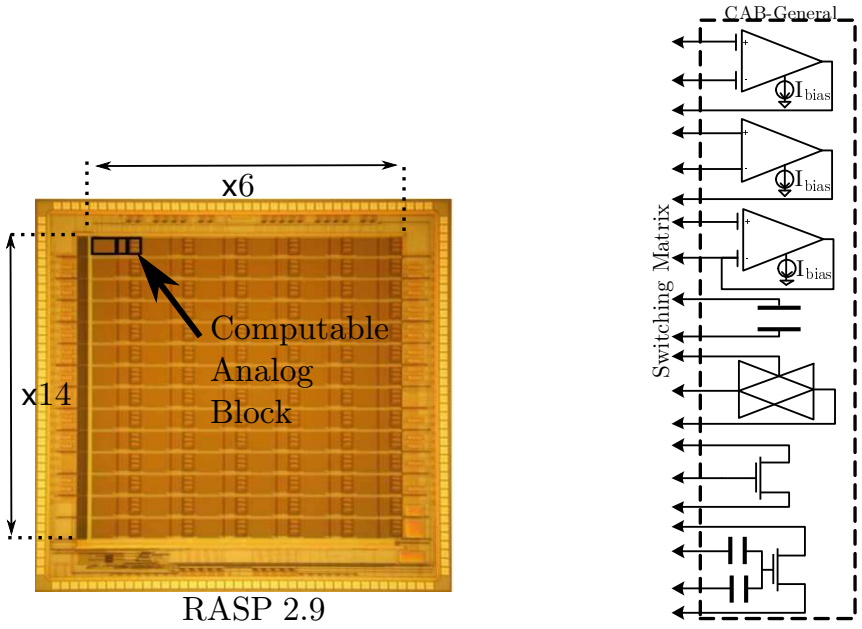

Figure 4.4 – *(a) Die photograph of the RASP FPAA, an array of* 6×14 *CABs can be observed (b) equivalent schematic of a CAB, with access to various components that can be interconnected within or outside of the CAB.*

As mentioned by Hasler (2005), the FG charge can be accurately tuned using Fowler-Nordheim tunnelling to reduce its value (Lenzlinger and Snow, 1969) and hot electron injection to increase its value (Duffy and Hasler, 2003). Consequently, the drain current versus gate voltage curve can be shifted to control the FG charge, and the resulting MOS transistor has a virtual W/L ratio that can be modified after fabrication. From the designer point of view, FGMOS-based circuits are blocks whose behaviour can be modified after the chip fabrication, thus adapted to a particular function. They were used to design adaptive circuits, as illustrated by Srinivasan et al. (2005), or large arrays of inter-connected basic components, as performed by Basu et al. (2008).

Next, a topology for accurate charge balancing is designed, based the use of the *RASP 2.9*. This component is a large scale FPAA that was recently designed as detailed by Brink et al. (2014). A die photography of this FPAA can be viewed on Figure 4.4(a).

The system is divided into subparts called *Computable Analog Blocks* (CAB). All CABs can be connected from one to another using long inter-connections and switch matrices of FGMOS. A CAB is a group of individual available components, as illustrated in the schematic view of a CAB of the RASP 2.9 in Figure 4.4(b). It is composed of:

- 3 slots of 3 FGMOS P transistors with common gates,
- standard nFET ($\times 2$) and pFET ($\times 2$) transistors,
- a transfer gate with access to the command signal,
- a fixed capacitor of $500 fF$

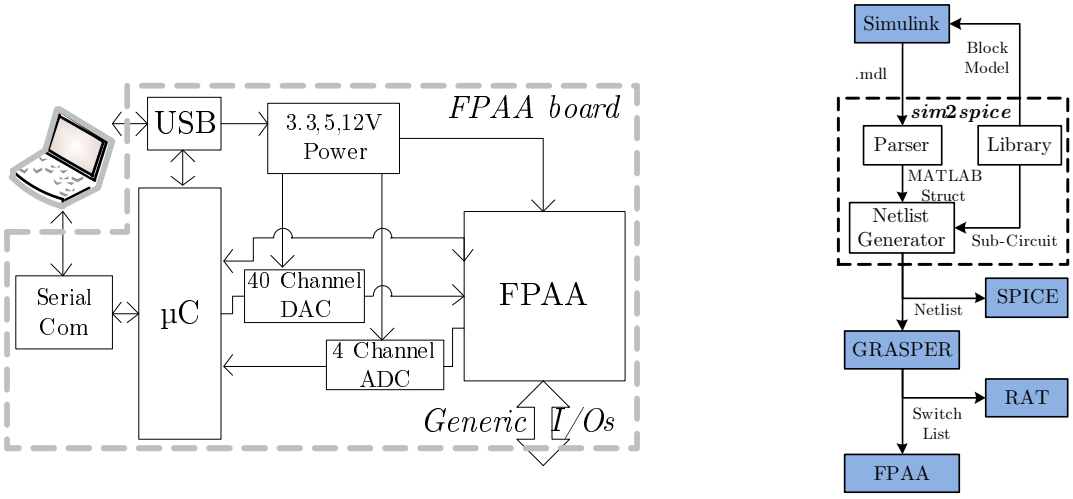

(a) (b)

Figure 4.5 – *(a) Architecture of the development board used for the experiments. (b) Flow chart of the RASP programming, from the designer-defined Simulink schematic to a 'Switch-List' controlling the FPAA.*

- various OTA structures: a FGOTA with a unitary feedback, an FGOTA (OTA with capacitive inputs), and one standard OTA. All these OTAs can be biased over a wide range of current as their biasing source is realized with a FG current mirror.

The RASP 2.9 is composed of 84 (4×16) CABs that can be interconnected with input/output pads to implement analog functions.

A development board has been fabricated, in Figure 4.5(a). This board is USB connected to a PC hosting the design software tool. The interface is made with a micro-controller, in charge of programming the RASP (FGMOS tuning to program interconnections and bias tuning). The micro-controller is also the interface between the analog component and the user interface, as it drives Digital-to-Analog and Analog-to Digital converters controlled by the software user interface. These converters permit to test the developed structures and to bias some components of the RASP. The development board also includes various supplies ($3.3V$, $5V$ and $12V$).

The user can design an analog architecture using a Matlab/Simulink interface: a schematic can be built using elementary components of the CABs or using already developed libraries. The global design flow, as detailed in Schlottmann et al. (2012), is presented on Figure 4.5(b). The schematic is then compiled into a standard netlist that is itself transformed into a *Switch List* that contains the coordinates and biasing currents, finally programmed in the RASP.

Considering all these elements, the RASP circuit, its development board and software interface give the opportunity for analog designers to test and use topologies without fabricating dedicated ASICs. The global design flow is the same as discrete electronics prototyping however parasitics (such as inter-connexions capacitances) have to be taken into account. Existing schematics can then be integrated to a library - as functional sub-circuits - and give the opportunity of rapid development of experimental systems, particularly in the context of hybrid biological/artificial interfaces; some elements have already been addressed (for neural pre-amplification

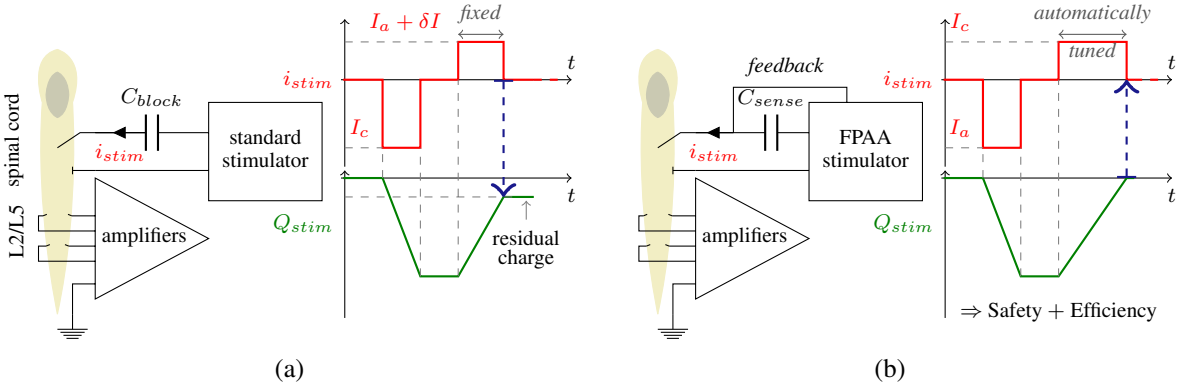

Figure 4.6 – *Experimental setup used for research on functional rehabilitation, on an ex-vivo spinal cord. The stimulator delivers a current to the upper part (above L1 ventral roots) and signal is recorded in the lower part (L2/L5 ventral roots). (a) Standard stimulation is generated with a predefined waveform; defects of the stimulator imply charge imbalance that can lead to tissue damage.(b) The proposed stimulator is based on charge metering feedback; anodic timing is controlled to ensure charge balancing*

see Zbrzeski et al. (2010), for neuromorphic circuits see Shapero and Hasler (2012)).

4.2.2 Biological context

The designed FPAA-based stimulator with automatic charge balancing was designed in the context of experiments on the spinal cord for locomotor rehabilitation (HYRENE project as described in chapter 1). The final goal of this project is to construct a hybrid bridge on a spinal cord lesion so that brain-stem incoming locomotion orders are reconstructed under the lesion that produces locomotor patterns on efferent lumbar ventral roots axons. The experimental setup is based on an artificial spiking neural network modelling a spinal CPG dynamics. This artificial CPG will be connected from neural recording and detection on the upper part of the lesion and will drive the stimulator triggering tissues under the lesion. All together they form a hybrid closed-loop system.

First step in the system design is to develop an open-loop version and test the global dynamics induced by circuits. The goal of such experiment is to reproduce and observe a normal locomotor activity on ventral roots. This has already been successfully performed with commercial stimulation hardware as explained in Joucla et al. (2013). In the stimulation path, three parts can be distinguished. First, the artificial CPG is mimicking neural signal for motoneurons. This first circuit is connected to our stimulator with electrodes implanted near the upper lumbar section of the spinal cord. The third part is the bioware.

A schematic view of the hybrid experiment is drawn in Figure 4.6(a). With a long term objective of a rehabilitation implant, the stimulation stage has to be isolated with the mandatory DC blocking capacitor. If it prevents from direct DC current flow for one channel an under charge balance would induce a blocking of cathodic pulse, resulting in stimulation inefficiency. A comparison with the stimulation induced on Parkinsonian rats on previous chapter can be drawn. As DBS is permanently delivered and as stimulation induces physiological reaction, the stimulation inefficiency can be easily detected. The situation in the context described in Figure 4.6 is slightly different: the stimulation is directly triggered by the artificial CPG and the efficiency is only assessed by the empirical observation of cell reaction by recording the activity on ventral roots. In these conditions only the perfect charge balancing and the blocking

capacitor can ensure the effectiveness of the stimulator and the tissue safety; in such conditions the absence of cell reaction testifies directly for a sub-threshold stimulation.

4.3 Design of the automatic charge balancing topology

4.3.1 Method

The charge balancing method must estimate the injected cathodic charge to control the anodic pulse, whatever the exact form of the cathodic pulse is. This is particularly crucial in case of saturation, or artefacts due to the imperfection of current sources that deliver the stimulus. In this context charge metering is the most suitable technique. Capacitors in series with the electrode are natural candidates as their voltage is directly proportional to the charge. In this case, using a capacitor C_{sense} with a voltage drop $V_{C_{sense}}$:

$$V_{C_{sense}} = \frac{Q_{sense}}{C_{sense}} = \frac{\int_t i_{stim}(t) \cdot dt}{C_{sense}} \tag{4.6}$$

Thus accurate charge balancing can be performed by controlling the $V_{C_{sense}}$ on the stimulation period, so that the final condition is equal to the initial condition. With a null initial condition, a correct anodic compensation has to reach a null voltage over the sensing capacitor. Moreover, as a blocking capacitor is mandatory in implanted stimulators, the re-use of its voltage seems interesting. However, the first issue is that DC blocking capacitors are chosen to respect:

$$\Delta V_{electrode} \gg \Delta V_{C_{DC}} \tag{4.7}$$

in order to limit the power of the system on the output stage and the DC/DC converters. This implies that the voltage variation of the sensor will be small compared to the voltage across the electrode, resulting in the need for sensed voltage amplification. In order not to induce current loss, the input impedance of the amplification stage has to be as high as possible. With these considerations, a sensing loop can be constructed as shown in Figure 4.7(a). For this design a symmetric power and thus a dual source stimulation channel were used. This choice is arbitrary and the developed topology could be adapted to the H-bridge topology.

The stimulation output is connected to the sensing capacitor C_{sense}. However, this last capacitor cannot be the only blocking device, as one amplification input would be directly connected to the electrode. Long term safety could be affected by phenomena such as time-dependant gate oxide breakdown, leading to default DC currents over the electrode. For this purpose, a second blocking capacitor is used as shown in Figure 4.7(a).

The voltage $V_{C_{sense}}$ over the sensing capacitor is amplified as $G \cdot V_{C_{sense}}$ and controls a feedback circuit in charge of driving the switch of the anodic source. The complete sequence of stimulation is illustrated by the chronogram in Figure 4.7(b). The stimulation can be divided in three phases:

- The cathodic pulse is initiated by V_c that is the output of two cascaded monostable circuits. The first monostable circuit has generated a high logic level on V_{int} during a time corresponding to the addition of the cathodic time T_c and interpulse delay T_{inter}. V_{int} triggers a monostable generating a high logic level on V_c during T_c. V_c is directly driving the cathodic switch and induces a cathodic stimulation over the electrode. V_{int} is connected on a NOR gate driving the anodic switch so that no anodic current is applied on the electrode during the cathodic stimulation. As the current on the electrode is negative,

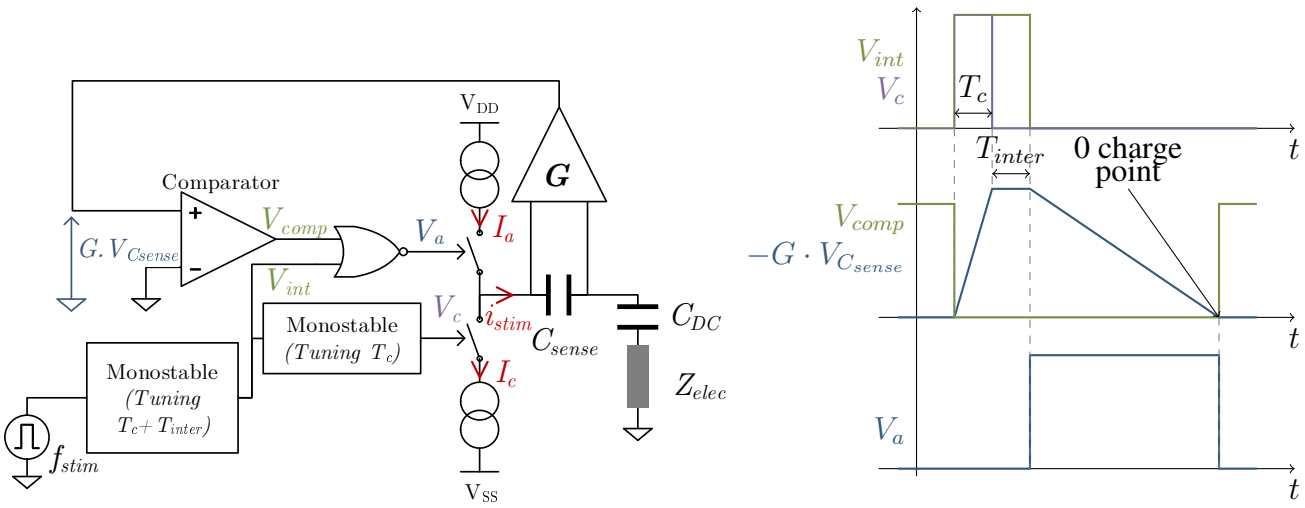

(a) (b)

Figure 4.7 – *(a) Closed-loop topology for automatic balancing with capacitive charge sensing. User defined timings are generated by monostable circuits, anodic switch is tuned by the feedback. (b) Voltages during a stimulation sequence. V_c controls the cathodic pulse; V_{int} inhibits the trigger of anodic pulse during the cathodic and inter-pulse time; V_a shapes the anodic pulse and is constructed from V_{comp}, the feedback voltage that attests of the charge state.*

the feedback signal, proportional to the stimulation charge, is decreasing ($-G \cdot V_{sense}$ is increasing on the chronogram).

- At the end of T_c the second monostable circuit generates a low voltage level on V_c so that cathodic stimulation stops. V_{int} remains high so that any anodic stimulation is inhibited during interpulse timing. The feedback voltage remains stable. The result of the comparison of $G \cdot V_{sense}$ is a low logic signal since a negative charge has been applied.

- When V_{int} has a falling edge, the inhibition of the anodic switch stops and the result of the comparison induces a anodic stimulation. The feedback signal increases as the stimulation charge is reducing. The anodic stimulation stops when the charge is equal to 0 and the stimulation waveform balanced.

Due to the presence in the decision loop of a comparison block which is sensitive only to the charge sign, the global loop is immune to the cathodic current shape and to the amplification stage saturation.

The used FPAA in which we implemented our topology is fabricated in a low voltage process, we had to use external devices for the current sources and the feedback amplification. The current sources (*PSSI2021SAY*) and the first stage amplification were made with an external instrumentation amplifier (*INA2128*). Other circuits were realized with internal components of the FPAA CABs. An internal oscillator was realized to trigger the stimulation. This circuit was implemented using a ring oscillator with 3 inverting followers made of FGOTAs. Its frequency can be tuned by changing the biasing of these OTAs. The range of frequency and corresponding biasing currents are summed up in Figure 4.8(b).

The most critical blocks are the two monostable circuits. They are based on a RC cell driven by two OR logic gates as shown in Figure 4.8(a). All logic gates are made from individual MOS

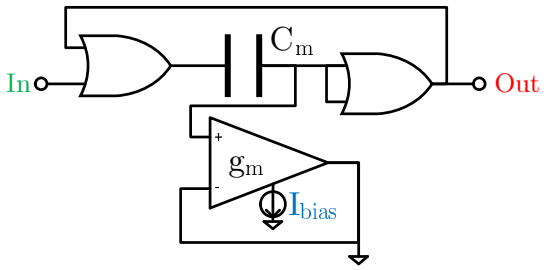

(a)

	f_{stim} (Hz)	T_c (μs)	$T_c + T_{inter}$ (μs)
min	50	50	100
$(I_{bias}\ (nA))$	(0.5)	(88)	(33)
max	350	1000	2000
$(I_{bias}\ (nA))$	(8.2)	(3.9)	(1.5)

(b)

Figure 4.8 – *(a) Topology of the monostable circuits on the FPAA, (b) Table of tunable parameters and corresponding biasing current on the FPAA; all biasing currents can be tuned via the Simulink files or directly in the switch list without reprogramming the entire FPAA.*

transistors available in CABs. These circuits have a tunable unstable-state duration:

$$T_{high} = \frac{C_m}{g_m} ln\,(2) \tag{4.8}$$

where C_m is the capacitance of the monostable and g_m the transconductance of the OTA as illustrated in Figure 4.8(a). This transconductance can be tuned on the FPAA with:

$$g_m = I_{bias}/2V_T \tag{4.9}$$

In order to reach large durations (from $50\mu s$ up to $2ms$), large capacitors and low transconductances have to be used. The capacitor is constructed from parallelizing individual capacitors of common CABs; a fixed number of 40 individual components have been used so that $C_m \approx 20pF$. The range of unstable-state durations and corresponding biasing currents to tune g_m are summed up in Figure 4.8(b). The currents are externally tuned and can be set from $20\mu A$ to $1mA$, without repercussion on circuits implemented in the FPAA as the charge balancing is independent of the exact current shape.

4.3.2 Results

The circuit was tested on different resistive loads, for electrical characterization, and with implanted electrodes to confirm the efficiency of the stimulation.

Electrical characterization

Characterization results are shown in Fig. 4.9. To check the ability of the topology to accurately balance the charge, variations of the stimulation waveform were imposed.

On Figure 4.9(a), a fixed anodic current is set. Then the cathodic current is increased. These kinds of variations are processed by physiologists for stimulation threshold evaluation. When increasing the cathodic current, the stimulation charge is proportionally tuned. As a result the anodic timing is directly increased by the circuit. Waveform integrals are null and especially, short current peaks, caused by non-ideal switching, are automatically balanced.

Measurements were then recorded with a fixed cathodic charge and varying the anodic current, as shown in Figure 4.9(b). Physiologically, the cathodic phase is responsible for target cells depolarization. However, anodic current hyper-polarizes the same cells. Reduction of anodic current is therefore often used by physiologists to optimize stimulation efficiency. Results

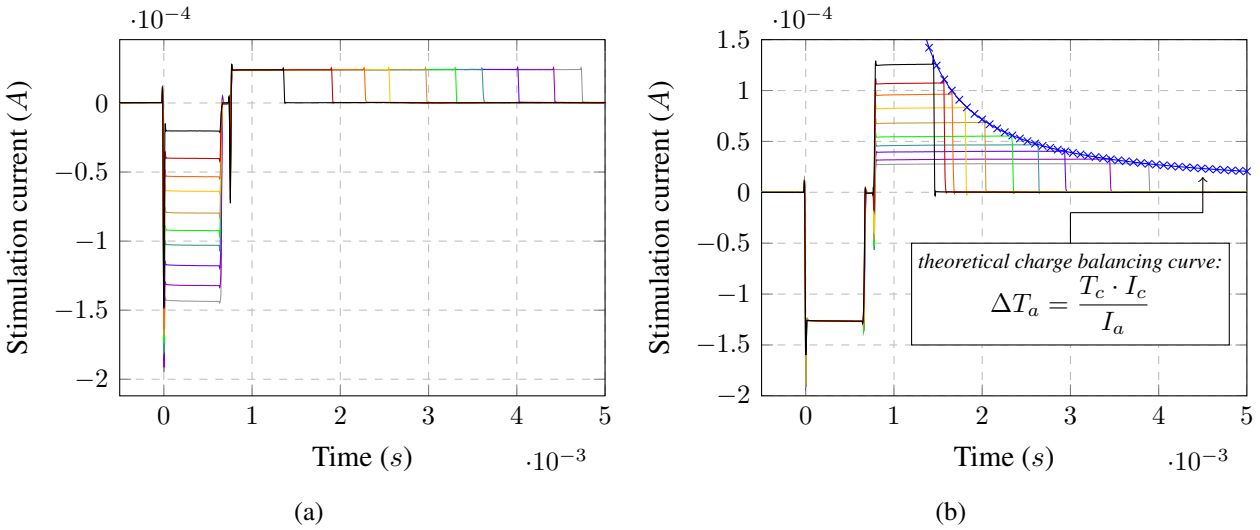

Figure 4.9 – *(a) Characterization with a constant anodic current and variable cathodic current; as the cathodic charge is growing, the anodic time increases to respect the total null charge over the stimulation period. (b) Characterization with a constant cathodic current and variable anodic current; in this situation the compensation time is supposed to follow an hyperbolic curve (plotted in blue), the small variations over this theoretical curve correspond to the balancing of parasitic charges.*

show automatic tuning of anodic timing with respect to a theoretical hyperbolic curve. Small variations over this last curve are due to automatic balancing of parasitic charges.

In order to check the balancing accuracy, additional measurements were performed using a *picoammeter/voltage source Keithley 6487* in series with the load. The voltage source was set to $0V$ and the current was measured with the maximal averaging time constant, in the range of seconds, to measure the DC current resulting from unbalanced charge. With the maximal cathodic current ($I_c = 200\mu A$), a cathodic time of $500\mu s$, a frequency of $20Hz$, a maximal DC current of $0.9nA$ was obtained for a low value of anodic current (about $20\mu A$). This measurement shows slow variations around $0A$ and larger integration time constant could lead to lower results. This behaviour can be understood by considering that if a parasitic phenomenon is resulting in charge unbalance, the accumulated exceeding charge will be detected and balanced in the next stimulation periods.

Experimental validation on ex vivo spinal cord

Stimulation was then performed on a Wistar neonatal rat's *ex-vivo* spinal cord as described in section 1.4.4. As described in Fig. 4.6, stimulation electrodes (32 probe array, *Neuronexus*) were placed in intra-spinal cells pool. Bilateral lumbar ventral roots were recorded using glass suction electrode to evaluate tissue response. The global experimental setup is based on coupling of artificial and biological neural network in open loop. The setup is shown in Figure 4.10(a). An artificial spiking neural network detailed in Ambroise et al. (2013) is used to reproduce a locomotor-like activity. This digital block, implemented on a FPGA, outputs two triggering signals, corresponding to the start of right and left motor activity. These two triggers are then translated into stimulation orders.

This setup was been used with a commercial stimulator (*Multichannel Systems STG4002* $1.6mA$) as described in Joucla et al. (2013). Stimulation protocol for each trigger is as follows:

- a succession of 10 stimulation periods with a frequency of $f_{stim} = 100Hz$,

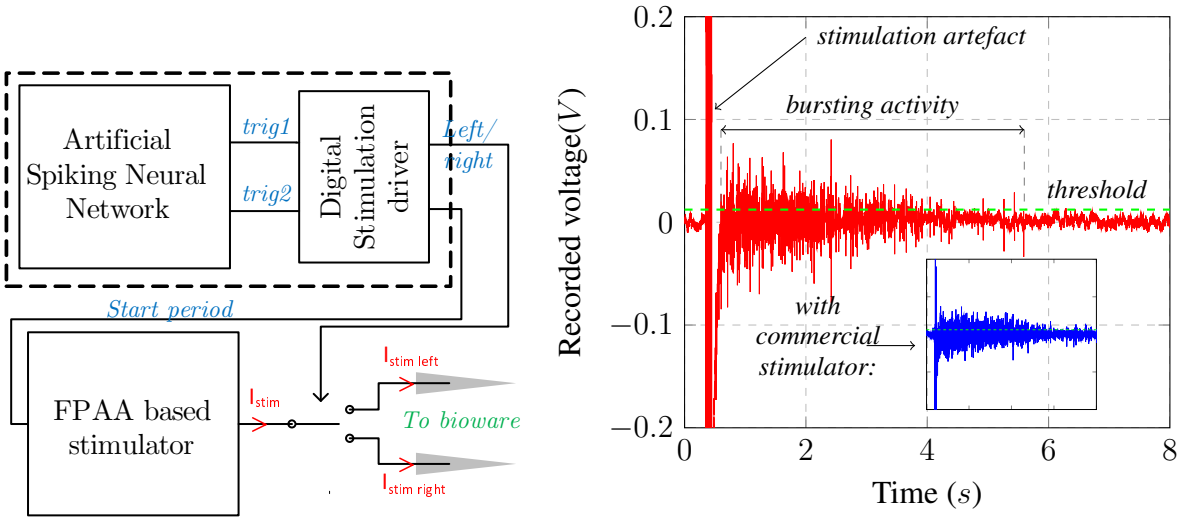

Figure 4.10 – *(a) Architecture of the open loop stimulation path, based on FPGA blocks (artificial neural network and digital stimulation driver), and the FPAA based stimulator whose output is steered on right or left stimulation electrode. (b) Recording of lumbar ventral root neural signal after a 10-periods stimulation burst. The plotted fixed threshold corresponds to 3 times the standard deviation of observed signal for spike detection. As a comparison, the blue curve shows the observed tissue-response for stimulation with a commercial stimulator with the same waveform parameters.*

- within a stimulation period, a cathodic current of $100\mu A$ during $500\mu s$,
- the stimulation is performed on right or left electrode depending on incoming trigger.

To compare the FPAA-based stimulator with the commercial one as used in Joucla et al. (2013), we performed the experiments with the two setups. We present now results obtained with the FPAA-based stimulator.

As the developed stimulator is a one channel system, the stimulation current has to be steered to the correct electrode depending on the neural network activity. This technique is possible as the two electrodes are not stimulating at the same time. Consequently, a digital block manages the interface between the triggers from the artificial CPG and the stimulator by generating the correct number of stimulation periods, and drives a switch in charge of electrode (right/left) selection as illustrated by Figure 4.10(a).

Recorded neural activity on L5 left - as performed in Joucla et al. (2013) and illustrated in Figure 4.6(b) - are presented in Figure 4.10(b). After the stimulation artifact, a bursting activity can be observed on both tissue responses. Spike detection was performed with constant threshold computation of three times the standard deviation of the noise. For both stimulators similar bursting duration (between $5s$ and $6s$) were observed.

4.4 Partial conclusion

The objective of accurate charge balancing was achieved. The DC-equivalent current obtained was less than previously reported Figures in the literature ($< 0.9nA$ for this design, $\approx 1nA$ in Dai Jiang et al. (2011) and $\approx 6nA$ in Sit and Sarpeshkar (2007)). Consequently, tissue safety is

maximized, stimulation effectiveness is guaranteed and satisfying proof-of-concept stimulation results were obtained *ex vivo*, preparing for further experiments with a hybrid closed-loop design.

In this context, the use of FPAA architecture was particularly interesting for fast development and prototyping of the additional circuits necessary for the charge-metering technique. Moreover, as consumption was related to the biasing of the circuits used (mainly OTAs), the use of transconductance-controlled architecture was an advantage, as the low frequency range - or long duration - implied a decrease in transconductance. Interestingly, a quasi-optimal architecture for charge balancing was built using non-optimal components.

Apart from this particular design, FPAA-based structures offer promising alternatives to highly-specific designs for developing new systems to interact with living organisms. The system presented is specific to one setup, but the programmability of FPAAs makes them compatible with multi-application circuits and a global approach.

PART III

GLOBAL MULTI-APPLICATION APPROACH

"Je suis de ceux qui pensent que la Science a une grande beauté, répond-elle à ses interlocuteurs. *Un savant dans son laboratoire n'est pas seulement un technicien : c'est aussi un enfant placé en face des phénomènes naturels qui l'impressionnent comme un conte de fées. Nous ne devons pas laisser croire que tout progrès scientifique se réduit à des mécanismes, des machines, des engrenages, qui, d'ailleurs, ont aussi leur beauté propre."*

E. CURIE, *Madame Curie*, P. 465, *Edition Gallimard, 1938*

CHAPTER 5

ELECTRODE IMPEDANCE MEASUREMENT AND MODELLING

THE divergence between the numerous applications of stimulation is correlated to the multiplicity of electrodes. A specific target tissue is often associated with a particular electrode, with specific geometry and materials. For example, the two designs described above are based on macro- or micro-electrodes, resulting in different current levels for the same waveform, as well as two different terminal impedances. This impedance is a sizing quantity for the electrical design of the front-end, but has little impact on its architecture. Consequently, focusing on electrical characterization offers a promising basis for a global approach. First, the physics of electrodes is reviewed and commonly-used models are described. Then, as required by the phenomena involved, a measurement bench was designed and a fractional, non-linear model was developed.

5.1 Physical considerations of the stimulation load

The stimulation load is composed of the DC blocking capacitor and the electrode implanted in the biological medium, next to the target excitable cells. This chapter focuses on the global impedance of this last electrode in contact with the biological tissue, as the impedance of the capacitor is known and controlled by the designer. A general overview of the impedance under investigation is drawn in Figure 5.1. The global interface between electrical circuits and the biological medium can be divided in three parts:

- A metal shape in contact with an electrolyte formed by the biological medium, forming a electrochemical half-cell. This corresponds to the stimulating contact and forms a physical interface between electronic(in the metal 1) and ionic conductions (in the electrolyte). Its impedance is noted Z_{elec1} on Figure 5.1.

- The biological medium, composed of extra-cellular medium and cells. This part is governed by the ionic conduction, characterized by the electrical conductivity of the solution and the non-homogeneity due to the presence of cells and cells membranes. Its impedance is noted Z_{bio} on Figure 5.1, and V_{bio} corresponds to the extra-cellular potential described in chapter 1.

- A second electrochemical electrode half-cell, formed by the biological medium and a second metal. This correspond to the current return electrode of the stimulation. Its Impedance is noted Z_{elec2} on Figure 5.1.

This global impedance has already been widely addressed in the literature. However, electrical model are often over-simplified and designs are not always based on considerations over underlying physical phenomena. In this section, a physical approach of the stimulation load is adopted, and main properties of this load are exhibited in order to propose a model for electrical design of stimulation circuits.

First the main properties of the electrochemical half cell is detailed, then some characteristics of the biological medium are explain. In a third subsection, existing electrical models are shown.

5.1.1 Physical phenomena at the electrode-electrolyte interface

The electrode-electrolyte interface is a complex transducing surface forming a natural border between electronic and ionic conductions. This transduction is not only used in electrodes for biological application but is exactly the same as in other field of electro-chemistry as for example accumulator. In the metal, basic electrical transport phenomena take place. In the conductive

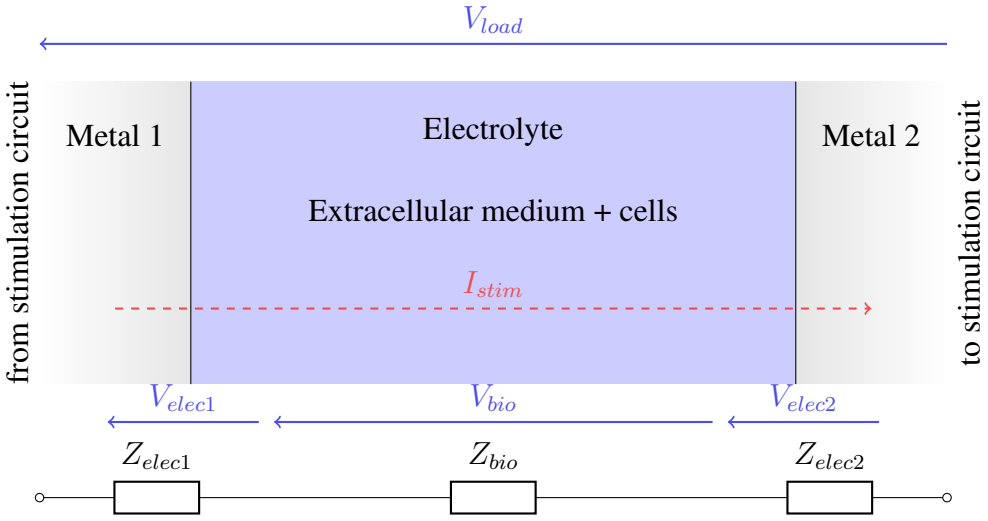

Figure 5.1 – *Schematic description of the stimulation load, excluding the blocking capacitor; the global impedance can be separated in two metal electrolyte junctions and a piece of the biological tissue.*

electrolyte, the Maxwell's equations can be superimposed to chemical equations that governs quantities such as local concentration. These last phenomena are of major importance near the interface and will be explained. Basically, phenomena can be separated in two categories:

- field phenomena, forming a double layer capacitance,
- charge transfer, forming a more complex impedance model.

In this section these two contributions are studied separately.

Double layer capacitance

The boundary between an electrode and an electrolyte is characterized by a double layer of charges as explained in Bard and Faulkner (2001). At the equilibrium, all reverse reactions are equal resulting in a null current over the interface.

The charge repartition can be in first approximation described using two separated planes. As presented in Figure 5.2, electronic charges accumulate in the metal part. In the electrolyte a first layer of water molecules accumulate next to the interface forming the Inner Helmholtz Plane. The first layer of solvated ions that fit the interface forms the Outer Helmholtz Plane. The distance from this plane to first layer of charge (d_{OHP}) is responsible for the Helmholtz capacitance calculated as:

$$C_H = \frac{\varepsilon_0 \varepsilon_r A}{d_{OHP}} \tag{5.1}$$

where ε_0 is the vacuum permittivity, ε_r the relative permittivity of the solution and A the area of the interface. The distance d_{OHP} small, usually less than 10 Å. The maximal Helmholtz surfacic capacitance is estimated to $0.11 pF/\mu m^2$ by Kovacs (1994). Between the electronic charge layer and the OHP, the electric potential is decreasing linearly with the distance, as no charge is present.

In the electrolyte, the electrical potential is determined by the spatial repartition of ions. Far from the electrode, species concentrations are independent from the position with the hypothesis of an homogeneous solution, forming a bulk electrolyte. Near the interface, the

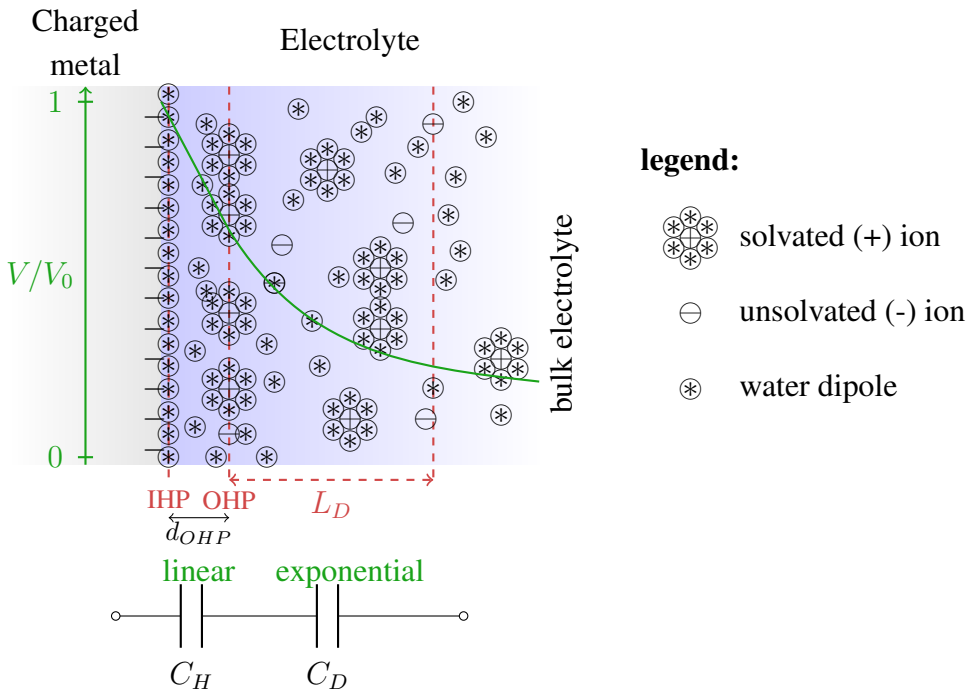

Figure 5.2 – *Charge repartition around the metal-electrolyte interface and normalized potential evolution in the electrolyte; charges in the metal are formed by the accumulation of electrons, however, the charge in the electrolyte is governed by ion localisation. The resulting electrical field can be expressed by giving two separated capacitive phenomena.*

ionic concentrations follow a Boltzmann statistic distribution, as explained in Bard and Faulkner (2001), is described by:

$$c_i\left(x\right) = c_i^0 e^{\frac{-q_i \Phi_x}{RT}} \tag{5.2}$$

where c_i^0 is the steady state concentration, q_i is the signed charge of the considered element, R is the Boltzmann constant and T the temperature. In order to evaluate the electrical potential Φ_x, let consider the Poisson-Boltzmann equation:

$$\frac{\partial^2 \Phi_x}{\partial x^2} = -\frac{4\pi\rho_x}{\varepsilon_0 \varepsilon_r} \tag{5.3}$$

where ρ_x is the charge density that can be expressed by summing the concentrations repartitions. The Charge of the electrode can be obtained by integrating the charge density in equation 5.3 over x:

$$Q = -\frac{\varepsilon_0 \varepsilon_r}{4\pi}\left(\frac{\partial \Phi}{\partial x}\right)_{x=0} = \sqrt{\frac{2RT\varepsilon_0\varepsilon_r}{\pi}} c_i \sinh\left(\frac{q_i \Phi_0}{2RT}\right) \tag{5.4}$$

where Φ_0 is the potential over the junction. This equation of the charge depending on the potential exhibits a capacitive phenomenon, quantified by:

$$C_D = \frac{\partial Q}{\partial \Phi_0} = \frac{\varepsilon_0 \varepsilon_r}{L_D} \cosh\left(\frac{q_i \Phi_0}{2RT}\right) \tag{5.5}$$

where L_D is a quantity homogeneous to a distance, called the Deby-length:

$$L_D = \sqrt{\frac{\varepsilon_0 \varepsilon_r}{2RTc_i q_i}} \tag{5.6}$$

As the two expressed capacitive phenomena describe successive charge repartitions, as illustrated in Figure 5.2, the effective capacitance of the electrode-electrolyte interface can be expressed as:

$$C_{dl} = \left(\frac{1}{C_H} + \frac{1}{C_D} \right)^{-1} \tag{5.7}$$

Kovacs (1994) evaluated this global capacitance to approximatively $0.05pF/\mu m^2$ for extracellular electrodes. As reported by Sapoval (1995) and Kerner and Pajkossy (1998), the state of surface can modify the capacitive behaviour, so that the observed behaviour tends to respect pseudo capacitive effect of a constant phase element. Such phenomena can be described by fractional derivation that will be detailed in a further section.

Charge transfer phenomena and Warburg impedance

The field phenomena previously expressed does not take into account the redox reactions induced by species at the electro-chemical junction. The electrical current of such process is governed by the Butler-Volmer equation, and represented Faradic current, expressed as:

$$i_{faradaic} = i_{anodic} - i_{cathodic} = i_0 \left(e^{\frac{q_a \eta}{2RT}} + e^{-\frac{q_c \eta}{2RT}} \right) \tag{5.8}$$

where i_0 is the current exchange and η is the over potential, quantifying the variations around the half-cell potential imposed by the junction's material. This equation is illustrated by Figure 5.3(a) ($\eta = \Phi - \Phi_{half-cell}$). Two conclusions can be extracted from this equation. The first is that for small signal ($\eta < 0.01V$ as bounded in Franks et al. (2005)), a charge transfer resistance can be calculated using a first order Taylor expansion:

$$R_t = \left(\frac{\partial \eta}{\partial i} \right)_{\eta=0} = \frac{RT}{qJ_0A} \tag{5.9}$$

where J_0 is the exchange current density and A the surface of the interface. However, the second element is that these small signal variations over the equilibrium are an hypothesis that is not compatible with high voltages imposed during electrical stimulation of excitable cells. Therefore, charge transfer phenomena are responsible for the highly non linear behaviour of the electrode impedance, as indicated by equation 5.8.

Finally, a last equation can add contribution in electrode impedance. All previously described phenomena do not model eventual species diffusion. A faradaic current density can be computed, considering the solution of the Nernst-Plank problem (Planck, 1890) leading to :

$$J_{non-faradaic} = -D_i \frac{\partial c_i}{\partial x} - \frac{q_i F}{RT} D_i c_i \frac{\partial \Phi_x}{\partial x} + c_i v_i(x) \tag{5.10}$$

where the first term represents the diffusion with D_i the diffusion parameter, the second term represent migration with F the Faraday constant, and the last term represents the movement with v_i the velocity of species. If this last equation has, in most of the cases, no analytic solution; the hypothesis of an infinite linear diffusion leads to the expression of an impedance element in series with the transfer resistance R_t, called a Warbug Impedance (Bard and Faulkner, 2001) and defined as:

$$W(\omega) = \frac{R_w y}{\sqrt{\jmath\omega}} \tag{5.11}$$

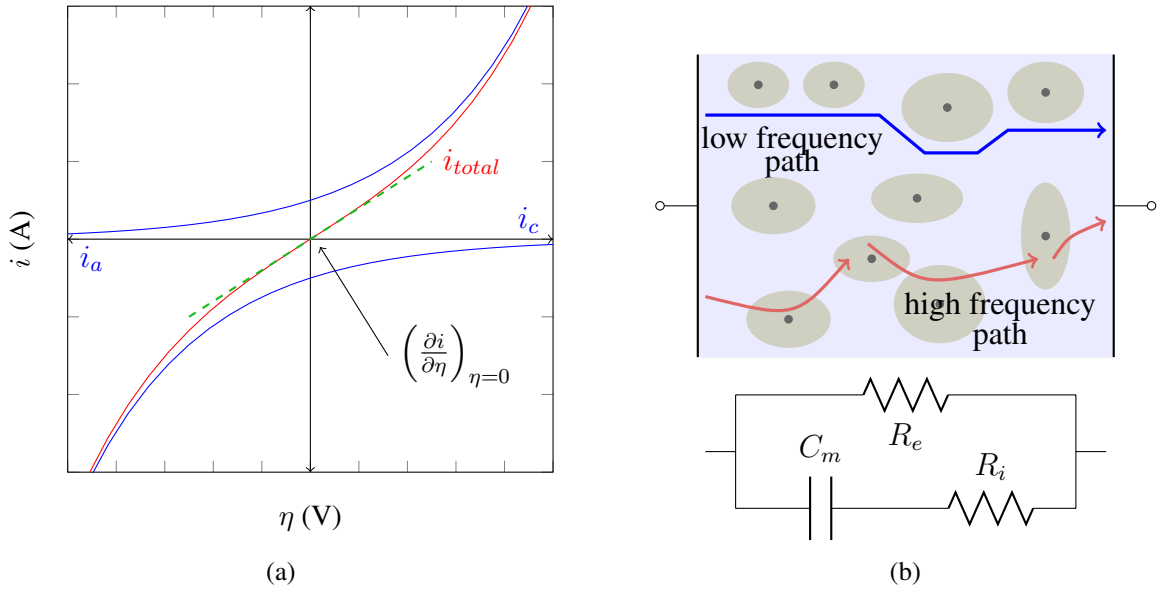

(a) (b)

Figure 5.3 – *(a) Graphical representation of the current given by the Butler-Volmer equation, which is the combination of two exponential anodic and cathodic current. Near the equilibrium a quasi linear resistivity can be expressed. (b) Illustration of the current paths in the biological medium formed by the extra-cellular medium and excitable cells.*

where R_w is a resistive term and y defined by :

$$y = \frac{k_{redf}}{D_{red}} + \frac{k_{ox}}{D_{ox}} \tag{5.12}$$

were ω is the angular frequency, D the diffusion coefficients of the reactants. This impedant element is characterized by a fractional power of the angular frequency and is associated to fractional derivative of the order $^1/_2$.

If considering all contributions, the global current at the interface is:

$$i = i_{faradaic} + i_{non-faradaic} \tag{5.13}$$

5.1.2 Tissue impedance

In the tissue, the electrical conduction is purely ionic. The extra-cellular medium is characterized by its conductivity that depends on ionic concentrations. This conductivity depends on the nature of the stimulated cells as the homoeostatic conditions can vary for different tissues. This impedance has a purely resistive model of a value R_e.

However, as illustrated by the Figure 5.3(b) and explained by McAdams and Jossinet (1995), the tissue represent a non-homogeneous medium where cells are placed. At higher frequency, the capacitive membranes have a decreasing impedance. In this cases, a parallelized path, composed of a capacitance C_m formed by the membranes in series with a resistance R_i modelling the electrical conductivity of the intra-cellular medium, becomes dominant, as expressed by the equivalent schematic presented in Figure 5.3(b). The capacitive term was also reported (McAdams and Jossinet, 1995) to be a source of fractional derivative contribution.

This impedance is subject to variation with time as observed by Lempka et al. (2009b), as the tissue can react after implantation. Particularly, fibrosis or gliosis (see Cogan (2008)) can change

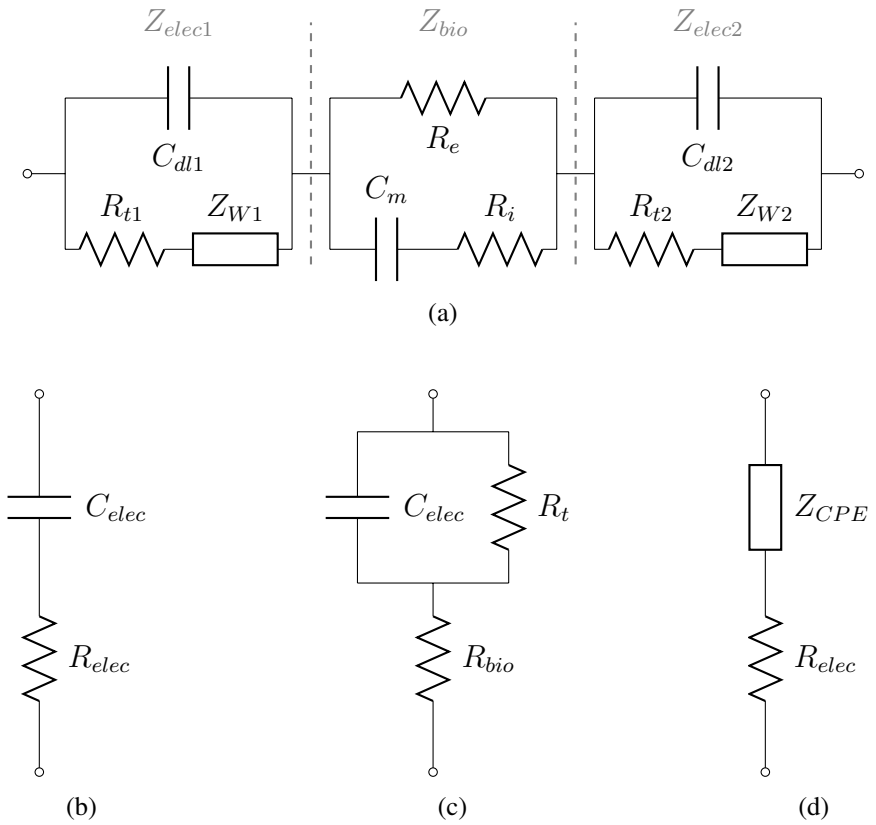

Figure 5.4 – *(a) Complete linear electrical model of the stimulation load. This complex schematic is often simplified in models presented in schematics (b), (c) and (d)*

tissue properties and affect the impedance. Such phenomena also change the medium near the metal and can affect the values of impedances resulting from the previously described equations.

5.1.3 Overall electrical modelling

The global electrical model that can be drawn from expressed physical phenomena is shown in Figure 5.4(a). This schematic includes the capacitive nature of the metal-electrolyte interface, that can also be fractional, the linearised charge transfer impedance and the impedance of the tissue. This schematic is only linear and does not consider any variation of a parameter versus electrical quantities. As the impedances of both boundary regions are similar, simplification can be made and this complex schematic is never used in this form for electrical design. However, three simple models for the frequency range of electrical stimulation ($\approx 1Hz$ to $\approx 85kHz$) can be found in the literature.

These models are shown in Figure 5.4:

- the electrical model presented in Figure 5.4(b) is a first approximation model developed by Fricke (1932) only taking into account the capacitance of electrodes and the tissue equivalent resistance. This oversimplified model is still widely used for electrical design of stimulators as in Kelly and Wyatt (2011) for instance.

- The electrical model presented in Figure 5.4(c) as often simplified from Randles (1947). This model includes a minimalist description of the real part charge transfer phenomena.

This model is also used in the electrical design as by Brown et al. (2008) for example. However, this model has no fractional dynamics; if simulation can in first approximation be satisfying, the modelled dynamics fails to fit observations and physical phenomena.

- The electrical model presented in Figure 5.4(d) includes a constant phase element and a resistive part. This model is used as a support to extract qualitative information about the tissue or interface properties as in McAdams et al. (1995). However, this model is due to its fractional aspect not directly compatible with electrical CAD simulators.

Considering this latter model, the next section introduces used mathematical rules for fractional derivative computation. Moreover, as none of these models includes non-linear elements, a multi-model strategy will be used to model observed non-linearities. These results make possible a complex model extraction and simulation.

5.2 Fractional calculus and computation of fractional systems

If the fractional integration or derivation remain unusual in classical electrical modelling, first definitions of a mathematical derivation and integration extended to the real and complex powers goes back to the 19th century. Such mathematical objects are required for the modelling of Constant Phase Elements and fractional behaviour is associated to fractal surface or even modified diffusion equations. Fractional differential equation are already used in mathematical and physical field as detailed by Podlubny (1998). In this section, the temporal and frequential responses of a fractional derivator is exhibited leading to a recursive approximation allowing for fractional derivative computation in classical simulation algorithms.

5.2.1 Response of a fractional derivator/integrator

As the electrode impedance will be model using fractional operators, let us consider the response of such systems. The mathematical basis of this section are summed up in Appendix B. First the temporal response to a step function will be detailed; this analysis is of major concern since it illustrates the electrode response to current steps as it can be observed with the typical current stimulus waveform. Then, the frequential response is studied; this response is the basis for a recursive approximation enabling fractional system simulation. Let us consider $\boldsymbol{I}$ and $\boldsymbol{D}$, respectively the integral and derivative operators. For a real fractional derivator system ($\gamma \in \mathbb{R}$), the output signal $y(t)$ is equal to the result of the derivative of the input signal $x(t)$ with a gain determined by the time constant τ:

$$y(t) = \tau^{\gamma} \boldsymbol{D}_t^{\gamma} x(t) \tag{5.14}$$

As γ can be positive or negative, the operator $\boldsymbol{D}$ represent since then whether the derivator or the integrator. If the initial conditions of the system are null, the Laplace transform of the previous equation is:

$$Y(s) = (\tau s)^{\gamma} X(s) \tag{5.15}$$

by considering $\omega_u = \frac{1}{\tau}$, the unity gain angular frequency, the system is characterized by:

$$Y(s) = \left(\frac{s}{\omega_u}\right)^{\gamma} X(s) \tag{5.16}$$

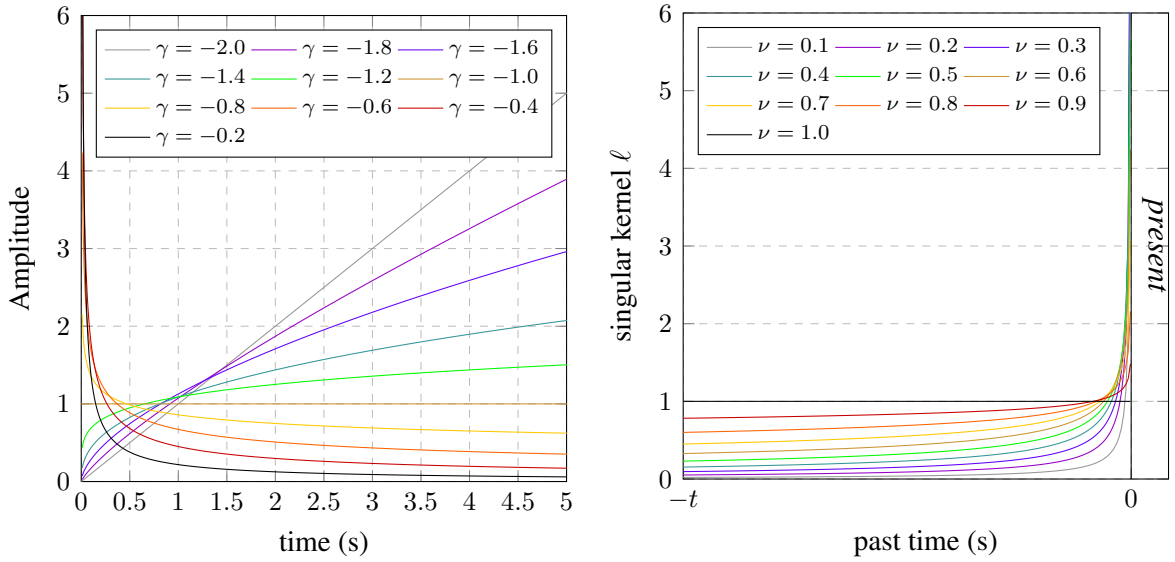

(a) (b)

Figure 5.5 – *(a) Impulse response of a fractional integrator (negative order deritavor) for different γ values, with $\omega_u = 1\ rad.s^{-1}$. (b) Graphical representation of the singular kernel ℓ, for order $\nu < 1$, the decreasing value imply a selective memory effect in which old events tend to be forgotten due to the decreasing weight in the convolution product;*

In the Laplace domain, the transmittance D of the fractional derivator is:

$$D(s) = \left(\frac{s}{\omega_u}\right)^{\gamma} \tag{5.17}$$

Temporal response

This result leads to the temporal impulse response $y_{imp}(t)$ of the system, considering the inverse Laplace transform:

$$y_{imp}(t) = \mathcal{L}^{-1}\{D(s); s\} = \left(\frac{1}{\omega_u}\right)^{\gamma} \frac{t^{-\gamma-1}}{\Gamma(-\gamma)} u(t) \tag{5.18}$$

where $u(t)$ is the Heaviside function. The temporal response of the integrator (derivator with $\gamma \in \mathbb{R}^*_-$) shown in Figure 5.5(a) can be understood by focusing on the non integer part of the derivation:

$$\boldsymbol{D}_t^{\gamma}(f(t)) = \boldsymbol{I}_t^{n+\nu}(f(t)) = \boldsymbol{I}_t^{n}(\boldsymbol{I}_t^{\nu}(f(t))) \tag{5.19}$$

where $n \in \mathbb{N}$ and $\nu \in]0,1[$. Considering the Riemann-Liouville definition of the integration expressed by equation B.4 as written in Appendix B, the purely fractional part of the previous integral can be expressed as convolution product:

$$\boldsymbol{I}_t^{\nu}(f(t)) = \ell(t) * f(t) \tag{5.20}$$

where ℓ is a Riemann-Liouville singular kernel defined by:

$$\ell \triangleq \frac{t^{\nu-1}}{\Gamma(\nu)} \tag{5.21}$$

A graphical representation of this kernel is shown in Figure 5.5(b). This last equation gives a better understanding of the the fractional phenomena. For $\nu = 1$, and thus the typical integration of order one, the kernel value at the origin is 1 and constant for negative values, which means that by convolution in the time domain, events are equally memorised and held. For $\nu < 1$, the kernel is non constant, undefined in 0 with an infinite limit on 0 and a 0 limit on $-\infty$. For $\ell > 1$, the convolution favors the near event in the memory effect. On the contrary, when the time distance increases (τ increasing in the convolution product), events influence decreases with a higher dynamic when ν is near 0. If $\nu = 0$, the integration becomes the identity, meaning that no memory effect can be observed. This reasoning associated to equation 5.19, allows for a better understanding of the impulsional response shown in Figure 5.5(a).

Frequential response

Considering the equation 5.17 and that $s = \jmath\omega$, the transmittance D of the fractional derivator in the frequential domain is:

$$D\left(\jmath\omega\right) = \left(\frac{\jmath\omega}{\omega_u}\right)^{\gamma} \tag{5.22}$$

Consequently, the gain and the phase of the system are defined by:

$$\begin{cases} \left|D\left(\jmath\omega\right)\right|_{dB} = 20\gamma \log\left(\dfrac{\jmath\omega}{\omega_u}\right) \\ \angle D\left(\jmath\omega\right) = \gamma\dfrac{\pi}{2} \end{cases} \tag{5.23}$$

This equation, illustrated in Figure 5.6, lead to remarkable properties:

- the phase of the system is constant and can be any value unlike integer order operators. This property gives the name to the *Constant Phase Element*, often discussed for electrochemical system's modelling.
- the gain curve is characterized by a slope of $20\gamma\ dB$ per decade.

Thus, fractional systems allow to model any gain slope observed on measure, and fit constant phase behaviour.

5.2.2 Recursive approximation of a fractional derivator

If the existence and properties of fractional devirator and integrator can be easily expressed as the generalization of the integer derivative and integral, modern numerical computation is exclusively based on discretisation of the derivative, considering approximation of equation B.9 of Appendix B. If this result is generalized by equation B.14 of Appendix B, actual numeric solvers do not allow for derivative re-definition. Thus an approximation of the fractional derivator computable on commonly used solvers is required. A recursive approach has been developed in Oustaloup et al. (2000).

This approximation can be made considering a bounded fractional derivator in the frequential domain. With $\gamma \in \mathbb{R}$, equation 5.22 bounded over $[\omega_b, \omega_h]$ becomes:

$$\left(\frac{s}{\omega_u}\right)^{\gamma}\Bigg|_{[\omega_b,\omega_h]} = C_0'\left(\frac{1 + {}^{s}/_{\omega_{min}}}{1 + {}^{s}/_{\omega_{max}}}\right)^{\gamma} \tag{5.24}$$

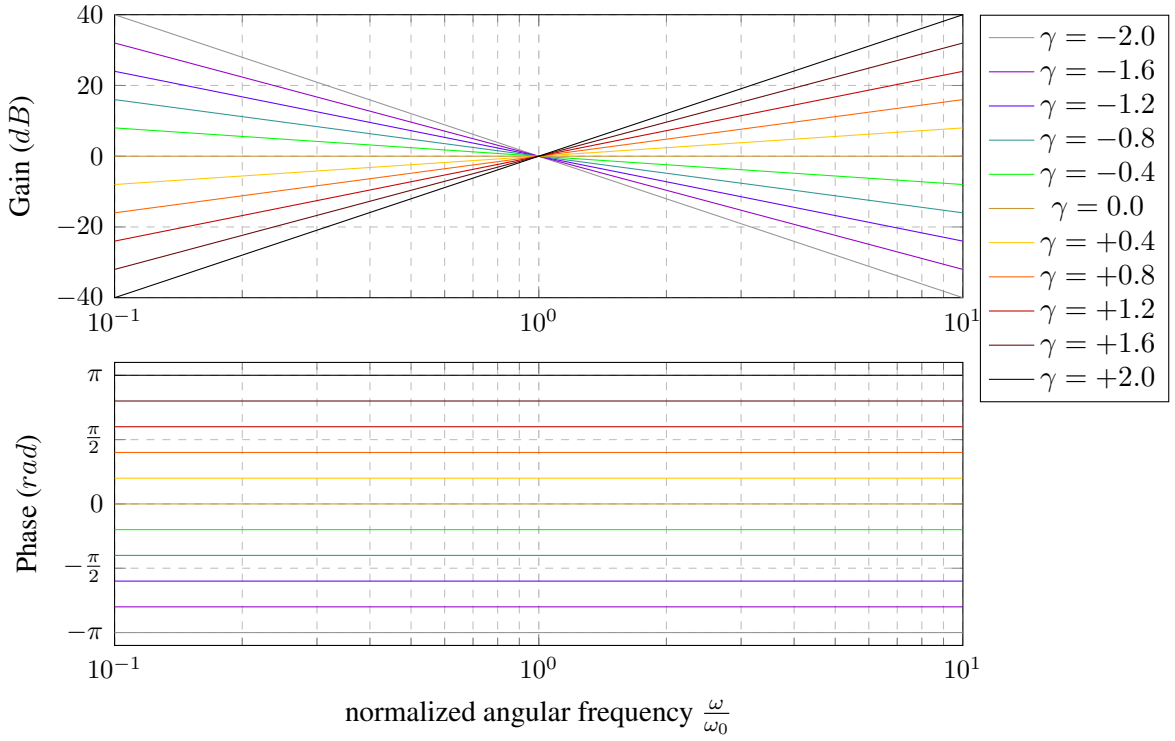

Figure 5.6 – *Frequential representation of fractional derivator for different γ values.*

where $C_0^{'} = (C_0)^{\gamma}$, with $C_0 = \dfrac{\omega_{min}}{\omega_u} = \dfrac{\omega_u}{\omega_{max}}$, and $\sqrt{\omega_{min} \cdot \omega_{min}} = \omega_u$. This approximation can be used under the hypothesis:

$$\begin{cases} \omega_{min} \ll \omega_b \\ \omega_{max} \gg \omega_h \end{cases} \tag{5.25}$$

using a recursive approach, it can be proven that:

$$\left(\frac{s}{\omega_u}\right)^{\gamma}\Bigg|_{[\omega_b,\omega_h]} = C_0^{'} \lim_{N \to +\infty} \left(\prod_{k=-N}^{N} \frac{1 + {}^{s}/_{\omega_{z,k}}}{1 + {}^{s}/_{\omega_{p,k}}} \right) \tag{5.26}$$

where the $\omega_{z,k}$ and $\omega_{p,k}$ are zeros and poles calculated as:

$$\begin{cases} \dfrac{\omega_{z,k+1}}{\omega_{z,k}} = \dfrac{\omega_{p,k+1}}{\omega_{p,k}} = \alpha\eta \\ \dfrac{\omega_{p,k}}{\omega_{z,k}} = \alpha \\ \dfrac{\omega_{z,k+1}}{\omega_{p,k}} = \eta \end{cases} \tag{5.27}$$

with α and η, two constants depending on the fractional order γ and the number of poles and zeros $2N + 1$:

$$\begin{cases} \alpha = \left(\dfrac{\omega_{max}}{\omega_{min}}\right)^{{}^{\gamma}/(2N+1)} \\ \eta = \left(\dfrac{\omega_{max}}{\omega_{min}}\right)^{{}^{(1-\gamma)}/(2N+1)} \end{cases} \tag{5.28}$$

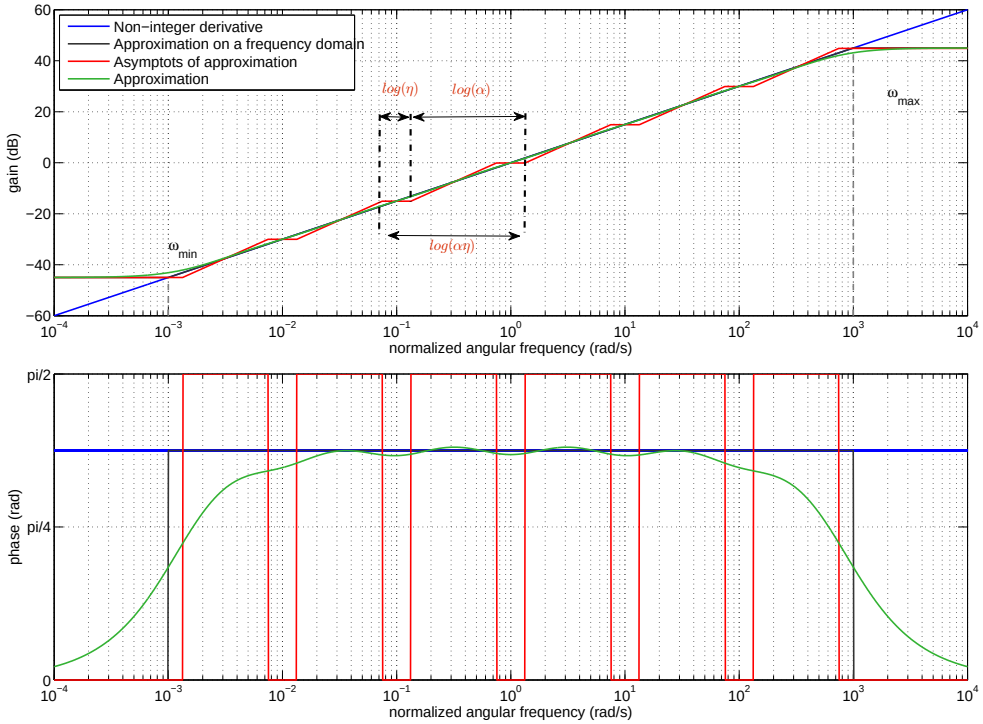

Figure 5.7 – *Bode plot of a normalized frequential differentiator on a frequency domain* $[\omega_{min}; \omega_{max}]$ *and the construction of the recursive approximation transmittance. In this example the number of zeros and poles is 6, one per decade, to allow for approximation's ripple observation; imposed distances* α *and* η *are represented on a single zero/pole pair.*

Considering the equation 5.26, the following approximation can be used:

$$\left(\frac{s}{\omega_u}\right)^{\gamma}_{[\omega_b,\omega_h]} \approx C_0' \prod_{k=-N}^{N} \frac{1 + {}^{s}/_{\omega_{z,k}}}{1 + {}^{s}/_{\omega_{p,k}}} \tag{5.29}$$

with the same notation as previously expressed. The fixed N is a parameter that is defined considering the frequencial range of the required approximation. This last equation only uses integer order derivation and can be used as a classical transmittance in any numerical solver. The generalized derivator only consists in a product of individual first order transmittances with one zero and one pole. Moreover, an electrical analogy can be drawn from this equation.

This recursive transmittance can be interpreted as a series of electrical corner frequencies resulting from associations of reactive elements. This corresponds to the lumped model which can be used to approximate bode curves exhibiting non integer behaviours as in Scaramuzza et al. (2012) for example.

An illustration of such transmittance is shown in Figure 5.7. In this graphical representation, a ripple can be observed either in the magnitude or phase. This ripple decreases with high values of N. Typically simulation performed in the following sections are done using 2 pairs of zeros and poles per decade, with boundary frequencies one decade under the minimal frequency imposed by the observation window, and one decade over the Nyquist frequency of the discretized measurement signal.

As a conclusion of this mathematical introduction of the fractional derivative, general ideas can be summed up as:

- Fractional phenomena that appears considering physical representation of the stimulation are based on generalization of the traditional integer derivation or integration.
- Such systems can be combined as traditional systems.
- A physical understanding and representation of such systems can be constructed, either in the temporal of frequencial spaces.
- By using recursive approach, these systems can be computed using algorithm for ordinary differential equation computation, only using a product of first order admittances.

In the next section, based on these physical phenomena and this possibility of mathematical modelling, a measurement bench is described with the objective to obtain an empiric model of the stimulation load.

5.3 In vivo compatible measurement bench and protocol

Electrical stimulation of biological tissues is preferably done by a current source (Merrill et al. (2005a); Cogan (2008)), as it is a natural way to control the injected electrical charge. Balancing the total injected charge is important to avoid tissue damage (Merrill et al. (2005a)). In order to reach these specifications, a specific measurement bench has been developed. This bench has been characterized to avoid measurement bias. Then a protocol has been developed taking into account the stimulation waveform characteristics and the requirements for *in vivo* measurement.

5.3.1 Measurement bench

The measurement bench shown in Figure 5.8(a) uses of a programmable arbitrary waveform generator (*Agilent 33250A*) to control the stimulus applied to the electrode. This generator has a voltage output, nevertheless the stimulation of the tissue has to be provided in current mode. For this purpose, the electrode under measurement is driven by a voltage-controlled current source. The voltage across the electrode is then sensed through an amplification stage, and recorder with an *Agilent MSO6034A 300 MHz* Oscilloscope.

In order to lessen the measurement error, the output impedance of the stimulation current source has to be as high as possible. The most adapted topology for this purpose is the Howland current source as presented in Figure 5.8(a). In first approximation, considering the input impedance of the amplification stage as infinite, the current in the electrode is determined by:

$$I_{elec} = G \cdot V_{in} - \frac{V_{elec}}{r_{out}} \tag{5.30}$$

where:

$$\begin{cases} G = \dfrac{1}{R_1} \\ r_{out} = \dfrac{R_1 R_2 \left(R_2 + R_3\right)}{R_3^2 - R_2^2} \end{cases} \tag{5.31}$$

This result allows to tune separately the transconductance G and the output resistance. The transconductance was set using precision resistors with a tolerance of 0.1%. Two different

transconductances have been used:

$$\begin{cases} G = 0.1mS & \Rightarrow R_1 = 10k\Omega \\ G = 1mS & \Rightarrow R_1 = 1k\Omega \end{cases} \tag{5.32}$$

These values allow to stimulate in the range of $1\mu A$ to $5mA$ with voltages in the range of $10mV$ to $5V$; this range corresponds to the possibility of the *Agilent 33250A* and typical stimulation current levels.

The output resistance has been set to be theoretically infinite choosing $R_2 = R_3 = R$. However, this condition is never satisfied due to the distribution of values of the used component. As electrode impedance can be expected to reach a magnitude of several mega-ohms, the condition $r_{out} > 1G\Omega$ was ensured by correct sizing of $R1$ with the given tolerances of $R2$ and $R3$. Finally $R2 = R3 = 100k\Omega$ with a tolerance of 0.01% was required for the performed transconductances.

The operation amplifier (*LT1001*) for the current source was chosen to have a precision output, good linearity and a tunable offset to compensate any DC current on the load. The amplification stage provides a high input impedance to reduce influence of sensing on the impedance measurement. This stage can also provide gain if the recorded signal is small. The adopted topology is an instrumentation amplifier (*INA2128*), achieving an input impedance of $10G\Omega||2pF$ that can be considered as negligible compared to the current source r_{out}, and consequently to the range of impedance to measure. The gain A_v is controlled with the resistance R_g as presented in Figure 5.8(a). This gain can reach $0dB$, $20dB$ or $40dB$, however, the use of higher gain obviously reduces the bandwidth of this stage.

In order to confirm that no frequencial effect can disturb the measurement, the bench was characterized on a resistive load. The Figure 5.8(b) shows the temporal response of the bench, with a transconductance G of $0.1mS$, a gain A_v of $0dB$ on a resistance ($10k\Omega \pm 1\%$). This test load was accurately measured using a *Keithley 6487 Picoammeter* in ohm-meter configuration, and then characterized with current heaviside functions with the bench as it will be performed with electrodes. The obtained voltage transient response is shown in Figure 5.8(b).

This response was identified to a linear third order system. The magnitude of the bode plot of the identified transfer function of the step response of Figure 5.8(b) is presented on Figure 5.8(c). The gain is normalized considering the product of the used transconductance G and the measured load resistance to calibrate the measurement bench. The static gain K_m and the lower observed resonance frequency f_l are:

$$\begin{cases} K_m = 1.004 \\ f_l = 130.2kHz \ (= 2.71 \cdot 10^6 rad \cdot s^{-1}) \end{cases} \tag{5.33}$$

As a conclusion the developed bench allows accurate measurement (less than 0.5% error) of phenomena for frequencies under f_l

5.3.2 Methods for current mode impedance measurement and model verification

Whatever the chosen model for electrode characterization, the methods for solicitations, measurement and verification should remain the same. In the two following sections, a method for charge balanced measurement and the accuracy quantification of the resulting model are discussed.

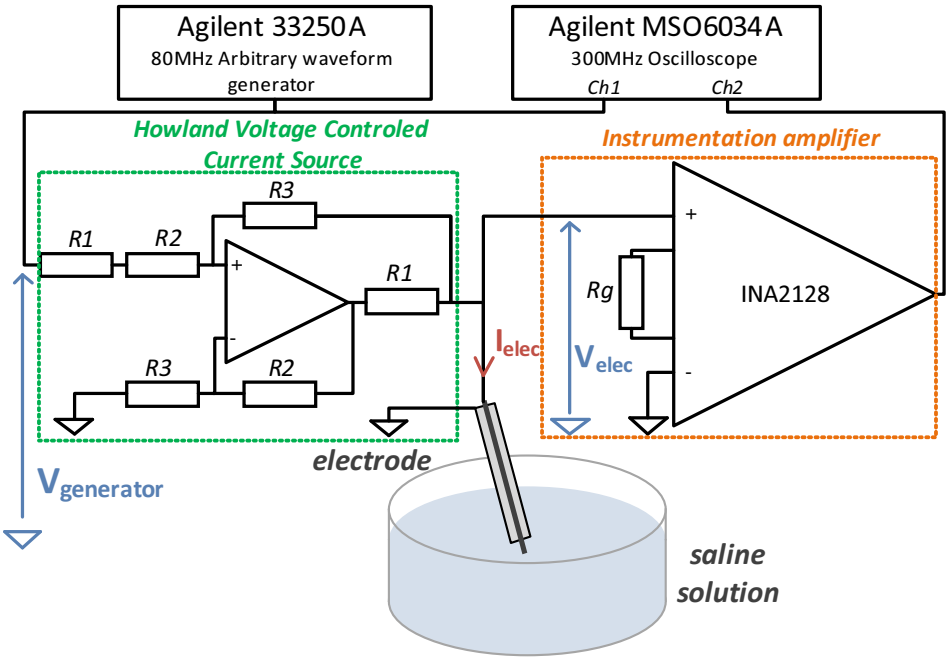

(a)

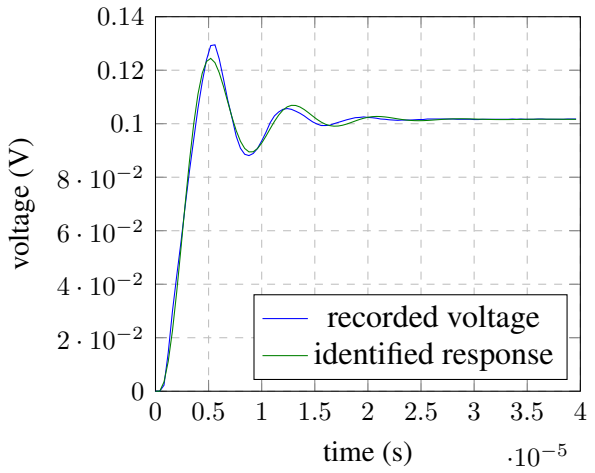

(b)

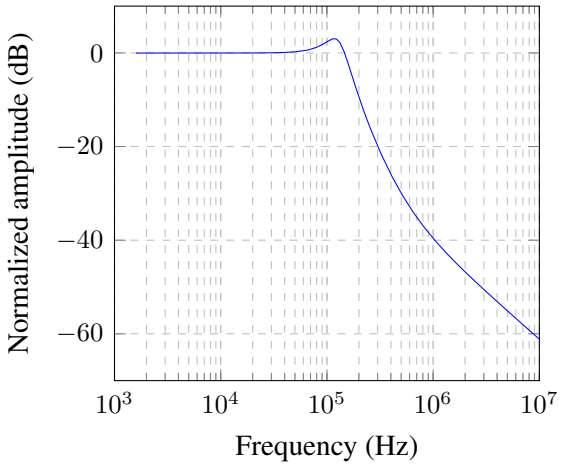

(c)

Figure 5.8 – *5.8(a) Impedance measurement system. The arbitrary generator is connected to a Howland Voltage Controlled Current Source (VCCS) and to the electrode; the voltage across the electrode V_{elec} is recorded through an instrumentation amplifier, which gain can vary from 0 to 40 dB.5.8(a) Step response of the measurement bench on a calibration resistive load, the response show complex response that can be identified to compare with electrode measurement. 5.8(c) Bode plot of the identified behaviour of the measurement bench on a resistive calibration load.*

Charge balanced current measurement

Since the electrode impedance is defined as :

$$Z_{elec}(s) = \frac{V_{elec}(s)}{I_{elec}(s)} \tag{5.34}$$

where s is the Laplace-domain variable, the recording setup as presented in Figure 5.8(a) provides impedance evaluation with respect of :

$$\begin{cases} i_{elec}(t) = G \cdot V_{Ch1}(t) \\ v_{elec}(t) = \dfrac{V_{Ch2}(t)}{A_v} \end{cases} \tag{5.35}$$

The goal of the developed bench is to perform measurement for the identification of both fractional order aspect and non-linearity. However, the input stimulus of the system is *a priori* undefined. As the protocol has to satisfy requirement for *in vivo* impedance measurement and for being realistic regarding the stimulation waveform, some conditions can be expressed :

- the measurement current pattern has to be charge balanced, not to produce tissue damage and electrode corrosion,
- the current range has to be the same as the corresponding stimulation range for a particular electrode, as used in biological conditions,
- the frequencial spectrum has to be the same as the one of typical waveform applied on the particular electrode, as used in biological conditions.

The spectroscopic exploration of the impedance with sinusoidal stimuli appears as an interesting solution, however, this method has to be avoided as the impedance is non-linear. The typical biphasic current waveform is a robust alternative as each current edge represent a step response of load to a solicitation. The edges contain sufficient frequential information to identify a model with traditional algorithms. Moreover, this waveform is by definition charge-balanced. The models are identified using a gradient descend algorithm minimizing the distance between the model simulated voltage and recorded curves.

Method for impedance model verification

A second measurement stimulus is required to allow for model accuracy verification. The verification stimulus was chosen to be a white noise sequence of a maximal frequency over $f_{\text{pulse max}}$ and under f_l and a root mean square current value in the range of the considered electrode as used in biological conditions. This signal was centred on a null mean value so that the global sequence is charge balanced, and can also be used under *in vivo* conditions. This verification also allows impedance representation considering:

$$Z|_{dB}(f) = 20log\left(|\widehat{v}_{elec}(f)|\right) - 20log\left(\left|\widehat{i}_{elec}(f)\right|\right) \tag{5.36}$$

where $\widehat{v}_{elec}(f)$ and $\widehat{i}_{elec}(f)$ are the Fourier transforms of the recorded sequences corresponding to $v_{elec}(t)$ and $i_{elec}(t)$.

Finally, the model simulations can be compared with the recorded responses using the Normalized Root Mean Square Error (NRMSE). Considering v_{rec} the recorded signal from the

measurement bench and v_{sim} the result of the stimulus computation through the identified model, the discrete time definition of the NRMSE is:

$$NRMSE = \frac{\sqrt{\frac{1}{N}\sum_{k=1}^{N}\left(v_{rec}\left(k\right) - v_{sim}\left(k\right)\right)^2}}{\Delta v_{rec}} \tag{5.37}$$

where N is the number of samples on the considered time window and $\Delta v_{rec} = max\left(v_{rec}\left(k\right), k\right) - min\left(v_{rec}\left(k\right), k\right)$ on the same time window. In order to increase the accuracy of the model, this error has to be decreased.

5.4 Non-linear and fractional modelling

The protocol described in the previous section has first been applied on a macro-electrode (NEX100, *Phymep, France*) used for DBS experiments on rats. The electrode was placed in a Hank's Balanced Salt Solution (*Thermo Scientific HyClone, SH3058801*), which has a composition similar to extra-cellular environment. This first measurement has been used to determine a mathematical model for electrodes. This model is described in detail by the two following subsections.

5.4.1 Preliminary results on macro-electrode measurement

The use of the developed bench and protocol are shown in Figure 5.9(a). The applied current varies from $50\mu A$ to $1mA$ with $50\mu A$ steps. As it can be observed on Figure 5.9(a), during the first pulse the voltage rises to a positive value at the first current edge ; then the voltage increases, showing in first approximation an integrator-like behaviour, however, the slope is not constant. At the falling edge of current at the end of the first pulse and during the inter-pulse, a memory effect can be observed, however, the voltage decreases with time. For the second cathodic pulse, a symmetrical description can be drawn. The integrator-like behaviour can be understood by the previously described capacitive behaviour of the interface's double layer. This effect also explains the memory effect during the interpulse.

The dynamics of this memory effect nevertheless leads to discussion. Commonly used electrical models for stimulation (as in Williams and Constandinou (2013) for electrical design) consider it as a memory with loss, and associate a parallelized resistor to the double layer capacitor. This model implies that the voltage follows an integer ordinary differential equation of the first order, and thus this behaviour could be approximated using exponential curves. However, this memory effect does not fit accurately with such equations. This memory effect can then be compared with the plot of the singular kernel ℓ weight evolution of Figure 5.5(b). The fractional integration appears to be an accurate approach to fit the observed slow dynamics taking into account both integration and memory effects.

Despite the previous theoretical discussion of section 5.1, the identification algorithm was used with a black-box equation as described bellow:

$$Z_{elec}\left(s\right) = K\frac{\left(s/\omega_u\right)^{\gamma} + 1}{\left(s/\omega_u\right)^{\gamma}} \tag{5.38}$$

with K in Ω and ω_u in $rad \cdot s^{-1}$. This last expression allows for simulation considering the frequencial recursive approximation of the fractional integrator detailed in the previous section.

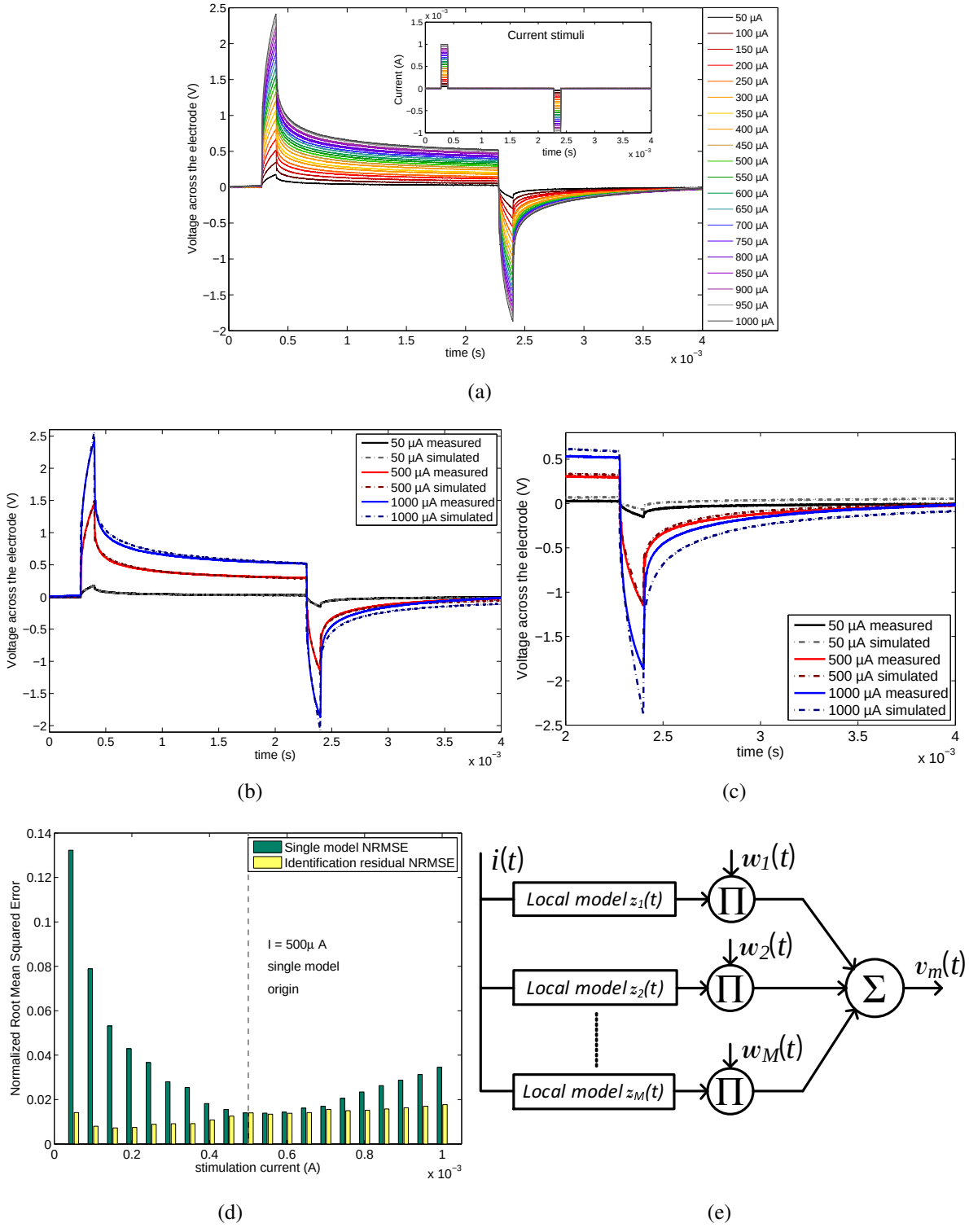

Figure 5.9 – *(a) Recorded voltage across the electrode for symmetric biphasic stimulation of* $60\mu s$*, (b) Results of the simulation of the identified model and comparison to the recorded voltage. (c) Simulation results with the model identified for* $I = 500\mu A$ *and the comparison with recorded voltages exhibiting the deviation of local model due to the non-linearity of the impedance. (d) Quantification of the NRMSE of local models in their range of measurement and comparison with the NRMSE for the local model of* $I = 500\mu A$ *with all measured responses. (e) Schematic representation of the multi-model used for non-linear simulation based on previously identified linear local models.*

Numerical results of identification are presented in table 5.1. These results show significant variations of all K, ω_u and γ versus the level of current.

$I\ (\mu A)$	$K_k\ (\Omega)$	$\omega_{uk}\ (rad \cdot s{-}1)$	γ_k	$\lambda_{1,k}$	$\lambda_{2,k}$
50	601	$7.36 \cdot 10^4$	0.594	0	$2.2 \cdot 10^3$
250	770	$3.32 \cdot 10^4$	0.623		
500	927	$1.64 \cdot 10^4$	0.674	$2.2 \cdot 10^3$	$2 \cdot 10^3$
750	985	$1.09 \cdot 10^4$	0.709		
1000	1002	$8.68 \cdot 10^3$	0.730	$2 \cdot 10^3$	0

Table 5.1 – *example of identified values for the adopted model and corresponding affine piecewise coefficients for a multi-model with 3 local models*

The ability of an extracted model to fit locally the pulse for a current value is shown in Figure 5.9(b). The simulation results are close to the recorded voltage with a growing deviation on the highest part of the current range. The Figure 5.9(c) confirms the inability of a particular model to fit other current values. All these preliminary results clearly show that the stimulation load is governed by non-linear phenomena that have to be modelled.

The bar graph represented in Figure 5.9(d) sums up the final errors of the optimization algorithm and compare the simulation of all current level stimuli response with a single local model, for this picture the model at the mean value of investigated current levels. This second set of data clearly shows the growing deviation if the current is far from the measurement, however, a single model gives satisfying results in a local current range.

5.4.2 Multi-model

The approach developed for the non-linearity modelling is based on the need for minimizing the NRMSE in every situation. The adopted strategy is based on the re-use of the model presented in equation 5.38, and to explore the non-linearity simulation considering the set of identified linear models.

Method

A multi-model approach have been used to obtain a global non-linear model. The multi-model approach has been of interest since Johansen and Foss (1995). To describe the non-linear behaviour of a system, it uses a set of local linear models (or affine) of the system operation in various areas, as shown by Figure 5.9(e), each local model is used for a particular current range. The output of a local model is weighted by an activation function close to one if the operating point is near the center of the area associated to the local model, and decreasing towards zero when it moves away.

The standard form of a multi-model is:

$$v_m(t) = \sum_{k=1}^{M} w_k(\varphi(t))\, z_k(\varphi(t)) \tag{5.39}$$

where $\varphi(t)$ is an input-output observation vector at time t, $w_k(\varphi(t))$ is the activation function of the local model z_k, M the number of local models. Depending on the operating point, the

activation function defines the contribution of the local model in the global model. It provides a gradual transition of this local model to the other neighbouring local models. The following conditions must be imposed:

- the activation function is positive and less than 1,

$$0 \leq w_k\left(\varphi\left(t\right)\right) \leq 1, \forall k, \forall t \tag{5.40}$$

  so that the contribution of a particular single model is between 0 and 100%,

- the activation functions sum is equal to 1 at any point:

$$\sum_{k=1}^{M} w_k\left(\varphi\left(t\right)\right) = 1, \forall t \tag{5.41}$$

  so that the sum of the contribution of the models is 100% at any time.

For the results presented in Figure 5.9(a), the non-linearity appears to be current dependant, so that the function φ is directly the physical quantity i_{elec}. The activation functions $w_k\left(t\right)$ can have an arbitrary shape respecting previously expressed conditions. A first implementation of the multimodel was done using linear piecewise functions defined as:

$$w_k\left(t\right) = \begin{cases} 1 - \lambda_{1,k}\left(I_k - i\left(t\right)\right) & \text{if } i\left(t\right) \in \left[I_{k-1}, I_k\right] \\ 1 - \lambda_{2,k}\left(i\left(t\right) - I_k\right) & \text{if } i\left(t\right) \in \left[I_k, I_{k+1}\right] \\ 0 & \text{else} \end{cases} \tag{5.42}$$

where I_k denotes the operating point and where $\lambda_{j,k}$ is a coefficient that permits to meet equation (5.41). An example of activation function implementation for a multi-model with 3 local models ($I_1 = 50\mu A$, $I_1 = 500\mu A$ and $I_1 = 1000\mu A$) is shown on Figure 5.10(a), and corresponding λ values are given in table 5.1.

Results and discussion

In order to validate the obtained model, the pseudo-random current sequence was injected through the electrode. This gaussian distributed sequence has a duration of $2ms$, a sampling frequency of $1MHz$, a root mean square of $308.3\mu A$ and a maximal amplitude of $1mA$ for the presented sequence. The measured voltage was then compared to simulation results using 3 different models :

- A fractional multi-model as previously described.
- A single fractional model with the same form as equation (5.38), extracted from the $500\mu A$ step response.
- A linearised RC model as shown in Kelly and Wyatt (2011) extracted from the $500\mu A$ step response.

Results are shown in Figure 5.10(b). The linearised model clearly presents a deviation from the measured voltage. A $30\mu s$ zoomed view of the obtained signal is shown in Figure 5.10(c). Both others fit with a smaller error the measured voltage.

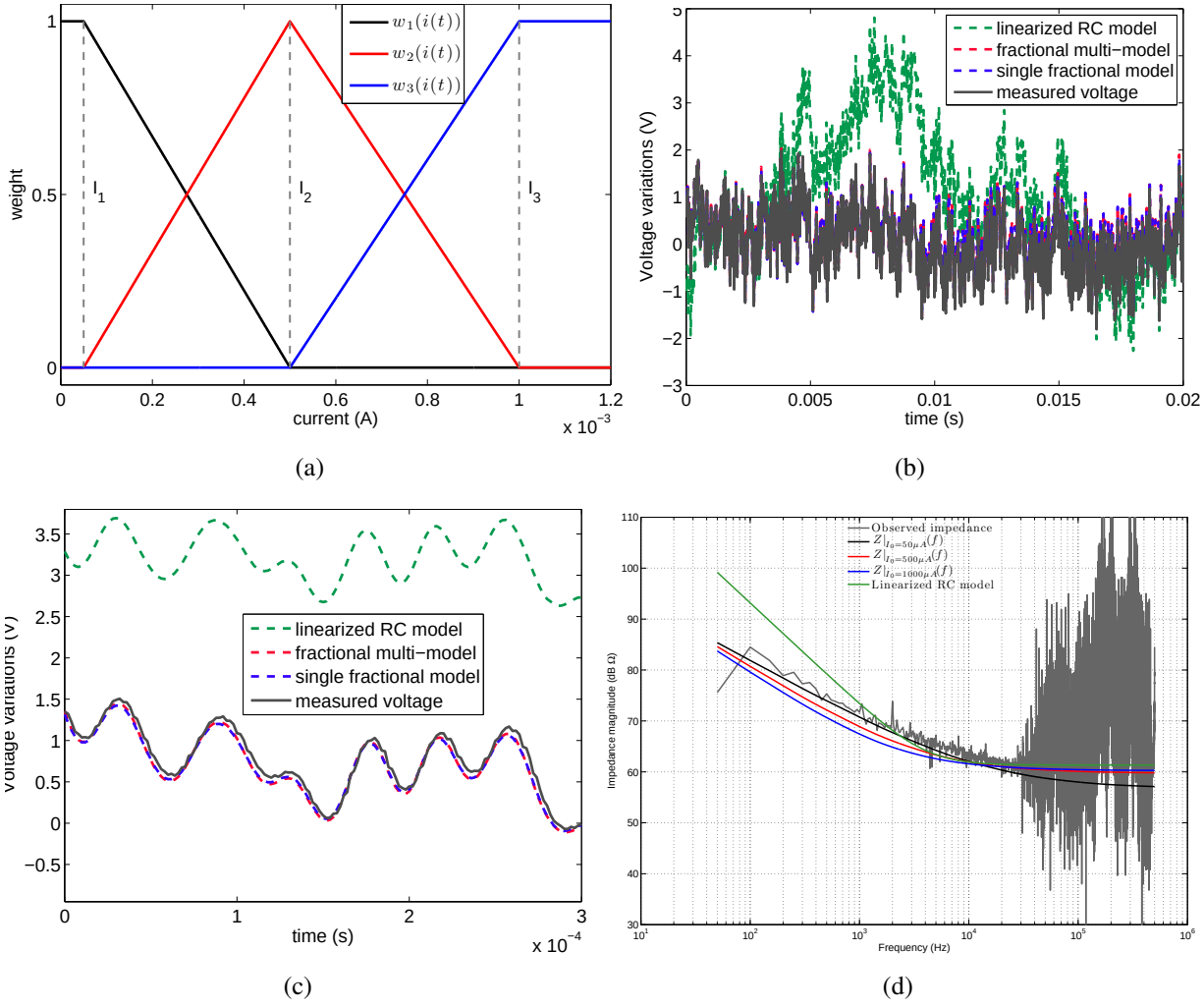

Figure 5.10 – *(a) Graphical representation of the weighting functions versus the current for a multi-model with 3 local models for $50\mu A$, $500\mu A$ and $1000\mu A$. (b) Simulation with a RC linearised model, a single fractional model and the multi-model (based on 3 local models) with the pseudo-random measurement sequence. (c) Zoom of the previous curve on a particular time window showing the divergences between the different models (d) Bode representation of the observed impedance compared to the Bode plots of the RC linearised model and the tree local models used for the multi-model simulation.*

For the linearised RC model response, the NRMSE is as high as 41.5%, for the single fractional model, this error is 4.9% and for the multi-model NRMSE is 4.6%. The multi-model shows a slightly better performance than the single model. However, the choice of the Gaussian distribution focuses on values around 0 to the detriment of high signal values, where the multi-model should be the most efficient. To complete this analysis, Figure 5.10(c) provides a zoom on the high values of voltage; on this interval, the NRMSE is 3.7% and 5.0% for the multi-model and the single fractional model respectively.

A spectral view of the observed impedance with the pseudo-random sequence is give in Figure 5.10(d) using the method expressed by equation 5.36. The 3 used local models for the multi-model implementation and the linearised RC model spectral magnitudes are also drawn on this plot. The curve of the RC linearised model only cross the observation for two frequencies, explaining its inability to give satisfying results. The 3 local models have a lower slope and are nearer to the observation ; particularly, the first local mode ($I = 50\mu A$) is near the observation in low frequency and the two others (respectively $500\mu A$ and $1000\mu A$) fit the higher frequency ; this effect is due to the gaussian repartition of the used noise sequence where high current values are less reached and associated with higher frequencies. However, the succession of the local model curves illustrate the ability of the multi-model approach to simulate complex dynamic signals.

Nb of models	1	3	5	10	20
time (ms)	31.6	129	199	382	749
$\Delta\,(NRMSE)\,(\%)$	0.3	0	-0.08	-0.1	-0.14

Table 5.2 – *Simulation time and error difference compared to the error for 3 local models versus the number of local models used for the multi-model approach*

Finally, the accuracy of the multimodel can be examined considering the number of used local models. Simulation results are given in table 5.1. The simulation time is obviously growing with the number of parallelized local models. At the same time the NRMSE is decreased when adding models. The multi-model approach appears to be a tool for rapid measurement, identification and simulation of fractional and non linear behaviour of the stimulation load.

5.5 Partial conclusion

This chapter investigated the impedance modelling of stimulation electrodes. Physical considerations on the metal-to-electrolyte junction and biological tissues revealed a need for fractional, non-linear models. A method for fractional model computation was then outlined, based on mathematical assumptions concerning fractional derivatives. Considering the requirements of electrical stimulation (current stimuli, charge balancing, etc.), a measurement bench and protocol were designed and used to model a macro-electrode. These measurements led to the development of a fractional, non-linear model based on the multi-model approach. This model gave interesting results in terms of accuracy compared to commonly-used models in the field of electrical design.

We will further try to generalize this approach to different electrodes used for stimulation in different contexts. However, the equations expressed in the first section of this chapter were dependent on electrode surface area, making it possible to reason in terms of scale effects. Electrode impedance modelling thus formed the basis of the multi-application approach.

CHAPTER 6

MULTI-APPLICATION ORIENTED CIRCUIT DESIGN

EXTERNAL electrical stimulation has various applications, but the circuits are generally designed for a specific context, as in the second part of this document. This approach still restricts the development of new experimental setups and also increases the cost of therapeutic devices. A global approach is a promising avenue for overcoming these drawbacks. This chapter proposes an original approach to electrical stimulator design and development adaptable to various experimental setups.

6.1 Multi-application design strategy

The aim of the multi-application strategy is to propose an architecture capable of driving a large variety of electrodes, from micro- to macro-electrodes. The geometry of the electrode depends on the target tissues and is correlated with the electrode impedance. Therefore the strategy will be based on considerations about the stimulation load impedance and the stimulation shape, resulting in the specification the stimulator voltage constraints. In the next section, a strong hypothesis is made on the electrode impedance model, to permit the use of a scale effect that will be the basis of the system design. Then the robustness of this scale effect is shown.

6.1.1 The RC-model hypothesis

In the previous chapter, based on both theoretical and empirical approaches, a model of electrode impedance has been established. This model is both fractional and non-linear. If this realistic model is interesting for exact simulation with CAD software, the equations cannot be used for rapid evaluation at the first steps of circuit design. To allow for simple reasoning, a simplification of the model is performed; however, the previous model, more reliable, can be used to verify the circuit behaviour in the final steps of the design flow.

A first hypothesis consists in not taking into account this non-linearity in the mathematical description of the stimulation load. This non-linearity can be considered as beneficial for electrical design as it is correlated to the Buttler-Volmer equation 5.8: the the impedance decreases when the signal gets larger.

In our case, only the form of the local model shown in equation 5.38 is studied. Considerations on the fractional order γ have to be done to simplify the model. Let us consider the limit:

$$\lim_{\gamma \to 1} \mathcal{L}^{-1}\{\left(R_{elec} + \frac{1}{Q_{elec} s^{\gamma}}\right) \cdot \mathcal{L}\{i_{stim}(t)\}\} \tag{6.1}$$

This limit is illustrated by the simulation results presented in figure 6.1. Figure 6.1(a) presents the temporal response for a charge balanced stimulus with a normalized cathodic current of -1 and a five times smaller anodic current. In these simulations, R_{elec} and Q_{elec} are constant and γ is swept. The integrative component is predominant when the fractional order is close to 1. During the cathodic phase, $\gamma = 1$ appears as a worst case, however, the behaviour during the anodic phase is non-monotonic. Thus, the voltage variation with γ for different ratios of anodic versus cathodic current with charge balancing were computed. Results show that $\gamma = 1$ is a worst case whatever the ratio between anodic and cathodic phases. In this case the cathodic phase is responsible for the major part of the voltage variation. $\gamma = 1$ corresponds to the purely capacitive constant phase element.

Simplifications over both the non-linearity and the fractional order make the over-simplified RC-model good candidate for worst case analysis or reasoning. Therefore, if this model presents drawbacks for accurate simulation of bio-interface phenomena, it is advantageous for rapid electrical sizing, as it provides an ease of calculation and security margins.

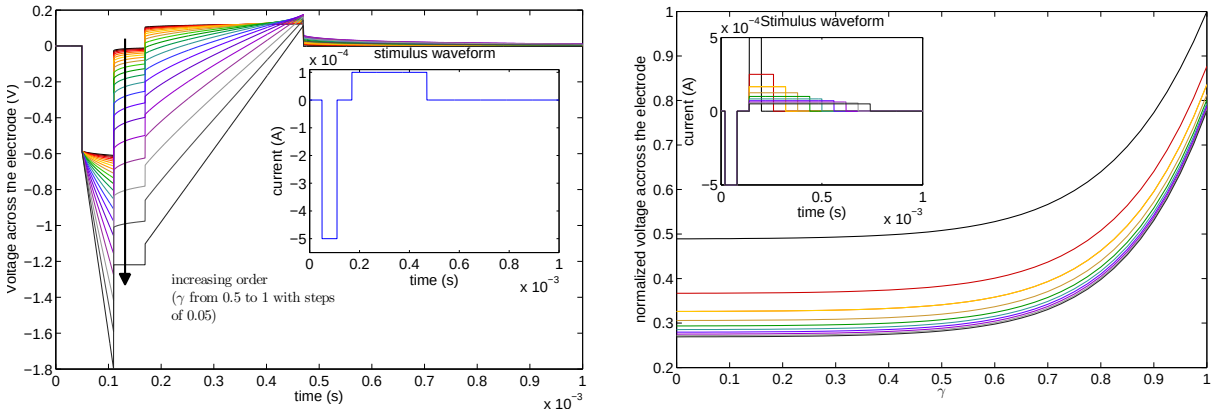

(a) (b)

Figure 6.1 – *(a) Evolution of the voltage response for a fixed resistance and reactance for different fractional orders γ. (b) Voltage ripple on the electrode for a charge balanced current waveform versus the fractional order γ of the impedance model for different ratios of $I_{anodic}/I_{cathodic}$.*

6.1.2 Electrical scale effect for current stimulation

Expression of the scale effect

Reasoning on the scale effect is based on the following hypotheses:

- the electrode electrical model is the resistive/capacitive one as a worst case. This hypothesis is particularly powerful as it allows to express the voltage in a simple way for current pulses of typical stimulation waveforms.
- The two elements of this electrical model (R_{elec} and C_{elec}) are related to the electrode geometry under the assumption:

$$\begin{cases} R_{elec} \propto \dfrac{1}{A_{elec}} \\ C_{elec} \propto A_{elec} \end{cases} \tag{6.2}$$

  where A_{elec} is the area of the electrode. For the capacitive part, this hypothesis is justified by the surface dependence of all phenomena - as presented in chapter 5 - that induce a reactance in the stimulation load impedance. As we only consider the electrode, the blocking capacitor is not taken into account. Under the assumption of a resistive effect mostly due to the electrolyte conductivity, the resistance is then dependant on surface as for traditional materials.
- The stimulation waveform is composed of series of pulses of constant current value. This is obviously right in case of typical biphasic stimulations, which represent a vast majority of cases. Here the pulse duration ΔT is chosen considering the chronaxie of the target cells (see Plonsey and Barr (2007)), which presents small variations versus the exact neural cell localization and can be considered as constant in first approximation.

Under these assumptions, the voltage variation across the electrode for I_{stim} is:

$$\Delta V_{elec} = I_{stim} \left(R_{elec} + \frac{\Delta T}{C_{elec}} \right) \tag{6.3}$$

This equation has to be estimated for different electrode geometries, specific to each application. However, considering the former hypothesis, let us divide electrode surface in small areas $A_{\square}$. This area virtually corresponds to the smallest micro-electrode addressed by a multi-application design; every quantity referring to this will be qualified as 'atom' (from the Greek ἄτομος, "indivisible"). Larger electrodes can be subdivided in virtual atom electrodes:

$$A_{elec} = N \cdot A_{\square} \tag{6.4}$$

A geometrical effect on the impedance can be expressed by considering proportionality formulated in 6.2:

$$\begin{cases} R_{elec} = \dfrac{R_{\square}}{N} \\ C_{elec} = N \cdot C_{\square} \end{cases} \tag{6.5}$$

where $R_{\square}$ and $C_{\square}$ are respectively the resistance and capacitance per atom surface. If the current is expressed in terms of current density J_{stim}:

$$I_{stim} = N \cdot J_{stim} A_{\square} \tag{6.6}$$

then by substitution in equation 6.3:

$$\Delta V_{elec} = \cancel{N} J_{stim} S_{square} \left(\frac{R_{\square}}{\cancel{N}} + \frac{\Delta T}{\cancel{N} C_{\square}} \right) \tag{6.7}$$

In this last equation, the factor N is not present meaning that the voltage constraint is an invariant if the current density of a N-atom-large electrode is stimulated with $N \cdot J_{stim} A_{\square}$ current, where $J_{stim} A_{\square}$ is the maximal current on the atom-surface electrode. This hypothesis is even a worst case considering the tissue safety stimulation charge per electrode quantified by Shannon (1992). The Shannon criteria is expressed as the maximal cathodic charge for a given electrode surface:

$$Q_{max} = I_{stim} \Delta T \propto \sqrt{A_{elec} 10^k} \tag{6.8}$$

where k is a coefficient so that, with $k > 2$, damages are systematically observed and with $k \leq 1.5$ no damages are observed. Considering the surface division by the atoms, the maximal current $I_{max,N\square}$ can be written:

$$I_{max} \propto \frac{\sqrt{N}\sqrt{A_{\square} 10^k}}{\Delta T} < \frac{N\sqrt{A_{\square} 10^k}}{\Delta T} \propto N \cdot J_{\square max} A_{elec} = N \cdot I_{max,\square} \tag{6.9}$$

where $I_{max,\square}$ is the maximal value of the Shannon criterion for the atom electrode. Consequently, an atom stimulation channel will correspond to the smallest electrode. Combining these atoms for larger electrodes by current addition for larger electrodes is sufficient to reach the maximal current requirements. This principle is the basis of the global approach as illustrated on figure 6.2.

The atom channel topology has to be one-pole output as the return electrode can be shared for different channels. Consequently, the voltage supply of the system is symmetric to allow asynchronous stimulation of any channels combination as specified in section 2.2. Different combinations of atom-channels can be used:

- **stand alone channels:** atom-channels are used independently; as the chosen topology is symmetric, stimulation patterns can be asynchronous and driven independently. In this case the maximal voltage across the electrode is in first approximation $\Delta V_{supply}/2$.

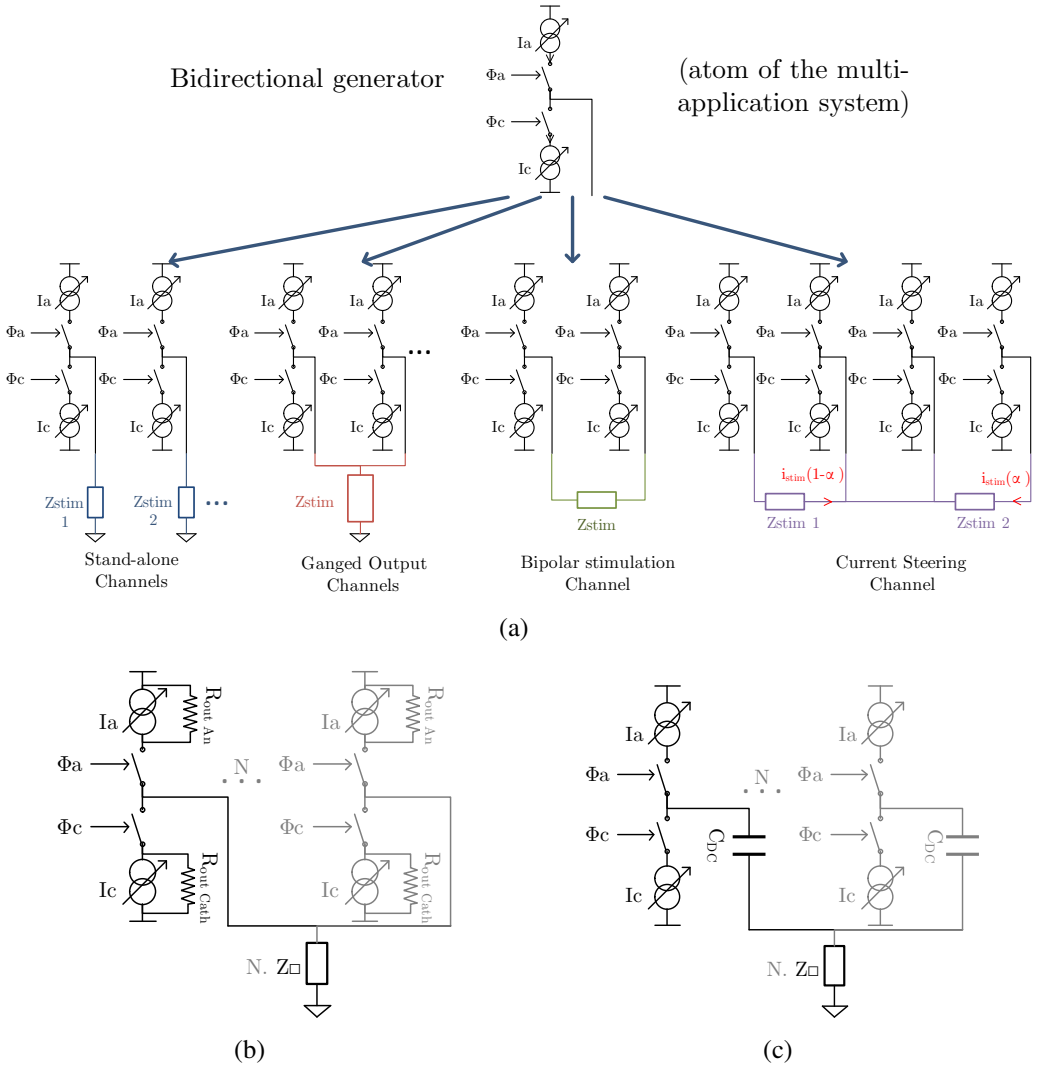

Figure 6.2 – *(a) Illustration of the multi-application approach. (b) Evaluation of the robustness of the scale effect versus the output parasitics. (c) Evaluation of the robustness of the scale effect versus the DC blocking capacitance*

- **ganged channels:** for larger electrode geometries, the atom-channels are combined and output are ganged on the electrode. The number of ganged atoms can vary with respect to the total current requirement in regard to the the maximal current of the atom-channel. In this case, the DC blocking capacitor is placed before the current adding point as discussed in the next section.

- **bipolar stimulation channels:** as both poles of the electrodes can be separately accessed, a bipolar channel based on a pair of atom or ganged channels can be constructed. In this case a side is stimulating in normal mode (source mode) and the opposite side is stimulating in inverting mode (sink mode). With this topology the maximal voltage across the electrode is in first approximation ΔV_{supply}.

- **current steering channels:** atom or ganged channels can also be combined to provide complex structures capable of current steering over multi-polar electrodes, as made by

Valente et al. (2010).

Therefore a multi-application and multi-configuration system can be build for a defined number of atom-channels. These atom-channels requires some additional circuits in charge of the stimulation current generation and eventual copying or weighting, so as for commutation orders management.

Robustness against parasitics and blocking capacitor

If the scale effect is valid with formal current source, it has to be assessed with second order models of electrical stimulation. In particular, the output parasitics cannot be ignored. The atom-stimulator will be fabricated using CMOS technology, so that the current source can be considered as the gate-controlled drain-source current source of a typical CMOS transistor. For the output modelling, the parasitic capacitance can be ignored as it is only a minor parasitic for short channel devices. However, the output resistance has to be taken into account. When connected to the electrode, this resistance induces a current loss. The graphical representation of the output parasitics estimation is illustrated in figure 6.2(b). Let us consider the output as an equivalent MOS transistor generating $I_{stim\square}$. Thus the parallel association of N sources is resulting in an equivalent transistor generating $N \cdot I_{stim\square}$. In this case, in the saturation region, the output resistance is:

$$R_{out} = \frac{1}{\lambda N \cdot I_{stim}} = \frac{R_{out\square}}{N} \tag{6.10}$$

where λ is the channel-length modulation parameter. Then, the ratio between the current loss I_{loss} and the current applied on the electrode I_{elec} is:

$$\frac{I_{loss}}{I_{elec}} = \frac{Z_{elec}}{Z_{elec} + R_{out}} = \frac{\frac{1}{N}\left(R_{\square} + \frac{\Delta T}{C_{\square}}\right)}{\frac{1}{N}\left(R_{\square} + \frac{\Delta T}{C_{\square}}\right) + \frac{R_{out\square}}{N}} \tag{6.11}$$

which is also an invariant versus the parameter N, meaning that the scale effect is robust versus the ratio of current loss.

The influence of the DC blocking capacitor is evaluated with respect to the schematic presented in figure 6.2(c). The ganged outputs are shorted after the atom-DC blocking capacitors. In this case, based on the equality of the currents, all voltage on independent atom-capacitors are equal, so that the virtual resulting DC capacitor is:

$$C_{DC} = N \cdot C_{DC\square} \tag{6.12}$$

In this case, the ratio between the DC blocking capacitor and the electrode voltage is:

$$\frac{\Delta V_{CDC}}{\Delta V_{elec}} = \frac{\frac{\Delta T}{N C_{DC\square}}}{\frac{1}{N}\left(R_{\square} + \frac{\Delta T}{C_{\square}}\right)} \tag{6.13}$$

which is also invariant versus N, meaning that the scaling can include fixed DC blocking capacitors per atom-channel. In case of mismatch on the atom channels current sources, charge unbalance can be different for each contribution; however, the fact that the blocking capacitor is near each atom will in steady state force the balancing on each atom separately.

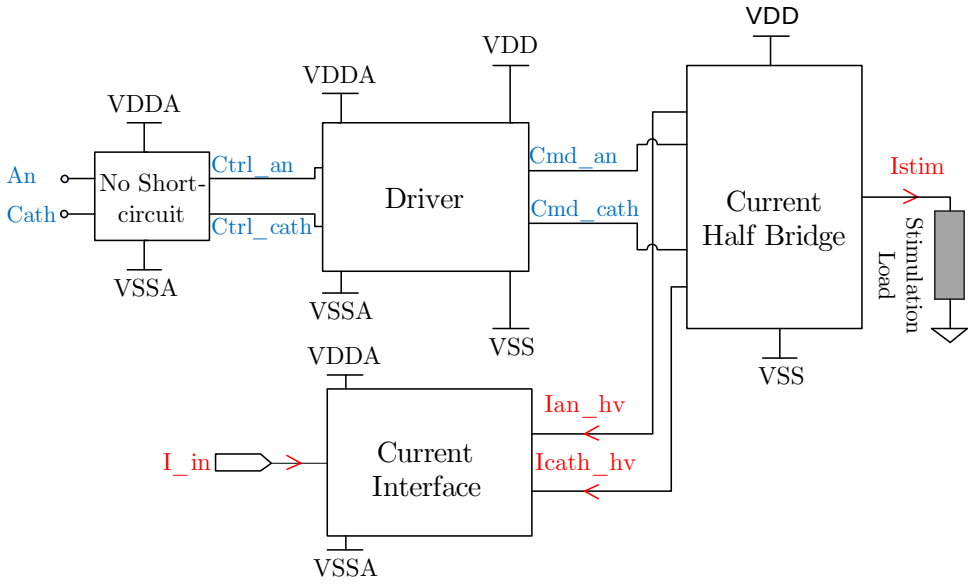

Figure 6.3 – *Structure of an atom stimulation channel*

6.2 ASIC integration

This multi-application strategy has been developed to deliver stimulation for different projects; in this section the designed proof-of-concept ASIC based on the global approach is detailed. Then, the hosting boards and system are described.

System sizing requirements can be summed up by:

- the atom-electrode has to reach a maximal current of $250\mu A$ (corresponding to the maximal current on a a contact of the micro-electrode array used in the project HYRENE),
- 32 independent atom-channels have to be available (corresponding to the maximal channel number for both projects HYRENE and BRAINBOW).

In order to limit the number of the ASIC IO pins, the developed chip includes 8 atom-channels, allowing to generate a stimulus of $2mA$ in case of full ganged channels (this level corresponds to the maximal observed current on the electrode for DBS on rodents). The full chip includes both stimulation channels and a combination of analog and digital circuits. Several chips can be combined to reach the 32 channels as requested by the specification.

6.2.1 Structure of the stimulation atom channel

The atom-channel is the minimal circuit able to drive the electrode in order to be easily combined. Its only inputs are a current and the commutation signals for the cathodic and anodic phases. These signals are low voltage, however, the electrode voltage can reach levels higher than the CMOS supply voltage. Therefore high-voltage processes have to be used. Such high-voltage processes have been adapted for classical CMOS technologies, as shown in Ballan et al. (1999); they require only two additional fabrication mask. The $0.35\mu m$ technology includes $50V$ transistors on classical CMOS processes, as developed in Knaipp et al. (2006); basic circuits for these technologies are explained in Ballan et al. (1999) and Forsyth (2003).

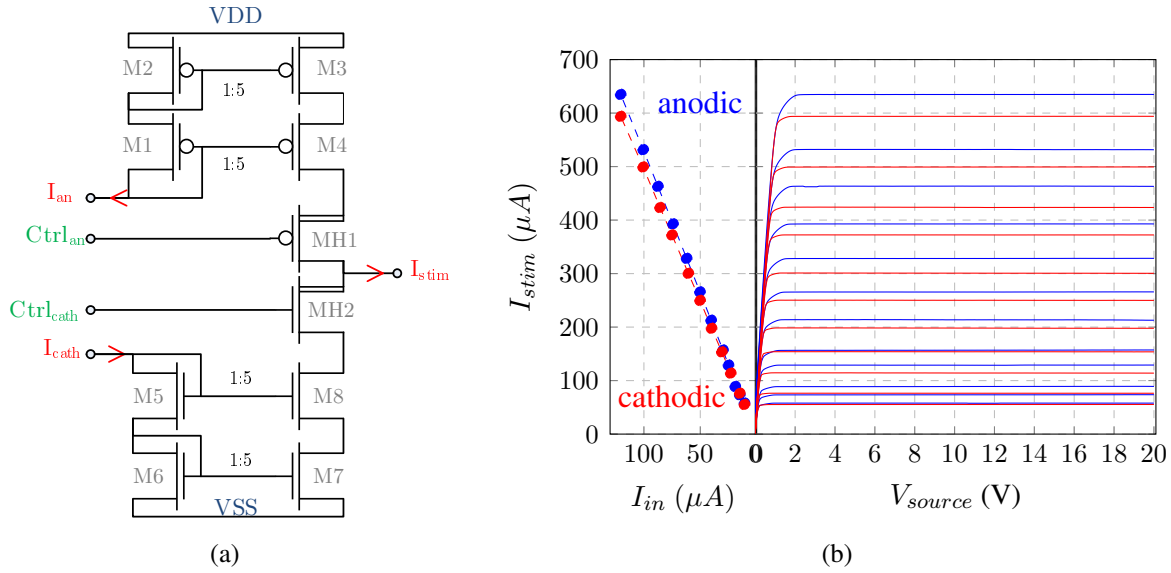

Figure 6.4 – *(a) Schematic of the current amplification output stage. (b) ASIC output characteristics measured on the stimulation output stage and transfer characteristic of the channel with a picoammeter/voltage source Keithley 6487.*

The basic structure of the atom-channel is shown in figure 6.3. This schematic is divided in four blocks:

- **the current half-bridge:** this circuit is in contact with the electrode through the DC blocking capacitor; it delivers the stimulus and is supplied with high voltages $VDD = 20V$ and $VSS = -20V$,
- **the driver:** this block converts the low voltage levels - $VSSA = 0V$ and $VDDA = 3.3V$ - to high voltages logic levels for the current half-bridge,
- **the current interface:** this circuit is a current follower at the interface between the low-voltage part and the high-voltage part,
- **No short-circuit:** this logic block prevents from short-circuits between the two current sources of the output stage. The block 'No Short-circuit' is described in Appendix C.

Current half bridge

As explained in the previous section, this topology is a symmetric two-current-sources generator. The power supply (VDD and VSS) is symmetric $\pm 20V$. As this topology is a high-voltage circuit, the thick oxide High Voltage *(HV)* transistors could be natural candidate to implement the current sources, however, these components suffer from a low gain factor and a high Early effects. Therefore, they cannot be used in the context of accurate high output impedance current sources. We used Low Voltage *(LV)* CMOS transistors that present a higher gain factor and lower Early effect as presented in Figure 6.4(a).

LV transistors $M1$ to $M4$ and $M5$ to $M8$ form a cascode current mirror that generates the anodic and cathodic current respectively. Cascode sources present a high output impedance

suitable for small electrodes with high impedance. The two sources where designed to have a theoretical current gain of 5 and a symmetrical behaviour was imposed by:

$$\begin{cases} \frac{(W/L)_{NMOS}}{(W/L)_{PMOS}} = \frac{\mu_N}{\mu_P} \\ (W \cdot L)_{NMOS} = (W \cdot L)_{PMOS} \end{cases} \tag{6.14}$$

where μ_N and μ_N are the mobilities of the carriers in the P and N materials. In this last equation, the first line permits to have the same output real part, and the product permits to reach the same output parasitics capacitances to have the same frequential behaviour.

As v_{ds} of the low-voltage transistors cannot exceed $3.3V$, this voltage output is controlled using the stimulation switches formed by $MH1$ and $MH2$. Both transistors are HV transistors with thin gate oxide, having approximatively the same V_{th} as LV transistors, and handling v_{gs} in the range of $0 - 3.3V$. Therefore, for $M3$ and $M4$ or $M7$ and $M8$:

$$2v_{ds} < |V_{DD/SS} - V_{gsMHX}| - v_{thMHX} < 3.3V \tag{6.15}$$

Consequently accurate analog current mirrors can be obtained on the HV structure with a combination of LV and HV transistors.

	Current gain(G)	f_t (MHz)	r_{out} ($M\Omega$)	$V_{drop}\|_{min}$ (V)
anodic	5.27	2.5	55.5	2.1
cathodic	4.96	2.5	40	1.7

Table 6.1 – *Main figures of the atom-channel output*

This circuit was characterized on the fabricated ASICs. The source transfer and output curves are exhibited in Figure 6.4(b). From these curves the global parameters of the output stages can be extracted. Main characterization results are summed up in Table 6.1. An asymmetry can be observed in the anodic and cathodic source observed gains. This divergence was not observed on design simulation and could result from the layout.This error, although small, cannot be neglected for charge balancing; it is corrected in the code that generates the numerical values for the current generation with respect of:

$$I_{an} = \frac{G_{cath}}{G_{an}} \cdot \frac{I_{cath} T_{cath}}{T_{an}} \tag{6.16}$$

The measured compliance allows stimulation of the electrode on a voltage range of $[-18.3V; 17.9V]$, and the source equivalent output resistance is of several $10M\Omega$. These two characteristics confirm that this front end is able to drive accurately electrodes which impedance is in first approximation less than the $M\Omega$.

Driver and Current interface

In order to reach the high-voltage input of the bi-directional current source, two high voltage interfaces have been designed as shown in Figure 6.5, performing level shifting from low to high voltages.

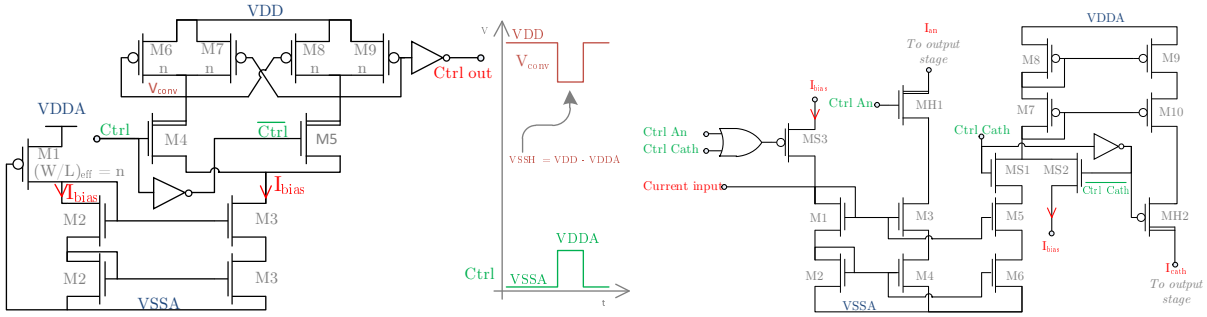

(a) (b)

Figure 6.5 – *(a) Level shifter for the control signal of the high voltage output stage. (b) High voltage shifter for the currents of the output stimulation stage.*

First the low-voltage levels switching commands are shifted using the differential circuit presented in Figure 6.5(a). In this schematic again, LV transistors are used in the low voltage part ($VDDA$ supplied), and the high voltage part (VDD supplied). In this topology a current is copied to ensure a voltage across transistors of the same gate dimensions, and transmits a constant potential difference from the LV part to the HV part.

The current generation is ensured by transistor $M1$ and transmitted through a cascoded current mirror (M_2 and M_3) to transistors M_{6-9}, controlled by transistors M_4 and M_5. These last two components are controlled with the command and its complement, so that only one branch of the topology is active at one time. For these two branches, transistors M_{6-7} and M_{8-9} have crossed gate potential so that only one is blocked and the other in saturation, ensuring:

$$V_{conv} = VDD - k \cdot VDDA \text{ with } k \in \{0, 1\} \tag{6.17}$$

as illustrated in the figure, where the secondary supply level $VSSH = 16.7V (= VDD - VDDA)$ is introduced. The obtained level shifted logic signal is then buffered with a LV logic gate supplied between $VSSH$ and VDD. As the $M_{4,5}$ have low voltage controlled gates, these two transistors have a thin-oxide gate ensuring fast commutation by limiting the gate-source capacitance.

The circuit presented in Figure 6.5(a) is in charge of controlling the switch of the anodic source. A symmetrical controls the cathodic source. Properties of the level shifter are summed up in Table 6.2.The transmission of the stimulation order is performed in a time that can be considered negligible compared to stimulation pulse duration (around $60\mu s$ for shortest duration). Moreover the static consumption is in the range of μA in low voltage, so that the driver is the most consuming circuit of the atom channel.

The current interface between the LV and HV supplied part is presented in Figure 6.5(b). It connects two sided mirrors, the first from the low voltage part and the second from the channel output stage of the figure 6.4. In the case of an anodic current, the first mirror, formed by transistors M_1 to M_4, is used. In the case of a cathodic current, this mirror is doubled and the whole current path implicates transistors M_{1-2} and M_{5-10}. All these mirrors have a theoretical current gain of 1. Moreover, to prevent from useless power consumption of this last path, the MS_1 transistor disables the two mirrors when no cathodic current is required.

These mirrors are cascoded with high voltage transistors MH_{1-2} to limit their drain voltage and ensure a safe HV interface. These two transistors are driven by the LV switching signals.

	static current consumption (μA)	commutation time (ns)
level shifter	8.3	≈ 410
current interface	1.6	≈ 230

Table 6.2 – *Main characteristics of the digital and analog level shifters obtained by circuit simulation before fabrication*

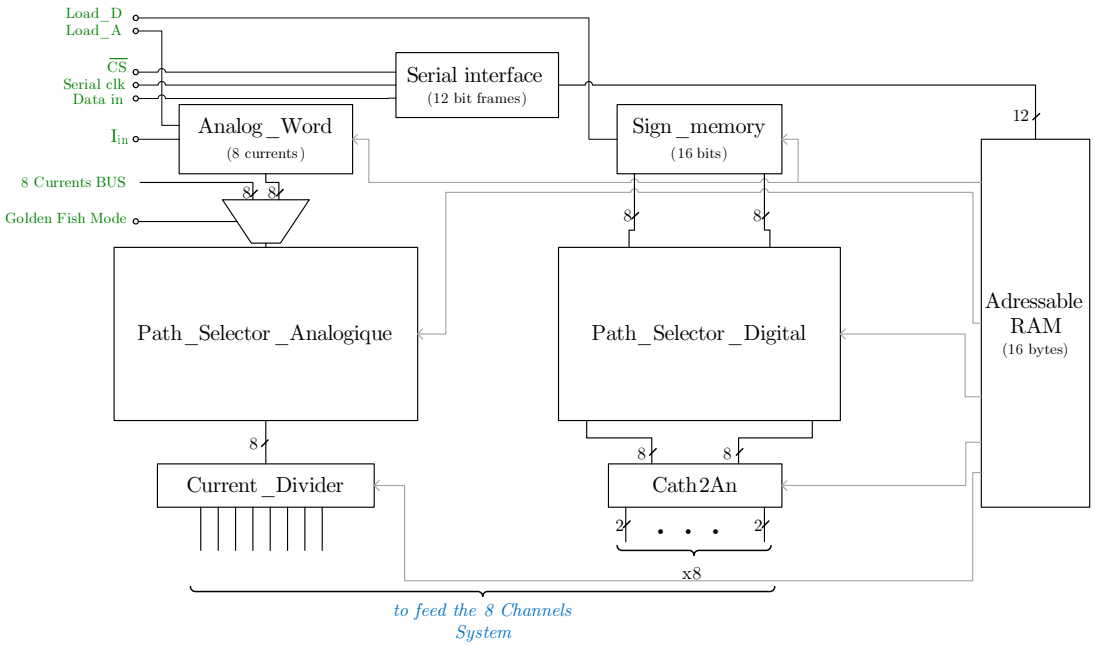

Figure 6.6 – *low power circuits in charge of stimuli generation and shaping, including both analog and digital circuits*

However, according to the simulations performed, drain-source voltages from M_3 and $M10$ can reach unsafe values when no stimulation current is required (low logic levels on both commutation orders). Therefore, a small bias current I_{bias} is consumed by all branches to control all drain potentials. In order not to modify the anodic or cathodic values, the biasing path is controlled by transistors MS_{2-3}. The main features of this current interface circuit are summed up in table 6.2. The current transmission is performed in a smaller delay than the commutation order so that the half bridge current edges are ensured with biased current sources.

6.2.2 Stimulus shaping circuits

Eight stimulation channels are implemented in one chip; on the same die, low voltage circuits that allow control are included. The global architecture of these stimulus shaping circuit is presented in figure 6.6. It can be subdivided in three parts:

- **A serial interface and a digital memory:** these circuits allow external parameters reception and storage, the RAM memory is directly connected to the further described circuit configuration inputs. This block allows both static configuration of the system and commutation commands reception.

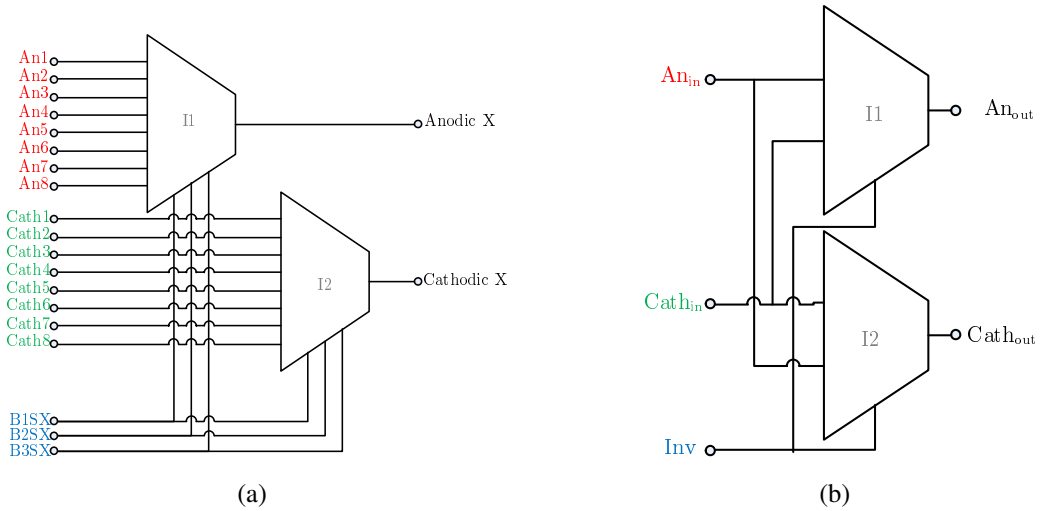

Figure 6.7 – *(b) Schematic of the digital path cell for one channel. (a) Schematic of the digital inversion cell for one channel*

- **Digital control circuits:** they process 8 virtual channels commutation input signals to a 8-channel bus, allowing for copying and sign inversion. The commands are stored in the *'sign_memory'* register and copied from the address 0 of the RAM block using the logic signal *'Load_D'*. This part is detailed in the next section.

- **Analog current shaping blocks:** these blocks allow for current combination and weighting. This last operation is simply based on an association of dividing current and is detailed in Appendix C. The designed ASIC, aimed at multiple application, allows two different input paths for the current. The first one is a 8 currents bus, and the second is based on a one-current input associated with current memory cells. This part is not detailed in this section and design details are given in Appendix C.

Digital configuration blocks

As the chip input is a serialized interface, atom-channels combinations have to be made internally and share rigorously the switching orders. These commands are stored in the first byte of the RAM as described in table 6.3. When a rising edge occurs, the current signs are stored in RS flip-flops from the *'sign_memory'*. This 16-bit memory has an external reset to prevent from any direct current flow at the start-up of the chip.

A digital path selector block allows for commutation order sharing. This block is based on eight similar structures, which basic cell is presented in Figure 6.7(a). Two multiplexers with the same command select the commutation source from the 8 input channels. All the configuration signals for the multiplexers are stored in the RAM between addresses 1 and 4, with 3 bits per channel. This circuit allows the ganging of channels but does not allow bipolar topology. For this purpose, a second circuit is required. Changing the sign of the current is simply done by exchanging the anodic and cathodic commands. The *'Inverter'* block is based on 8 cells as described in figure 6.7(b). The 8 commands of the multiplexers are stored on one byte at the RAM address 5. The combination of these both blocks allows for ganging and bipolar topologies. Moreover the combination for current steering is possible with current weighting.

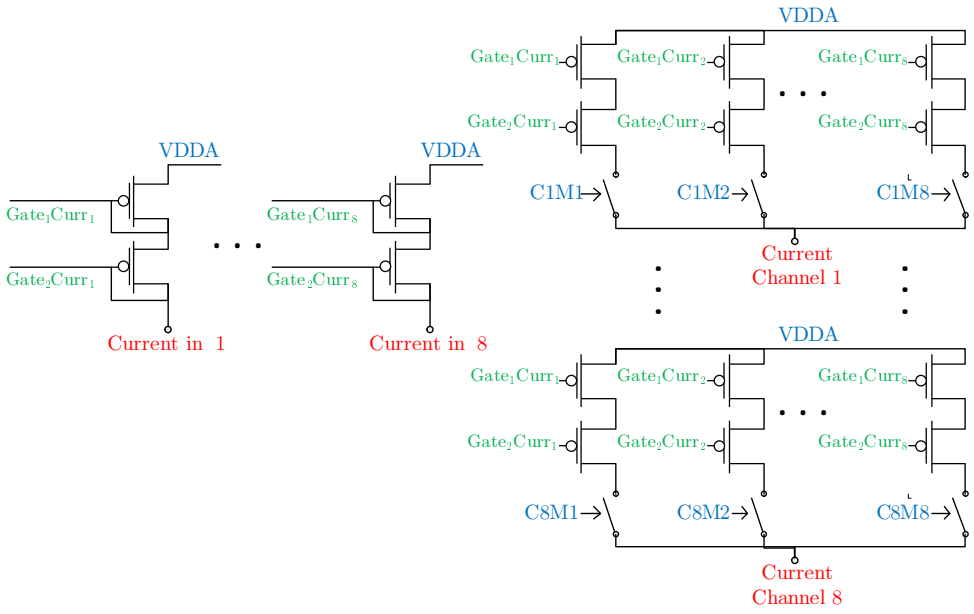

Figure 6.8 – *Schematic of the analog current path selector; this schematic corresponds to a matrix of current adders.*

Current combination

From the external 8-current bus or using the analog current memory cells, 8 currents specified for the 8 virtual inputs in the analog part. This input vector can be combined using a structure presented in figure 6.8. In this structure, inputs are realized by two MOS in diode forming the input stage of a cascode current mirror. The 8 outputs are realized by current addition as standard in current DAC topologies. This 8-bit DAC-like structure, comprises a 8-output current 64-current mirror matrix.

The ASIC uses switches based on a minimal transfer gate with charge injection compensation which use is not limited to static configurations. All digital commands $CXMX$ are connected to 8 bytes in the RAM, from the addresses 8 to F. This block is followed by the current weighting

@	group	LSB							MSB
0	General purpose	$\overline{CH0}$	$\overline{CH1}$	$\overline{CH2}$				An	Cath
1	Digital path	B1S1	B2S1	B3S1	B1S2	B2S2	B3S2		
2	selector	B1S3	B2S3	B3S3	B1S4	B2S4	B3S4		
3		B1S5	B2S5	B3S5	B1S6	B2S6	B3S6		
4		B1S7	B2S7	B3S7	B1S8	B2S8	B3S8		
5	Inverters	Inv1	Inv2	Inv3	Inv4	Inv5	Inv6	Inv7	Inv8
6	Current	C1B0	C1B1	C2B0	C2B1	C3B0	C3B1	C4B0	C4B1
7	Dividers	C5B0	C5B1	C6B0	C6B1	C7B0	C7B1	C8B0	C8B1
8	Analog path	C1M1	C1M2	C1M3	C1M4	C1M5	C1M6	C1M7	C1M8
9	Selector	C2M1	C2M2	C2M3	C2M4	C2M5	C2M6	C2M7	C2M8
A		C3M1	C3M2	C3M3	C3M4	C3M5	C3M6	C3M7	C3M8
B		C4M1	C4M2	C4M3	C4M4	C4M5	C4M6	C4M7	C4M8
C		C5M1	C5M2	C5M3	C5M4	C5M5	C5M6	C5M7	C5M8
D		C6M1	C6M2	C6M3	C6M4	C6M5	C6M6	C6M7	C6M8
E		C7M1	C7M2	C7M3	C7M4	C7M5	C7M6	C7M7	C7M8
F		C8M1	C8M2	C8M3	C8M4	C8M5	C8M6	C8M7	C8M8

Table 6.3 – *Memory mapping of the digital register controlling stimulus shaping*

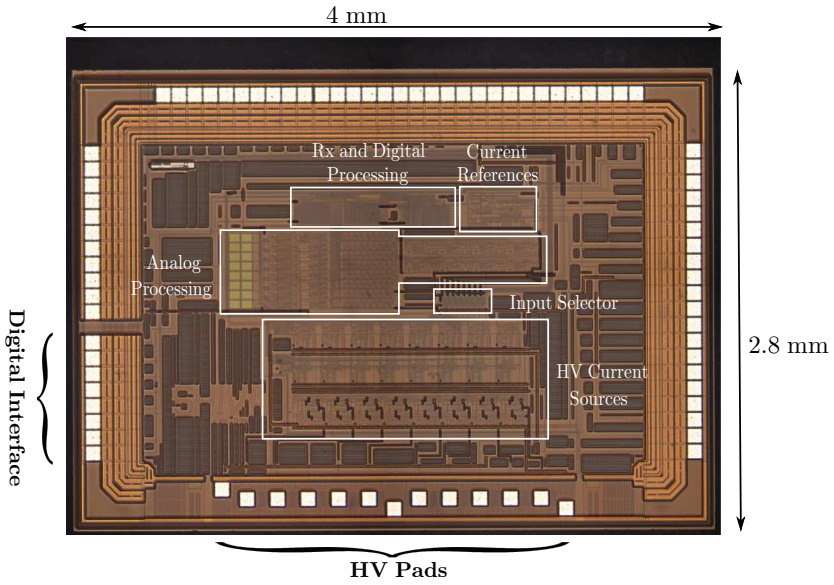

Figure 6.9 – *Micro-photography of the fabricated ASIC SHIVA.*

block that permits to reach weights of 1, $^3/_4$, $^1/_2$ and $^1/_4$, and driven by 2 bytes for the 8 channels at the RAM addresses 6 and 7. The use of these two blocks allows for 8 bits current generation and weighting.

All currents can be tuned separately and independently from the commutation commands; thus the 4 announced configurations of atom-channels can be defined by the digital circuits and the current weighting circuits; related stimulation can then be performed by applying to the chip inputs serial frames for current tuning per electrode and switching controls per electrode.

The global mapping of the embedded memory is shown in table 6.3. All these parameters allow to write the output 8-current vector versus the input 8-current vector as:

$$[I_{out}] = \begin{pmatrix} \frac{4\cdot(-1)^{Inv1}}{1+(C1B1\ C1B0)_2} & 0 & \cdots & & 0 \\ 0 & & & & \\ \vdots & & \ddots & \ddots & \vdots \\ & & & & 0 \\ 0 & & \cdots & 0 & \frac{4\cdot(-1)^{Inv8}}{1+(C8B1\ C8B0)_2} \end{pmatrix} \begin{pmatrix} C_1M1 & \cdots & C_1M8 \\ \vdots & \ddots & \vdots \\ C_8M1 & \cdots & C_8M8 \end{pmatrix} [I_{in}] \tag{6.18}$$

From this equation, different configurations of the chip can be considered:

- as a 8 channels DAC, using an input current vector provided by current references weighted as powers of 2, or by loading and refreshing these values in the analog current memories. This configuration is the most useful and permits to have 1 to 8 8-bits DAC with a tunable output range, selecting the correct values for the current references.
- with a combination of N channels ($N \neq 0$), as an equivalent DAC is obtained with an effective number of bits M:
$$M = 8 + \log_2(N) \tag{6.19}$$
- as an array that permits pattern combination for complex wave-shape stimuli, with transient current inputs for dynamic stimulation experiments.

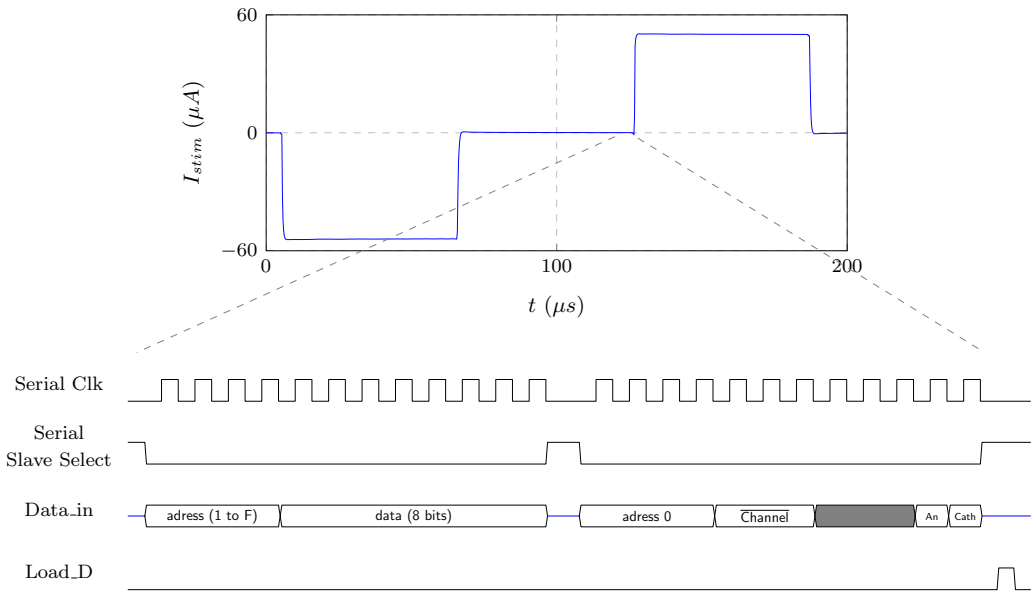

Figure 6.10 – *Measured current output from an atom channel of the ASIC SHIVA, with pulses of* $60\mu s$ *and anodic and cathodic current of* $50\mu A$*. Lower chronograms show the associated control signals.*

6.2.3 SHIVA: Stimulator with High-voltage compliance for Various Applications

The ASIC was fabricated in AMS $0.35\mu m$ HV technology. The chip photograph is shown in Figure 6.9. The size of the die is $11.2mm^2$ ($4mm \times 2.8mm$), and is pad-limited; the stimulation core is about $3.255mm^2$ ($\approx 2.1mm \times 1.55mm$). The chip includes circuits described in the previous section and two additional parts.

The first is an input selector block that enables direct driving of the eight atom-channels and skip the low-voltage processing, which is particularly helpful for test and characterisation. The second is a block of current references. It includes one voltage-independent temperature-independent current reference that is weighted to produce 8 current references for the DAC configuration plus a ninth biasing reference. This block is described in Appendix C. This block was tested as functional, and the current value for the biasing of the circuit is satisfying; however, the 8 weighted references present a difference between simulation and measurement, so that the resulting DAC is not sufficient to provide the $250\mu A$ maximal current output per atom-channel that fit the requirements for the target applications. As the use of these internal current sources is not mandatory for the stimulation (it can be replaced by external references), this failure did not penalize the ASIC.

6.3 System integration

The designed ASIC requires additional circuitry to be used on application projects as presented in chapter 1. For this purpose a full system that can be adapted to the various experiments has been designed. As one ASIC can provide up to 8 atom channels, the 32 atom-channels system has to include 4 chips and provide with correct timings the orders for multi-channel stimulation without any risk of charge unbalance.

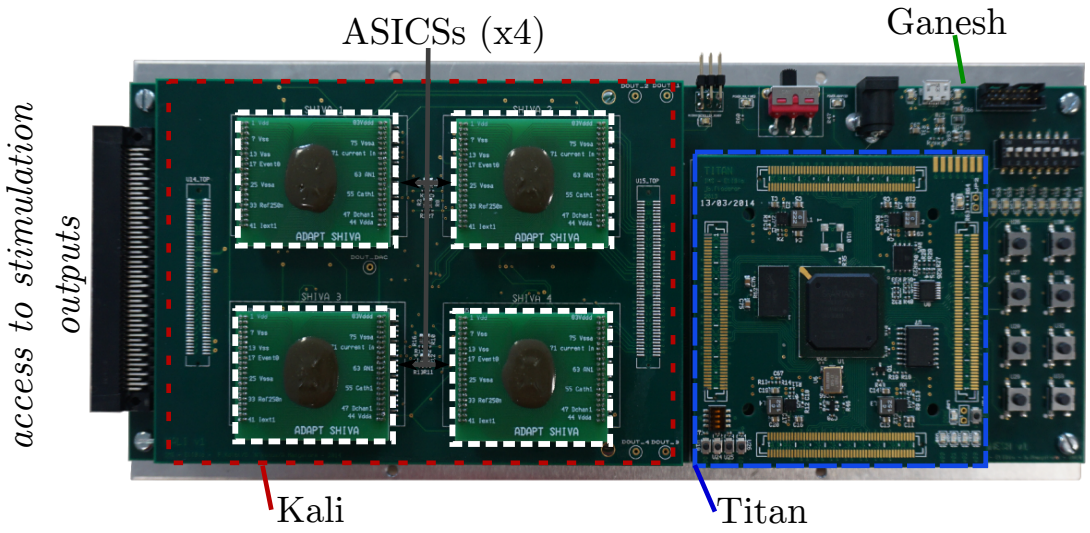

Figure 6.11 – *Photography of the fabricated 1 to 32-channels stimulation system supporting 4 SHIVA ASIC.*

6.3.1 Hardware level: KALI and GANESH boards

The driving sequence for one channel is illustrated in Figure 6.10. This diagram shows a test measurement of a symmetric biphasic current waveform generated by one channel. Each current transition is requested by sending an order in a 12-bit frame at the address 0 of the chip; this commutation can be either for cathodic, anodic or a null current. If the current value has to be changed from it previous value, this is performed by sending a 12-bit frame to the addresses 8 to F with the corresponding digitized current value. All communications with the ASICs are based on a serial interface (clock, a data in with 2 bits of address and 8 bits of value, a chip select), and one additional signal (*Load_ D*) which validates the request. The integration of a 32-channel system implies to generate the frames for all channels corresponding to the parameters imposed by physiologists.

The hardware used for this application has been separated in three levels, each level corresponding to one board. The assembly of these boards plus the ASICs can be viewed on Figure 6.11 and is divided in:

- *GANESH (Generic Access on Neural Electrical Stimulation for Hybridation):* this board is the stimulation mother-board. It contains the basic circuits for power supply generation (LV and HV levels). Symmetrical $\pm 20V$ and $\pm 16.7V$ are generated using two boost circuits for the positive voltages, and inverting converters for the negative voltages. An additional micro-controller with analog switches provides a soft-start supply ramp at the start-up; it prevents from current inrush on ASICs due to the large zones of secondary bulk biasing. This board also supports the connectors for the daughter-boards and a generic connection to stimulation electrode via 32 DC blocking capacitors, as this component can be integrated regardless of the output configuration.

- *Titan*: this board contains the FPGA driving the stimulation. It was developed for other projects (Nguyen et al., 2013), and uses a *Xilinx Spartan 6* FPGA with generic digital input/outputs.

- *KALI (Kali Allows in-Line Implementation)*: this board is the only chip-specific one. It

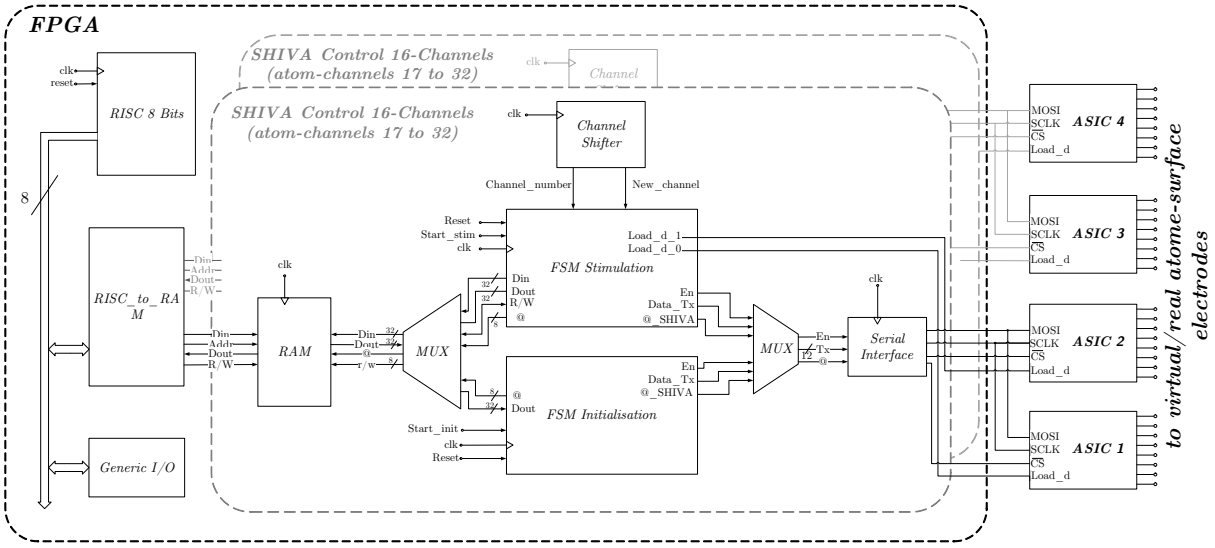

Figure 6.12 – *Structure of the digital architecture for the control of 4 ASICs to stimulate up to 32 atom-channels.*

contains discrete analog components and supports the 4 ASICs. This board includes weighted current references, external current DACs and switches enabling the different configurations of the ASICs. It also integrates additional analog switches for passive charge balancing in case of circuit failure.

As the stimulation should be used in different contexts, and more specifically in configuration for hybrid closed-loop, the stimulation system is designed as a peripheral device for a soft-core RISC architecture commonly used on FPGA. This development is explained in the next section.

6.3.2 Soft-core level and preliminary results

Controlling the SHIVA chips is similar to a memory access. A first initialisation of the memory, shown in table 6.3, is performed at the start-up, then stimuli are shaped with frames as described with Figure 6.10. One biphasic channel stimulus is based on a succession of 4 current edges, two of them require to program a current value in the general case. An immediate solution would be to include 32 possibly used Finite State Machines (FSM), with cathodic, anodic and idle states, which timer and current values come from the used RISC architecture; nevertheless this full-parallel approach is not suitable with FPGA resources and has also for major drawback possible conflict of some channels on the shared communication bus. We optimize the control circuit by the compromise we describe now.

In order to reach the specification imposed by the projects, a 1 to 16-channel architecture with a reduced number of FSM have been developed. This architecture is doubled as described in Figure 6.12 to reach 32 channels. In this figure, the RISC core is communicating to the 1-to-16-channels architecture via an interface block directly connected to the data bus. The designed architecture contains two FSM, sharing the input access to the RAM and the Serial Interface block as an output connected to two ASICs via two multiplexors. Consequently, ASICs are associated two by two on the KALI board, and two Serial Interface blocks are implemented in the FPGA (see Figure 6.12).

The first FSM of the 1-to-16-channels architecture controls the initialisation of the RAM at

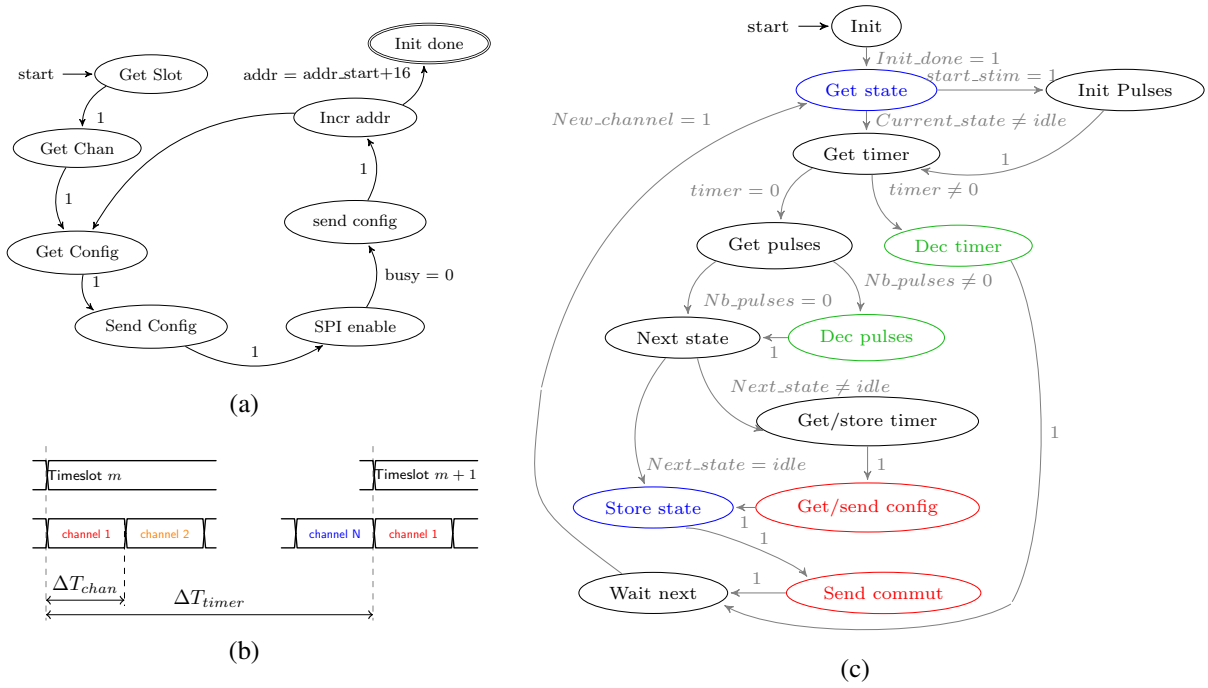

Figure 6.13 – *(a) Initialization FSM for 2 ASICs. (b) Time diagram of a timeslot; this timeslot is divided in up to 16 sections, on each section the FSM controlling the waveform for one channel is applied. (c) FSM controlling one channel, this machine load the parameters and the state of a specific channel, decrement the used timers and if required sends the programming commands to the ASICs.*

the powering-up. This FSM, illustrated by Figure 6.13(a), consists in a loop sending data at the 16 addresses of the ASIC's RAM for a given configuration. First, based on the memory address, a timeslot value is charged for the next FSM, then a loop is in charge of programming all the addresses ('Send Config' for ASIC number selection, 'SPI enable' and 'send config') of one chip by copying the RAM data ('Get Config').

The second FSM (stimulation FSM) is in charge of sending the correct current values and to the effective stimulation channels. This FSM is driven by an additional block called the *Channel Shifter*. To avoid the parallelization of one FSM per channel, all channels are pipelined and a generic FSM is used. In this situation channels are driven using a time multiplexing. This operation is illustrated by Figure 6.13(b). With this strategy a timeslot is defined and divided by the number of effective channels. With the notations of Figure 6.13(b), one channel is processed, during a timing of ΔT_{chan}, during which the timers are decremented and the needed frame are sent. One channel is processed every ΔT_{timer}, corresponding to the time period of the timer. If N is the number of effective stimulating channels:

$$\Delta T_{timer} = N \cdot \Delta T_{chan} \tag{6.20}$$

where the minimum of ΔT_{chan} is set by the necessary time to send two successive 12-bit frames with the serial interface and validate the requests, which is performed over 26 periods of the

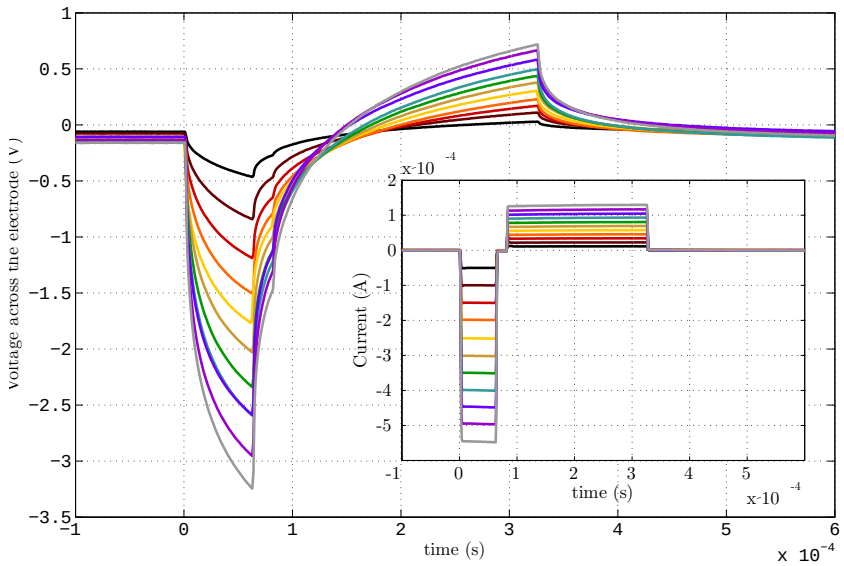

Figure 6.14 – *Voltage response and corresponding current stimuli obtained by stimulating a micro-electrode with an atom-channel*

serial interface clock. The communication with the ASICs was successfully tested at $50MHz$ on the multi-application boards, so that in the worst case of 16 effective channels:

$$\Delta T_{timer} = 16 \cdot \frac{1}{50MHz} \cdot 26 = 8.32\mu s \tag{6.21}$$

This result gives a timer period under the minimal pulse duration (several decades of micro-seconds) in any case. As the 16-channel architecture is parallelized to obtained 32 channels, the communication with the 32 atom channels is also performed in $8.32\mu s$ in the worst case.

The stimulation FSM is presented in Figure 6.13(c). This FSM controls the frame data sent per channel during a timeslot. On Figure 6.13(c), the blue states indicate if the system is changing the number of channel; in this case, the system needs to get all stimulus waveform parameters and the current state of the channel from the memory ('Get State') or store this state ('Store state'). The green states correspond to operations of decrementing the timers used to control the time to the next current edge ('Dec timer') or the amount of pulses to go before stopping the train of pulses ('Dec pulses'). The red states control the SPI circuits to send commands to the ASICs. These commands can be either a current configuration (Get/send config) to be stored in the addresses 8 to F of the ASICs RAM, or an edge - to begin/stop the stimulation, the anodic stimulation or cathodic stimulation - ('Send commut').

The digital design was described in *vhdl* and implemented in the *Spartan 6* of the *Titan* board. The synthesis report for this component shows that the designed block can be clocked up to $180MHz$, significantly more than the $100MHz$ crystal of *Titan*. The digital system is using four 8-bit block RAMs, 372 Slices over 23038 ($\approx 1.64\%$), 1035 Slices Register over 184304 ($\approx 0.56\%$) and 1062 Look Up Tables over 92152 ($\approx 1.15\%$). As the system is synchronous no latches has been implemented during the synthesis. The 32-channel system design requires only a small part of the Spartan 6 resources, so that more complex block for automatized control the stimulation parameters in the case of closed-loop development can be supported by the Spartan 6. This will be the case on the projects *HYRENE*, *BRAINBOW* and *CENAVEX*.

As the hardware for the final system is currently under test (the assembly of GANESH and

KALI), a stimulation experiment was performed using the test-board of SHIVA with a *Xilinx Spartan 3 testing* board. These tests validate the system specification and architecture and led to stimulation verification by recording the current/voltage curves for realistic stimulation patterns.

Preliminary results are shown in Figure 6.14. It plots the recordings of the electrode voltage induced by biphasic current shapes generated by one atom-channel of SHIVA. In that experiment, SHIVA is driven by the digital core presented earlier. The channel was connected to a micro-electrode (Cottance et al., 2013) used in the *HYRENE* project, which corresponds to the smallest electrode of our specification. In order to obtain realistic responses, the electrode was implanted on a cortical zone of an *ex-vivo* pig brain. The timing were chosen as short as specified in the literature to observe a worst case of stimulation; consequently, results of Figure 6.14 are obtained with a cathodic timing of $60\mu s$ and an inter-pulse delay of $20\mu s$. The ratio between the cathodic and anodic currents is of four to one with a balanced waveform. The current is successfully generated with the ASIC; rising times on current curves are negligible and no peak or variation of current can be observed.

6.4 Partial conclusion

This chapter presents a global approach to stimulation circuit design. This approach is based on a simplification of the impedance model for a first approximation reasoning, corresponding to a mathematical worst case. A strategy relying on atom-stimulation channels was devised, based on this model and considering a scale effect on the stimulation current and electrode surface area. A proof-of concept ASIC containing 8 atom-channels was designed and a stimulation system with up to 32 channels was developed. Preliminary results validated the functionality of the proof-of-concept chip and the architecture for digital control of the 32 channels was successfully implemented on an FPGA with reduced resources. The multi-application system will be used and validated in the four experimental contexts described in chapter 1.

CHAPTER 7

TOWARDS A FIGURE OF MERIT FOR CURRENT STIMULATION

FOLLOWING the work presented in the previous chapters, two specific stimulation systems were produced in part II. A global approach led to the fabrication of a multi-application proof-of-concept ASIC and experimental boards. That study raised a novel issues concerning the quantification of optimization, as follows:

- under the assumption of the scale effect described in chapter 6, the fabricated ASIC was suited to multiple contexts, but was not, by definition, optimally sized for a given application. How far from optimum for a specific application was the global solution? What quantities are involved in evaluating optimization?

- two different optimizations were presented in chapters 3 and 4 of part II. The power optimization for the Deep Brain Stimulator (see chapter 3) was based on drastic topological simplification and dynamic power management to minimize consumption. On the contrary, the charge-metering approach described in chapter 4 required additional circuits, improving tissue safety, but increasing overall consumption. Are both optimizations orthogonal? If not, what is the reasonable loss that can be tolerated for each criterion to achieve a certain degree of optimization?

- under the assumption of the scale effect, is the ASIC atom-channel as well-suited and-or optimized as the combination of N atom-channels on an N-scaled electrode? If not, what is the loss and is it inherent to the global approach?

Answering all these questions requires a quantified optimization criterion for un-biased evaluation of stimulator designs. There is currently a lack of a global, unified performance metrics for quantifying the actual degree of optimization: stimulation circuits and systems are currently ranked using variable criteria, as presented in chapter 2.

As presented in Figure 2.4, biomedical systems are subdivided into blocks, including stimulation. The electrical design of other blocks, such as bio-signal amplification (Steyaert and Sansen, 1987) and, more recently, wireless-power-transmission circuits (Kiani and Ghovanloo, 2013), may be evaluated by specific Figures Of Merit (*FOMs*). The example of bio-signal amplification is particularly interesting: the Noise Efficiency Factor (*NEF*) was introduced in Steyaert and Sansen (1987) to assess the performance of a neural signal pre-amplifier by normalizing the input referred noise to an equivalent BJT transistor, biased with the amplifier consumption current. The relevance of this criterion was noted by Harrison and Charles (2003) over 10 years ago. It provides quantified information about the balance between the noise figure and power consumption. This useful tool has led to successive improvements in existing techniques and design rules, as reported recently in Wang et al. (2014). This criterion was also recently modified to evaluate impact on recording systems - in contrast to circuits Han et al. (2013), thus proving the sustained interest of designers for quantified FOM dedicated to bio-electronic interfaces.

This chapter presents a stimulation-dedicated FOM, addressing both tissue safety and power optimization issues, as these design constraints are preponderant in the literature. Trends in optimizing charge balancing for safe stimulation were presented in chapter 4. The next section presents a parallel in terms of power optimization, featuring recent solutions for front-end evolution, related to an emergent efficiency factor in the literature. This factor is analysed and used in the second section, together with a balancing criterion, to propose a unique stimulation-dedicated FOM. This work was performed in collaboration with the Sensors Systems and Circuits research group at *University College London* (UK). The third section re-evaluates the global multi-application approach in light of this new FOM.

7.1 Current trends in power optimization

The front end power optimization is limited by electrode impedance. For a given electrode, as explained in chapter 2, the stimulation circuit is supplied with a high voltage generated by a DC/DC converter. Most stimulators use a fixed level for that voltage considering the worst case stimulus and a security margin to comply with impedance increase after implantation. Recent advances have been performed to adapt the generated supply to minimize consumption. Solutions can be divided in two groups: first the adaptation of the power supply level on the stimulation period and, second, dynamic evolution of the supply level with smaller time constants than the stimulation period.

7.1.1 Adaptive power supply

As the power supply is usually sized for the worst case stimulation (maximal current for maximal loading), it is in most cases over-estimated. This leads to superfluous energy loss during stimulation. This unused power is associated to high voltage generation, as well as decreasing over higher output levels of DC/DC converters efficiency, dramatically increasing the overall consumption on the primary power energy source. An immediate solution is to adapt the effective voltage supply to the effective load using additional circuits.

A representative example of this technique is performed in Lee et al. (2013). As it can be seen on Figure 7.1(a), an additional circuit (*V-detect*) is in charge of absolute maximal voltage detection on the stimulated load (V_{REC}). This circuit supplies a feedback loop controlling the power converter. The originality of this device is to combine the rectification circuit inherent to the wireless power transmission and the DC/DC converter. It results in the direct generation of V_{REC} and is a way to improve the efficiency of the power converter. The corresponding stimulation front-end topology is presented in Figure 7.1(b). This schematic is a classical two-source two-switch topology: two symmetric blocks (gray squared) of paired transistors are forming 5-bits DACs. These current sources are connected to the electrode with $P21$ and $N22$, used as switched cascoded devices for the anodic and cathodic phases.

The main drawback of this technique is that, if the electrode impedance increases, the detection of the maximal voltage is performed when current sources are almost pinched. In Lee et al. (2013), additional active charge balancing is performed, suggesting that this method has a direct impact on charge balancing performance; however, this phenomenon is not quantified. Moreover, since the load is capacitive in first approximation and the voltage during a current pulse is not constant, this technique only limits the energy loss and further optimization can be performed.

7.1.2 Dynamic power supply

Considering this last assumption, it can be observed that power loss is higher at the beginning of the stimulation pulse than before the anodic or cathodic falling edge if the power supply is constant. This principle is explained in Williams and Constandinou (2013) and illustrated in Figure 7.1(c). This figure shows a typical stimulation waveform (c.a), the voltage on an electrode resulting from the RC model (c.b), the corresponding power (c.c) and the loss (in gray) with a minimal constant power supply. Authors suggest to limit this power by dynamically changing the power supply during the stimulation pulse as illustrated in (c.d).

This technique was historically introduced in Kelly and Wyatt (2011), however, performed by directly applying voltage steps on a RC-modelled load. This solution leads to uncontrolled

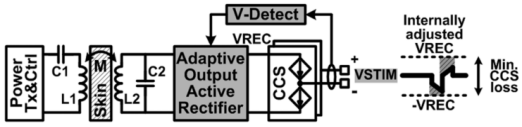

(a)

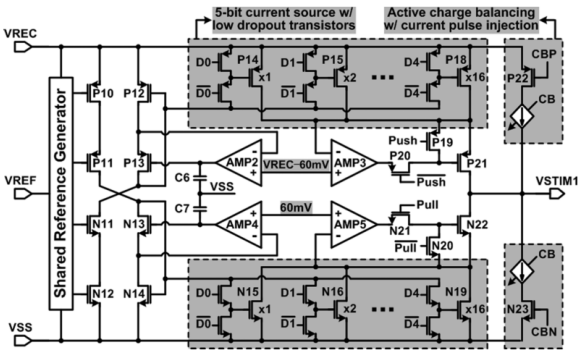

(b)

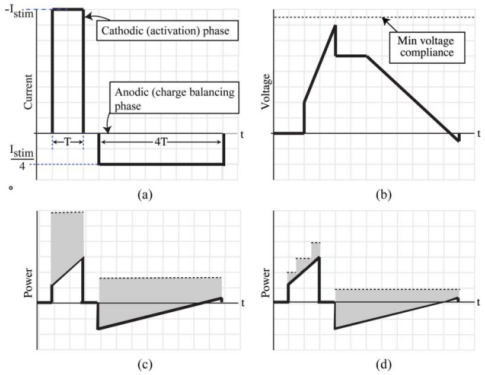

(c)

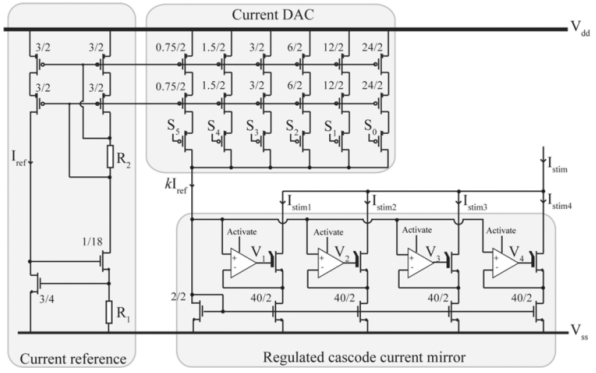

(d)

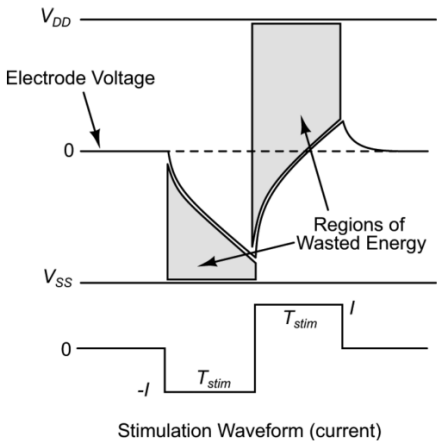

(e)

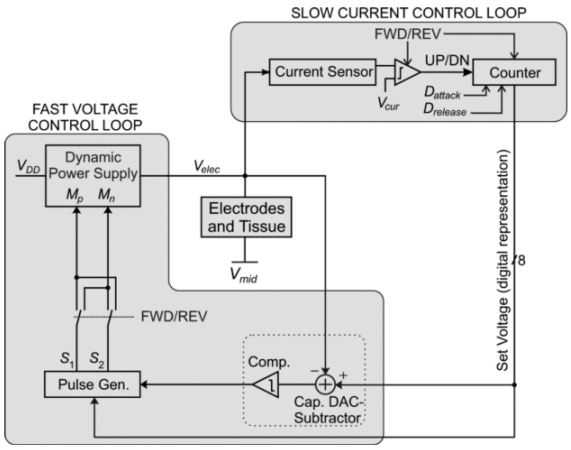

(f)

Figure 7.1 – *Review of most competitive topologies for front-end power consumption:(a) and (b) from Lee et al. (2013) illustrating the adaptive power supply strategy; (c) and (d) from Williams and Constandinou (2013) with dynamic power supply based on voltage steps; (e) and (f) from Arfin and Sarpeshkar (2012) with continuous power supply variations.*

stimulation waveform and the accurate charge balancing is not addressed or even possible. In Williams and Constandinou (2013), the DC/DC converter is controlled using fixed steps of voltage. For this design, the front-end topology is presented in Figure 7.1(d), where the H-bridge is not represented; a current source is driven by a DAC and the stimulus is clearly current controlled. The authors quantify a reduced unbalanced charge ($\leq 0.5\%$). However, the energy loss on the front-end is non null and especially in low current the optimization is limited.

As a parallel to Figure 7.1(c), Figure 7.1(e) from Arfin and Sarpeshkar (2012) illustrates the power loss on a realistic voltage waveform. The principle of the front-end presented by Arfin et al. (2009) is illustrated by Figure 7.1(f). This architecture is based on the direct application of the endlessly changed power supply. A closed loop is controlling the DC/DC converter; however, one can object that the current control is indirect, as the current sensor is not in series with the load. Therefore the control loop is based on the knowledge of the exact load impedance, which is clearly over-simplified considering the physics of involved phenomena as described in chapter 5. Moreover, this circuit is based on a step down converter, limiting the effective compliance of the stimulator to only low voltage levels ($\leq 3V$).

This last attempt of optimization led Arfin and Sarpeshkar (2012) to express the minimal energy as a quantity correlated with electrode impedance. This assumption limits the ability to compare devices, as electrodes are often specific to the application. However, they propose to normalize the consumed energy on a stimulation period by the energy spent by a constant current source supplied by a constant voltage energy on the same load. As it will be shown further in the text, this last quantity is electrode invariant and seems a promising normalization quantity for a consistent FOM.

7.2 Construction of a stimulation dedicated Figure Of Merit

7.2.1 Functional comparison between DACs and stimulators

The most suitable circuits to be compared with stimulation circuits and systems are Digital-to-Analog converters. The parallel is illustrated by Figure 7.2.

The DAC is a structure taking digits for input and generating an analog value; it is characterized by:

- its power consumption or energy on a clock period; this power P on Figure 7.2(a) is related to the internal structure and is independent of the load, as this load can be considered as ideal (quasi-infinite load for voltage DAC, quasi-null load for a current DAC).

- its Effective Number of Bits (ENOB); this quantity expresses the noise performances of the DAC, taking into account digital value encoding. The Signal to Noise Ratio (SNR) is expressed by:

$$SNR = 20 \log \left(\frac{v_{\text{signal, RMS}}}{v_{\text{noise, RMS}}} \right) \tag{7.1}$$

  where the noise and signal root mean square values are obtained considering respectively the quantization noise and a ENOB-bit peak-to-peak sinusoidal signal:

$$\begin{cases} v_{\text{noise, RMS}} = \sqrt{\int_{-\frac{1}{2}}^{\frac{1}{2}} \varepsilon^2 \cdot d\varepsilon} = \frac{1}{2\sqrt{3}} \\ v_{\text{signal, RMS}} = \dfrac{2^{ENOB-1}}{\sqrt{2}} \end{cases} \tag{7.2}$$

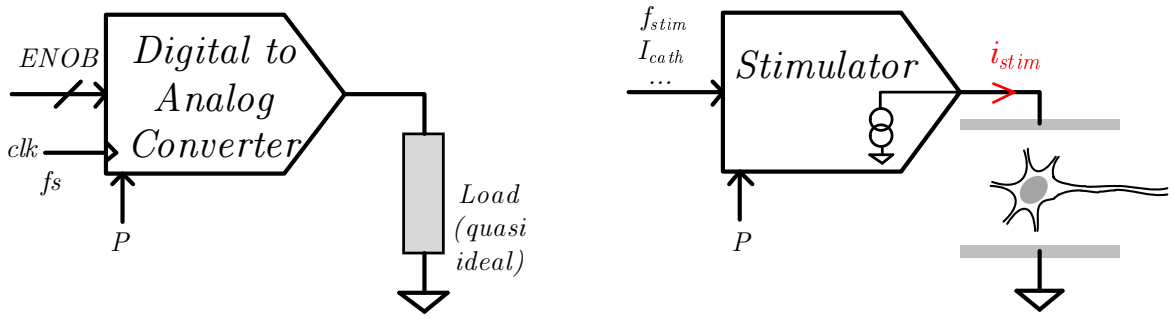

(a) (b)

Figure 7.2 – *(a) Symbolic representation of a DAC, clocked with f_{clk} and receiving data with the effective number of bits ($ENOB$). (b) Symbolic representation of a stimulator, receiving parameters and generating an electrical signal capable of neural triggering.*

By combination of equations 7.1 and 7.2, the effective number of bits of the converter as a function of the measured SNR - illustrating its effective dynamic - is expressed by:

$$ENOB = \frac{SNR - 10\log\left(\frac{3}{2}\right)}{20\log(2)} \approx \frac{SNR - 1.67}{6.02} \tag{7.3}$$

As a comparison, the stimulator can be considered as a block converting parameters related to the physiological need of the target cells (cathodic current, cathodic pulse duration, stimulation frequency and charge-balancing parameters) into an analog waveform. It is characterized by:

- its power consumption or the energy over a stimulation period. This energy is directly correlated to the stimulation load impedance which is by definition non-ideal; however, a load-independent normalization is possible according to Arfin and Sarpeshkar (2012).
- its charge imbalance resulting in an un-wanted leakage current.

For both DACs and stimulators, the designer choice is impacting one or the other, or even both, characteristics (power and ENOB for DACs, power and equivalent leakage current for stimulators).

7.2.2 DAC dedicated FOM

The comparison with a DAC is particularly interesting since this structure benefits from an established FOM as expressed in Walden (1994) and further developed in Walden (1999), given by:

$$FOM_{DAC} = \frac{P}{2^{ENOB} \times f_{clk}} \tag{7.4}$$

where f_{clk} is the sampling frequency. It is expressed in Joule per Least Significant effective Bit and represents the energy required per minimal effective code change.

This quantity cannot be directly computed for stimulation circuits and systems for two reasons:

- it is expressed with a energy unit, making no sense in the context of stimulation where the minimal energy is electrode dependent;
- the DAC's noise performances cannot be generalized to the stimulation pattern composed of succession of analog values.

These two issues will be addressed using a normalization of the energy and the re-definition of the charge imbalance as a parasitic noise source.

7.2.3 Stimulation dedicated FOM

Due to the non-ideality of the stimulation load, the energy will be normalized considering the approach adopted in Arfin and Sarpeshkar (2012). The minimal energy consumed on a stimulation period is given by:

$$E_{sim}|_{min} = \int_0^{T_{stim}} i\left(t\right) \mathcal{TF}^{-1}\left\{\widehat{z}_{elec}\left(f\right)\widehat{i}_{stim}\left(f\right)\right\} \cdot dt \tag{7.5}$$

where $\mathcal{TF}^{-1}$ denotes the invert Fourier Transform and $\widehat{z}_{elec}$ $\widehat{i}_{stim}$ are respectively the stimulation impedance model and the stimulation current in the frequency domain. By comparison, as it can be observed on Figure 7.3(a), once the supply voltage level is sized, a constant current source used with a fixed supply consumes the minimal energy defined by:

$$E_{CS} = \Delta V_{supply}\left(I_{cath}\Delta T_{cath} + I_{an}T_{an}\right) \tag{7.6}$$

This quantity is not directly dependent on the electrode impedance model. Moreover, as the signal is formed by charge-balanced current pulses:

$$I_{an} = I_{cath}\frac{T_{cath}}{T_{an}} \tag{7.7}$$

By substitution, the energy can be expressed as:

$$E_{CS} = 2\Delta V_{supply}I_{cath}T_{cath} \tag{7.8}$$

Consequently, this quantity is invariant to the balancing strategy. Finally, the consumed energy can be normalized, so that an Energy Efficiency compared to a Current Source can be computed as:

$$E_{ECS} = \frac{E_{stim}}{E_{CS}} = \frac{P_{stim}}{f_{stim}\cdot 2\Delta V_{supply}I_{cath}T_{cath}} \tag{7.9}$$

From Figure 7.3(a), it can be observed that E_{CS} is much higher than the minimal energy for a stimulation period. Consequently, the E_{ECS} can be lower than 1, meaning that the supply voltage is lower than the constant level corresponding to the minimum compliance. Strategies presented in section 7.1.2, could satisfy $E_{ECS} < 1$, if the quantity ΔV_{supply} is considered as the maximal compliance of the front-end.

Let us consider the charge unbalance risk. In the typical waveform as presented in Figure 7.3(b), only the cathodic part is responsible for cells triggering. This injected cathodic charge corresponds to:

$$Q_{cath} = I_{cath}T_{cath} \tag{7.10}$$

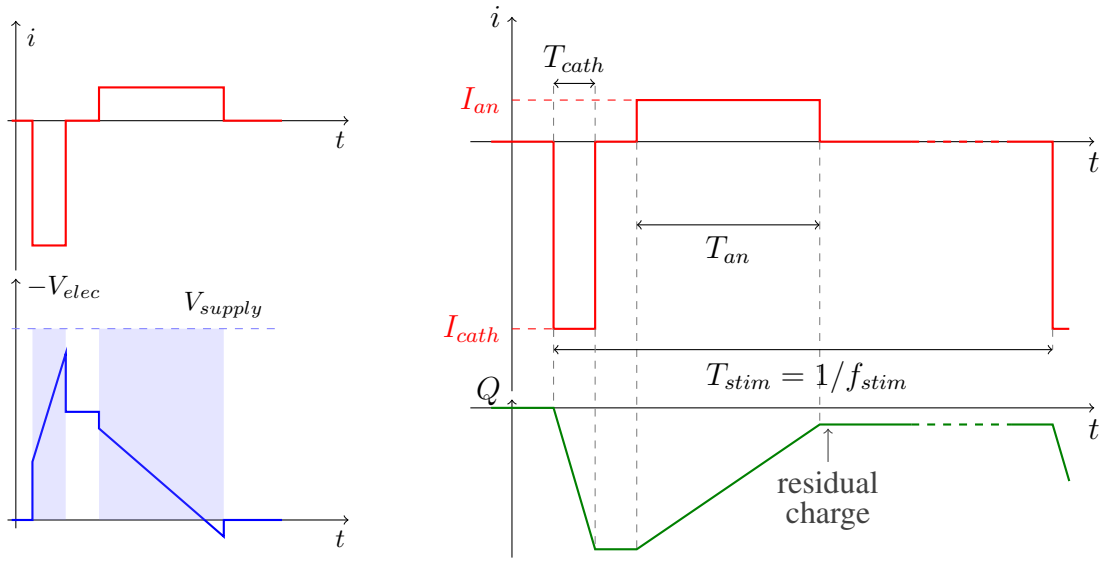

Figure 7.3 – *Illustrations of stimulation electrical quantities. (a) Balanced waveform and voltage over the RC-model load; the coloured voltage range is involved in the consumed energy over the stimulation period by a constant current source supplied with a constant voltage level; the area under the voltage response only is involved in the minimal energy imposed by the load. (b) Unbalanced current waveform with an arbitrary residual charge responsible for an equivalent leakage current.*

This charge has to be balanced to avoid electro-chemical reactions, however, the unbalanced residual charge shown in Figure 7.3(b) can be measured through:

$$Q_{residual} = \frac{I_{DC}}{f_{stim}} \tag{7.11}$$

where I_{DC} is the equivalent DC current as explained in chapter 4. By analogy to DACs, a stimulation dynamic range can be computed. Let the Stimulation Equivalent Number Of Bits be:

$$SENOB = \log_2\left(\frac{Q_{cath}}{Q_{residual}}\right) \tag{7.12}$$

This equation expresses the dynamic range between the effective triggering charge contained in the ideal waveform and a noise due to the front-end parasitics. As an illustration, if the waveform has no anodic phase, the $SENOB$ is 0, meaning that there is no difference between the stimulation triggering charge and the leakage.

Taking into account both E_{ECS} and $SENOB$ and considering a stimulation system with N channels, the stimulation specific FOM is defined as:

$$FOM_{stim} = \frac{E_{ECS}}{N2^{SENOB}} = \frac{P_{system}}{NE_{CS}2^{SENOB}f_{stim}} \tag{7.13}$$

where P_{system} is the measured average power of the stimulator. Which gives:

$$FOM_{stim} = \frac{I_{DC}P_{system}}{2N\Delta V_{supply}\left(I_{cath}T_{cath}f_{stim}\right)^2} \tag{7.14}$$

where ΔV_{supply} is the difference between the highest and lowest supply potentials in case of fixed supply stimulator, or the maximal compliance in case of dynamic evolution of the front-end supply. FOM computation has to be performed using maximal current values and typical timings for the biological application; the average power and equivalent DC current should be measured for these conditions. The obtained quantity is unit-less and can be measured as involved parameters can be observed and quantified.

7.2.4 Graphical representation

The ideal stimulator has a FOM_{stim} equal to 0. However, as this synthesizes two orthogonal design strategies, it is not bijective to electrical topologies; hence, two identical results can be obtained for two systems with different $SENOB$ and E_{ECS} and the same number of channels.

In order to highlight each aspect of performances, a two-dimensional representation can be drawn considering the logarithm of the FOM_{stim}:

$$\log\left(FOM_{stim}\right) = \log\left(\frac{P_{system}}{NE_{CS}f_{stim}}\right) - \log\left(2\right)\cdot SENOB \tag{7.15}$$

In the right side of the equation, the first term corresponds to the logarithm of the E_{ECS} per channel. As the $SENOB$ quantity can be extracted from equation 7.15, a semi-logarithmic diagram can be drawn. An illustration of this two-dimensional representation is presented in Figure 7.4(a). By choosing for the axes the FOM and the $SENOB$, overall performances and balancing can be directly considered; the x-axis corresponds to $SENOB = 0$, representing totally unbalanced systems (without any balancing phase). In addition to this view, iso-efficiency (iso-E_{ECS}) lines can be plotted enabling visual ranking.

Among the scientific contributions considered for the state-of-the-art of this document (chapters 2,4 and 7), only few papers give enough figures to compute the FOM. Results are summarized in table 7.1. At this level, one can note a difference between autonomous stimulation systems and stimulation front-ends which require additional circuits. As these circuits have a direct influence on the energy consumption, it seems fair to divide the graphical representation with 'front-end' and 'systems' categories, as performed in Figure 7.4(b).

Two groups of points can be observed in this diagram. The first with low FOM values has a high $SENOB$ (points 2,3 and 4) corresponding to devices explicitly optimized on the charge balancing performance (Sit and Sarpeshkar (2007), Jiang et al. (2010), Fang et al. (2007)). In this group the efficiency is highly variable and one point (#2 corresponding to Sit and Sarpeshkar (2007)) has an efficiency less than 1, however, the supply of the circuit is constant. This result is particularly surprising and is difficult to associate with explicitly published schematic. It could be explained by a lack of information on power measurement method (during or without stimulation).

The two other points (#1 and #5) are in a zone of higher FOM ($> 1\cdot 10^{-2}$). If the overall performances are relatively close to each other, there is a clear difference in terms of charge-balancing and power optimization. In Williams and Constandinou (2013) (#5), the major objective is to limit the overall power; the fully implanted system is only consuming twice the energy required for a constantly supplied constant current source. As a comparison, point 1 corresponding to our work (chapter 3) is less optimized in power consumption as the efficiency is more than 5 times higher; but it presents better charge balancing performances compared to the maximal injected charge.

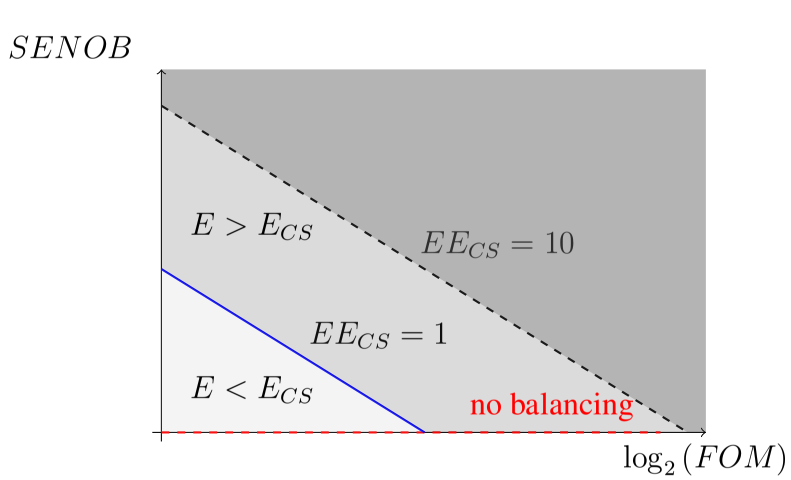

(a)

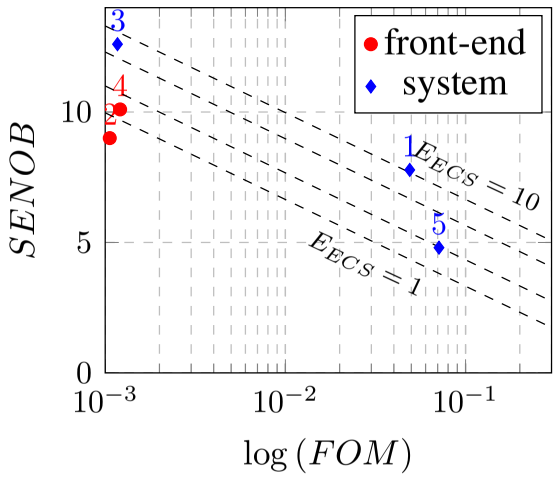

(b)

Figure 7.4 – *(a) Representation of the stimulation performances in two dimensions. (b) FOM computation resulting from the literature available characteristics, four iso-efficiency lines are plotted corresponding to 1, 2, 5 and 10 from bottom to top.*

		I_{cath} (μA)	I_{DC} (nA)	T_{cath} (μs)	f_{stim} Hz	ΔV_{supply} (V)	P_{system} μW	N	$SENOB$	E_{ECS}	FOM
1	this work (DBS chap. 3)	2036	72	60	130	17.4	6080	1	7.78	10.8	$49.9 \cdot 10^{-3}$
2	Sit and Sarpeshkar (2007)	1000	6	30	100	15	48	1	9	0.54	$1.06 \cdot 10^{-3}$
3	Jiang et al. (2010)	1020	4.5	50	526	18	6770	1	12.6	7.2	$1.17 \cdot 10^{-3}$
4	Fang et al. (2007)	600	5	93	100	3.3	50	1	10.1	1.3	$1.21 \cdot 10^{-3}$
5	Williams and Constandinou (2013)	504	18	100	10	11,5	185	8	4.8	1.98	$71.2 \cdot 10^{-3}$

Table 7.1 – *Some FOM computable references in the litterature*

From these simple comparisons it is clear that systems forming the state-of-the-art of a particular optimization strategy - point 3 (Jiang et al. (2010)) for charge balancing and point 5 (Williams and Constandinou (2013)) for the energy efficiency - are not optimized in the other criteria. The proposed FOM helps quantifying that discrepancy, and is a promising tool for global optimization. One of the emerging ideas in the research field is the combination of most performing structures for the emergence of a third group of points, in the range of FOM of only few $1 \cdot 10^{-4}$.

7.3 Multi-application design evaluation and perspectives

Although three types of stimulation systems have been presented in this document (the small stimulator for rodents, the FPAA-based stimulator, and the multi-application stimulator), only the small stimulator for rodents developed in chapter 3 is presented in Table 7.1 and Figure 7.4(b). This lack of results can be explained by two difficulties:

- For the FPAA based structure, charge balancing performances have been quantified, enabling the $SENOB$ computation; it results in a dynamic of 11.44 equivalent bits which is near the maximum of Figure 7.4(b). However, the consumed energy quantification over a stimulation period is not directly possible as this circuit was designed on a standard development FPAA board.
- For the multi-application ASIC, only tests and characterization results are available and final performances depends on each application.

As the obtained FOM enables direct ranking, one of the priority of multi-application stimulation system evaluation will be the quantification of figures required to compute this criterion.

However, some comments can be made. The global approach used for the SHIVA ASIC is based on a current subdivision or combination. Consequently, an atom channel has been designed to stimulate a corresponding atom electrode. An N-large-electrode is then stimulated using the combination of N atom-channel. The global approach will be fully satisfying if the scale effect is robust when evaluated by the FOM. For this evaluation, let the FOM_{stim} be a function; an invariance versus the scale effect would mean that the FOM of a N-channels system is equal to the FOM of 1 channel composed of N-ganged atom-channels:

$$FOM_{stim}\left(N\left\{\square\right\}\right) = FOM_{stim}\left(\left\{N\square\right\}\right) \tag{7.16}$$

As for the scale effect formulation, the hypothesis of constant timings and a N-scaled cathodic current is considered. From the theory, the invariance can be ensured by an infinite number of solutions satisfying the following equation:

$$I_{DC}|_{N\{\square\}}\ P_{system}|_{N\{\square\}} = N \cdot I_{DC}|_{\{\square\}}\ P_{system}|_{\{\square\}} \tag{7.17}$$

Thus, one obvious solution of the scale effect invariance to the FOM would be:

$$\begin{cases} P_{system}|_{N\{\square\}} = P_{system}|_{\{\square\}} \\ I_{DC}|_{N\{\square\}} = N \cdot I_{DC}|_{\{\square\}} \end{cases} \tag{7.18}$$

It corresponds to the invariance of the consumed power and the linearity of the charge balancing error.

The linearity conditions is difficult to assess from circuit theory; but it can be empirically investigated to examine the robustness to scale effects. The equation of the power seems *a priori* unreasonable as it imposes an over consumption for a unique N-scaled channel. However, the adopted strategy for multi-application system design is a digital pipelined organisation of the variable number of channels, which is one possible solution to satisfy the equality. If not satisfied by our ASIC and hosting board, these conditions can guide the design of second generation of multi-application circuits and systems.

The designs of chapter 3 and chapter 4 are clearly orthogonal considering this optimization criterion; their overall performances are to be compared using the FOM and their optimization degree can be quantified. This FOM is also a powerful tool to highlight high-performances designs that can be found in the literature. Finally the FOM can be used as a reference criterion for stimulator design. This mathematical expression and the minimization of this figure is not only a ranking tool but also a sizing criterion, which would be extremely helpful in automated sizing procedure.

Conclusion & Perspectives

THIS thesis summarizes three years of research into the electrical stimulation of neural cells, in the context of four multi-disciplinary projects: the '*Brainbow*'[1] project, the '*STN-Oscillation*'[2] project, the '*Hyrene*'[3] project and the '*Cenavex*'[4] project. In these four projects, electrical stimulation is only one part of a more complex paradigm, including biosignal acquisition for feedback control. This number of target pathologies - cognitive disorders, Parkinson's Disease, paraplegia and breathing disorders - and the multiplicity of target neural tissues to stimulate led us to investigate the a multi-application system design. In addition to this objective, we developed circuits and systems specific to certain applications. Finally, this overview highlighted the lack of a unique FOM for quantifying the performance of stimulation architectures.

Synthesis

Part 1: scientific context

The first chapter reviewed the basic principles of extra-cellular electrical stimulation, summarizing physiological and physical mechanisms. The second chapter described the state of the art in electrical stimulation materials and circuits. These chapters revealed the following:

- the electrical stimulation may be applied to neural cells in numerous tissues throughout the nervous system, thus enhancing the treatment of various pathologies and disabilities,
- the waveform used to trigger the neural cells presents a typical shape, common to the various applications, based on cell-triggering conditions and constraints, such as charge balancing for tissue safety. Current levels vary according to the application,
- a specific application imposes the current levels and type of electrode, chosen to suit the target tissue, and its impedance is a sizing factor for stimulators,
- only a limited number of state of the art front-end topologies are available for stimulators.

Part 2: specific systems design

Chapter 3 presented the design of an embedded stimulator for chronic Deep Brain stimulation in rats, which was then fabricated and assessed. This design offered an example of optimized power consumption. This stimulator is currently being used for further experiments on DBS mechanisms and side effects. Chapter 4 presented a novel architecture for accurate charge balancing, tested using FPAA circuits. The charge-balancing circuit was based on a capacitive charge-metering technique and is adaptable to all stimulation topologies with only few additional devices. This stimulator was used for *ex vivo* spinal cord stimulation experiments.

Part 3: multi-application stimulator design

As described in part 1, the differences between the specific applications mainly concerned the electrodes. Chapter 5 focused on the characterization and modelling of tissue-electrode impedance. The findings may be summarized as follows:

[1] European project FP7-ICT-2011-C
[2] French ANR 08-MNPS-036
[3] French ANR 2010-Blan-031601
[4] French ANR and American NSH AN13-NEIC-0001-01

- interface impedance depends on electro-chemical phenomena; physics suggests that the metal/tissue interface is fractional and non-linear;
- the fractional derivative may be approximated using a recursive series of first order cells; this approximation is compatible with classic ODE solvers, which produce accurate simulation electrode impedance models in an electrical design environment;
- a measurement bench and protocols were developed; measurement was based on charge-balanced waveforms compatible with *in vivo* stimulation;
- an original multi-model approach was devised, taking into account non-linearity and fractional behaviour;

Chapter 6 outlined the multi-application design strategy, summarized as follows:

- the first order RC-model of interface impedance is a worst-case model suitable for first approximation analysis and rapid sizing; the accurate model is suitable for the later verification phases in the design process;
- an architecture for a multi-application stimulator was proposed, on the basis of the RC-model approximation and a sizing effect; this architecture relies on atom-channels that may be combined to drive different electrode configurations; the robustness of this strategy was demonstrated considering front-end parasitics and the mandatory DC blocking capacitor;
- a proof-of-concept ASIC was designed and successfully tested; a stimulation system with 32 configurable channels was designed and is currently deployed in the ongoing projects;

The degree of optimization of a specific stimulator had not previously been quantified due to the lack of an established Figure Of Merit. Chapter 7 describes how this problem was solved. The similarities between DACs and stimulators were highlighted; as DACs may be ranked using a recognised FOM, the specifics of stimulation in terms of energy efficiency and charge-balancing optimization formed the basis for defining a performance metric. This metric was discussed in relation to the multi-application strategy and provides a tool to guide the design of a new generation of multi-application circuits.

Perspectives

The investigations and developments described in this PhD thesis open up three perspectives for future research:

- First, the deployment of the embedded system hosting the multi-application ASIC in experimental demonstrations in the context of the *HYRENE*, *BRAINBOW*, and *CENAVEX* projects. The high level of configurability of this device is ideal for that purpose and Jonathan Castelli will explore this aspect in his PhD thesis. The expected results relate to the field of experimental neuroscience and neuro-engineering, as the aim is to prove the relevance of adaptive closed-loop stimulation, with a view to developing neuro-prostheses. In the broader context of electrical stimulation, this highly-configurable system is also suited to other investigations, for example: generating less-conventional waveforms or controlling multi-pole electrodes for fine-field steering in tissue.

- Second, the FOM devised in the context of this research should lead to a complete formulation and eventually be supported by other characterizations. This is one of the objectives of a collaboration with A. Demosthenous. The FOM will also lead to guidelines for designing and optimizing other stimulation systems.

- Third, electrical characterization of the electrode-tissue interface can be taken a step further by studying the stimulator in its biological environment. Especially in the case of implanted devices, the major weakness is located at this bio-electric interface, as the implant induces inflammatory reactions, such as gliosis or fibrosis, which alter the properties of the tissue in contact with the electrode and, sometimes, the metal itself. This change is reflected in the interface impedance and its continuous *in situ* monitoring is an interesting approach for evaluating gliosis or fibrosis encapsulation over time. This may lead to smarter implants with auto-diagnostic capabilities, representing a major advance in the long-term safety of implanted electrical prostheses.

Finally, fourth perspective concerns the field of industrial transfer. The prototype DBS stimulator for rodents responds to widespread demand in research experiments on Parkinson disease. A licensing contract with an industrial partner is currently under negotiation.

APPENDIX A

EXAMPLES OF ELECTRODE GEOMETRY AND CORRESPONDING ELECTRIC POTENTIAL REPARTITION

ELECTRODES are sub-divided into two subgroups:

- micro-electrodes, corresponding to small areas; these electrodes are optimized to enable focal stimulation of small groups of cells. Usually the number of micro-electrodes is large (from 8 up to 64).
- macro-electrodes, corresponding to large areas stimulating large volumes of tissue. Usually a small number of stimulation channel are used with macro-electrodes.

For these two groups, particular geometries can be observed, corresponding to different electric potential repartition. In the next section, example of commonly found geometries are illustrated. The electrical field have been calculated with Finite Element Solvers for a Poisson's current problem with a homogeneous medium; for convenience, all represented quantities have been normalized. For each electrode, a negative (cathodic) current has been imposed on the active electrode, the other metallic contact is considered as a ground current return. In any case, the potential near the active electrode is negative and the lowest on the entire geometry; this potential is in blue. The ground potential is then the highest potential; this potential is in red. The cells are triggered proportionally to the spatial second derivative of the electric potential along the neural fibers.

Micro-electrode geometries

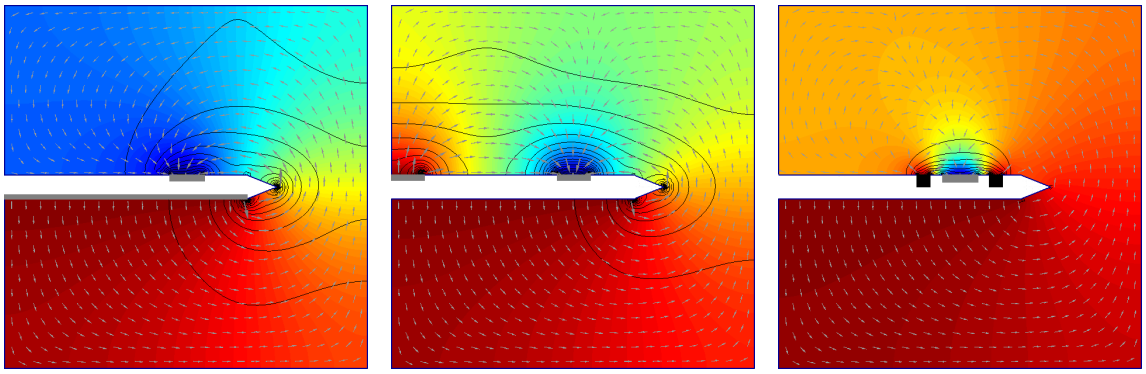

(a) (b) (c)

Figure A.1 – *Electric potential (coloured), electric field (iso-lines) and current density (arrows) for different planar micro-electrode geometries (a) active pad on the top (in gray) and current return on the other side of the surface of the electrode, (b) active pad and current return on the top of the electrode, the current return is common and is the first pad on the left, (c) active pad surrounded by a ring of current return contact.*

Planar micro-electrodes are based on metallic contact fabricated on a planar surface or a tissue-penetrating needle; several needles can be assembled to form a fork-like structure. The active electrode is formed by a metallic contact as represented in Figure A.1. The return contact is determining the focality of the electrode. In case of a current return electrode on the bottom of the needle (A.1(a)), the electrical potential is decreasing around the mechanical angles of the structure, and targeted tissue can be located not directly around the active electrode. In case a current return electrode at the basis of the needle (A.1(b)), the electrical potential evolution is located on the top of the structure and the triggered volumes are located near the border

of the active pad; as explained in chapter 1, tissues near the return path may be activated by high invert current. A more focal geometry of electrode can be used (A.1(c)), where the active electrode is surrounded by a ring of current return electrode. In this case the voltage repartition is concentrated around the active electrode, decreasing the required cathodic current and the volume of triggered tissue.

Macro-electrode geometries

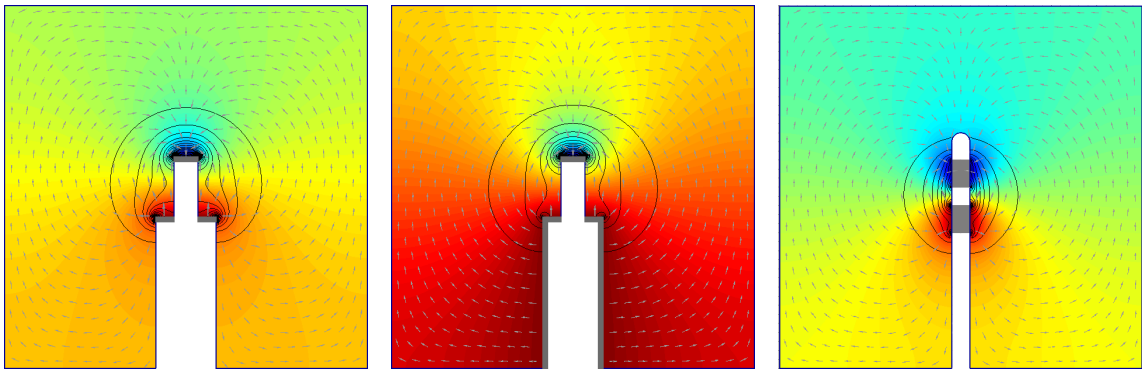

(a) (b) (c)

Figure A.2 – *Electric potential (coloured), electric field (iso-lines) and current density (arrows) for different planar macro-electrode geometries (a) needle-like electrode, (b) needle-like electrode with large current path formed by the holding tube, (c) typical geometry of human-implanted electrode for Deep Brain Stimulation.*

Macro-electrodes are designed to trigger a large neuronal structure, three examples are illustrated by Figure A.2. A first simple macro electrode can be fabricated with two twisted wires, their terminal sections are used as active and current return electrodes; in this case, the field repartition is the same as the example of the two quasi-point dipoles drawn on chapter 1. In the case of stimulation for rodent, a typical geometry is the needle-like electrode. This geometry is illustrated by the Figures A.2(a) and A.2(b). On Figure A.2(a), the current return path is only formed by the section of the holding tube, in Figure A.2(b) the entire holding tube is used as a current return path so that the electric potential evolution is only concentrated around the active electrode, making of this structure a more focal electrode. For a same implantation volume, the electrode of Figure A.2(a) will potentially activate a higher volume than the electrode of Figure A.2(b). In Figure A.2(c), the shape of typical human implanted DBS electrode is illustrated. This shape consists in two pads that, activated tissues are located laterally and near the active electrode pad.

Current steering technique

The commercial electrodes for human DBS, which basic geometry is illustrated on Figure A.2(c), often include more than two pads. The additional pads can be used for current steering as illustrated by Figures A.3 and A.4 In this case, the stimulation current I_{stim} is divided into two

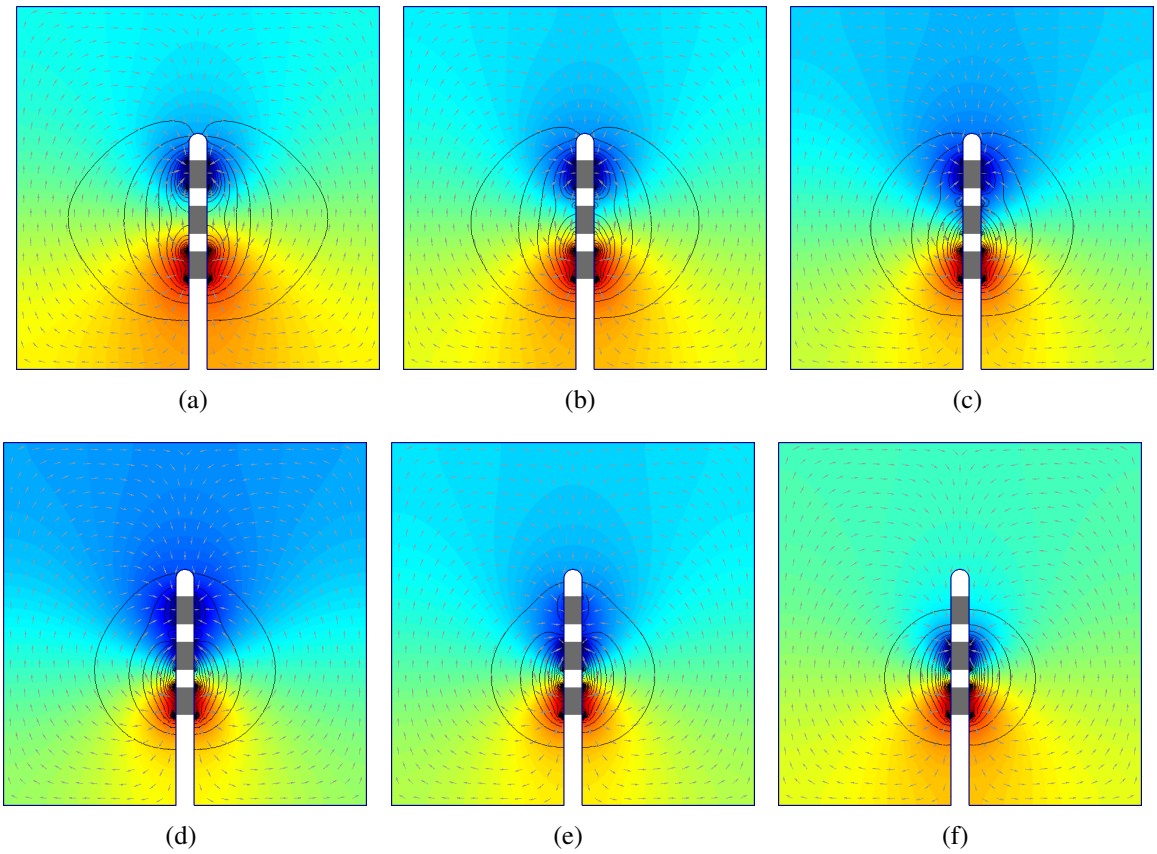

Figure A.3 – *Electric potential (coloured), electric field (iso-lines) and current density (arrows) with a typical commercial DBS electrode with 3 pads illustrating the current steering technique; the lowest pad is the current return electrode and the highest pads are active electrode, the central pad has a current* $I_1 = \alpha I_{stim}$*, the highest has a current* $I_2 = (1-\alpha)I_{stim}$*: (a)* $\alpha = 0$*, (b)* $\alpha = 0.2$*, (c)* $\alpha = 0.4$*, (d)* $\alpha = 0.6$*, (e)* $\alpha = 0.8$*, (f)* $\alpha = 1$

currents so that:

$$\begin{cases} I_1 = \alpha I_{stim} \\ I_2 = (1-\alpha) I_{stim} \end{cases} \tag{A.1}$$

where $0 \leq \alpha \leq 1$, so that I_1 and I_2 are steered on two different pads, the current return pad remains unique. By tuning the value of $alpha$ without changing the implantation of the electrode, the electric potential can be shifted. The active pads can be neighbour pads as represented in Figure A.3, so that one activation volume is shifted along the electrode structure, or opposed pads as illustrated by Figure A.4 where two activation zones can be obtained around the current return path.

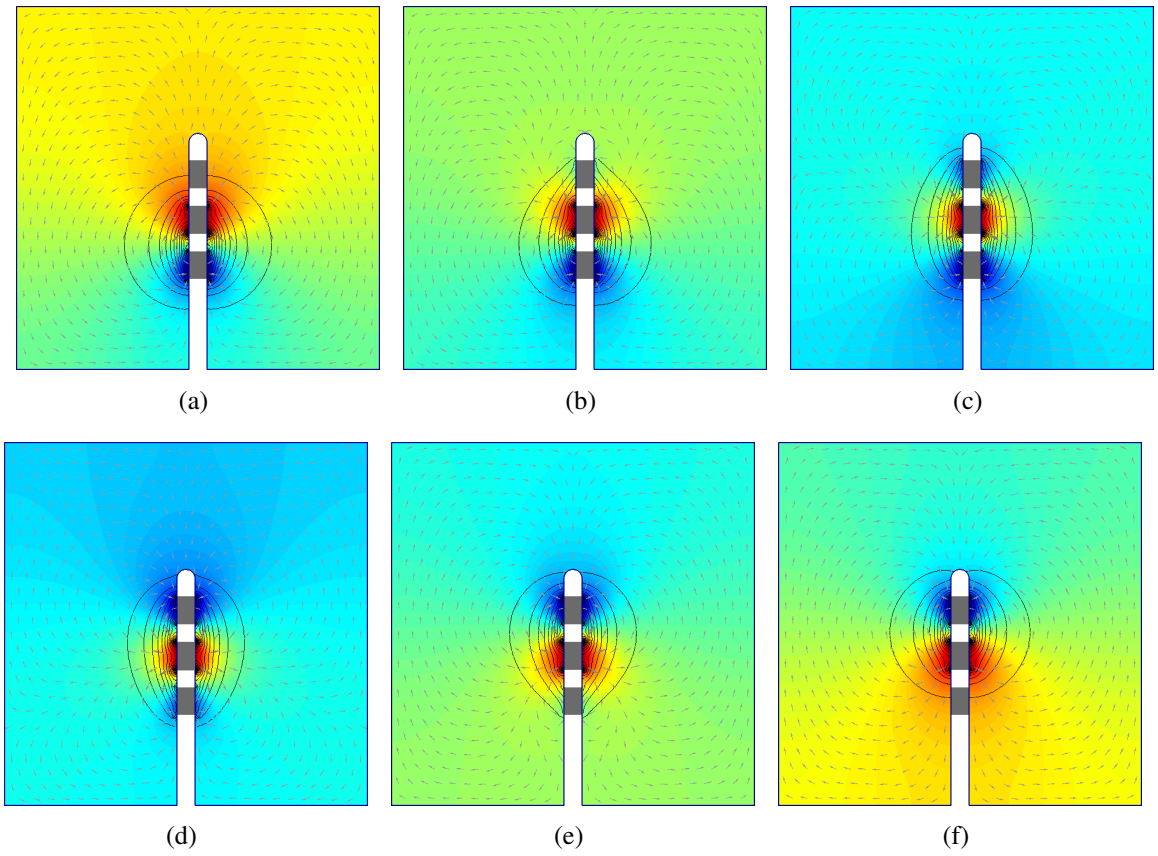

Figure A.4 – *Electric potential (coloured), electric field (iso-lines) and current density (arrows) with a typical commercial DBS electrode with 3 pads illustrating the current steering technique; the central pad is the current return electrode and the two extrema are active electrode, the highest pad has a current* $I_1 = \alpha I_{stim}$*, the lowest has a current* $I_1 = (1-\alpha)I_{stim}$*: (a)* $\alpha = 0$*, (b)* $\alpha = 0.2$*, (c)* $\alpha = 0.4$*, (d)* $\alpha = 0.6$*, (e)* $\alpha = 0.8$*, (f)* $\alpha = 1$

APPENDIX B

FRACTIONAL DERIVATIVE AND INTEGRATION

THIS appendix sums up the mathematical definitions and calculus rules and properties of the fractional derivation and integration.

Mathematical definitions

Let $f : \mathbb{R} \Rightarrow \mathbb{R}$ be a continuous function. $\boldsymbol{I}$ and $\boldsymbol{D}$ are respectively the integral and derivative operators.

Riemann-Liouville integration and derivative

A first generalized formulation of integration can be expressed considering definitions of integer integration. The Cauchy formula for repeated integration gives for $n \in \mathbb{N}$:

$$\boldsymbol{I}_{t_0}^{(n+1)} f(t) = {}_{t_0}\boldsymbol{D}_t^{-(n+1)} f(t) = \frac{1}{n!} \int_{t_0}^{t} (t-\tau)^n f(\tau)\, d\tau \tag{B.1}$$

The factorial term can be extended to the complex considering the gamma function defined as:

$$\Gamma(z) = \int_0^{\infty} t^{z-1} e^{-t} dt \tag{B.2}$$

where $z \in \{\mathbb{C} \setminus \mathbb{Z}_-\}$. This last equation gives for a positive integer n:

$$\Gamma(n+1) = n! \tag{B.3}$$

so that equation B.1 and the use of the gamma function lead to the Riemann-Liouville integral definition:

$$\boldsymbol{I}_{t_0}^{\gamma} f(t) \triangleq \frac{1}{\Gamma(\gamma)} \int_{t_0}^{t} (t-\tau)^{\gamma-1} f(\tau)\, d\tau \tag{B.4}$$

with the following conditions:

$$\begin{cases} t_0 \in \mathbb{R} \\ t > t_0 \\ \gamma \in \mathbb{C} \text{ and } \Re(\gamma) > 0 \end{cases} \tag{B.5}$$

This definition is exclusively based on a theoretic mathematical approach and gives no room for physical interpretation. Particularly, the use of this definition for fractional integration does not allow for reasoning on units because of the abstraction level.

A generalized definition of the derivative can be obtained as:

$${}_{t_0}\boldsymbol{D}_t^{\gamma} f(t) = {}_{t_0}\boldsymbol{D}_t^{(\gamma-m+m)} f(t) = \left(\frac{d}{dt}\right)^n {}_{t_0}\boldsymbol{D}_t^{-(n-\gamma)} f(t) \tag{B.6}$$

where $n = \lceil \Re(\gamma) \rceil$, so that $n \in \mathbb{N}^*$.
As:

$${}_{t_0}\boldsymbol{D}_t^{-(n-\gamma)} f(t) = \boldsymbol{I}_{t_0}^{(n-\gamma)} f(t) \tag{B.7}$$

equation B.4 allows to define the Riemann-Liouville fractional derivative as:

$${}_{t_0}\boldsymbol{D}_t^{\gamma} f(t) = \left(\frac{d}{dt}\right)^n \int_{t_0}^{t} \frac{1}{\Gamma(n-\gamma)\,(t-\tau)^{1-(n-\gamma)}} f(\tau)\, d\tau \tag{B.8}$$

Grünwald-Letnikov derivative

A second definition of the fractional derivative is studied. This definition is based on the expression of the derivative as a limit:

$$f'(t) = \lim_{\varepsilon \to 0} \frac{f(t+\varepsilon) - f(t)}{\varepsilon} \tag{B.9}$$

for the second-order derivative, assuming that f is synchronously converging:

$$f''(t) = \lim_{\varepsilon \to 0} \frac{f'(t+\varepsilon) - f'(t)}{\varepsilon} = \lim_{\varepsilon \to 0} \frac{f(t+2\varepsilon) - 2f(t+\varepsilon) + f(t)}{\varepsilon^2} \tag{B.10}$$

More generally, applying this recursive principle to a n-order derivative gives:

$$f^{(n)}(t) = \lim_{\varepsilon \to 0} \frac{\sum_{0 \leq m \leq n} (-1)^m \binom{n}{m} f(t + (n-m)\varepsilon)}{\varepsilon^n} \tag{B.11}$$

The binomial coefficients can be generalized to the complex numbers as defined by:

$$\binom{\gamma}{\beta} = \frac{\Gamma(\gamma+1)}{\Gamma(\beta+1)\Gamma(\gamma-\beta+1)} \tag{B.12}$$

where α and $\beta \in \{\mathbb{C} \setminus \mathbb{Z}_-\}$. To simplify notation, let set:

$$\Delta_\varepsilon^\gamma f(t) = \sum_{m=1}^{\infty} (-1)^m \binom{\gamma}{m} f(t + (\gamma - m)\varepsilon) \tag{B.13}$$

Thus, the generalized Grünwald-Letnikov fractional derivative is:

$$\boldsymbol{D}_t^\gamma f(t) \triangleq \lim_{\varepsilon \to 0} \frac{\Delta_\varepsilon^\gamma f(t)}{\varepsilon^\gamma} \tag{B.14}$$

This last equation lead to a definition of the generalized derivative more adapted to the physical interpretation of the integer derivative as a change of a first quantity with the infinitesimal variation of a second quantity. However this last equation does not allow for general understanding of the fractional phenomena. The next subsections aims at giving basic properties of fractional operators and further representation of fractional system outputs.

Properties and Laplace transform

In this part, some interesting properties of the fractional derivation are explained. These properties are useful for system computation and for a better understanding of electrode modelling underlying behavioural phenomena. As in the previous part, let f and $g : \mathbb{R} \to \mathbb{R}$ be two continuous functions.

Existence and general properties

The conditions for the existence of the fractional integral or derivative are:

- $\boldsymbol{I}_{t_0}^\gamma f(t)$ exists if $f(t)$ is piecewise-continuous on $[t; +\infty[$ and integrable on $]t_0; t[\, \forall t_0 < t$

- $\boldsymbol{D}_{t_0}^{\gamma} f(t)$ exists if $f(t)$ can be written as:

$$f(t) = (t - t_0)^{\upsilon} \xi(t - t_0) \tag{B.15}$$

or

$$f(t) = (t - t_0)^{\upsilon} \ln(t - t_0) \xi(t - t_0) \tag{B.16}$$

where $\upsilon \in \mathbb{C}$, $\Re(\upsilon) > -1$ and $\xi(t - t_0)$ is an analytical function of $\mathbb{C}$ for t_0

Fractional derivative and integration of a opposite order composition is the operator identity:

$$\boldsymbol{I}_{t_0}^{\gamma} \circ \boldsymbol{I}_{t_0}^{-\gamma} f(t) = f(t) \tag{B.17}$$

Both operators are linear:

$$\boldsymbol{I}_{t_0}^{\gamma} (\alpha f(t) + \beta g(t)) = \alpha \boldsymbol{I}_{t_0}^{\gamma} f(t) + \beta \boldsymbol{I}_{t_0}^{\gamma} g(t) \tag{B.18}$$

$$\boldsymbol{D}_{t_0}^{\gamma} (\alpha f(t) + \beta g(t)) = \alpha \boldsymbol{D}_{t_0}^{\gamma} f(t) + \beta \boldsymbol{D}_{t_0}^{\gamma} g(t) \tag{B.19}$$

Two integrators operator follow semi-group properties:

$$\boldsymbol{I}_{t_0}^{\gamma_1} \circ \boldsymbol{I}_{t_0}^{\gamma_2} f(t) = \boldsymbol{I}_{t_0}^{\gamma_1 + \gamma_2} f(t) \tag{B.20}$$

where $\Re(\gamma_1) > 0$ and $\Re(\gamma_1) > 0$. At this point, these properties are generalisation of derivation an integral properties, so that fractional systems can be computed as integer order systems. However, the semi-group properties can be generalized for the fractional derivation under specific conditions:

$$\boldsymbol{D}_0^{\gamma_1} \circ \boldsymbol{D}_0^{\gamma_2} f(t) = \boldsymbol{D}_0^{\gamma_1 + \gamma_2} f(t) \tag{B.21}$$

if $\Re(\gamma_1) > 0$ and $\Re(\gamma_1) > 0$, and :

$$\boldsymbol{D}_{t_0}^{n} \circ \boldsymbol{D}_{t_0}^{\gamma} f(t) = \boldsymbol{D}_{t_0}^{n+\gamma} f(t) \tag{B.22}$$

if $\Re(\gamma) > 0$ and $n \in \mathbb{N}$.

Laplace transform

For the fractional integration, the Laplace transform can be expressed as:

$$\mathcal{L}\{\boldsymbol{I}_0^{\gamma} f(t); s\} = \mathcal{L}\{\frac{t^{\gamma-1} u(t)}{\Gamma(\gamma)} * f(t); s\} \tag{B.23}$$

where $u(t)$ is the Heaviside function. Finally, the Laplace transform is:

$$\mathcal{L}\{\boldsymbol{I}_0^{\gamma} f(t); s\} = \frac{1}{s^{\gamma}} F(s) \tag{B.24}$$

where $F(s) = \mathcal{L}\{f(t); s\}$. This result generalizes the formula used for integer order integration.

For integer-order n-derivative, the Laplace transform can be expressed as:

$$\mathcal{L}\{\boldsymbol{D}_t^{n} f(t); s\} = s^n F(s) - \sum_{k=0}^{n} s^{k-1} \left(\boldsymbol{D}^{n-k} f(t)\right)\Big|_{t=0^+} \tag{B.25}$$

in the case of a complex order γ, let consider $n = \lceil \Re(\gamma) \rceil$, so that the Laplace transform of the fractional derivative becomes:

$$\mathcal{L}\{{}_0\boldsymbol{D}^{\gamma} f(t); s\} = \mathcal{L}\{{}_0\boldsymbol{D}^{n} \left(\boldsymbol{I}_0^{n-\gamma} f(t)\right); s\} \tag{B.26}$$

by substitution with equations B.24:

$$\mathcal{L}\{{}_0\boldsymbol{D}^{\gamma} f(t); s\} = s^n \mathcal{L}\{\boldsymbol{I}_0^{n-\gamma} f(t); s\} - \sum_{k=0}^{n} s^{k-1} \left(\boldsymbol{D}^k \left(\boldsymbol{I}_0^{n-\gamma} f(t)\right)\right)\Big|_{t=0^+} \tag{B.27}$$

finally, considering equation B.25:

$$\mathcal{L}\{{}_0\boldsymbol{D}^{\gamma} f(t); s\} = s^{\gamma} F(s) - \sum_{k=0}^{n} s^{k-1} \left(\boldsymbol{D}^k \left(\boldsymbol{I}_0^{n-\gamma} f(t)\right)\right)\Big|_{t=0^+} \tag{B.28}$$

As for the integrator, this last result generalizes the commonly used formula for the derivation. As a consequence, the output signal of fractional integrator or derivator can be studied with the same mathematical reasoning as for ordinary differential equations.

APPENDIX C

ADDITIONAL CIRCUITS OF THE ASIC SHIVA

THIS appendix presents the schematic fabricated on the ASIC SHIVA performing the current biasing with the internal current references, the current memory cell, the current divider and the logic block preventing short-circuit configuration on the output stage.

Current references

A current reference block has been designed in order to provide the biasing current to the analog circuits and to provide 8 weighted current for the current shaping circuits described in chapter 6. The schematic of this block is presented in Figure C.1. This circuit is based on two

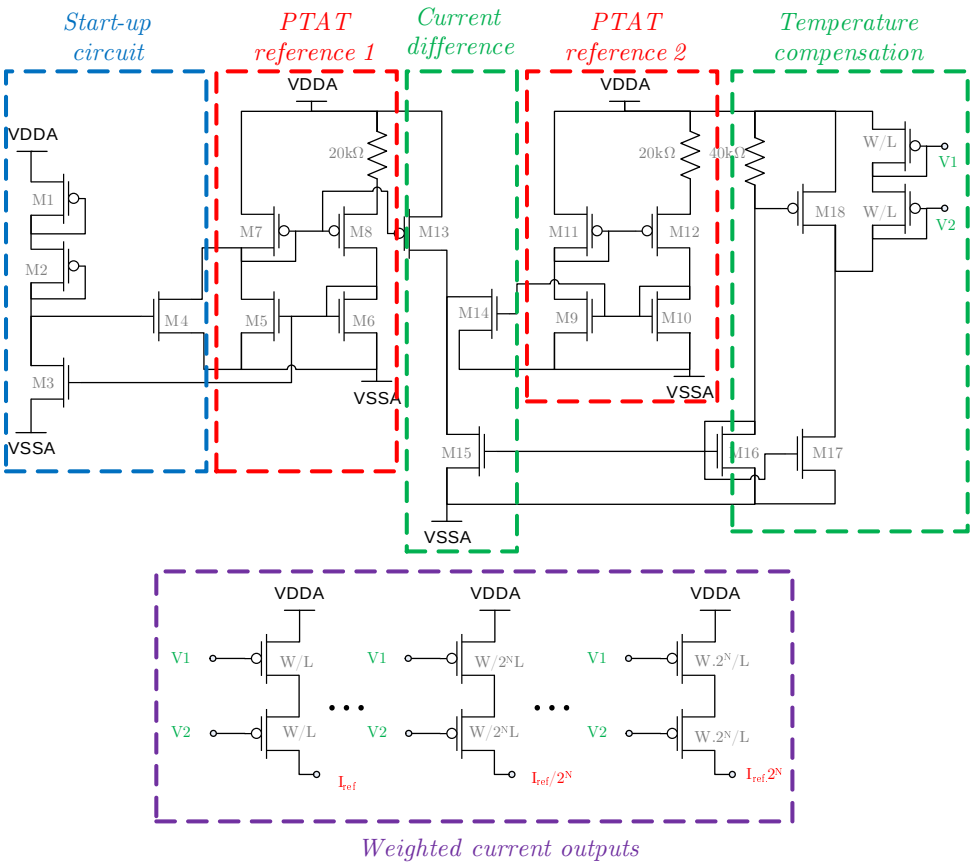

Figure C.1 – *Schematic of the current reference block with weighted current outputs.*

PTAT current references blocks (the first built around $M5$ to $M8$, the second around $M9$ to $M12$). These two blocks are designed with an integrated resistor fixing the generated current. As these two block have a deviation with the modification of the supply - here $VDDA = 3.3V$ and $VSSA = 0V$ - a compensation is made by current difference made by $M13$ and $M14$ and buffered through $M15$. A extra temperature compesation is provided by transistors $M16$, $M17$ and $M18$ with the connected resistor. These two compensations (supply and temperature) are further detailed in Yoo and Park (2007). To avoid the possible unbiasing of the structure, a start-up circuit is built around $M1$ to $M4$.

As the required current are multiple of the obtained $1.92\mu A$ (simulation result), a weighted transistor network is set at the output of the reference, where two transistors in diode form the imput of a cascode current miror. The overall static current consumtion (with outputs unconnected) is 23.6μ (simulation result).

I_{static} (nA)	τ_{load} (ns)	$t_{discharge\,1\%}$ (s)
304	106	$> 1 \cdot 10^{-3}$

Table C.1 – *Results of the characterization of the current memory cell obtained by simulation.*

Current memory cells

In order to use one current input to drive 8 output channels, current memory cells have been used. The design of this block is illustrated in Figure C.2. This block is based on a cascode current

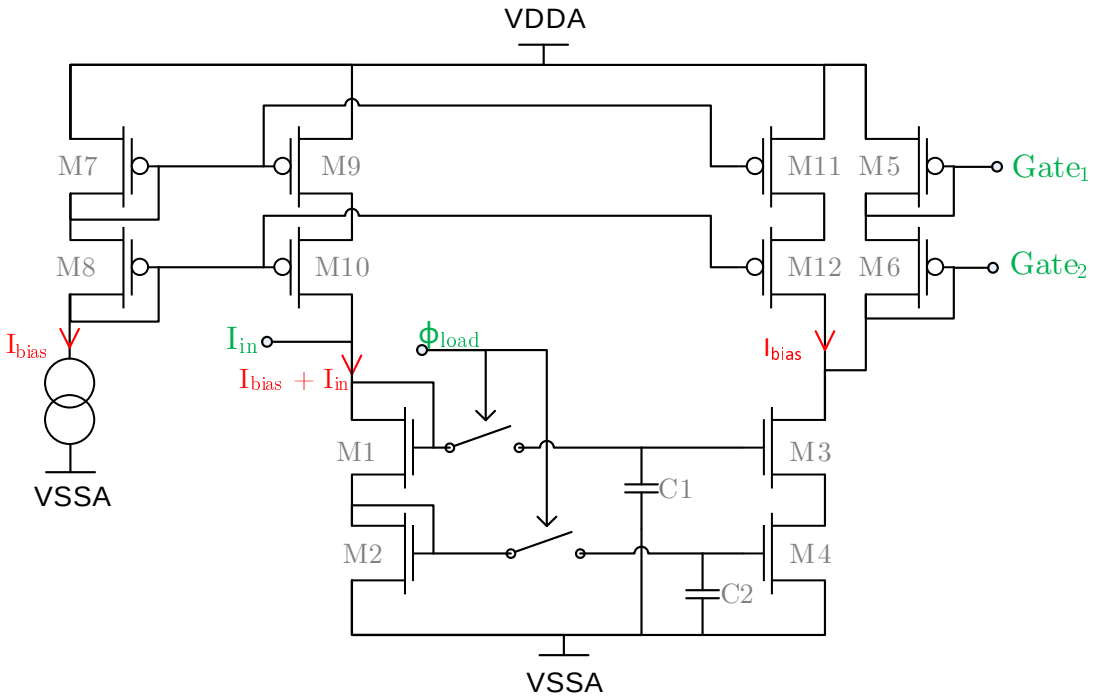

Figure C.2 – *Schematic of the current memory cell.*

miror ($M1$ to $M4$) whose gate voltage is memorized with the capacitors $C1 = C2 = 3pF$. In order to keep the current miror biased in any case, a biasing current is applied on $M1$ and $M2$ through $M9$ and $M10$; in order not to modify the memorized value, this current is substracted to the $M5$, $M6$ -forming the input of a cascode current miror- output through $M11$ and $M12$. The ouptut can be isolated from the input with the switches driven by the memorization order Φ_{load}. These two switches have been implemented with charge-injection reduced transfer gate to ensure the accuracy of the current value memorization. Characteristics obtained by simulation of this current memory cell are summed up in table C.1.

Current divider

The current divider is a circuit controled by two bits and providing a current division of:

- 1 (with the digital input '11'),

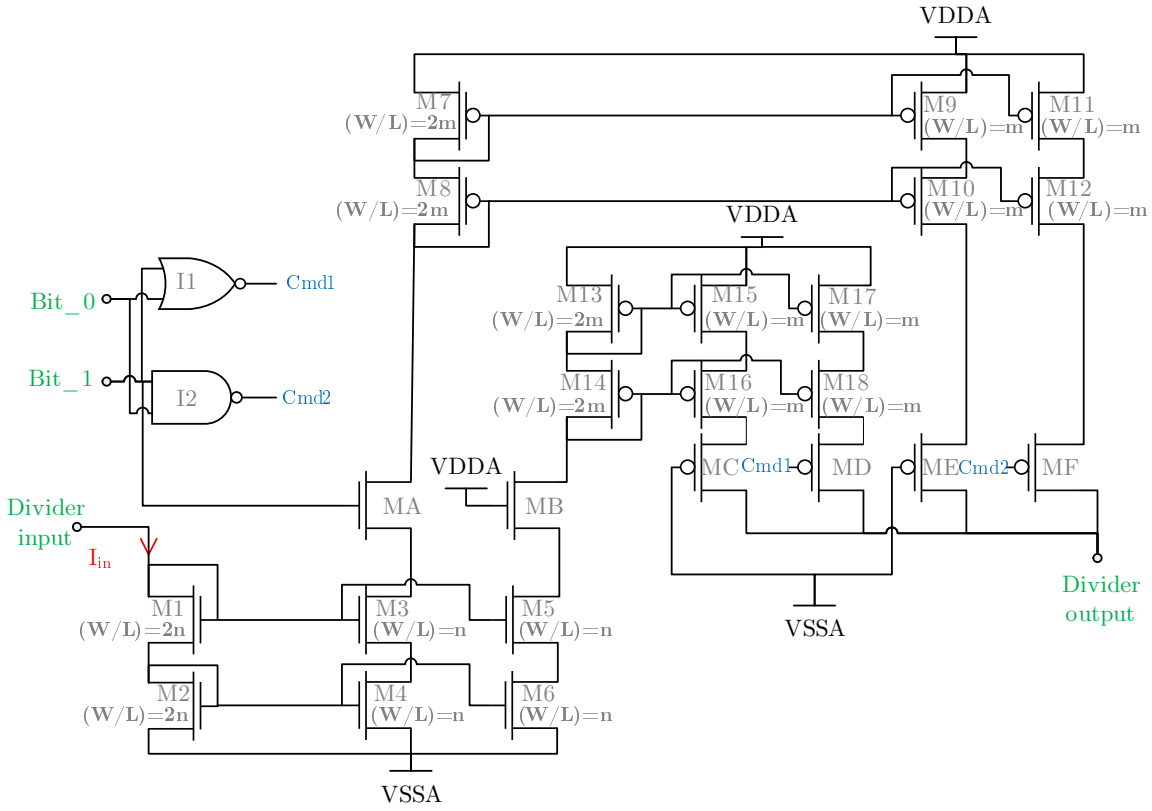

Figure C.3 – *Schematic of the current divider.*

- $^3/_4$ (with the digital input '10'),
- $^1/_2$ (with the digital input '01'),
- $^1/_4$ (with the digital input '00').

the schematic of this circuit is presented in Figure C.3

The input current is first divided by two using cascode current miror formed by $M1$ to $M5$. The transistor MA is used as a switch controled by the most significant bit; in order to respect a symmetry ensuring current equality on mirors ouput, a dummy transistor MB is added on the uncontroled current miror. Each N mirror output is loaded by a P double cascode current miror dividing the current by two, formed by $M7$ to $M12$ and by $M13$ to $M18$. The four output are selected using two switches (MD and MF), driven by logic gates, the un-switched outputs are commected to dummy transistors MC and ME ensuring an equality of each branch output.

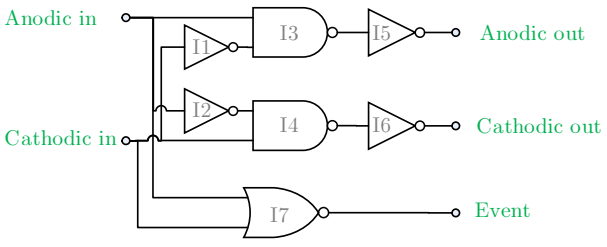

Figure C.4 – *Schematic of the logic block ensuring that no short circuit configuration is applied on the front-end.*

Shotcircuit prenventing block

In order not to request an anodic and cathodic current a logic block is added to the drivers of the stimulation front-end as described in chapter 6. This block is presented in Figure C.4.

If the cathodic and anodic commands are at the high logic level, the outputs are set to a low logic level, if only one or no input is at a high logic level, they are copied on the ouput. An additional *'event'* is also computed. Its logic level is high if both command inputs are low; when a cathodic or anodic or both commands are one, the *'event'* is set to a low level, provinding information to other circuits for artifact blanking or debug.

AUTHOR'S PUBLICATIONS

Journal

Kolbl, F., N'Kaoua, G., Naudet, F., Berthier, F., Faggiani, E., Benazzouz, A., Renaud, S., and Lewis, N. (2014). An embedded deep brain stimulator for biphasic chronic experiments in freely moving rodents. *accepted in IEEE Transactions on Biomedical Circuits and Systems*.

International conferences

Kolbl, F., Guillaume, R., Hasler, J., Joucla, S., Yvert, B., Renaud, S., and Lewis, N. (2014). A closed-loop charge balancing fpaa cicuit with sub-nano-amp dc error for electrical stimulation. In *Biomedical Circuits and Systems Conference (BioCAS), 2014 IEEE*, pages 000–000.

Kolbl, F., Sabatier, J., N'Kaoua, G., Naudet, F., Faggiani, E., Benazzouz, A., Renaud, S., and Lewis, N. (2013). Characterization of a non linear fractional model of electrode-tissue impedance for neuronal stimulation. In *Biomedical Circuits and Systems Conference (BioCAS), 2013 IEEE*, pages 338–341.

Kolbl, F., Zbrzeski, A., Syed, E., Renaud, S., and Lewis, N. (2010). In vivo electrical characterization of deep brain electrode and impact on bio-amplifier design. In *Biomedical Circuits and Systems Conference (BioCAS), 2010 IEEE*, pages 210–213.

Zbrzeski, A., Hasler, P., Kolbl, F., Syed, E., Lewis, N., and Renaud, S. (2010). A programmable bioamplifier on fpaa for in vivo neural recording. In *Biomedical Circuits and Systems Conference (BioCAS), 2010 IEEE*, pages 114–117.

National conferences

Kolbl, F., Guillaume, R., Hasler, J., Joucla, S., Yvert, B., Renaud, S., and Lewis, N. (2014). Circuit de stimulation nerveuse à contre-réaction d'équilibrage des charges sur fpaa. In *GdR Soc-Sip, 2014 IEEE*.

BILIOGRAPHY

Abdelhalim, K. and Genov, R. (2011). CMOS DAC-sharing stimulator for neural recording and stimulation arrays. In *2011 IEEE Int. Symp. Circuits Syst.*, pages 1712–1715. IEEE.

Ambroise, M., Levi, T., Joucla, S., Yvert, B., and Saïghi, S. (2013). Real-time biomimetic central pattern generators into fpga for hybrid experiments. *Frontiers in Neuroscience*, 7(215).

Arabi, K. and Sawan, M. A. (1999). Electronic Design of a Multichannel Programmable Implant for Neuromuscular Electrical Stimulation. *IEEE Transactions on Rehabilitaion Engineering*, 7(2):11.

Arfin, S. K., Long, M. A., Fee, M. S., and Sarpeshkar, R. (2009). Wireless Neural Stimulation in Freely Behaving Small Animals. *Journal of Neurophysiology*, 102(1):8.

Arfin, S. K. and Sarpeshkar, R. (2012). An Energy-Efficient, Adiabatic Electrode Stimlulator With Inductive Energy Recycling and Feedback Current Regulation. *IEEE Transactions on Biomedical Circuits and Systems*, 6(1):14.

Azin, M., Guggenmos, D. J., Barbay, S., Nudo, R. J., and Mohseni, P. (2011). A Battery-Powered Activity-Dependent Intracortical Microstimulation IC for Brain-Machine-Brain Interface. *IEEE J. Solid-State Circuits*, 46(4):731–745.

Ballan, H., Declercq, M., and Declercq, M. (1999). *High voltage devices and circuits in standard CMOS technologies*. Springer.

Bankiewicz, K. S., Oldfield, E. H., Chiueh, C. C., Doppman, J. L., Jacobowitz, D. M., and Kopin, I. J. (1986). Hemiparkinsonism in monkeys after unilateral internal carotid artery infusion of 1-methyl-4-phenyl-1,2,3,6-tetrahydropyridine (MPTP). *Life Sci.*, 39(1):7–16.

Bard, A. J. and Faulkner, L. R. (2001). *Electrochemical Methods: Fundamentals and Applications*. John Wiley & Sons, Inc.

Basu, A., Twigg, C. M., Brink, S., Hasler, P., Petre, C., Ramakrishnan, S., Koziol, S., and Schlottmann, C. (2008). Rasp 2.8: A new generation of floating-gate based field programmable analog array. In *Custom Integrated Circuits Conference, 2008. CICC 2008. IEEE*, pages 213–216. IEEE.

Bellemare, F. and Bigland-Ritchie, B. (1984). Assessment of human diaphragm strength and activation using phrenic nerve stimulation. *Respiration physiology*, 58(3):263–277.

Belujon, P., Bezard, E., Taupignon, A., Bioulac, B., and Benazzouz, A. (2007). Noradrenergic modulation of subthalamic nucleus activity: behavioral and electrophysiological evidence in intact and 6-hydroxydopamine-lesioned rats. *The Journal of Neuroscience*, 27(36):9595–9606.

Benabid, A. L. (2003). Deep brain stimulation for Parkinson's disease. *Curr. Opin. Neurobiol.*, 13(6):696–706.

Benabid, A. L., Pollak, P., Hoffmann, D., Gervason, C., Hommel, M., Perret, J., De Rougemont, J., and Gao, D. (1991). Long-term suppression of tremor by chronic stimulation of the ventral intermediate thalamic nucleus. *The Lancet*, 337(8738):403–406.

Bergman, H., Wichmann, T., and DeLong, M. R. (1990). Reversal of experimental parkinsonism by lesions of the subthalamic nucleus. *Science*, 249(4975):1436–1438.

Bernstein, J. (1902). Untersuchungen zur thermodynamik der bioelektrischen ströme. *Pflügers Archiv European Journal of Physiology*, 92(10):521–562.

Bihr, U., Ungru, T., Xu, H., Anders, J., Becker, J., and Ortmanns, M. (2013). A Bidirectional Neural Interface with a HV Stimulator and a LV Neural Amplifier. *Circuits and Systems (ISCAS), 2013 IEEE International Symposium on*, page 4.

Binnie, C. (2000). Vagus nerve stimulation for epilepsy: a review. *Seizure*, 9(3):161–169.

Blum, R. A., Ross, J. D., Brown, E. A., and DeWeerth, S. P. (2007). An Integrated System for simultaneous, Multichannel Neuronal Stimluation and Recording. *IEEE Transactions on circuits and systems - I: Regular papers*, 54(12):11.

Bock, D. C., Marschilok, A. C., Takeuchi, K. J., and Takeuchi, E. S. (2012). Batteries used to Power Implantable Biomedical Devices. *Electrochim. Acta*, 84:155–164.

Bontorin, G., Garenne, A., Tomas, J., Lopez, C., Morin, F. O., and Renaud, S. (2009). A real-time system for multisite stimulation on living neural networks. *Joint IEEE North-East Workshop on Circuits and Systems and TAISA Conference*, page 4.

Borton, D., Micera, S., Millán, J. d. R., and Courtine, G. (2013). Personalized neuroprosthetics. *Science translational medicine*, 5(210):210rv2–210rv2.

Boyer, S., Sawan, M., Abdel-Gawad, M., Robin, S., and Elhilali, M. M. (2000). Implantable Selective stimulator to improve bladder voiding: Design and Chronic Experiments in Dogs. *IEEE Transactions on Rehabilitaion Engineering*, 8(4):7.

Brindley, G. S. and Lewin, W. (1968). The sensations produced by electrical stimulation of the visual cortex. *The Journal of physiology*, 196(2):479–493.

Brink, S., Hasler, J., and Wunderlich, R. (2014). Adaptive Floating-Gate Circuit Enabled Large-Scale FPAA. *IEEE Trans. Very Large Scale Integr. Syst.*, PP(99):1–1.

Brown, E. A., Ross, J. D., Blum, R. A., Nam, Y., Wheeler, B. C., and DeWeerth, S. P. (2008). Stimulus-artifact elimination in a multi-electrode system. *Biomedical Circuits and Systems, IEEE Transactions on*, 2(1):10–21.

Carobrez, A. P. and Bertoglio, L. J. (2005). Ethological and temporal analyses of anxiety-like behavior: the elevated plus-maze model 20 years on. *Neurosci. Biobehav. Rev.*, 29(8):1193–205.

Chang, C. W., Chung, W. Y., Chuang, C. C., Wei, R. L., and Dai, J. X. (2004). A novel system design for implantable stimulator application.

Chang, S.-J., Chung, W.-Y., and Chuang, C.-C. (2006). System Design of Implantable Microstimulator for Medical Treatments. In *APCCAS 2006 - 2006 IEEE Asia Pacific Conf. Circuits Syst.*, pages 478–481. IEEE.

Chaturvedi, A., Foutz, T. J., and McIntyre, C. C. (2012). Current steering to activate targeted neural pathways during deep brain stimulation of the subthalamic region. *Brain stimulation*, 5(3):369–377.

Chen, K., Yang, Z., Hoang, L., Weiland, J., Humayun, M., and Liu, W. (2010). An Integrated 256-Channel Epiretinal Prosthesis. *IEEE Journal of Solid-State Circuits*, 45(9):11.

Chow, A. Y., Chow, V. Y., Packo, K. H., Pollack, J. S., Peyman, G. A., and Schuchard, R. (2004). The artificial silicon retina microchip for the treatment of visionloss from retinitis pigmentosa. *Archives of ophthalmology*, 122(4):460–469.

Chun, A. H., Kavehei, O., Tran, N., and Skafidas, S. (2013). A Flexible Biphasic Pulse Generating and Accurate Charge Balancing Stimluator with a 1 microW Neural Recording Amplifier. *Circuits and Systems (ISCAS), 2013 IEEE International Symposium on*, page 4.

Chun, H., Lehmann, T., and Yang, Y. (2010). Implantable stimulator for bipolar stimulation without charge balancing circuits. In *2010 Biomed. Circuits Syst. Conf.*, pages 202–205. IEEE.

Cobb, M. (2002). Exorcizing the animal spirits: Jan swammerdam on nerve function. *Nature Reviews Neuroscience*, 3(5):395–400.

Cogan, S. F. (2008). Neural stimulation and recording electrodes. *Annu. Rev. Biomed. Eng.*, 10:275–309.

Collins, K. L., Lehmann, E. M., and Patil, P. G. (2010). Deep brain stimulation for movement disorders. *Neurobiology of disease*, 38(3):338–345.

Constandinou, T. G., Georgiou, J., and Toumazou, C. (2008). A partial-current-steering biphasic stimulation driver for neural prostheses. In *2008 IEEE Int. Symp. Circuits Syst.*, pages 2506–2509. IEEE.

Cottance, M., Nazeer, S., Rousseau, L., Lissorgues, G., Joucla, S., Yvert, B., Lewis, N., Bornat, Y., and Renaud, S. (2013). Challenges in recording and stimulation of living neural network based on original micro-electrode array (mea) developments. In *New Circuits and Systems Conference (NEWCAS), 2013 IEEE 11th International*, pages 1–4.

Coulombe, J., Sawan, M. A., and Gervais, J.-F. (2007). A Highly Flexible System for Microstimluation of the Visual Cortex: Design and Implementation. *IEEE Transactions on Biomedical Circuits and Systems*, 1(4):12.

Courtine, G., Gerasimenko, Y., van den Brand, R., Yew, A., Musienko, P., Zhong, H., Song, B., Ao, Y., Ichiyama, R. M., Lavrov, I., et al. (2009). Transformation of nonfunctional spinal circuits into functional states after the loss of brain input. *Nature neuroscience*, 12(10):1333–1342.

Curtis, H. J. and Cole, K. S. (1940). Membrane action potentials from the squid giant axon. *Journal of Cellular and Comparative Physiology*, 15(2):147–157.

Dai Jiang, Demosthenous, A., Perkins, T., Xiao Liu, and Donaldson, N. (2011). A Stimulator ASIC Featuring Versatile Management for Vestibular Prostheses. *IEEE Trans. Biomed. Circuits Syst.*, 5(2):147–59.

De Ridder, D., De Mulder, G., Walsh, V., Muggleton, N., Sunaert, S., and Møller, A. (2004). Magnetic and electrical stimulation of the auditory cortex for intractable tinnitus: case report. *Journal of neurosurgery*, 100(3):560–564.

Delaville, C., Chetrit, J., Abdallah, K., Morin, S., Cardoit, L., De Deurwaerdère, P., and Benazzouz, A. (2012). Emerging dysfunctions consequent to combined monoaminergic depletions in parkinsonism. *Neurobiology of disease*, 45(2):763–773.

DeMarco, S. C., Liu, W., Singh, P. R., Lazzi, G., Humayun, M. S., and Weiland, J. D. (2003). An Arbitrary Waveform Stimulus Circuit for Visual Prostheses USing a Low-Area Multibias DAC. *IEEE Journal of Solid-State Circuits*, 38(10):12.

Dhillon, G. S. and Horch, K. W. (2005). Direct neural sensory feedback and control of a prosthetic arm. *Neural Systems and Rehabilitation Engineering, IEEE Transactions on*, 13(4):468–472.

DiMarco, A. F. (2005). Restoration of respiratory muscle function following spinal cord injury: review of electrical and magnetic stimulation techniques. *Respiratory physiology & neurobiology*, 147(2):273–287.

DiMarco, A. F., Onders, R. P., Kowalski, K. E., Miller, M. E., Ferek, S., and Mortimer, J. T. (2002). Phrenic nerve pacing in a tetraplegic patient via intramuscular diaphragm electrodes. *American journal of respiratory and critical care medicine*, 166(12):1604–1606.

Dimitrijevic, M. R., Gerasimenko, Y., and Pinter, M. M. (1998). Evidence for a spinal central pattern generator in humans. *Annals of the New York Academy of Sciences*, 860(1):360–376.

Djourno, A. and Eyries, C. (1957). [auditory prosthesis by means of a distant electrical stimulation of the sensory nerve with the use of an indwelt coiling.]. *La Presse Médicale*, 65(63):1417–1417.

Dommel, N. B., Wong, Y. T., Lehmann, T., Dodds, C. W., Lovell, N. H., and Suaning, G. J. (2009). A CMOS retinal neurostimulator capable of focussed, simultaneous stimulation. *Journal of Neural Engineering*, 6(1):10.

Duffy, C. and Hasler, P. (2003). Modeling hot-electron injection in pfet's. *Journal of Computational Electronics*, 2(2-4):317–322.

Dulawa, S. C., Grandy, D. K., Low, M. J., Paulus, M. P., and Geyer, M. A. (1999). Dopamine D4 receptor-knock-out mice exhibit reduced exploration of novel stimuli. *J. Neurosci.*, 19(21):9550–6.

Dupont, F., Condemine, C., Beche, J., and Belleville, M. (2012). Multi-application Electrical Stimulator Architecture Dedicated to Waveform Control by Electrode-Tissue Impedance Spectra Monitoring. *Electronics, Circuits and Systems (ICECS), 2012 19th IEEE International Conference on*, page 4.

Eftekhar, A., Constandinou, T. G., Triantis, I. F., Toumazou, C., and Drakakis, E. M. (2007). Towards a reconfigurable sense-and-stimulate neural interface generating biphasic interleaved stimulus. *Proceedings of the 3rd International IEEE EMBS Conference on Neural Engineering*, page 4.

Egon, G., Barat, M., Colombel, P., Visentin, C., Isambert, J., and Guerin, J. (1998). Implantation of anterior sacral root stimulators combined with posterior sacral rhizotomy in spinal injury patients. *World journal of urology*, 16(5):342–349.

Ehringer, H. and Hornykiewicz, O. (1998). Distribution of noradrenaline and dopamine (3-hydroxytyramine) in the human brain and their behavior in diseases of the extrapyramidal system. *Parkinsonism & related disorders*, 4(2):53–57.

Elmgvist, R., Landegren, J., Pettersson, S. O., Senning, Å., and William-Olsson, G. (1963). Artificial pacemaker for treatment of adams-stokes syndrome and slow heart rate. *American Heart Journal*, 65(6):731–748.

EN45502-1, E. S. (1998). *EN45502-1 for safety, marking and information to be provided by the manufacturer in Active Implantable Medical Devices*. European Standard, CENELEC, Brussels.

Ewing, S. E., Porr, B., Riddel, J., Winter, C., and Grace, A. A. (2013). SaBer DBS: a fully programmable , rechargeable, bilatera, charge-balanced preclinical microstimulator for long-term neural stimulation. *Journal of Neurscience Methods*, 213(1):8.

Fang, X., Wills, J., Granacki, J., LaCoss, J., Arakelian, A., and Weiland, J. (2007). Novel Charge-Metering Stimulus Amplifier for Biomimetic Implantable Prosthesis. In *2007 IEEE Int. Symp. Circuits Syst.*, pages 569–572. IEEE.

Farahmand, S., Vahedian, H., Abedinkhan, M., and Sodagar, A. M. (2012). Wearable, Battery-Powered, Wireless, Programmable 8-Channel Neural Stimulator. *34th Annual International Conference of the IEEE EMBS*, page 4.

Feiner, A.-S. and McEvoy, A. (1994). The nernst equation. *Journal of chemical education*, 71(6):493.

Ferrandez, J. M., Liano, E., Bonomini, P., Martinez, J. J., Toledo, J., and Fernandez, E. (2007). A Customizable Multi-channel Stimulator for Cortical Neuroprosthesis.

Forni, C., Mainard, O., Melon, C., Goguenheim, D., Kerkerian-Le Goff, L., and Salin, P. (2012). Portable microstimulator for chronic deep brain stimulation in freely moving rats. *J. Neurosci. Methods*, 209(1):50–7.

Forsyth, R. M. (2003). Technology and design of integrated circuits for up to 50 v applications. In *Industrial Technology, 2003 IEEE International Conference on*, volume 1, pages 7–13. IEEE.

Franks, W., Schenker, I., Schmutz, P., and Hierlemann, A. (2005). Impedance characterization and modeling of electrodes for biomedical applications. *Biomedical Engineering, IEEE Transactions on*, 52(7):1295–1302.

Fricke, H. (1932). The theory of electrolytic polarization. *The London, Edinburgh, and Dublin Philosophical Magazine and Journal of Science*, 14(90):310–318.

Galvani, L. and Aldini, G. (1792). *De Viribus Electricitatis In Motu Musculari Comentarius Cum Joannis Aldini Dissertatione Et Notis; Accesserunt Epistolae ad animalis electricitatis theoriam pertinentes*. Apud Societatem Typographicam.

Georgiou, J. and Toumazou, C. (2005). A 126-μW Cochlear Chip for a Totally Implantable System. *IEEE Journal of Solid-State Circuits*, 40(2):14.

Giszter, S. F. (2008). Spinal cord injury: present and future therapeutic devices and prostheses. *Neurotherapeutics*, 5(1):147–162.

Gong, C.-S. A., Shiue, M.-T., Su, C.-H., and Chang, Y. (2006). An Efficient Micro-Stimulator Array Using Unitary-Size DAC With Adiabatic Baseband Scheme. In *2006 13th IEEE Int. Conf. Electron. Circuits Syst.*, pages 29–32. IEEE.

Gong, W., Haburcakova, C., and Merfeld, D. M. (2008). Vestibulo-ocular responses evoked via bilateral electrical stimulation of the lateral semicircular canals. *Biomedical Engineering, IEEE Transactions on*, 55(11):2608–2619.

Greenwald, E., Chen, C., Thakor, N., Maier, C., and Cauwenberghs, G. (2013). A cmos neurostimulator with on-chip dac calibration and charge balancing. In *Biomedical Circuits and Systems Conference (BioCAS), 2013 IEEE*, pages 89–92.

Gudnason, G., Bruun, E., and Haugland, M. (1999). An implantable mixed Analog/Digital Neural Stimulator Circuit. *Proceedings of the 1999 IEEE International Symposium on Circuits and Systems*, page 4.

Gulak, P. (1995). Field programmable analog arrays: past, present and future perspectives. In *Microelectronics and VLSI, 1995. TENCON '95., IEEE Region 10 International Conference on*, pages 123–126.

Haddad, S. A., Houben, R. P., and Serdijn, W. A. (2006). The evolution of pacemakers. *IEEE Engineering in Medicine and Biology Magazine*, 25(3):38–48.

Hamill, O., Marty, A., Neher, E., Sakmann, B., and Sigworth, F. (1981). Improved patch-clamp techniques for high-resolution current recording from cells and cell-free membrane patches. *Pflügers Archiv*, 391(2):85–100.

Hammond, C., Ammari, R., Bioulac, B., and Garcia, L. (2008). Latest view on the mechanism of action of deep brain stimulation. *Mov. Disord.*, 23(15):2111–21.

Hamzaid, N. A. and Davis, G. M. (2009). Health and fitness benefits of functional electrical stimulation-evoked leg exercise for spinal cord–injured individuals. *Topics in Spinal Cord Injury Rehabilitation*, 14(4):88–121.

Han, D., Zheng, Y., Rajkumar, R., Dawe, G., and Je, M. (2013). A 0.45 v 100-channel neural-recording ic with sub-micro-w /channel consumption in 0.18 micro-m cmos. *Biomedical Circuits and Systems, IEEE Transactions on*, 7(6):735–746.

Harnack, D., Meissner, W., Paulat, R., Hilgenfeld, H., Müller, W.-D., Winter, C., Morgenstern, R., and Kupsch, A. (2008). Continuous high-frequency stimulation in freely moving rats: development of an implantable microstimulation system. *Journal of neuroscience methods*, 167(2):278–291.

Harrison, R. and Charles, C. (2003). A low-power low-noise cmos amplifier for neural recording applications. *Solid-State Circuits, IEEE Journal of*, 38(6):958–965.

Hasler, P. (2005). Floating-gate devices, circuits, and systems, invited. In *System-on-Chip for Real-Time Applications, International Workshop on*, pages 482–487. IEEE Computer Society.

Hauser, R. A. (2009). New considerations in the medical management of early parkinson's disease: impact of recent clinical trials on treatment strategy. *Parkinsonism & related disorders*, 15:S17–S21.

Heikkila, R., Hess, A., and Duvoisin, R. (1984). Dopaminergic neurotoxicity of 1-methyl-4-phenyl-1,2,5,6-tetrahydropyridine in mice. *Science (80-.).*, 224(4656):1451–1453.

Helmholtz, H. (1850). Note sur la vitesse de propagation de l'agent nerveux dans les nerfs rachidiens. *CR Acad Sci (Paris)*, 30:204–206.

Hitzelberger, C., Manoli, Y., Hakenes, R., and Gross, S. (2001). A Microcontroller Embedded ASIC for an Implantable Electro-Neural Stimulator. *Proceedings of the 27th European Solid-State Circuits Conference*, page 4.

Hodgkin, A. L. and Huxley, A. F. (1952). A quantitative description of membrane current and its application to conduction and excitation in nerve. *The Journal of physiology*, 117(4):500.

Holsheimer, J., Dijkstra, E. A., Demeulemeester, H., and Nuttin, B. (2000). Chronaxie calculated from current–duration and voltage–duration data. *Journal of neuroscience methods*, 97(1):45–50.

Hu, J. and Gordon, C. (2008). A General Adaptive Charge-Balancing Stimulator. *51st Midwest Symposium on Circuits and Systems*, page 4.

Ichiyama, R., Gerasimenko, Y. P., Zhong, H., Roy, R., and Edgerton, V. (2005). Hindlimb stepping movements in complete spinal rats induced by epidural spinal cord stimulation. *Neuroscience letters*, 383(3):339–344.

Jackson, A. and Zimmermann, J. B. (2012). Neural interfaces for the brain and spinal cord—restoring motor function. *Nature Reviews Neurology*, 8(12):690–699.

Jarrett, M., Mowatt, G., Glazener, C., Fraser, C., Nicholls, R., Grant, A., and Kamm, M. (2004). Systematic review of sacral nerve stimulation for faecal incontinence and constipation. *British Journal of Surgery*, 91(12):1559–1569.

Jiang, D., Demosthenous, A., Cirmirakis, D., Perkins, T., and Donaldson, N. (2010). Design of a stimulator asic for an implantable vestibular neural prosthesis. In *Biomedical Circuits and Systems Conference (BioCAS), 2010 IEEE*, pages 206–209.

Jiang, D., Demosthenous, A., Perkins, T. A., Liu, X., and Donaldson, N. (2012). An Implantable 3-D Vestibular Stimulator with Neural Recording. *ESSCIRC (ESSCIRC), 2012 Proceedings of the*, 1(1):4.

Johansen, T. A. and Foss, B. A. (1995). Identification of non-linear system structure and parameters using regime decomposition. *Automatica*, 31(2):321–326.

John, J. K., Kim, E., Tu, H., Zhang, J., Loeb, J. A., and Xu, Y. (2013). Multifunctional chronic 3d electrode arrays based on a simple folding process. In *Solid-State Sensors, Actuators and Microsystems (TRANSDUCERS & EUROSENSORS XXVII), 2013 Transducers & Eurosensors XXVII: The 17th International Conference on*, pages 1476–1479. IEEE.

Joucla, S., Ambroise, M., Levi, T., Lafon, T., Chauvet, P., Rousseau, L., Lissorgues, G., Saïghi, S., Bornat, Y., Lewis, N., Renaud, S., and Yvert, B. (2013). Generation of locomotor-like activity in the isolated rat spinal cord by electrical microstimulations driven by an artificial CPG. In *2013 IEEE Neural Eng. Short Pap. No. 0079*, page 5218.

Joucla, S., Rousseau, L., and Yvert, B. (2012). Focalizing electrical neural stimulation with penetrating microelectrode arrays: A modeling study. *Journal of Neuroscience Methods*, 209(1):250 – 254.

Joucla, S. and Yvert, B. (2012). Modeling extracellular electrical neural stimulation: from basic understanding to mea-based applications. *Journal of Physiology-Paris*, 106(3):146–158.

Kandel, E. R., Schwartz, J. H., Jessell, T. M., et al. (2000). *Principles of neural science*, volume 4. McGraw-Hill New York.

Kelly, S. K. and Wyatt, J. L. (2011). A power-efficient neural tissue stimulator with energy recovery. *Biomedical Circuits and Systems, IEEE Transactions on*, 5(1):20–29.

Kerner, Z. and Pajkossy, T. (1998). Impedance of rough capacitive electrodes: the role of surface disorder. *Journal of Electroanalytical Chemistry*, 448(1):139–142.

Kiani, M. and Ghovanloo, M. (2013). A figure-of-merit for designing high-performance inductive power transmission links. *Industrial Electronics, IEEE Transactions on*, 60(11):5292–5305.

KIN450 (2009). Synaptic transmission. http://kin450-neurophysiology.wikispaces.com/Synaptic+Transmission.

Kjaerulff, O. and Kiehn, O. (1996). Distribution of networks generating and coordinating locomotor activity in the neonatal rat spinal cord in vitro: a lesion study. *The Journal of neuroscience*, 16(18):5777–5794.

Kleiner-Fisman, G., Herzog, J., Fisman, D. N., Tamma, F., Lyons, K. E., Pahwa, R., Lang, A. E., and Deuschl, G. (2006). Subthalamic nucleus deep brain stimulation: summary and meta-analysis of outcomes. *Mov. Disord.*, 21 Suppl 1:S290–304.

Knaipp, M., Park, J. M., and Vescoli, V. (2006). Evolution of a cmos based lateral high voltage technology concept. *Microelectronics journal*, 37(3):243–248.

Kolbl, F., Sabatier, J., N'Kaoua, G., Naudet, F., Faggiani, E., Benazzouz, A., Renaud, S., and Lewis, N. (2013). Characterization of a non linear fractional model of electrode-tissue impedance for neuronal stimulation. In *2013 IEEE Biomed. Circuits Syst. Conf.*, pages 338–341. IEEE.

Kovacs, G. T. (1994). Introduction to the theory, design, and modeling of thin-film microelectrodes for neural interfaces.

Langlois, P. J., Demosthenous, A., Pachnis, I., and Donaldson, N. (2010). High-power integrated stimulator output stages with floating discharge over a wide voltage range for nerve stimulation. *IEEE Trans. Biomed. Circuits Syst.*, 4(1):39–48.

Latham, R. (2004). Biomedical applications of batteries. *Solid State Ionics*, 172(1-4):7–11.

Lee, H.-M., Park, H., and Ghovanloo, M. (2013). A Power-Efficient WIreless System With Adaptive Supply Control for Deep Brain Stimulation. *IEEE Journal of Solid-State Circuits*, 48(9):14.

Lee, J., Rhew, H. G., Kipke, D., and Flynn, M. (2008). A 64 Channel Programmable Closed-loop Deep Brain Stimulator with 8 Channel Neural Amplifier and Logarithmic ADC. *2008 Symposium on VLSI Circuits Digest of Technical Papers*, page 2.

Lee, J., Rhew, H.-G., Kipke, D. R., and Flynn, M. P. (2010). A 64 Channel Programmable Closed-Loop Neurostimulator With 8 Channel Neural Amplifier and Logarithmic ADC. *IEEE J. Solid-State Circuits*, 45(9):1935–1945.

Lempka, S. F., Miocinovic, S., Johnson, M. D., Vitek, J. L., and McIntyre, C. C. (2009a). In vivo impedance spectroscopy of deep brain stimulation electrodes. *J. Neural Eng.*, 6(4):046001.

Lempka, S. F., Miocinovic, S., Johnson, M. D., Vitek, J. L., and McIntyre, C. C. (2009b). In vivo impedance spectroscopy of deep brain stimulation electrodes. *Journal of neural engineering*, 6(4):046001.

Lenzlinger, M. and Snow, E. (1969). Fowler-nordheim tunneling into thermally grown sio2. *Journal of Applied Physics*, 40(1):278–283.

Limousin, P., Pollak, P., Benazzouz, A., Hoffmann, D., Le Bas, J., Perret, J., Benabid, A., and Broussolle, E. (1995a). Effect on parkinsonian signs and symptoms of bilateral subthalamic nucleus stimulation. *The Lancet*, 345(8942):91–95.

Limousin, P., Pollak, P., Benazzouz, A., Hoffmann, D., Le Bas, J. F., Broussolle, E., Perret, J. E., and Benabid, A. L. (1995b). Effect of parkinsonian signs and symptoms of bilateral subthalamic nucleus stimulation. *Lancet*, 345(8942):91–5.

Linderoth, B. and Foreman, R. D. (1999). Physiology of spinal cord stimulation: review and update. *Neuromodulation: Technology at the Neural Interface*, 2(3):150–164.

Liu, W., Vichienchom, K., Clements, M., DeMarco, S. C., Hughes, C., McGucken, E., Humayun, M. S., de Juan, E., Weilan, S. D., and Greenberg, R. (2000). A Neuro-Stimulus Chip with Telemetry Unit for Retinal Prosthetic Device. *IEEE Journal of Solid-State Circuits*, 35(10):11.

Liu, X., Demosthenous, A., and Donaldson, N. (2006). A Stimulator Output Stage with Capacitor Reduction and Failure-Checking Techniques. *IEEE ISCAS*, page 4.

Liu, X., Demosthenous, A., and Donaldson, N. (2008). Five valuable functions of blocking capacitors in stimulators. In *13th Annu. Int. Conf. FES Soc.*, pages 322–324.

Liu, X., Demosthenous, A., and Donaldson, N. (2011). An integrated Stimulator With DC-Isolation and Fine Current Control for Implanted Nerve Tripoles. *IEEE Journal of Solid-State Circuits*, 46(7):14.

Liu, X., Demosthenous, A., Vanhoestenberghe, A., Jiang, D., and Donaldson, N. (2012). Active Books: The Design of an Implantable Stimulator That Minimizes Cable Count Using Integrated Circuits Very Close to Electrodes. *IEEE Transactions on Biomedical Circuits and Systems*, 6(3):12.

Mantilla, C. B. and Sieck, G. C. (2011). Phrenic motor unit recruitment during ventilatory and non-ventilatory behaviors. *Respiratory physiology & neurobiology*, 179(1):57–63.

Margalit, E., Maia, M., Weiland, J. D., Greenberg, R. J., Fujii, G. Y., Torres, G., Piyathaisere, D. V., O'Hearn, T. M., Liu, W., Lazzi, G., et al. (2002). Retinal prosthesis for the blind. *Survey of ophthalmology*, 47(4):335–356.

Matsumura, H., Kinoshita, G., Satoh, S., Osaka, T., and Hayaishi, O. (1995). A novel apparatus that permits multiple routes for infusions and body-fluid collections in a freely-moving animal. *J. Neurosci. Methods*, 57(2):145–9.

Matteucci, C. (1842). *Deuxième mémoire sur le courant électrique propre de la grénouille et sur celui des animaux à sang chaud*.

Maxwell, J. C. (1863). A dynamical theory of the electromagnetic field. *Proceedings of the Royal Society of London*, 13:531–536.

Mayberg, H. S., Lozano, A. M., Voon, V., McNeely, H. E., Seminowicz, D., Hamani, C., Schwalb, J. M., and Kennedy, S. H. (2005). Deep brain stimulation for treatment-resistant depression. *Neuron*, 45(5):651–660.

McAdams, E. and Jossinet, J. (1995). Tissue impedance: a historical overview. *Physiological measurement*, 16(3A):A1.

McAdams, E., Lackermeier, A., McLaughlin, J., Macken, D., and Jossinet, J. (1995). The linear and non-linear electrical properties of the electrode-electrolyte interface. *Biosensors and Bioelectronics*, 10(1):67–74.

McCreery, D. B., Agnew, W. F., Yuen, T. G., and Bullara, L. (1990). Charge density and charge per phase as cofactors in neural injury induced by electrical stimulation. *Biomedical Engineering, IEEE Transactions on*, 37(10):996–1001.

McNeal, D. R. (1976). Analysis of a model for excitation of myelinated nerve. *Biomedical Engineering, IEEE Transactions on*, (4):329–337.

Meissner, W., Gross, C. E., Harnack, D., Bioulac, B., and Benazzouz, A. (2004). Deep brain stimulation for parkinson's disease: Potential risk of tissue damage associated with external stimulation. *Annals of neurology*, 55(3):449–450.

Merrill, D. R., Bikson, M., and Jefferys, J. G. (2005a). Electrical stimulation of excitable tissue: design of efficacious and safe protocols. *Journal of neuroscience methods*, 141(2):171–198.

Merrill, D. R., Bikson, M., and Jefferys, J. G. R. (2005b). Electrical stimulation of excitable tissue: design of efficacious and safe protocols. *J. Neurosci. Methods*, 141(2):171–98.

Minassian, K., Persy, I., Rattay, F., Pinter, M. M., Kern, H., and Dimitrijevic, M. R. (2007). Human lumbar cord circuitries can be activated by extrinsic tonic input to generate locomotor-like activity. *Human movement science*, 26(2):275–295.

Nadeau, P. and Sawan, M. (2006). A flexible high voltage biphasic current-controlled stimulator. *IEEE*, page 4.

Nguyen, Q. V., Caro, A., Raoux, M., Quotb, A., Floderer, J.-B., Bornat, Y., Renaud, S., and Lang, J. (2013). A novel bioelectronic glucose sensor to process distinct electrical activities of pancreatic beta-cells. In *Engineering in Medicine and Biology Society (EMBC), 2013 35th Annual International Conference of the IEEE*, pages 172–175.

Nishimura, Y., Perlmutter, S. I., and Fetz, E. E. (2013). Restoration of upper limb movement via artificial corticospinal and musculospinal connections in a monkey with spinal cord injury. *Frontiers in neural circuits*, 7.

Nonclercq, A., Lonys, L., Vanhoestenberghe, A., Demosthenous, A., and Donaldson, N. (2012). Safety of multi-channel stimulation implants: a single blocking capacitor per channel is not sufficient after single-fault failure. *Med. Biol. Engineering and Computing*, 50(4):403–410.

Noorsal, E., Sooksood, K., Xu, H., Hornig, R., Becker, J., and Ortmanns, M. (2012). A Neural Stimulator Frontend With High-Voltage Compliance and Programmable Pulse Shape for Epiretinal Implants. *IEEE J. Solid-State Circuits*, 47(1):244–256.

Normann, R. A. (2003). Microfabricated electrode arrays for restoring lost sensory and motor functions. In *TRANSDUCERS, Solid-State Sensors, Actuators and Microsystems, 12th International Conference on, 2003*, volume 2, pages 959–962. IEEE.

Nowak, K., Mix, E., Gimsa, J., Strauss, U., Sriperumbudur, K. K., Benecke, R., and Gimsa, U. (2011). Optimizing a rodent model of Parkinson's disease for exploring the effects and mechanisms of deep brain stimulation. *Parkinsons. Dis.*, 2011:414682.

Onders, R. P., Elmo, M., Khansarinia, S., Bowman, B., Yee, J., Bass, B., Dunkin, B., Ingvarsson, P. E., Oddsdóttir, M., et al. (2009). Complete worldwide operative experience in laparoscopic diaphragm pacing: results and differences in spinal cord injured patients and amyotrophic lateral sclerosis patients. *Surgical endoscopy*, 23(7):1433–1440.

Ortmanns, M., Rocke, A., Gehrke, M., and Tiedkte, H.-J. (2007). A 232-Channel Epiretinal Stimulator ASIC. *IEEE Journal of Solid-State Circuits*, 42(12):14.

Oustaloup, A., Levron, F., Mathieu, B., and Nanot, F. M. (2000). Frequency-band complex noninteger differentiator: characterization and synthesis. *Circuits and Systems I: Fundamental Theory and Applications, IEEE Transactions on*, 47(1):25–39.

Planck, M. (1890). Ueber die potentialdifferenz zwischen zwei verdünnten lösungen binärer electrolyte. *Annalen der Physik*, 276(8):561–576.

Plonsey, R. and Barr, R. C. (2007). *Bioelectricity A quantitative approach*. Springer.

Podlubny, I. (1998). *Fractional differential equations: an introduction to fractional derivatives, fractional differential equations, to methods of their solution and some of their applications*, volume 198. Academic press.

Qian, X., Hao, H., Ma, B., Wen, X., and Li, L. (2011). Study on DBS device for small animals. *Conf. Proc. IEEE Eng. Med. Biol. Soc.*, 2011:6773–6.

Randles, J. (1947). Kinetics of rapid electrode reactions. *Discussions of the faraday society*, 1:11–19.

Rattay, F. (1986). Analysis of models for external stimulation of axons. *Biomedical Engineering, IEEE Transactions on*, (10):974–977.

Rattay, F. (1989). Analysis of models for extracellular fiber stimulation. *Biomedical Engineering, IEEE Transactions on*, 36(7):676–682.

Rieu, I., Derost, P., Ulla, M., Marques, A., Debilly, B., De Chazeron, I., Chéreau, I., Lemaire, J. J., Boirie, Y., Llorca, P. M., and Durif, F. (2011). Body weight gain and deep brain stimulation. *J. Neurol. Sci.*, 310(1-2):267–70.

Russold, M. and Jarvis, J. C. (2007). Implantable stimulator featuring multiple programs, adjustable stimulation amplitude and bi-directional communication for implantation in mice. *Med. Biol. Eng. Comput.*, 45(7):695–9.

Sahin, M. and Tie, Y. (2007). Non-rectangular waveforms for neural stimulation with practical electrodes. *Journal of neural engineering*, 4(3):227.

Sapoval, B. (1995). Linear and non-linear behavior of fractal and irregular electrodes. *Solid State Ionics*, 75:269–273.

Scaramuzza, M., Ferrario, A., Pasqualotto, E., and Toni, A. D. (2012). Development of an electrode/electrolyte interface model based on pseudo-distributed elements combining comsol, {MATLAB} and {HSPICE}. *Procedia Chemistry*, 6(0):69 – 78. 2nd International Conference on Bio-Sensing Technology.

Schallert, T., Fleming, S. M., Leasure, J. L., Tillerson, J. L., and Bland, S. T. (2000). Cns plasticity and assessment of forelimb sensorimotor outcome in unilateral rat models of stroke, cortical ablation, parkinsonism and spinal cord injury. *neuropharmacology*, 39(5):777–787.

Schlottmann, C. R., Petre, C., and Hasler, P. E. (2012). A High-Level Simulink-Based Tool for FPAA Configuration. *IEEE Trans. Very Large Scale Integr. Syst.*, 20(1):10–18.

Schmidt, C. L. and Skarstad, P. M. (2001). The future of lithium and lithium-ion batteries in implantable medical devices. *J. Power Sources*, 97-98:742–746.

Sclafani, A. and Ackroff, K. (2003). Reinforcement value of sucrose measured by progressive ratio operant licking in the rat. *Physiol. Behav.*, 79(4-5):663–70.

Shahrokhi, F., Abdelhalim, K., Serletis, D., Carlen, P. L., and Genov, R. (2010). The 128-Channel Fully Differential Digital Integrated Neural Recording and Stimulation Interface. *IEEE Transactions on Biomedical Circuits and Systems*, 4(3):13.

Shannon, R. V. (1992). A model of safe levels for electrical stimulation. *Biomedical Engineering, IEEE Transactions on*, 39(4):424–426.

Shapero, S. and Hasler, P. (2012). Neuromorphic hardware for rapid sparse coding. In *Biomedical Circuits and Systems Conference (BioCAS), 2012 IEEE*, pages 396–399.

Shen, D.-L. and Chu, Y.-J. (2010). A linearized current stimulator for deep brain stimulation. *Conf. Proc. IEEE Eng. Med. Biol. Soc.*, 2010:6485–8.

Shulyzki, R., Abdelhalim, K., and Genov, R. (2010). CMOS current-copying neural stimulator with OTA-sharing. In *Proc. 2010 IEEE Int. Symp. Circuits Syst.*, pages 1232–1235. IEEE.

Sit, J.-J. and Sarpeshkar, R. (2007). A Low-Power Blocking-Capacitor-Free Charge-Balanced Electrode-Stimulator Chip With Less Than 6 nA DC Error for 1-mA Full-Scale Stimulation. *IEEE Trans. Biomed. Circuits Syst.*, 1(3):172–83.

Sivarprakasam, M., Liu, W., Humayun, M., and Weiland, J. D. (2005). A Variable Range Bi-phasic Current Stimulus Driver Circuitry for an Implantable Retinal Prosthetic Device. *IEEE Journal of Solid-State Circuits*, 40(3):9.

Song, D., Chan, R. H., Marmarelis, V. Z., Hampson, R. E., Deadwyler, S. A., and Berger, T. W. (2009). Nonlinear modeling of neural population dynamics for hippocampal prostheses. *Neural Networks*, 22(9):1340–1351.

Soulier, F., Lerat, J.-B., Gouyet, L., Bernard, S., and Cathébras, G. (2008). A Neural Stimulator Output Stage for Dodecapolar Electrodes. In *2008 IEEE Comput. Soc. Annu. Symp. VLSI*, pages 487–490. IEEE.

Spieles-Engemann, A. L., Behbehani, M. M., Collier, T. J., Wohlgenant, S. L., Steece-Collier, K., Paumier, K., Daley, B. F., Gombash, S., Madhavan, L., Mandybur, G. T., Lipton, J. W., Terpstra, B. T., and Sortwell, C. E. (2010). Stimulation of the rat subthalamic nucleus is neuroprotective following significant nigral dopamine neuron loss. *Neurobiol. Dis.*, 39(1):105–15.

Srinivasan, V., Graham, D. W., and Hasler, P. (2005). Floating-gates transistors for precision analog circuit design: an overview. In *Circuits and Systems, 2005. 48th Midwest Symposium on*, pages 71–74. IEEE.

Steyaert, M. and Sansen, W. (1987). A micropower low-noise monolithic instrumentation amplifier for medical purposes. *Solid-State Circuits, IEEE Journal of*, 22(6):1163–1168.

Suaning, G. J. and Lovell, N. H. (2001). CMOS Neurostimulation ASIC with 100 CHannels, Scaleable Output, and Bidirectional Radio-Frequency Telemetry. *IEEE Transactions on Biomedical Engineering*, 48(2):13.

Swammerdam, J. (1758). Biblia naturae. *Leyden: Isaack Severinus, Boubowyn Vander and Peter Vander. Translated in*.

Tan, J. Y. J., Liu, X., Wee, K. H., Yen, S. C., Xu, Y. P., and Tan, T. C. (2011). A Monolithic Programmable Nerve/ Muscle Stimulator.

Techer, S. D., Bernard, S., Bertrand, Y., Cathébras, G., and Guiraud, D. (2004). New Implantable Stimulator for the FES of Paralyzed Muscles. *Solid-State Circuits Conference, 2004. ESSCIRC 2004. Proceeding of the 30th European*, page 4.

Tokuda, T., Hiyama, K., Sawamura, S., Sasagawa, K., Terasawa, Y., Nishida, K., Kitaguch, Y., Fujikado, T., Tano, Y., and Ohta, J. (2009). CMOS-Based Multichip Networked Flexible Retinal Stimulator Designed for Image-Based Retinal Prosthesis. *IEEE Trans. Electron Devices*, 56(11):2577–2585.

Töreyin, H. and Bhatti, P. (2012). Low-Power Vestibular Signal Processing Circuitry Utilizing a Filed-Programmable Analog Array. *IEEE Transactions on Biomedical Circuits and Systems*, 7(3):6.

Troyk, P. R., Meshahwar, V. K., Stein, R. B., Suh, S., and Everaert, D. (2012). An Implantable Neural Stimulator for Intraspinal MicroStimulation. *34th Annual International Conference of the IEEE EMBS*, 1(1):4.

Ungerstedt, U. (1968). 6-Hydroxy-dopamine induced degeneration of central monoamine neurons. *Eur. J. Pharmacol.*, 5(1):107–10.

Valente, V., Demosthenous, A., and Bayford, R. (2010). Design of a Current-Steering Implantable Stimulator with Electric Field Shifting for Deep Brain Stimulation. *IEEE*, page 4.

Valente, V., Demosthenous, A., and Bayford, R. (2012). A Tripolar Current-Steerin Stimulator ASIC for Field Shaping in Deep Brain Stimulation. *IEEE Transactions on Biomedical Circuits and Systems*, 6(3):11.

van Dongen, M. and Serdijn, W. A. (2010). Design of a low power 100 dB dynamic range integrator for an implantable neural stimulator. In *2010 Biomed. Circuits Syst. Conf.*, pages 158–161. IEEE.

Vidal, J. and Ghovanloo, M. (2010). Towards a Switched-Capacitor Based Stimulator for Efficient Deep-Brain Stimulation.

Volkmann, J., Moro, E., and Pahwa, R. (2006). Basic algorithms for the programming of deep brain stimulation in Parkinson's disease. *Mov. Disord.*, 21 Suppl 1:S284–9.

Volta, A. (1800). On the electricity excited by the mere contact of conducting substances of different kinds. in a letter from mr. alexander volta, frs professor of natural philosophy in the university of pavia, to the rt. hon. sir joseph banks, bart. kbprs. *Philosophical Transactions of the Royal Society of London*, pages 403–431.

von Dongen, M. N. and Serdijn, W. A. (2013). A Switched-Mode Multichannel Neural Stimlulator with a Minimum Number of External Components. *Circuits and Systems (ISCAS), 2013 IEEE International Symposium on*, page 4.

Walden, R. H. (1994). Analog-to-digital converter technology comparison. In *Gallium Arsenide Integrated Circuit (GaAs IC) Symposium, 1994. Technical Digest 1994., 16th Annual*, pages 217–219. IEEE.

Walden, R. H. (1999). Analog-to-digital converter survey and analysis. *Selected Areas in Communications, IEEE Journal on*, 17(4):539–550.

Wall Iii, C., Merfeld, D., Rauch, S., and Black, F. (2003). Vestibular prostheses: the engineering and biomedical issues. *Journal of Vestibular Research*, 12(2):95–113.

Walter, J. S., Wurster, R. D., Zhu, Q., and Laghi, F. (2011). Respiratory muscle pacing with chronically implanted intramuscular permaloc electrodes: A feasibility study. *J Rehabil Res Dev*, 48(2):103–114.

Wang, R., Huang, X., Liu, G., Wang, W., Dong, F., and Li, Z. (2010). Fabrication and characterization of a parylene-based three-dimensional microelectrode array for use in retinal prosthesis. *Microelectromechanical Systems, Journal of*, 19(2):367–374.

Wang, T.-Y., Lai, M.-R., Twigg, C., and Peng, S.-Y. (2014). A fully reconfigurable low-noise biopotential sensing amplifier with 1.96 noise efficiency factor. *Biomedical Circuits and Systems, IEEE Transactions on*, 8(3):411–422.

Wei, X. and Liu, J. (2008). Power sources and electrical recharging strategies for implantable medical devices. *Front. Energy Power Eng. China*, 2(1):1–13.

Weinberg, A. M. (1961). Impact of large-scale science on the united states big science is here to stay, but we have yet to make the hard financial and educational choices it imposes. *Science*, 134(3473):161–164.

Williams, I. and Constandinou, T. G. (2013). An Energy-Efficient, Dynamic VOltage Scaling Neural Stimulator for a Proprioceptive Prosthesis. *IEEE Transactions on Biomedical Circuits and Systems*, 7(2):10.

Wilson, B. S. and Dorman, M. F. (2008). Cochlear implants: a remarkable past and a brilliant future. *Hearing research*, 242(1):3–21.

Wise, K. D., Sodagar, A. M., Yao, Y., Gulari, M. N., Perlin, G. E., and Najafi, K. (2008). Microelectrodes, microelectronics, and implantable neural microsystems. *Proceedings of the IEEE*, 96(7):1184–1202.

Wu, H.-C., Young, S.-T., and Kuo, T.-S. (2002). A versatile multichannel direct-synthesized electrical stimulator for fes applications. *Instrumentation and Measurement, IEEE Transactions on*, 51(1):2–9.

Wu, Y.-N., Hyland, B. I., and Chen, J.-J. J. (2007). Biomechanical and electromyogram characterization of neuroleptic-induced rigidity in the rat. *Neuroscience*, 147(1):183–96.

Yoo, C. and Park, J. (2007). Cmos current reference with supply and temperature compensation. *Electronics Letters*, 43(25):1422–1424.

Zbrzeski, A., Hasler, P., Kölbl, F., Syed, E., Lewis, N., and Renaud, S. (2010). A programmable bioamplifier on fpaa for in vivo neural recording. In *Biomedical Circuits and Systems Conference (BioCAS), 2010 IEEE*, pages 114–117.

Zeng, F.-G., Rebscher, S., Harrison, W., Sun, X., and Feng, H. (2008). Cochlear implants: system design, integration, and evaluation. *Biomedical Engineering, IEEE Reviews in*, 1:115–142.

Zhang, Y., Langforda, B., and Kozhevnikov, A. (2011). A simple miniature device for wireless stimulation of neural circuits in small behaving animals. *Journal of Neuroscience Methods*, 202:8.

Zheng, L., Shin, S., and Kang, S.-M. S. (2012). Design of a Neural Stimulator System with Closed-Loop Charge Cancellation. *VLSI and System-on-Chip (VLSI-SoC), 2012 IEEE/IFIP 20th International Conference on*, page 6.